A MODEL FOR NONLINEAR ELECTROKINETICS IN ELECTRIC FIELD GUIDED ASSEMBLY OF COLLOIDS

A Dissertation

by

JAMES G. STEUBER

Submitted to the Office of Graduate Studies of
Texas A&M University
in partial fulfillment of the requirements for the degree of

DOCTOR OF PHILOSOPHY

December 2009

Major Subject: Mechanical Engineering

A MODEL FOR NONLINEAR ELECTROKINETICS IN ELECTRIC FIELD GUIDED ASSEMBLY OF COLLOIDS

A Dissertation

by

JAMES G. STEUBER

Submitted to the Office of Graduate Studies of
Texas A&M University
in partial fulfillment of the requirements for the degree of

DOCTOR OF PHILOSOPHY

Approved by:

Chair of Committee,	J.N. Reddy
Committee Members,	Debjyoti Banerjee
	Anastasia Muliana
	James G. Boyd
Head of Department,	Dennis O'Neal

December 2009

Major Subject: Mechanical Engineering

ABSTRACT

A Model for Nonlinear Electrokinetics in Electric Field

Guided Assembly of Colloids. (December 2009)

James G. Steuber, B.S., Arkansas Tech University;

M.EN., Texas A&M University

Chair of Advisory Committee: Dr. J.N. Reddy

Electric field guided assembly of colloids is a new area of research in colloidal science where sub-micrometer particles, or colloids, are assembled using patterned electrodes. The design of these devices is often limited by an inability to characterize accurately forces and fluxes with linearized electrokinetic theory. The research presented in this dissertation describes an application of the finite element method to the nonlinear electrokinetic equations. The finite element model thus developed is then used to describe the nonlinear electrophoretic mobility of a dilute colloidal dispersion, investigate hydrodynamic and electric particle-particle interactions, and characterize particle-surface interactions. The effect of Stern layer conduction on the electrophoretic mobility and dielectric response is included using the generalized dynamic Stern layer model. The electrokinetic force is calculated using the Maxwell stress tensor method rather than the effective dipole method as it is more consistent with nonlinear electrokinetic theory.

Significant results of this dissertation demonstrate the effect of nonlinear electrokinetic phenomena and extend the present electrokinetic theory. The calculation

of nonlinear electrophoretic mobility of a dilute colloidal dispersion, which is valid for arbitrary particle surface charge or zeta potential, applied (AC) electric field strength, and applied AC electric field frequency. Also, the adsorption isotherm used by the generalized dynamic Stern layer theory is extended to include non-equilibrium reaction kinetics. This results in a model for Stern layer conduction which is valid for frequencies above 1 MHz. The utilization of the Maxwell stress tensor method results in a finite element model which is valid for arbitrary electric field strength and includes the effects of traveling-wave dielectrophoresis a nonlinear electrokinetic phenomena resulting from non-uniform electric field phase.

DEDICATION

This dissertation is dedicated to my son, Alex James, and my daughter, Emma Kay and to their mother, Lorie Ann, a woman I have loved my entire life. There is nothing more important to me than your love.

I dedicate the preparation of this document to my brother, Scott, and my sisters, Christie, Leanna, and Traci. I hope the presentation of my work makes you as proud of me as I am of all of you.

I dedicate the long nights spent at the computer producing results to my mother, Judith, who raised us by herself without ever complaining. I hope my effort reflects the great effort you made in raising us kids.

I dedicate the discussion of results to my aunt, Paula Phillips, who always encouraged and supported my college education. Thank you.

I dedicate the conclusions of this work to my grand-father, Herman George Steuber, a great man, of high intellect, whom I hold in great respect even though I was quite young when he died.

I dedicate the introduction to my grandmother, Pauline Phillips, whom I loved dearly. I miss you and hope that my dedication to being a loving father and husband reflects the love and attention you showed me.

TABLE OF CONTENTS

Page

LIST OF FIGURES

Page

Page

Page

Page

Page

Page

Page

Page

Page

Page

LIST OF TABLES

1 INTRODUCTION

The electric field guided assembly of colloids suspended in aqueous solution has found application in several areas of research since Green and Morgan[1] first concentrated latex particles using dielectrophoresis. Dielectrophoresis is an important nonlinear electrokinetic phenomenon that has opened up new areas of research. Dielectrophoretic assembly has been used by the medical research community to concentrate human cancer cells in lab-on-a-chip microfluidic devices[2]. These devices allow very small amounts of blood to be drawn from a patient for diagnostics. Also, the dielectrophoretic assembly of nano-wires[3, 4] has found application in both nanofabrication and micro-electro-mechanical-systems (MEMS).

The research reported in the following is motivated by the inability of the linear electrokinetic theory to describe nonlinear effects observed in colloidal assembly. However, the objectives in the following section outline the development of a finite element model for nonlinear electrokinetics with colloidal assembly in mind. To complete the finite element model one need only develop a method to handle the computational cost associated with representing the thousands of particles involved in colloidal assembly. For example, the cell model has been recently introduced to the linear electrokinetic theory to develop models for the mobility of concentrated colloidal dispersions [5-8]. However, more development is needed before the cell model might be implemented in a nonlinear electrokinetic finite element model.

This dissertation follows the Journal of Colloid and Interface Science.

1.1 OBJECTIVES

The ability to describe electric field guided assembly of colloids and characterize the stable structures resulting from assembly depends on the accurate calculation of electrokinetic forces and fluxes. Their accurate calculation in turn depends on capturing the distribution of electric potential, charge, and fluid velocity in a thin layer ($\sim$100 nm) adjacent to the particle surface called the electric double layer. It is the objective of this study to develop a robust finite element model that accurately calculates electrokinetic forces and fluxes by resolving the electric double layer and solving the full electrokinetic equations directly without linearization or limiting assumptions.

The model thus developed is then used to; describe the electric double layer in an applied electric field, determine the nonlinear electrophoretic mobility of a dilute colloidal dispersion, and investigate hydrodynamic and electric particle-particle and particle-surface interactions. A parametric study is then completed to determine the key parameters for directed assembly of colloidal structures.

1.2 SIGNIFICANCE

A robust electrokinetic finite element model will serve a micro/nano-electro-mechanical research community that is finding new applications for colloidal microfluidic devices every day. Most applications involve large non-uniform AC electric fields which induce nonlinear electrokinetic effects that have only recently gained wide attention due to their prevalence in these new applications. In the short term, such a model will provide experimental researchers a tool to synergistically design devices coupling experiment with finite element analysis. In the long term, the general

framework of the finite element formulation allows improvements to be made in a modular fashion as more information about the electrochemistry of the interface or governing theory develops.

1.3 OUTLINE OF THE DISSERTATION

In the exposition that follows we present the development of the nonlinear electrokinetic finite element model. In Section 2 the electric double layer is described, the linear and nonlinear electrokinetic theory is presented, and the generalized dynamic Stern layer theory is reviewed. Also in Section 2, the Maxwell stress tensor method is presented as the most general way to calculate electrokinetic forces acting on a particle. In Section 3 the finite element equations are developed and the implementation is discussed. In Sections 4-7 the results of the electrokinetic finite element model are presented and discussed. In Section 4 we present and discuss the finite element solution of the electric double layer which is described in Section 2.1. In Section 5 we investigate the nonlinear electrophoretic mobility of a dilute colloidal dispersion. In Section 6 the hydrodynamic and electric particle-particle interaction forces are calculated and compared with those calculated using the DLVO model[9, 10]. In Section 7 the electrokinetic forces leading to colloidal assembly are characterized for a single particle in a non-uniform electric field near a planar surface/electrode. Finally, a summary of the development of the nonlinear electrokinetic finite element model and the conclusions of this dissertation are presented in Section 8.

2 THEORY

2.1 THE ELECTRIC DOUBLE LAYER

The electric double layer (EDL) is the cloud of charge that forms near the surface of colloids suspended in an electrolyte solution (Figure 1a). It is composed of a diffuse layer were the charges are mobile and a Stern layer were the charges are usually assumed to be fixed[11] (Figure 2). The charge on the surface of the colloid is balanced by the charge of the EDL making the colloid-electrolyte cell electrically neutral. The electroneutrality condition is given by $\sigma^0 + \sigma^i + \sigma^d = 0$, where σ^0 is the surface charge, σ^i is the charge of the Stern layer, and σ^d is the charge of the diffuse layer[12].

In the presence of an applied electric field (Figure 1b), a positive ion traveling toward the negative electrode is accelerated as it approaches and decelerated as it passes a negatively charged particle. Thus, the positive ion cloud around the particle produces an electric field which opposes the applied electric field. In addition, the ions distort the velocity field around the particle as they drag fluid with them. Therefore, the effect of the EDL is to increase viscous drag and decrease the electric force on the particle. The electrical characteristics of a suspension of particles would also be altered by the presence of an EDL as the opposing electric field and decreased mobility of the ions near the particle affect the complex dielectric response and conductivity of the suspension.

An understanding of the EDL is fundamental to every aspect of colloidal science. Modeling of the EDL is essential in colloidal science where one is usually interested in determining the conditions for colloidal stability or determining the electric potential at the slip plane (ζ) from the mobility or dielectric response of colloidal dispersions.

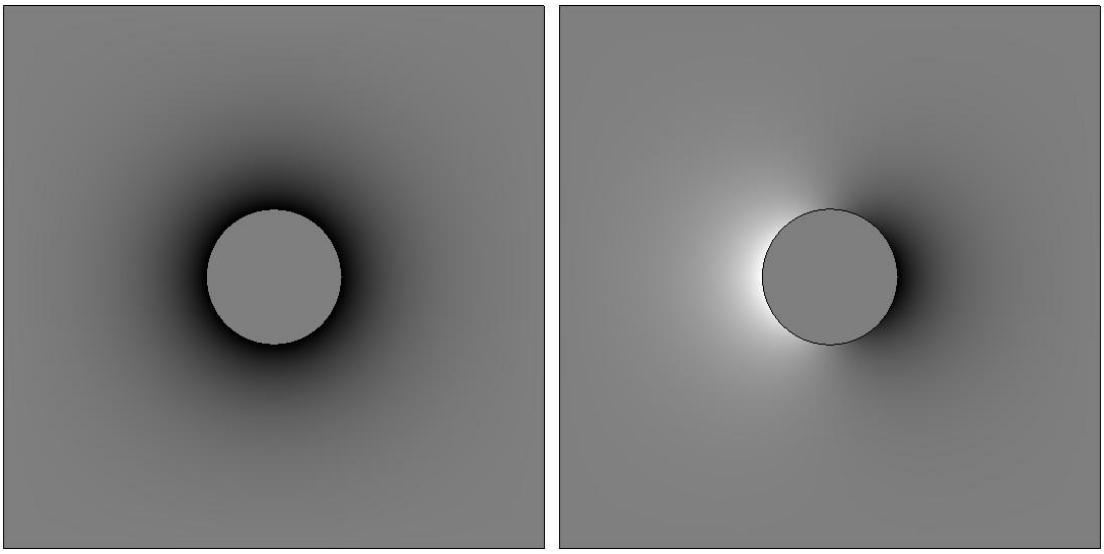

Figure 1: Electric double layer; a) without applied electric field, b) with applied electric field

black = positive charge, white = negative charge, grey = neutral charge

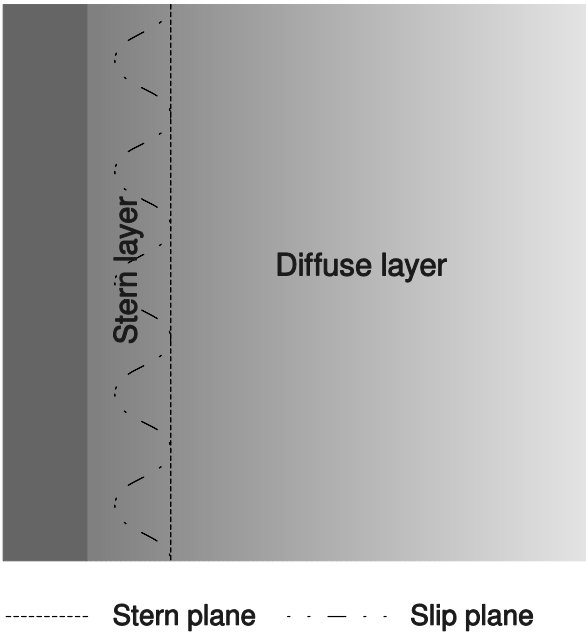

Figure 2: Structure of the electric double layer

2.1.1 Elementary theory of the EDL

Early EDL theories are credited to Helmholtz, Gouy-Chapman, and Stern near the turn of the century. The Gouy-Chapman theory[10] neglects the viscous and inertial forces on the ions in Equation 2.8 of the generalized electrokinetic theory reviewed in Section 2.2. It is further assumed that at some point away from the particle the electric potential and ion number densities are unaffected by the presence of the charged particle, i.e. $\psi \to 0$ & $n_i \to n_i^b$. Thus, by integrating the reduced equilibrium equation with the assumed far field boundary conditions, we have

$$n_i = n_i^b \exp(-z_i e\psi / k_b T) \tag{2.1}$$

Equation 2.1, known as the Boltzmann distribution of the ion number density n_i, is only valid for dilute dispersions of particles with no applied electric field since any interaction of particle EDL's or applied electric field violates the far field boundary condition. Substitution of Equation 2.1 into Equation 2.3 results in the Poisson-Boltzmann equation for electric potential

$$\nabla^2 \psi(\boldsymbol{r}, t) = -\frac{1}{\varepsilon} \sum_{\mathrm{i}} n_i^b z_i e \exp(-z_i e\psi / k_b T) \tag{2.2}$$

This differential equation is nonlinear, so traditionally approximate solutions were found using the Debye-Hückel approximation which uses the first term of the MacLaurin series for $\exp(-\boldsymbol{x}) \approx 1 - \boldsymbol{x}$ resulting in a linear ordinary differential equation for the electric potential valid for very small surface potentials $\psi(0) \cong \zeta \leq 25.7\ mV/z_k$. The Gouy-Chapman model is the solution of the equilibrium EDL as shown in Figure 1a.

2.2 ELECTROKINETIC THEORY

A complete description of a colloid/electrolyte system at time *t*, requires the solution of the electrokinetic potential (ψ), the ion number densities (n_j) and ion drift velocities $(\boldsymbol{v}_j)$, the fluid velocity $(\boldsymbol{u})$, and the pressure (p) at every point $(\boldsymbol{r})$ in the domain[13, 14]. The governing equations of the nonlinear electrokinetic theory are now presented with a short discussion of the intrinsic assumptions and limitations to follow. Finally, we discuss the appropriate boundary conditions (1) at the surface of the colloid and (2) in the far-field.

2.2.1 Governing equations

2.2.1.1 Poisson's equation

$$\nabla^2\psi(\boldsymbol{r},t) = -\frac{\rho(\boldsymbol{r},t)}{\varepsilon}, \tag{2.3}$$

where

$$\rho(\boldsymbol{r},t) = \sum_i z_j e n_j(\boldsymbol{r},t) \tag{2.4}$$

and ε is the permittivity of the medium.

2.2.1.2 Navier-Stokes equations

$$\eta_0\nabla^2\boldsymbol{u} - \nabla p = \rho\nabla\psi + \rho_0\frac{\partial \boldsymbol{u}}{\partial t} \tag{2.5}$$

and

$$\nabla\cdot\boldsymbol{u} = 0 \tag{2.6}$$

where η_0 and ρ_0 are the viscosity and mass density of the medium.

2.2.1.3 Conservation of ionic species equations

The i[th] ionic species obeys the conservation of mass

$$\frac{\partial n_i}{\partial t} + \nabla \cdot (n_i \boldsymbol{v}_i) = 0 \tag{2.7}$$

and Newton's second law of motion

$$-\lambda_i(\boldsymbol{v}_i - \boldsymbol{u}) - z_i e \, \nabla\psi - k_b T \, \nabla \ln n_i = m_i \frac{\partial \boldsymbol{v}_i}{\partial t} \tag{2.8}$$

where λ_i is the drag coefficient, $z_i e$ is the charge of the i^{th} ionic species, k_b is Boltzmann's constant, T is temperature, and m_i is the apparent ionic mass.

It is important to recognize that (1) time varying magnetic displacement fields are assumed to be zero in arriving in Equation 2.3, (2) nonlinear inertial terms are neglected in Equation 2.5, (3) source terms neglected in Equation 2.7, (4) only the viscous drag, electrokinetic, and thermodynamic forces are considered Equation 2.8, and (5) these equations are valid only for the diffuse layer because charges are taken as point charges.

2.2.2 Boundary conditions

To complete the description of the generalized electrokinetic theory, we must define the boundary conditions. Recall, that the electrokinetic equations are not valid for the Stern layer due to the assumption concerning the discreetness of the charge. Therefore, we need the boundary condition at the slipping plane, i.e., the plane between the Stern layer and the diffuse layer. To proceed we must replace the Stern layer with an appropriate boundary condition at the slipping plane using the generalized dynamic

Stern layer (GDSL) theory (Section 2.5). If one does not include a Stern layer model, it is normally assumed that

$$\left.\begin{array}{c}\psi_0 = \zeta \\ \boldsymbol{u} = 0 \\ \boldsymbol{v}_j \cdot \hat{n}\end{array}\right\} \text{ at } \boldsymbol{r} = a \qquad 2.9$$

Except for those EDL theories specifically interested in describing interacting electric double layers, the other boundary condition (away from the particle surface) is a far field type boundary condition as shown in Equation 2.10

$$\psi \to \boldsymbol{E} \cdot \hat{n} \quad \text{and} \quad n_j \to n_j^b \quad \text{as} \quad \boldsymbol{r} \to \infty \qquad 2.10$$

where $\boldsymbol{E}$ is the applied electric field and n_j^b is the bulk number density of the j[th] ionic species.

2.3 LINEARIZED ELECTROKINETIC THEORY

The linearized electrokinetic theories introduce linear expansions of the form

$$\xi(\boldsymbol{r}, t) = \xi^{(0)}(\boldsymbol{r}) + \xi^{(1)}(\boldsymbol{r}, t) + \mathcal{O}(\langle \boldsymbol{E}(t) \rangle^2) \qquad 2.11$$

where $\xi(\boldsymbol{r}, t)$ represents the field variables $\psi, \boldsymbol{u}, n_j,$ or p. In this way the linearized electrokinetic theories are first order approximations for the mobility and dielectric response of colloidal dispersions to an applied electric field. O'Brien and White[13] developed a method (O-W theory) to determine the zeta potential (ζ) from experimentally determined electrophoretic mobility (μ). They used perturbation theory (Equation 2.11) to linearize the electrokinetic equations based on the assumption that the applied electric field $\boldsymbol{E}$ is much less than the opposing electric field in the double layer.

After linearizing the equations they decomposed the problem into two simpler problems, as discussed below.

Problem U: Calculate the force required to move the particle at velocity $\boldsymbol{U}$ with no applied electric field.

Problem E: Calculate the force required to hold the particle fixed in the presence of an applied field $\boldsymbol{E}$.

Then $\psi, \boldsymbol{u}$, and $\boldsymbol{U}$ are determined with the additional constraint that the sum of these two forces is zero

$$F^{(1)} + F^{(2)} = 0 \quad \Longrightarrow \quad \alpha \boldsymbol{U} + \beta \boldsymbol{E} = 0 \tag{2.12}$$

Hence, the mobility is

$$\mu(\zeta, \kappa a) = -\frac{\beta}{\alpha} \tag{2.13}$$

Using linearity, they also show that the mobility is not a function of the electrostatic surface boundary condition or the permittivity of the particle. Recognizing this, the authors introduce the function Φ_{i} which further decouples the equations and is used in subsequent electrophoresis theories. Their results show the existence of a mobility maximum for $\kappa a \geq 3$ at $e\zeta/k_b T \approx 5/z_i$ where κa is the dimensionless particle radius and $e\zeta/k_b T$ is the dimensionless zeta potential. The theoretically determined maximum electrophoretic mobility can be compared with experimentally observed maximum as a validation of the model.

Although the O-W theory included a method to validate the theory experimentally based on the existence a mobility maximum, the large zeta potentials required $\zeta \geq 125\ mV/z_i$ prevented such a validation. So, DeLacey and White[15] developed a method (D-W theory) to verify ζ from the dielectric response of dilute dispersions of colloidal particles to time-varying electric field. The method is valid for all values of κa and ζ and z_i. They use the same perturbation technique and solution procedures as the O-W theory introducing theoretical expressions for; the complex conductance $\left(K^*(\omega)\right)$, the real part of the permittivity $\left(\varepsilon'(\omega)\right)$, and the complex part of the permittivity $\left(\varepsilon''(\omega)\right)$ which are correct to leading order of volume fraction of particles (ϕ), i.e. $\varepsilon'(\omega) = \varepsilon_0 + \phi\,\Delta\varepsilon'(\omega) + \sigma(\phi^2)$. Some key phenomena related to the dielectric response of colloidal dispersions where verified by the results of the D-W theory. Their results showed the large magnitude of $\Delta\varepsilon'(0)$ and the relaxation of $\Delta\varepsilon'(\omega)$ at large frequencies $\omega \geq 10^4$ rad/s. This phenomenon is responsible for the capacitive behavior of colloidal dispersions at low frequencies and the conductive behavior at high frequencies.

Mangelsdorf and White[16] noticed that the D-W theory yielded huge errors for frequencies $\omega/2\pi \geq 5 \times 10^5\ Hz$ especially for large particles. Therefore, they investigated the effect of the inertia term in the Navier-Stokes equation (Equation 2.5) and in the force balance on the particle (Equation 2.12). The relative importance of each term was investigated by comparing the theory with both inertia terms with that of the O-W theory and theories with only one or the other inertia terms included. The resulting M-W theory was limited by numerical difficulties at high frequencies.

The numerical difficulties encountered in the M-W theory were later resolved by Preston, Kornbrekke, and White [17] by using COLSYS, a general boundary value problem solver which uses collocation. Thus, they have developed a method for determining the functional form of the dynamic mobility

$$\mu \equiv \hat{\mu}(\zeta, \kappa a, \omega) \tag{2.14}$$

which is valid for arbitrary zeta potential, particle size, and applied electric field frequency. However, it is still based on the linearized electrokinetic theory developed in the O-W theory thus it is only for small applied electric fields. Also, it is only valid for dilute colloidal dispersions because it utilizes the Boltzmann distribution.

2.4 NONLINEAR ELECTROKINETICS

Nonlinear electrokinetic theory describes phenomena arising from non-uniform concentration polarization. In fact, nonlinear phenomena are usually classified by the origin of the concentration polarization. These phenomena are important in AC electrokinetics because they have non-zero time average velocities. Also, it is possible to apply large electric fields in AC electrokinetics where electrolysis at the electrode interfaces would prevent such high electric fields in DC electric fields. Therefore, nonlinear electrokinetic forces can become very large so that particles can be easily manipulated.

Nonlinear electrokinetic phenomena have been divided broadly by Dukhin as non-equilibrium electric surface phenomena[18] and electrokinetic phenomena of the 2nd kind[19]. The focus of this dissertation is in the former as the later is related to the

development of bulk charge which is normally not the case in AC electrokinetics except for very low frequencies. Before proceeding with the discussion we mention briefly the variety of non-equilibrium electric surface phenomena that have been observed.

The most common nonlinear electrokinetic phenomenon is dielectrophoresis (DEP) where the origin of non-uniform concentration polarization is a non-uniform electric field. For example, consider the colloid near an electrode surface shown in Figure 3. A positive electrode on the bottom-right portion of the boundary and a negative electrode on the bottom-left portion of the boundary result in non-uniform electric field. The surface plot shows the electrostatic free charge. The blue color is a negative charge, the red color is a positive charge, and the green color is neutral charge. The arrows in the fluid domain show the direction and relative magnitude of the electric field. The arrows on the boundary of the particle show the direction and relative magnitude of the Maxwell stress or traction. And, the fluid velocity streamlines show several traces of constant fluid velocity.

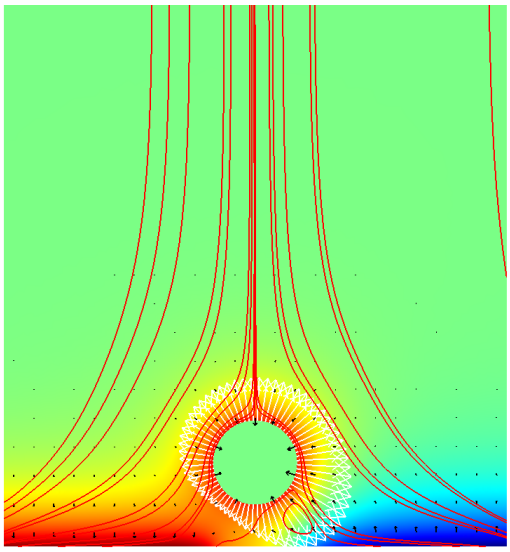

Figure 3: Non-uniform concentration polarization of a particle in a non-uniform electric field (DEP)

Bazant and others [20-22] have described another class of nonlinear electrokinetic phenomena which includes induced-charge electroosmosis (ICEO) and induced-charge electrophoresis (ICEP). In ICEO and ICEP the applied electric field is uniform, but the microfluidic devices incorporate various asymmetries to induce non-zero time average flows or motions. Figure 4 shows ICEO of a fixed cylindrical particle in a uniform applied electric field. The general direction of the fluid velocity which is plotted as arrows and streamlines in Figure 4 does not change with the application of an AC electric field. Therefore, a non-zero time average fluid flow exists. Further, a device which includes this type of ICEO flow can be used as a microfluidic mixer. Figure 5 shows ICEO of a fixed triangular particle in a uniform applied electric field. The non-uniform concentration polarization of Figure 4 is the result of the large applied electric field. The non-uniform concentration polarization of Figure 5 is the result of geometric asymmetry.

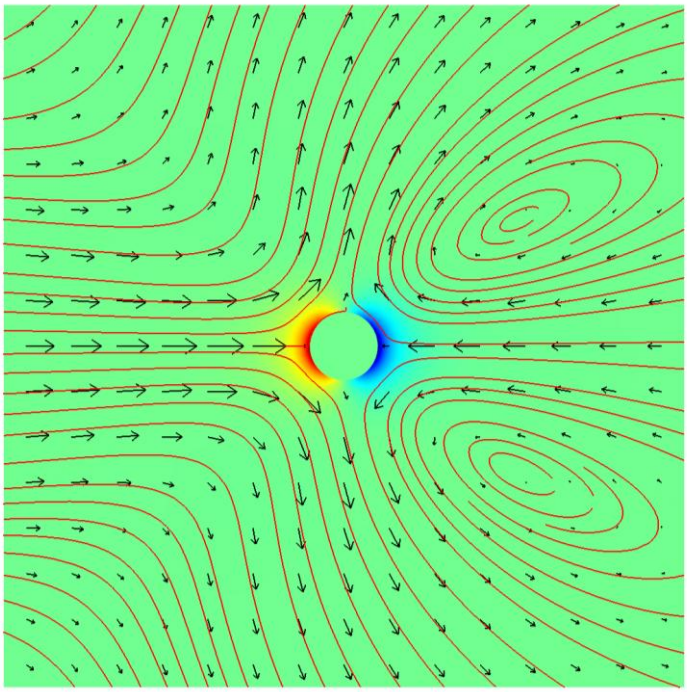

Figure 4: Non-uniform concentration polarization of a fixed particle in a uniform electric field (ICEO)

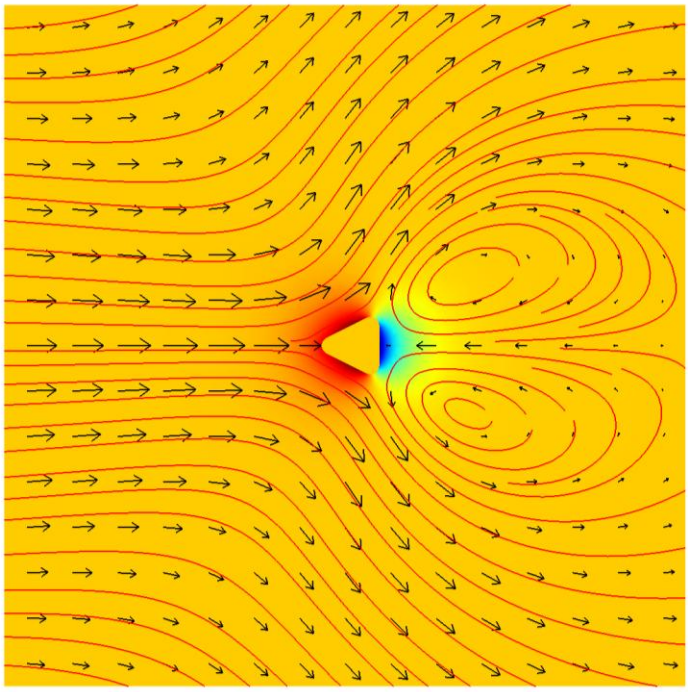

Figure 5: Non-uniform concentration polarization of a particle with geometric asymmetry

The surface plot of Figure 4 shows the electrostatic free charge where the green color is zero charge and the red color located on the left of the particle is the maximum positive free charge. The surface plot of Figure 5 also shows the electrostatic free charge except the zero charge is orange. The flow that develops around the triangular particle in Figure 5 is similar to that of Figure 4 but a much smaller applied electric field is required to polarize the EDL. In an AC applied electric field, a net time-average flow develops which is biased in one direction because it is easier to polarize in one direction due to the geometric asymmetry. Arrays of these devises have been shown to be very effective in microfluidic mixers[22].

Another common nonlinear electrokinetic phenomenon that arises from the nonlinear ion convection term of Equation 3.13 is shown in the electroosmotic pump of Figure 6. Electroosmotic pumps are used in inkjet printers where the small volumes of fluids to be pumped and the small size of the channels prohibit mechanical or pressure based pumping. Electroosmotic pumps are also used in medical devices including blood glucose testing equipment.

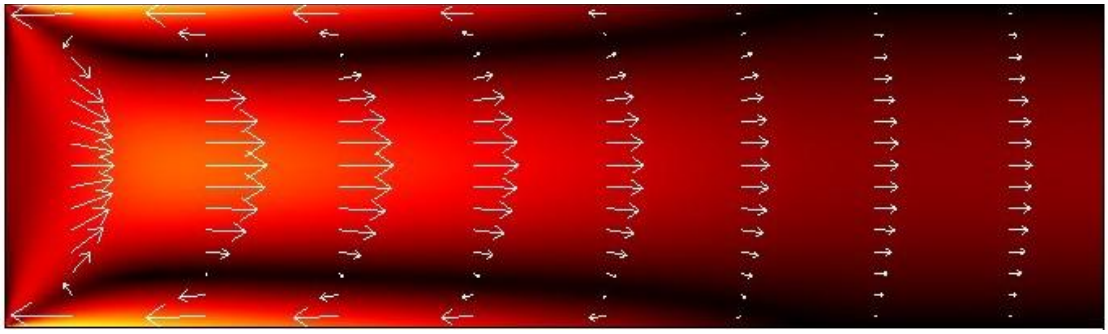

Figure 6: Electroosmotic pump

The electric potential decreases linearly from the inlet at the left side to zero at the midpoint of the boundaries on the top and bottom. This distribution of electric potential produces an electric field that is tangent to the surface. The tangent electric field drives ions and fluid to the left at the surface. This produces a current to the left at the surface which must be balanced by an equal and opposite current in the bulk of the fluid. As ions in the bulk move to the right they drag fluid with them which "pumps" the fluid. The surface shows the convective flux of ions where black is zero and the yellow color near the surface is the maximum value of convective flux. The arrows show the direction and relative magnitude of the fluid velocity.

2.5 GENERALIZED DYNAMIC STERN LAYER THEORY

It has been reported that a linearized electrokinetic theory utilizing constant potential slipping plane boundary condition disagrees with experimentally observed dielectric response by as much as 20% for dilute colloidal dispersions[16]. Since these theories utilize the linearized electrokinetic equations with the isolated particle far field boundary conditions, it is correct in as much as the governing equations are correct. It is assumed that they are indeed correct and that any error is associated with the slipping plane boundary condition. Thus, through investigation of the electrochemistry within the Stern layer more advanced boundary conditions are revealed.

The generalized dynamic Stern layer[23, 24] (GDSL) theory uses the techniques of O'Brien and DeLacey[15] to extend the dynamic Stern layer (DSL) theory developed by Zukoski and Saville[25, 26]. Unlike the DSL theory the GDSL theory is presented in such a way that it is easily extended to other adsorption isotherms. The GDSL theory

includes a framework for including Stern layer adsorption onto the available surface area and onto the underlying surface charge. Ions adsorbed onto the available surface area change the Stern layer charge $\left(\sigma^{i}\right)$ and ions adsorbed onto the underlying surface charge change the charge of the particle (σ^{0}). Thus, the boundary conditions at the slip plane are modified to include lateral movement of ions within the Stern layer and a time-dependent particle surface charge density.

To determine the boundary condition at the slip plane, the following assumptions are made in the GDSL theory: (i) the Stern plane is located at the slip plane, (ii) no convection takes place in the Stern layer, and (iii) only tangential conduction occurs within the Stern layer. The Stern plane is essentially fixed at the slip plane except when the induced electric field is very strong. If the entire Stern layer is assumed to be behind the slip plane the fluid velocity is zero, so no convection will occur. The Stern layer is usually thin with respect to the particle radius; therefore, only the tangential component of flux remains in the Stern layer. Furthermore, it is assumed that the Stern layer charge is concentrated at the inner Helmholtz layer (β_1). Figure 7 summarizes the assumptions made in the GDSL model.

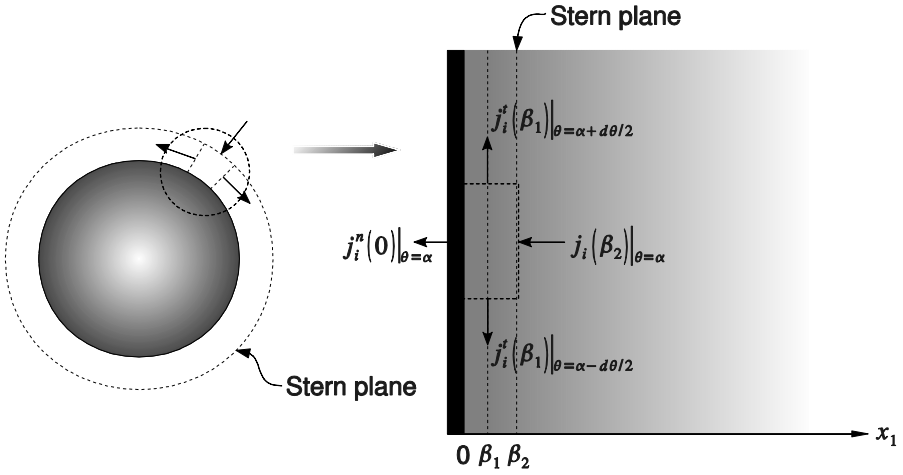

Figure 7: Surface conduction in the GDSL theory

Taking the control volume shown in Figure 7, the conservation of ionic species requires

$$\int_0^{\beta_2} \frac{\partial n_i}{\partial t}\, dx_1 + \int_0^{\beta_2} \nabla \cdot \boldsymbol{j}_i\, dx_1 = \int_0^{\beta_2} R_i\, dx_1$$
$$\int_0^{\beta_2} \frac{\partial n_i}{\partial t}\, dx_1 + \int_0^{\beta_2} -\nabla_{\mathrm{t}} \cdot \boldsymbol{j}_i\, dx_1 + \hat{n} \cdot \boldsymbol{j}_i\big|_0^{\beta_2} = \int_0^{\beta_2} R_i\, dx_1 \qquad 2.15$$

Since the Stern layer charge is assumed to be concentrated at β_1 the integrand in Equation 2.15 can be approximated by its value at $x_1 = \beta_1$. So, we have

$$\hat{n} \cdot \boldsymbol{j}_i|_{\mathrm{sp}} = \frac{\partial n_i^s}{\partial t} - \nabla_{\mathrm{t}} \cdot \boldsymbol{j}_i|_{\beta_1} - R_i^s + \hat{n} \cdot \boldsymbol{j}_i|_0 \qquad 2.16$$

and

$$\boldsymbol{j}_i|_{\beta_1} = -D_i^s \left(\nabla_t n_i^s + \frac{z_i e n_i^s}{k_b T} \nabla_t \psi^i \right) \qquad 2.17$$

where D_i^s is the Stern layer diffusion coefficient and $K_i^s = z_i e n_i^s / k_b T$ is the surface conductivity of the Stern layer. A similar boundary condition is found for the electric displacement at the Stern plane, i.e.

$$\hat{n} \cdot \left(\boldsymbol{D}_p - \boldsymbol{D}_f\right)\big|_{\text{sp}} = \sigma^0 + \sigma^i \qquad 2.18$$

where $\sigma^0 = z_i e n_i^a$ is the surface charge, $\sigma^i = z_i e n_i^s$ is the Stern layer charge, $\boldsymbol{D}_p$ is the electric displacement in the particle, and $\boldsymbol{D}_f$ is the electric displacement in the fluid. In this way the boundary conditions at the slip plane are derived. In most cases the diffusion coefficient and surface conductivity of the Stern layer are not experimentally accessible making all Stern layer models semi-quantitative at best.

It remains to define n_i^a and n_i^s using one of the adsorption isotherms which are summarized in Lyklema[12]. In general, the kinetics of the adsorption of the ith ionic species (n_i) onto an available site (α_i) can be described by a association reaction

$$\alpha_i + n_i \rightleftarrows n_i^\alpha \qquad 2.19$$

The rate r_i^α of this reaction is governed by the equation

$$r_i^\alpha = k_1 \alpha_i n_i - k_2 n_i^\alpha \qquad 2.20$$

where k_1 is the rate constant for association and k_2 is the rate constant for dissociation. Thus, the kinetics of the adsorption of ions onto the Stern layer can be described by

$$s_i + n_i \rightleftarrows n_i^s \qquad 2.21$$

and

$$r_i^s = k_1 s_i n_i - k_2 n_i^s \qquad 2.22$$

for each ion adsorbed onto the Stern layer. The kinetics of ions adsorbed onto the underlying surface charge can be described by

$$a_i + n_i \rightleftarrows n_i^a \tag{2.23}$$

for each ion adsorbed onto the surface of the particle. The rate equation for adsorption onto the underlying surface charge takes the form

$$r_i^a = k_1 a_i n_i - k_2 n_i^a \tag{2.24}$$

where the coefficients $k_1$and k_2 of Equation 2.24 are not necessarily the same as those in Equation 2.22.

The variables s_i and a_i in Equations 2.21 through 2.24 represent an available site on the Stern layer and the underlying surface charge, respectively. The various adsorption isotherms are introduced through these variables. "There are two main classes of Stern layer adsorption isotherms; (1) where adsorption of the ions is onto available free surface area and (2) where adsorption of the ion is onto specific surface sites not available to other ionic species, as in site binding models where the ion absorbs on the underlying surface charge σ^0." [23] The second class was chosen for the finite element model resulting in the following relationships for s_i and a_i

$$s_i = s_i^0 - n_i^s \tag{2.25}$$

and

$$a_i = a_i^0 - n_i^a \tag{2.26}$$

where s_i^0 and a_i^0 are the original available site number densities.

The GDSL theory assumes that the frequency of the applied electric field is low enough $(f \ll 1\ MHz)$ that an equilibrium reaction can occur, i.e. $r_i^\alpha = 0$. Frequencies

are often greater than $1\ MHz$ in electric field guided assembly of colloids. So, we must find a way to relax this assumption. The proper implementation of the non-equilibrium reaction rate equation is revealed through inspection of Equation 2.16 while recalling that Equation 2.20 only describes the kinetics of the reaction. Thus, it accounts for the transient term and the reaction term, i.e. $\left(\frac{\partial n_i^s}{\partial t}\right) \equiv r_i^s$ and $R_i^s \equiv k_1 s_i n_i - k_2 n_i^s$. Substituting these results into Equation 2.16 we arrive at the boundary condition at the slip plane which includes time-dependent Stern layer conduction and time-dependent adsorption onto the Stern plane and the underlying surface charge. That is,

$$\hat{n} \cdot \boldsymbol{j}_i|_{\mathrm{sp}} = \frac{\partial n_i^s}{\partial t} - \nabla_{\mathrm{t}} \cdot \boldsymbol{j}_i|_{\beta_1} - k_1(s_i^0 - n_i^s)n_i + k_2 n_i^s + \hat{n} \cdot \boldsymbol{j}_i|_0 \tag{2.27}$$

This completes the presentation of the GDSL theory. Some attempt has been to make the expression above as general as possible. The flux at the surface of the particle $\hat{n} \cdot \boldsymbol{j}_i|_0$ was taken as zero for the finite element model, but it could be easily included. In the absence of this flux the variable n_i^a is zero as no ions are adsorbed onto the particle surface. Such is the case for impermeable colloids which are commonly used in applications interested in the assembly of metallic colloids.

2.6 MAXWELL STRESS TENSOR METHOD

The most general way to calculate the electrokinetic force on a particle is to integrate the Maxwell stress on the surface which is called the Maxwell stress tensor (MST) method. Wang et al[27] derived general expressions for the dielectrophoretic force $(\boldsymbol{F}_{DEP})$ and torque $(\boldsymbol{\tau}_{DEP})$ and their time averages on a homogeneous dielectric

sphere using the MST method and compared them to the conventional DEP force derived using the effective dipole moment (EDM) method.

The conventional DEP force is shown to be a first order DEP force characterized by the first order Clausius-Mossotti factor $\left(f_{CM}^{(1)}\right)$. This force describes phenomena arising from non-uniformity in the magnitude of the electric field. It can be generalized to include the effect of non-uniformity in the field phase, a phenomenon called traveling-wave dielectrophoresis, which Wang et al termed generalized dielectrophoresis (gDEP). The time averaged gDEP force is

$$\langle \boldsymbol{F}_{gDEP} \rangle = \pi \varepsilon_L' a^3 \mathrm{Re}\left(f_{CM}^{(1)}\right) \nabla E_0^2 + Im\left(f_{CM}^{(1)}\right)\left(E_{0x}^2 \nabla \varphi_x + E_{0y}^2 \nabla \varphi_y + E_{0z}^2 \nabla \varphi_z\right) \quad 2.28$$

The first term is the conventional (first-order) dielectrophoretic force $\langle \boldsymbol{F}_{DEP} \rangle$ and the second term is the first-order traveling-wave dielectrophoretic force $\langle \boldsymbol{F}_{twDEP} \rangle$.

It is important to note some of the restrictions associated with the effective dipole moment method resulting in relations like Equation 2.28. The electric field in the fluid is assumed to be only slightly perturbed by the presence of the particle. Thus, the perturbed electric field $(\boldsymbol{E}_2)$ is approximated by the first-order Taylor series expansions around the center of the particle. The perturbed electric field is then expressed in terms of the applied electric field $(\boldsymbol{E}_0)$ using the Clausius-Mossotti factor. When particle concentrations are low this assumption is not significant, but for concentrated dispersions the Taylor expansion of $\boldsymbol{E}_2$ is a function of particle separation.

The second-order DEP force was also derived using the MST method and compared with that calculated by Washizu and Jones[28] using the EDM method. The second-order DEP force results from inhomogeneous electric field gradients and field gradient phase. The decomposition of the DEP force into a form similar to Equation 2.28 is important in the interpretation of nonlinear phenomena; however it is not necessary for the calculation of dielectrophoretic force in numerical methods of electrokinetics. Instead, the MST method can be applied directly using the integral relation between the force and the Maxwell stress, i.e.

$$\mathbf{F}_{DEP}(t) = \oint \mathbf{T} \cdot \hat{n}\, dA \tag{2.29}$$

with the assurance that it is consistent with the DEP force from the EDM method of the form of Equation 2.28. The second order Maxwell stress tensor ($\mathbf{T}$) in Equation 2.29 is given by

$$\mathbf{T} = \varepsilon \left(\mathbf{E} \otimes \mathbf{E} - \frac{1}{2} E^2 \mathbf{I} \right) \tag{2.30}$$

when there are no time varying magnetic fields. There is no implicit assumption on field strength, particle geometry, or surface homogeneity in Equation 2.29 so that it can capture all nonlinear electrokinetic phenomena.

3 THE FINITE ELEMENT METHOD

3.1 INTRODUCTION

The finite element method is a numerical method of solving differential equations based on a weighted residual statement of the governing equations. It consist of three basic steps or procedures; 1) discretization of the domain (geometry) into subdomains called finite elements, 2) generation of the algebraic equations for each element which satisfy the governing equations in a weighted integral sense, and 3) assembly of the element equations using continuity.[29, 30] The product of the finite element method is a set of algebraic equations which must be solved for the unknown variables. These algebraic equations are what is called the finite element model in the following.

3.2 DIMENSIONLESS ELECTROKINETIC EQUATIONS

A dimensional analysis was performed before applying the finite element method. A dimensionless set of governing equations results in a more computationally efficient finite element code as the scaled set of algebraic equations resulting from finite element discretization are more easily solved by numerical algorithms. Another advantage of the dimensional analysis is the identification of dimensionless parameters. Dimensional analysis is especially important in the case of electrokinetics because we have multiple equations with a large number of parameters. A reduction in the number of parameters makes the design of a colloidal microfluidic devices to assemble colloidal particles much easier. Also, results tabulated or plotted in dimensionless variables are preferred for experimental comparison. A complete discussion of the dimensional analysis of the electrokinetic equations can be found in the text of Russel, Saville, and Schowalter[11].

3.2.1 Poisson's equation

To begin the dimensional analysis the electric potential is scale by the "thermal voltage" ($\psi_T = k_B T/e$). Then, the dimensionless electric potential $\tilde{\psi} = e\psi/k_B T$ is introduced into Poisson's equation. Next, the gradient operator is scaled by the particle radius (a) so that $\tilde{\nabla} = a\nabla$. To complete the dimensional analysis, the ion number density is scaled by the bulk number density n_0 so that

$$\tilde{\nabla}^2\tilde{\psi} = -\frac{2e^2a^2n_0}{\varepsilon k_B T}\frac{\sum_i z_i\tilde{n}_i}{2} \tag{3.1}$$

The resulting equation can be simplified by the introduction of the fundamental electrokinetic quantity known as the Debye-Hückel parameter (κ). The Debye-Hückel parameter is the reciprocal of the characteristic length of the EDL; a physically relevant and fundamental parameter. Finally, we introduce the dimensionless free charge $(\tilde{\rho})$ and we arrive at the dimensionless Poisson's equation.

$$\tilde{\nabla}^2\tilde{\psi} = -(\kappa a)^2\tilde{\rho} \tag{3.2}$$

where

$$\tilde{\psi} = \frac{e\psi}{k_B T} \tag{3.3}$$

$$(\kappa a)^2 = \frac{2e^2a^2n_0}{\varepsilon k_B T} \tag{3.4}$$

$$\tilde{\rho} = \frac{\sum_i z_i\tilde{n}_i}{2} \tag{3.5}$$

and $$\tilde{n}_i = \frac{n_i}{n_0} \quad 3.6$$

3.2.2 Navier-Stokes equations

The dimensional analysis continues with the Navier-Stokes equations by solving Poisson's equation (Equation 2.3) for the free charge ρ and introducing the result into Equation 2.5. Then, introducing the dimensionless gradient operator $\tilde{\nabla}$ and the dimensionless electric potential $\tilde{\psi}$, we arrive at the dimensionless Navier-Stokes equations

$$\omega\tau_f \frac{\partial \tilde{u}}{\partial \tilde{t}} = -\tilde{\nabla}\tilde{p} + \tilde{\nabla}^2\tilde{u} - \tilde{\nabla}^2\tilde{\psi}\tilde{\nabla}\tilde{\psi} \quad 3.7$$

and $$\tilde{\nabla} \cdot \tilde{u} = 0 \quad 3.8$$

where the dimensionless fluid velocity and pressure

$$\tilde{u} = \frac{\eta_0 a}{\varepsilon_r^f \varepsilon_0}\left(\frac{e}{k_B T}\right)^2 \vec{u} \quad 3.9$$

$$\tilde{p} = \frac{a^2}{\varepsilon_r^f \varepsilon_0}\left(\frac{e}{k_B T}\right)^2 p \quad 3.10$$

have been introduced. Also, the time has been scaled by the frequency of the applied electric field, i.e.

$$\tilde{t} = \omega t \quad 3.11$$

leaving a dimensionless coefficient $(\omega\tau_f)$ in front of the transient term of Equation 3.7. The term τ_f is the characteristic diffusion time for fluid motion and is defined as

$$\tau_f = \frac{\rho_0 a^2}{\eta_0} \tag{3.12}$$

3.2.3 Conservation of ionic species equations

Introducing the dimensionless variables previously defined into Equations 2.7 and 2.8 and simplifying we arrive at the dimensionless conservation of species equation

$$\omega\tau_n \frac{\partial \tilde{n}_i}{\partial \tilde{t}} + Pe\ \tilde{u} \cdot \tilde{\nabla}\tilde{n}_i = \tilde{D}_i \tilde{\nabla} \cdot \left(\tilde{\nabla}\tilde{n}_i + z_i \tilde{n}_i \tilde{\nabla}\tilde{\psi}\right) \tag{3.13}$$

where

$$\tilde{D}_i = \frac{D_i}{D_0} \tag{3.14}$$

$$Pe = \frac{\varepsilon_r^f \varepsilon_0}{\eta_0 D_0}\left(\frac{k_B T}{e}\right)^2 \tag{3.15}$$

and

$$\tau_n = \frac{a^2}{D_0} \tag{3.16}$$

In the above equations; the diffusion coefficient for the ith ionic species (D_i) has been scaled by the bulk diffusion coefficient (D_0), the Peclet number (Pe) is used to quantify the relative importance of the convective term, and the characteristic time for ionic diffusion (τ_n) is defined.

3.2.4 Conservation of adsorbed Stern layer ions

Equation 2.27 is derived as a boundary condition at the slip plane which includes time-dependent Stern layer and surface charge adsorption. This is the traditional presentation of the GDSL theory which is informative and tailored for analytical or semi-analytical solution, but not the preferred form for the implementation of the finite

element method. It is better to think of the GDSL theory as a conservation of adsorbed ionic species, i.e. conservation of n_i^s at the slip plane. It is clear that this is in fact the case as Equation 2.27 was derived from conservation of ionic species (Figure 7). This idealization can be used to rearrange Equation 2.27 into a form more suitable for the finite element model. So, rearranging we have in dimensionless form

$$\omega\tau_n \frac{\partial \tilde{n}_i^s}{\partial \tilde{t}} = \widetilde{D}_i^s \widetilde{\nabla}_\mathrm{t} \cdot \left(\widetilde{\nabla}_\mathrm{t}\tilde{n}_i^s + z_i \tilde{n}_i^s \widetilde{\nabla}_\mathrm{t}\tilde{\psi}\right) + \tilde{k}_1(\theta_i - \tilde{n}_i^s)\tilde{n}_i - \tilde{k}_2 \tilde{n}_i^s \tag{3.17}$$

where

$$\widetilde{D}_i^s = \frac{D_i^s}{D_0} \tag{3.18}$$

$$\tilde{k}_1 = \tau_n k_1 \tag{3.19}$$

$$\tilde{k}_2 = \tau_n k_2 \tag{3.20}$$

$$\theta_i = \frac{s_i^0}{n_0} \tag{3.21}$$

and

$$\tilde{n}_i^s = \frac{n_i^s}{n_0} \tag{3.22}$$

Since we have restricted ourselves to impermeable particles $n_i^a = 0$ and we do not have to include conservation of adsorbed surface ions. If the particle is permeable we would include a conservation of the same form but for the variable n_i^a. Also, it is most often the case than only one ion is adsorbed into the Stern layer due to the electrostatic repulsion of similarly charged ions. So, in most cases Equation 3.17 only needs to be

solved for one ion. This simplifies the implementation of the GDSL theory, but it is most definitely not always the case. Several of the adsorption isotherms summarized in the text of Lyklema include adsorption of ions of both positive and negative charge.

3.2.5 Dimensionless groups

The dimensional analysis above introduced several scales which will now be quantified. The electric potential was scaled by ($\psi_T = k_B T/e$) which is approximately $25.7\ mV$ at room temperature. The gradient operator was scaled by the particle radius which is on the order of $1 \times 10^2\ nm$ for most applications. The number density of each ion was scale by the bulk number density n_0 which ranges from 6.022×10^{22} to 6.022×10^{26} for bulk concentrations of $0.1\ mM$ and $1\ M$, respectively.

The dimensionless groups used in this research agree with those used in the literature. Specifically, those suggested in the IUPAC Technical Report for "Measurement and Interpretation of Electrokinetic Phenomena" [31]. However, it is common to scale the gradient by the Debye length ($\lambda \equiv 1/\kappa$). This may seem to be more meaningful as the magnitude of the applied electric field relative to the EDL electric field ($\sim\kappa\zeta$) is a useful indicator of the degree of nonlinearity or polarization. One reason to use the particle radius rather than the Debye length is that in experimental design it is easy to change the Debye length by adding salt, but it is not so easy to change the size of the particles. From a finite element model point of view, it is easier to use the particle radius because the geometry (or mesh) is fixed and one does not necessarily have to re-mesh to solve for a different value of κa.

3.3 WEAK FORM

In this section we develop the weak forms for each of the dimensionless governing equations. The weighted integral statement will be presented for each of the governing equations of electrokinetic theory followed by the development of the weak form using the Green-Gauss theorem. By inspecting the weak form we can identify the primary and secondary variables. The primary variables are the essential boundary conditions and the secondary variables are the natural boundary conditions. The tilde notation for dimensionless variables will be dropped in the following equations. Thus, $\tilde{\psi} \rightarrow \psi$, $\tilde{u} \rightarrow \vec{u}$, $\tilde{n}_i \rightarrow n_i$, etc.

3.3.1 Poisson's equation

The weighted integral statement of the dimensionless Poisson's equation (Equation 3.2) in Cartesian coordinates is

$$0 = \int_{\Omega^e} w^1 \left[-\frac{\partial}{\partial x}\left(\frac{\partial \psi}{\partial x}\right) - \frac{\partial}{\partial y}\left(\frac{\partial \psi}{\partial y}\right) - (\kappa a)^2 \rho \right] dx\, dy \tag{3.23}$$

and the weak form is

$$\begin{aligned} 0 = \int_{\Omega^e} \left(\frac{\partial w^1}{\partial x}\left(\frac{\partial \psi}{\partial x}\right) + \frac{\partial w^1}{\partial y}\left(\frac{\partial \psi}{\partial y}\right) - (\kappa a)^2 w^1 \rho \right) dx\, dy \\ - \oint_{\Gamma^e} w^1 \left(\frac{\partial \psi}{\partial x} n_x + \frac{\partial \psi}{\partial y} n_y \right) ds \end{aligned} \tag{3.24}$$

The primary variable is the electric potential ψ and the secondary variable is the electric field $\boldsymbol{E}$ which has components $\boldsymbol{E}_x = -\frac{\partial \psi}{\partial x}$ and $\boldsymbol{E}_y = -\frac{\partial \psi}{\partial y}$.

3.3.2 Navier-Stokes equations

The Navier-Stokes equations are modeled using the velocity-pressure finite element model[29] without the convective term and with the body force vector taken as $\rho\vec{E}$. The weighted integral statements of Equations 3.7 and 3.8 in Cartesian coordinates are

$$0 = \int_{\Omega^e} w^2 \left[\omega\tau_f \frac{\partial u_x}{\partial t} - \frac{\partial}{\partial x}\left(2\frac{\partial u_x}{\partial x}\right) - \frac{\partial}{\partial y}\left(\frac{\partial u_x}{\partial y} + \frac{\partial u_y}{\partial x}\right) + \frac{\partial p}{\partial x} + \rho\frac{\partial \psi}{\partial x}\right] dx\, dy \tag{3.25}$$

$$0 = \int_{\Omega^e} w^3 \left[\omega\tau_f \frac{\partial u_y}{\partial t} - \frac{\partial}{\partial y}\left(2\frac{\partial u_y}{\partial y}\right) - \frac{\partial}{\partial x}\left(\frac{\partial u_x}{\partial y} + \frac{\partial u_y}{\partial x}\right) + \frac{\partial p}{\partial y} + \rho\frac{\partial \psi}{\partial y}\right] dx\, dy \tag{3.26}$$

and

$$0 = \int_{\Omega^e} w^4 \left(\frac{\partial u_x}{\partial x} + \frac{\partial u_y}{\partial y}\right) dx\, dy \tag{3.27}$$

The weak forms of these equations are

$$0 = \int_{\Omega^e} \left[\omega\tau_f w^2 \frac{\partial u_x}{\partial t} + \frac{\partial w^2}{\partial x}\left(2\frac{\partial u_x}{\partial x}\right) + \frac{\partial w^2}{\partial y}\left(\frac{\partial u_x}{\partial y} + \frac{\partial u_y}{\partial x}\right) + \frac{\partial w^2}{\partial x} p + \rho w^2 \frac{\partial \psi}{\partial x}\right] dx\, dy - \oint_{\Gamma^e} w^2 t_x\, ds \tag{3.28}$$

$$0 = \int_{\Omega^e} \left[\omega \tau_f w^3 \frac{\partial u_y}{\partial t} + \frac{\partial w^3}{\partial y}\left(2\frac{\partial u_y}{\partial y}\right) + \frac{\partial w^3}{\partial x}\left(\frac{\partial u_x}{\partial y} + \frac{\partial u_y}{\partial x}\right) + \frac{\partial w^3}{\partial y} p + \rho w^3 \frac{\partial \psi}{\partial y} \right] dx\, dy - \oint_{\Gamma^e} w^2 t_y \, ds \tag{3.29}$$

$$0 = \int_{\Omega^e} w^4 \left(\frac{\partial u_x}{\partial x} + \frac{\partial u_y}{\partial y}\right) dx\, dy \tag{3.30}$$

where

$$t_x = \left(2\frac{\partial u_x}{\partial x} - p\right) n_x + \left(\frac{\partial u_x}{\partial y} + \frac{\partial u_y}{\partial x}\right) n_y \tag{3.31}$$

$$t_y = \left(\frac{\partial u_x}{\partial y} + \frac{\partial u_y}{\partial x}\right) n_x + \left(2\frac{\partial u_y}{\partial y} - p\right) n_y \tag{3.32}$$

The primary variables of the Navier-Stokes equations are the Cartesian components of the fluid velocity u_x and u_y and the pressure p. The secondary variables from Equations 3.28 and 3.29 are the traction components t_x and t_y given in Equations 3.31 and 3.32.

3.3.3 Conservation of ionic species equations

The weighed integral statement of Equation 3.13 in Cartesian coordinates is

$$0 = \int_{\Omega^e} w_i^5 \left[\omega\tau_n \frac{\partial n_i}{\partial t} + Pe \left(u_x \frac{\partial n_i}{\partial x} + u_y \frac{\partial n_i}{\partial y} \right) \right.$$
$$- D_i \frac{\partial}{\partial x}\left(\frac{\partial n_i}{\partial x} + z_i n_i \frac{\partial \psi}{\partial x}\right) - D_i \frac{\partial}{\partial y}\left(\frac{\partial n_i}{\partial y}\right. \tag{3.33}$$
$$\left. \left. + z_i n_i \frac{\partial \psi}{\partial y}\right)\right] dx\, dy$$

and the weak form is

$$0 = \int_{\Omega^e} \left[\omega\tau_n w_i^5 \frac{\partial n_i}{\partial t} + Pe\, w_i^5 \left(u_x \frac{\partial n_i}{\partial x} + u_y \frac{\partial n_i}{\partial y} \right) \right.$$
$$+ D_i \frac{\partial w_i^5}{\partial x}\left(\frac{\partial n_i}{\partial x} + z_i n_i \frac{\partial \psi}{\partial x}\right) + D_i \frac{\partial w_i^5}{\partial y}\left(\frac{\partial n_i}{\partial y}\right. \tag{3.34}$$
$$\left. \left. + z_i n_i \frac{\partial \psi}{\partial y}\right)\right] dx\, dy - \oint_{\Gamma^e} w_i^5 (J_n)_i\, ds$$

where

$$(J_n)_i = \left(\frac{\partial n_i}{\partial x} + z_i n_i \frac{\partial \psi}{\partial x}\right) n_x + \left(\frac{\partial n_i}{\partial y} + z_i n_i \frac{\partial \psi}{\partial y}\right) n_y \tag{3.35}$$

is the normal component of the flux for the ith ion.

The weighted integral statement and weak form above represents (N) equations where N is the number of charge determining ions in the electrolyte suspension. For convenience we restrict the model to a 1:1 electrolyte and choose $n_1 = n_+$ and $n_2 = n_-$. The weights w_i^5 then change to a more common format; $w_1^5 = w^5$ and $w_2^5 = w^6$. The primary variables for the conservation of ionic species equations are the ion number

densities n_+ and n_-. The secondary variables are the normal components of the ion flux $(J_n)_+$ and $(J_n)_-$ given in Equation 3.35.

3.3.4 Conservation of adsorbed Stern layer ions

The weighed integral statement of Equation 3.17, with only the positive ion being adsorbed, in Cartesian coordinates is

$$\begin{aligned} 0 = \oint_{\Gamma^e} w^7 \Bigg[& \omega\tau_n \frac{\partial n^s}{\partial t} \\ & - D^s \frac{\partial}{\partial x}\left(\frac{\partial n^s}{\partial x} + n^s \frac{\partial \psi}{\partial x}\right) m_x - D^s \frac{\partial}{\partial y}\left(\frac{\partial n^s}{\partial y}\right. \\ & \left. + n^s \frac{\partial \psi}{\partial y}\right) m_y - k_1(\theta - n^s) n_+ \\ & + k_2 n^s \Bigg] \, dx \, dy \end{aligned} \tag{3.36}$$

and the weak form is

$$\begin{aligned} 0 = \oint_{\Gamma^e} \Bigg[& \omega\tau_n w^7 \frac{\partial n^s}{\partial t} \\ & + D^s \frac{\partial w^7}{\partial x}\left(\frac{\partial n^s}{\partial x} + n^s \frac{\partial \psi}{\partial x}\right) m_x + D^s \frac{\partial w^7}{\partial y}\left(\frac{\partial n^s}{\partial y}\right. \\ & \left. + n^s \frac{\partial \psi}{\partial y}\right) m_y - w^7 k_1(\theta - n^s) n_+ \\ & + w^7 k_2 n^s \Bigg] \, dx \, dy \end{aligned} \tag{3.37}$$

where m_x and m_y are the components of the unit tangent vector in the x and y directions, respectively. Therefore, the terms

$$(J_t)_x = \left(\frac{\partial n^s}{\partial x} + n^s \frac{\partial \psi}{\partial x}\right) m_x \tag{3.38}$$

and

$$(J_t)_y = \left(\frac{\partial n^s}{\partial y} + n^s \frac{\partial \psi}{\partial y}\right) m_y \tag{3.39}$$

are the scalar components of the tangential flux in the x-direction and the y-direction, respectively. The term that would normally result from applying the Green-Gauss theorem that contains boundary terms is zero because the surface of the particle is a closed curve.

3.4 FINITE ELEMENT MODEL

In this section we present the Ritz-Galerkin finite element model from the weak forms in Equations 3.24, 3.28, 3.29, 3.30, the (2) from Equation 3.34, and (1) from Equation 3.34. The weights $w^1 \rightarrow w^7$ in the Ritz-Galerkin finite element model are equated to the functions used in the finite element approximations of the primary variables. Therefore, if the primary variables are approximated with a function of the form

$$\Xi(\mathrm{x},\mathrm{y},\mathrm{t}) = \sum_{\mathrm{j}=1}^{\mathrm{m}} \varphi_{\mathrm{j}}(\mathrm{x},\mathrm{y})\Xi_{\mathrm{j}}(\mathrm{t}) \tag{3.40}$$

then the weight function is of the form

$$w = \varphi_i(x,y) \tag{3.41}$$

The primary variables, as identified in the development of the weak forms are

$$\psi, u_x, u_y, p, n_+, n_-, \text{ and } n^s \tag{3.42}$$

Next, approximations to these primary variables are introduced into the weak forms in the form of Equation 3.40. The electric potential is approximated with the function

$$\psi_h^e = \sum_{j=1}^{m_1} \varphi_j^1 \psi_j^e \tag{3.43}$$

The Cartesian components of the fluid velocity are approximated with the function

$$(u_x)_h^e = \sum_{j=1}^{m_2} \varphi_j^2 (u_x)_j^e \tag{3.44}$$

$$\left(u_y\right)_h^e = \sum_{j=1}^{m_3} \varphi_j^3 \left(u_y\right)_j^e \tag{3.45}$$

The pressure is approximated with the function

$$p_h^e = \sum_{j=1}^{m_4} \varphi_j^4 p_j^e \tag{3.46}$$

The positive ion density is approximated with the function

$$(n_+)_h^e = \sum_{j=1}^{m_5} \varphi_j^5 (n_+)_j^e \tag{3.47}$$

The negative ion density is approximated with the function

$$(n_-)_h^e = \sum_{j=1}^{m_6} \varphi_j^6 (n_-)_j^e \tag{3.48}$$

And, the adsorbed Stern layer ion density is approximated with the function

$$(n^s)_h^e = \sum_{j=1}^{m_7} \varphi_j^7 (n^s)_j^e \tag{3.49}$$

We complete the finite element model by substituting Equations 3.43 through 3.49 and there corresponding weight functions into the weak forms and arranging the resulting algebraic equations into a matrix form, i.e.

$$[C^e]\{\dot{\Delta}^e\} + [K^e]\{\Delta^e\} = \{F^e\} \tag{3.50}$$

where the coefficient matrices $[C^e]$ and $[K^e]$ are composed of sub-matrices of the form

$$\left[A_{ij}^{mn}\right] \tag{3.51}$$

These sub-matrices contain the coefficients of the algebraic equation from the mth weak form of the nth nodal variable. The process of developing the sub-matrices for the $[K^e]$ matrix will be demonstrated for the first weak form (Equation 3.24). The remaining sub-matrices will be presented without development.

First, we substitute the approximation functions into the weak form (Equation 3.24)

$$0 = \int_{\Omega^e} \left[\sum_{j=1}^{m_1} \left(\frac{\partial \varphi_i^1}{\partial x}\frac{\partial \varphi_j^1}{\partial x} + \frac{\partial \varphi_i^1}{\partial y}\frac{\partial \varphi_j^1}{\partial y} \right) \psi_j^e - (\kappa a)^2 \frac{\left(\sum_{j=1}^{m_5} \varphi_i^1 \varphi_j^5 (n_+)_j^e - \sum_{j=1}^{m_6} \varphi_i^1 \varphi_j^6 (n_-)_j^e\right)}{2} \right] dx\, dy + \oint_{\Gamma^e} \varphi_i^1 E_n \, ds \tag{3.52}$$

Then, by inspecting Equation 3.52 the elements of the sub-matrix from the 1st weak form for the 1st nodal variable $\left(\psi_j^e\right)$ are extracted. The resulting $m_1 \times m_1$ sub-matrix is

$$K_{ij}^{11} = \int_{\Omega^e} \left(\frac{\partial \varphi_i^1}{\partial x} \frac{\partial \varphi_j^1}{\partial x} + \frac{\partial \varphi_i^1}{\partial y} \frac{\partial \varphi_j^1}{\partial y} \right) dx\, dy \tag{3.53}$$

The elements of the sub-matrix from the 1st weak form for the 5th nodal variable $(n_+)_j^e$ are extracted. The resulting $m_1 \times m_5$ sub-matrix is

$$K_{ij}^{15} = -\int_{\Omega^e} \frac{(\kappa a)^2}{2} \varphi_i^1 \varphi_j^5\, dx\, dy \tag{3.54}$$

and for the 6th nodal variable $(n_-)_j^e$ we extracted

$$K_{ij}^{16} = \int_{\Omega^e} \frac{(\kappa a)^2}{2} \varphi_i^1 \varphi_j^6\, dx\, dy \tag{3.55}$$

which is a $m_1 \times m_6$ sub-matrix. Then, we note that all other sub-matrices are zero, i.e.

$$\left[K_{ij}^{1n}\right] = 0 \quad \text{for} \quad n = 2,3,4 \tag{3.56}$$

and that the C^e matrix is zero for the first weak form because the governing equation does not have a transient term. Finally, we extract the elements $\{F^1\}$ which is a sub-vector of $\{F^e\}$ of rank m_1. Thus,

$$F_i^1 = -\oint_{\Gamma^e} \varphi_i^1 E_n\, ds \tag{3.57}$$

where E_n is the normal component of the electric field and the minus sign comes from the definition $E_n = -\frac{\partial \psi}{\partial n}$. This concludes the development of the Ritz-Galerkin finite element model for the 1st weak form. The non-zero elements of $[K^e]$, $[C^e]$, and $\{F^e\}$ are recorded in Table 1, Table 2, and Table 3, respectively.

Table 1: The non-zero elements of the coefficient matrix $[K^e]$

$$K_{ij}^{11} = \int_{\Omega^e} \frac{\partial \varphi_i^1}{\partial x}\frac{\partial \varphi_j^1}{\partial x} + \frac{\partial \varphi_i^1}{\partial y}\frac{\partial \varphi_j^1}{\partial y}\, dx\, dy \tag{3.58}$$

$$K_{ij}^{15} = -\int_{\Omega^e} \frac{(\kappa a)^2}{2}\varphi_i^1 \varphi_j^5\, dx\, dy \tag{3.59}$$

$$K_{ij}^{16} = \int_{\Omega^e} \frac{(\kappa a)^2}{2}\varphi_i^1 \varphi_j^6\, dx\, dy \tag{3.60}$$

$$K_{ij}^{21} = \int_{\Omega^e} \rho \varphi_i^2 \frac{\partial \varphi_j^1}{\partial x}\, dx\, dy \tag{3.61}$$

$$K_{ij}^{22} = \int_{\Omega^e} 2\frac{\partial \varphi_i^2}{\partial x}\frac{\partial \varphi_j^2}{\partial x} + \frac{\partial \varphi_i^2}{\partial y}\frac{\partial \varphi_j^2}{\partial y}\, dx\, dy \tag{3.62}$$

$$K_{ij}^{23} = \int_{\Omega^e} \frac{\partial \varphi_i^2}{\partial y}\frac{\partial \varphi_j^3}{\partial x}\, dx\, dy \tag{3.63}$$

$$K_{ij}^{24} = \int_{\Omega^e} \frac{\partial \varphi_i^2}{\partial x}\varphi_j^4\, dx\, dy \tag{3.64}$$

$$K_{ij}^{31} = \int_{\Omega^e} \rho \varphi_j^3 \frac{\partial \varphi_i^1}{\partial y}\, dx\, dy \tag{3.65}$$

$$K_{ij}^{32} = K_{ji}^{23} \tag{3.66}$$

$$K_{ij}^{33} = \int_{\Omega^e} 2\frac{\partial \varphi_i^3}{\partial y}\frac{\partial \varphi_j^3}{\partial y} + \frac{\partial \varphi_i^3}{\partial x}\frac{\partial \varphi_j^3}{\partial x}\, dx\, dy \tag{3.67}$$

Table 1: Continued

$$K_{ij}^{34} = \int_{\Omega^e} \frac{\partial \varphi_i^3}{\partial y} \varphi_j^4 \, dx \, dy \tag{3.68}$$

$$K_{ij}^{42} = K_{ji}^{24} \tag{3.69}$$

$$K_{ij}^{43} = K_{ji}^{34} \tag{3.70}$$

$$K_{ij}^{51} = \int_{\Omega^e} D_+ n_+ \left(\frac{\partial \varphi_i^5}{\partial x} \frac{\partial \varphi_j^1}{\partial x} + \frac{\partial \varphi_i^5}{\partial y} \frac{\partial \varphi_j^1}{\partial y} \right) dx \, dy \tag{3.71}$$

$$K_{ij}^{55} = \int_{\Omega^e} \left[Pe \, u_x \varphi_i^5 \frac{\partial \varphi_i^5}{\partial x} + Pe \, u_y \varphi_i^5 \frac{\partial \varphi_i^5}{\partial y} + D_+ n_+ \left(\frac{\partial \varphi_i^5}{\partial x} \frac{\partial \varphi_j^5}{\partial x} + \frac{\partial \varphi_i^5}{\partial y} \frac{\partial \varphi_j^5}{\partial y} \right) \right] dx \, dy \tag{3.72}$$

$$K_{ij}^{61} = \int_{\Omega^e} D_- n_- \left(\frac{\partial \varphi_i^6}{\partial x} \frac{\partial \varphi_j^1}{\partial x} + \frac{\partial \varphi_i^6}{\partial y} \frac{\partial \varphi_j^1}{\partial y} \right) dx \, dy \tag{3.73}$$

$$K_{ij}^{66} = \int_{\Omega^e} \left[Pe \, u_x \varphi_i^6 \frac{\partial \varphi_i^6}{\partial x} + Pe \, u_y \varphi_i^6 \frac{\partial \varphi_i^6}{\partial y} + D_- n_- \left(\frac{\partial \varphi_i^6}{\partial x} \frac{\partial \varphi_j^6}{\partial x} + \frac{\partial \varphi_i^6}{\partial y} \frac{\partial \varphi_j^6}{\partial y} \right) \right] dx \, dy \tag{3.74}$$

Note that the variable ρ in K_{ij}^{21} (Equation 3.61) and K_{ij}^{31} (Equation 3.65) is the dimensionless free charge not the density of the fluid (ρ_0).

Table 2: The non-zero elements of the coefficient matrix $[C^e]$

$C_{ij}^{22} = \int_{\Omega^e} \omega\tau_f \varphi_i^2 \varphi_j^2 \, dx \, dy$	3.75
$C_{ij}^{33} = \int_{\Omega^e} \omega\tau_f \varphi_i^3 \varphi_j^3 \, dx \, dy$	3.76
$C_{ij}^{55} = \int_{\Omega^e} \omega\tau_n \varphi_i^5 \varphi_j^5 \, dx \, dy$	3.77
$C_{ij}^{66} = \int_{\Omega^e} \omega\tau_n \varphi_i^6 \varphi_j^6 \, dx \, dy$	3.78

Table 3: The non-zero elements of the right-hand side vector $\{F^e\}$

$F_i^1 = -\oint_{\Gamma^e} \varphi_i^1 E_n \, ds$	3.79
$F_i^2 = \oint_{\Gamma^e} \varphi_i^2 t_x \, ds$	3.80
$F_i^3 = \oint_{\Gamma^e} \varphi_i^3 t_y \, ds$	3.81
$F_i^5 = \oint_{\Gamma^e} \varphi_i^5 (J_n)_+ \, ds$	3.82
$F_i^6 = \oint_{\Gamma^e} \varphi_i^6 (J_n)_- \, ds$	3.83

3.4.1 Stern layer finite element model

The additional coefficients and necessary modifications to the coefficients previously defined when Stern layer adsorption is included are presented in Table 4. The elements of these coefficients are only assembled for elements on the boundary of the particle.

Table 4: Non-zero elements of the coefficient matrices $[K^e]$ and $[C^e]$ when Stern layer adsorption is included

$$K_{ij}^{51} = \oint_{\Gamma^e} -n_+ \varphi_i^5 \left(\frac{\partial \varphi_j^1}{\partial x} n_x + \frac{\partial \varphi_j^1}{\partial y} n_y \right) ds \tag{3.84}$$

$$K_{ij}^{55} = \oint_{\Gamma^e} -\left[\varphi_i^5 \left(\frac{\partial \varphi_j^5}{\partial x} n_x + \frac{\partial \varphi_j^5}{\partial y} n_y \right) + k_1(\theta - n^s) \varphi_i^5 \varphi_j^5 \right] ds \tag{3.85}$$

$$K_{ij}^{57} = \oint_{\Gamma^e} k_2 \varphi_i^5 \varphi_j^7 \, ds \tag{3.86}$$

$$K_{ij}^{71} = \oint_{\Gamma^e} \left[D^s n^s \left(\frac{\partial \varphi_i^7}{\partial x} \frac{\partial \varphi_j^1}{\partial x} m_x + \frac{\partial \varphi_i^7}{\partial y} \frac{\partial \varphi_j^1}{\partial y} m_y \right) \right] ds \tag{3.87}$$

$$K_{ij}^{75} = \oint_{\Gamma^e} -k_1 \theta \varphi_i^7 \varphi_j^5 \, ds \tag{3.88}$$

Table 4: Continued

$$K_{ij}^{77} = \oint_{\Gamma^e} \left[D^s \left(\frac{\partial \varphi_i^7}{\partial x} \frac{\partial \varphi_j^7}{\partial x} m_x + \frac{\partial \varphi_i^7}{\partial y} \frac{\partial \varphi_j^7}{\partial y} m_y + (k_1 n_+ + k_2) \varphi_i^7 \varphi_j^7 \right) \right] dx dy \quad 3.89$$

$$C_{ij}^{77} = \oint_{\Gamma^e} \omega \tau_n \varphi_i^7 \varphi_j^7 \, ds \quad 3.90$$

The right-hand side vector $\{F^e\}$ does not change when Stern layer adsorption is included.

The finite element model developed and presented in this section was implemented using the commercially available software COMSOL Multiphysics®, (COMSOL, Inc, Burlington, MA). In most cases, the governing equations can be input directly into the software and the weak forms are developed internally. However, when Stern layer adsorption is included the weak form must be developed and implemented manually using a boundary weak form module. COMSOL Multiphysics® was selected because it has the ability to adaptively remesh during mesh refinement studies. However, future research will necessitate the development and use of a standalone finite element code because COMSOL Multiphysics® is not capable of space-time coupled methods.

4 THE ELECTRIC DOUBLE LAYER

4.1 PROBLEM STATEMENT

The objective of this section is to use analytical solutions for the electric double layer surrounding a particle which is quiescent in the absence of an applied electric field and moving at constant velocity in the presence of a constant applied electric field to validate the finite element model. In addition, some insights into the mechanisms of nonlinearity are exposed by investigating the effect of particle size, particle permittivity, and applied electric field strength on the distribution of the EDL. The distribution of the EDL in an applied electric field ultimately determines the dielectrophoretic force on the particle as described by Equation 2.28 using the EDM or by Equation 2.29 and Equation 2.30 using the MST method and the electroosmotic velocity of the fluid surrounding the particle resulting from polarization of the EDL. In Section 4.2 we present the steps taken to verify the accurate solution of the electric potential, free charge, and average ion density in the EDL.

4.2 RESULTS

The process of verifying the FEM solution of the EDL was accomplished in two stages. First, the FEM model was verified by comparing the FEM solution with analytical solutions available in the literature for an equilibrium EDL for different values of κa. Then, the model was verified in the same way for an EDL in an applied electric field. After verifying the finite element model, we present and discuss the nonlinear effects of large applied electric fields, particle permittivity, and surface boundary condition on the distribution of the EDL.

4.2.1 The equilibrium electric double layer

The objective of the following section is to validate the finite element solution of the equilibrium EDL for different values of κa. Exact analytical solutions exist for the equilibrium EDL, so the solutions resented in this section are included as a benchmark for the FEM model. In the following we present the analytical solution of the equilibrium EDL, present and discuss some figures that help visualize the equilibrium electric double layer, and validate the FEM model by comparing the electric potential at one Debye length (ψ_λ) with that of the analytical solution (Equation 4.1).

At equilibrium, the analytical solution for the dimensionless potential surrounding a cylindrical particle is given by

$$\tilde{\psi} = \tilde{\psi}_0 \frac{K_0(\kappa r)}{K_0(\kappa a)} \tag{4.1}$$

where K_0 is a zeroth order modified Bessel function of the second kind[32]. This analytical solution of the Poisson-Boltzmann equation is based on the Debye-Hückel approximation with the constant surface potential boundary condition. Therefore, it is only valid for small surface potentials (ψ_0). So, the finite element model solution should be the same as the analytical solution when the surface potentials are small and begin to deviate when $\psi_0/\psi_T > 1$. The dimensionless electric potential (ψ/ψ_T), dimensionless free charge (ρ/n_0), and dimensionless average ion density $(\eta/n_0 \equiv (n_+ + n_-)/2n_0)$ of the equilibrium EDL is shown in Figure 8 for $\kappa a = 1$ and Figure 9 for $\kappa a = 10$.

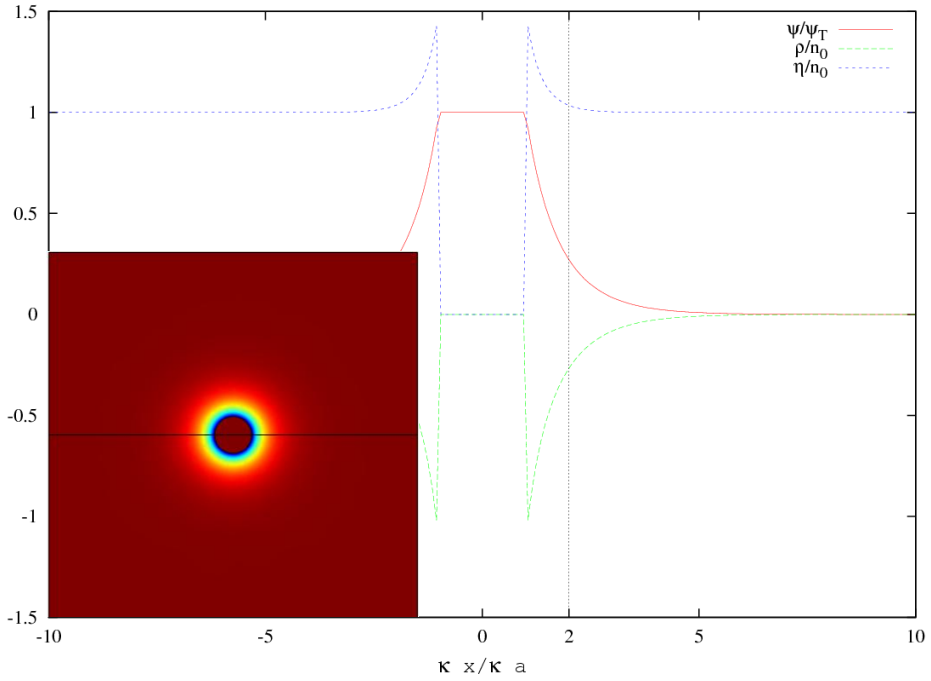

Figure 8: Equilibrium EDL with $\kappa a = 1$

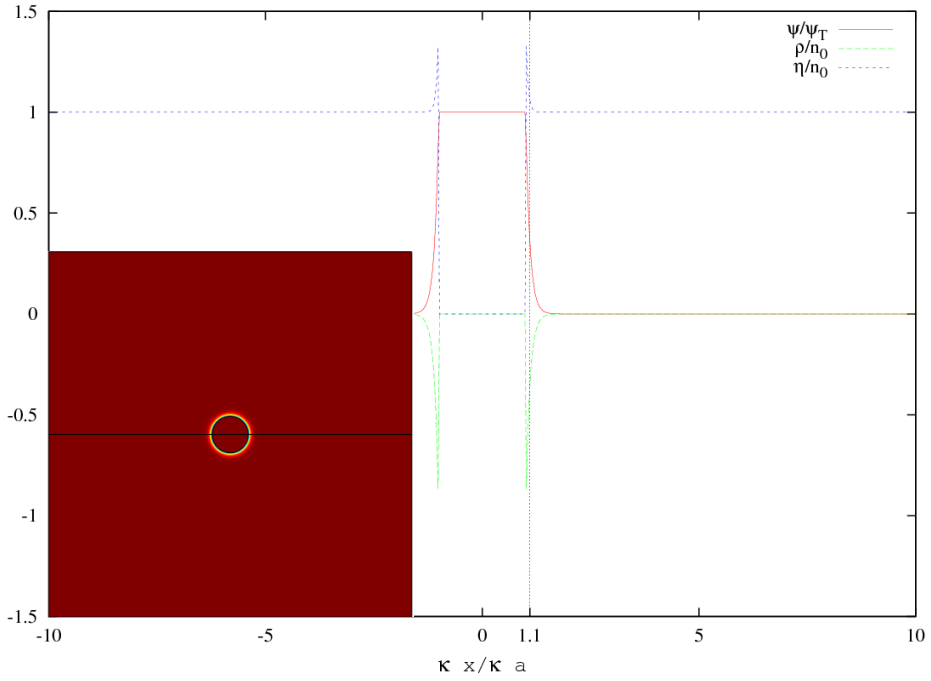

Figure 9: Equilibrium EDL with $\kappa a = 10$

Figure 8 and Figure 9 illustrate the exponential distribution of the EDL and the concentration of the EDL with an increase in κa. The horizontal line through the mid-plane of the surface plot shown in Figure 8 and Figure 9 shows the position of the section plot. The dotted vertical line in each figure shows the position of ψ_λ which changes with κa. The surface plot of the free charge is inset into each figure to show the symmetry of the EDL at equilibrium and will be used in the next section to show polarization of the EDL when (strong) electric fields are applied.

In order to validate the FEM solutions presented in Figure 8 and Figure 9, the potential at one Debye length (ψ_λ) is compared with that of the analytical solution. To illustrate the onset of nonlinearity the results of Figure 10 have been scaled by the surface potential (ψ_0).

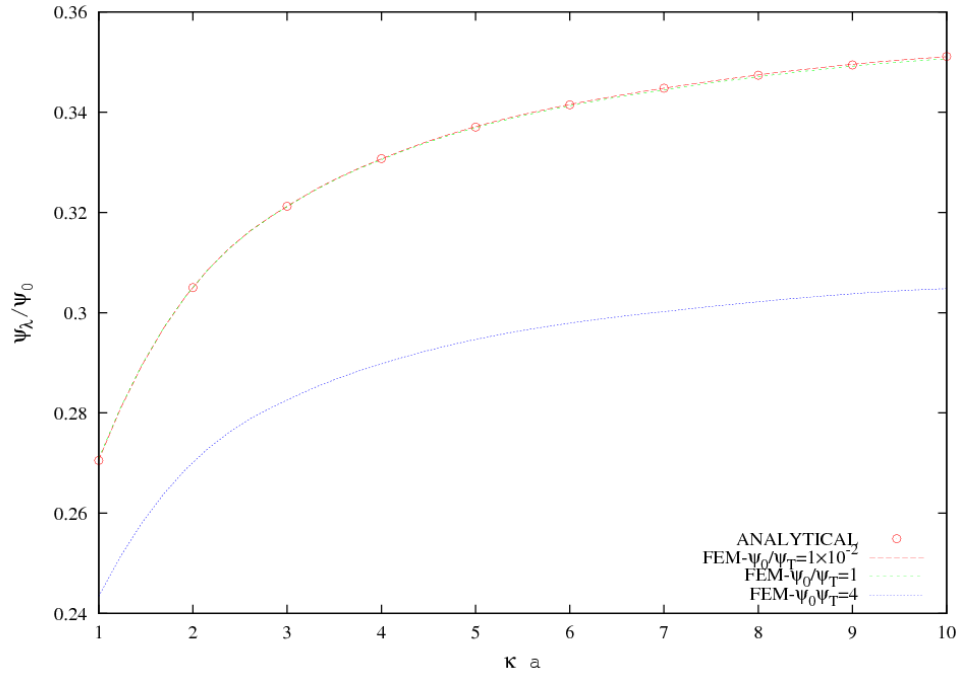

Figure 10: Scaled electric potential at one Debye length for the equilibrium EDL

The finite element solution and analytical solution of ψ_λ/ψ_0 compare well for a dimensionless surface potential of $\psi_0/\psi_T = 1 \times 10^{-2}$ and $\psi_0/\psi_T = 1$. The maximum error of the results shown in Figure 10 is 0.01% for $\psi_0/\psi_T = 1 \times 10^{-2}$ and 0.05% for $\psi_0/\psi_T = 1$. The FEM solution with $\psi_0/\psi_T = 4$ shows that nonlinearity becomes significant for dimensionless surface potentials $\psi_0/\psi_T > 1$. The maximum error in the analytic solution is about 5% for $\psi_0/\psi_T = 4$.

In the process of solving the equilibrium EDL problem we learned a great deal about the mesh needed to resolve the EDL. This information was then used to select a mesh to solve other problems such as the EDL in an applied electric field which is presented in the following section. The mesh needed to resolve the electric double layer depends on the value of κa. Figure 8 and Figure 9 show that as the dimensionless particle radius is increased from $\kappa a = 1$ to $\kappa a = 10$ the electric double layer is condensed to a smaller region of the domain. Thus, more elements are needed to resolve the EDL. The results of Figure 10 were achieved using the finite element mesh shown in Figure 11 which contains approximately 8500 elements. The half-symmetry domain used to calculate the distribution of the EDL (and the electrophoretic mobility presented in the Section 5) is considerably larger than that shown in the surface plots of dimensionless free charge inset into Figure 8 and Figure 9. The solution from a larger (80×40) domain, as shown in Figure 11, is mapped onto a smaller (20×10) domain for better presentation of the results.

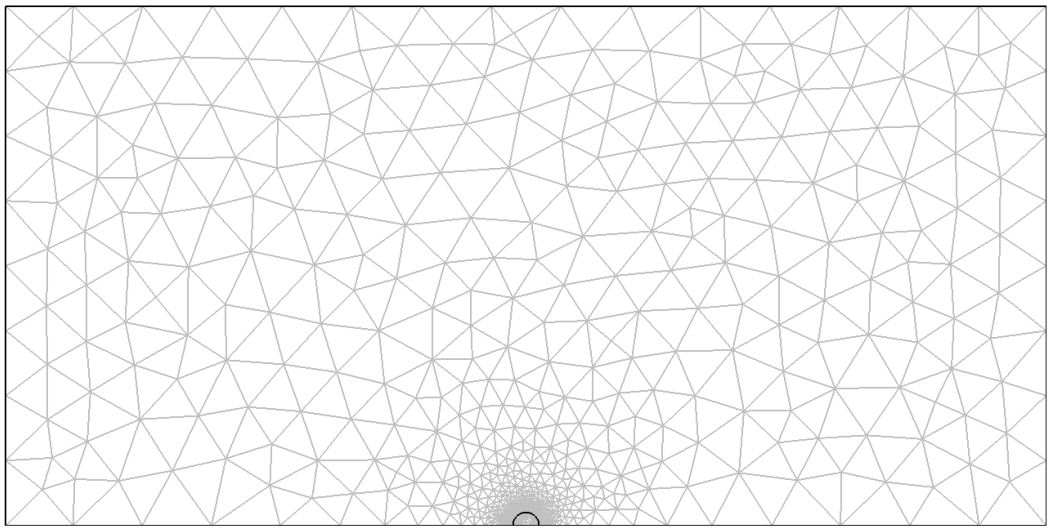

Figure 11: Typical finite element mesh for the resolution of the EDL

4.2.2 The electric double layer in an applied electric field

The objective of this section is to consider the effect of the dimensionless particle radius (κa), dimensionless particle permittivity $\left(\varepsilon_r^p/\varepsilon_r^f\right)$, and particularly the dimensionless applied electric field $(E_0/\kappa\psi_T)$ on the EDL. As we did with the equilibrium EDL, the dimensionless electric potential (ψ/ψ_T), dimensionless free charge (ρ/n_0), and dimensionless average ion density (η/n_0) along the mid-plane is plotted with a surface plot of the dimensionless free charge inset into each figure to show polarization of the EDL in applied electric fields.

A constant surface charge boundary condition was used for the results of Figure 12 through Figure 19 using a value which results in a dimensionless surface potential of one when no electric field is applied. Thus, the results of Figure 12 through Figure 19 can be

compared directly with the results of Figure 8 and Figure 9 (the equilibrium EDL) to demonstrate the effect of the applied electric field.

The two values of dimensionless relative permittivity considered (Table 5) represent two of the most common types of particles used in electrophoresis experiments. For example, Preston, Kornbrekke, and White [17] have presented results for a latex particle and Murtsovkin [33] has presented results of an uncharged infinitely polarizable particle.

Table 5: Dimensionless relative permittivity

Dielectric particle (latex)	$\frac{\varepsilon_r^p}{\varepsilon_r^f} = 0.025$
Infinitely polarizable particle (metallic)	$\frac{\varepsilon_r^p}{\varepsilon_r^f} = 8000$

Figure 12 and Figure 13 show the EDL of a latex particle $\left(\varepsilon_r^p/\varepsilon_r^f = 0.025\right)$ and a metallic particle $\left(\varepsilon_r^p/\varepsilon_r^f = 8000\right)$ of dimensionless particle radius $\kappa a = 1$ in a weak applied electric field, respectively. Figure 16 and Figure 17 show the same particles in a strong applied electric field. Figure 14, Figure 15, Figure 18, and Figure 19 show the same for larger particles or equivalently a more concentrated electrolyte solution, i.e. $\kappa a = 10$. The dimensionless applied electric field $(E_0/\kappa\psi_T)$ is 0.1 for a weak applied electric field and 1 for a strong applied electric field.

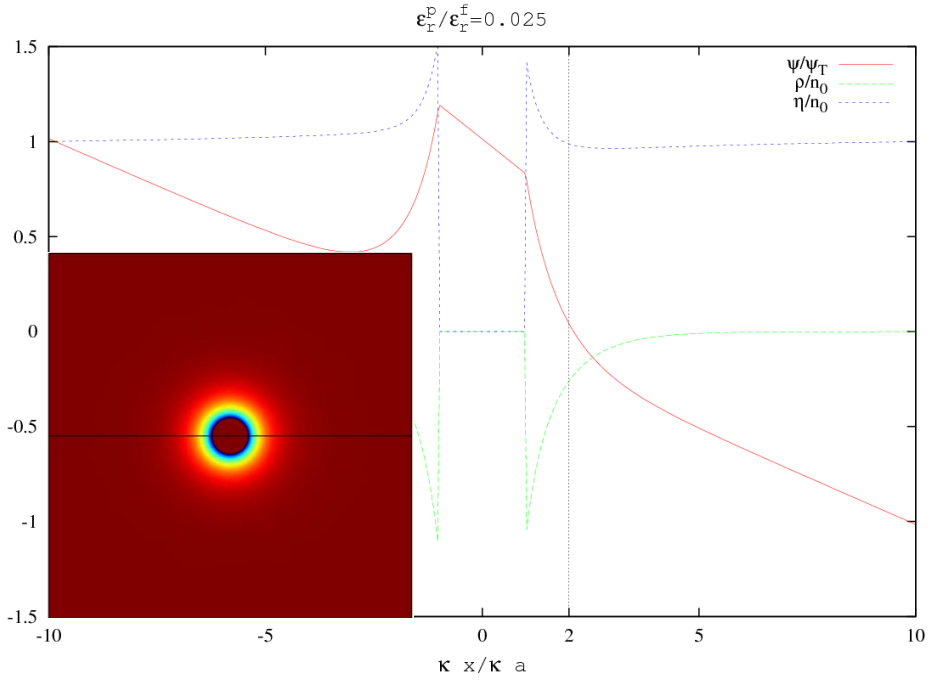

Figure 12: EDL with $\varepsilon_r^p/\varepsilon_r^f = 0.025$, $E_0/\kappa\psi_T = 0.1$, and $\kappa a = 1$

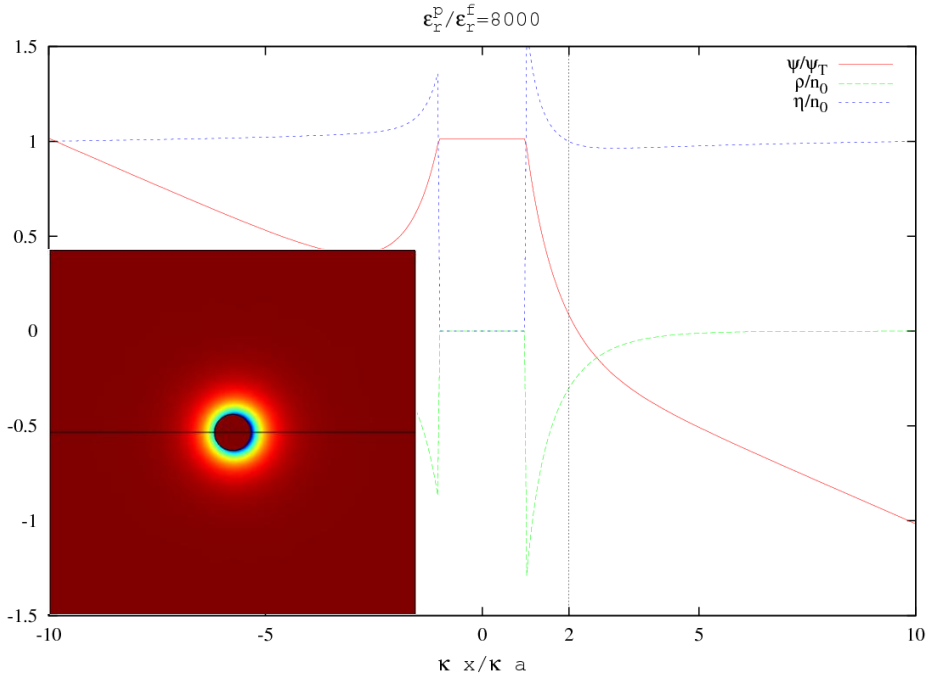

Figure 13: EDL with $\varepsilon_r^p/\varepsilon_r^f = 8000$, $E_0/\kappa\psi_T = 0.1$, and $\kappa a = 1$

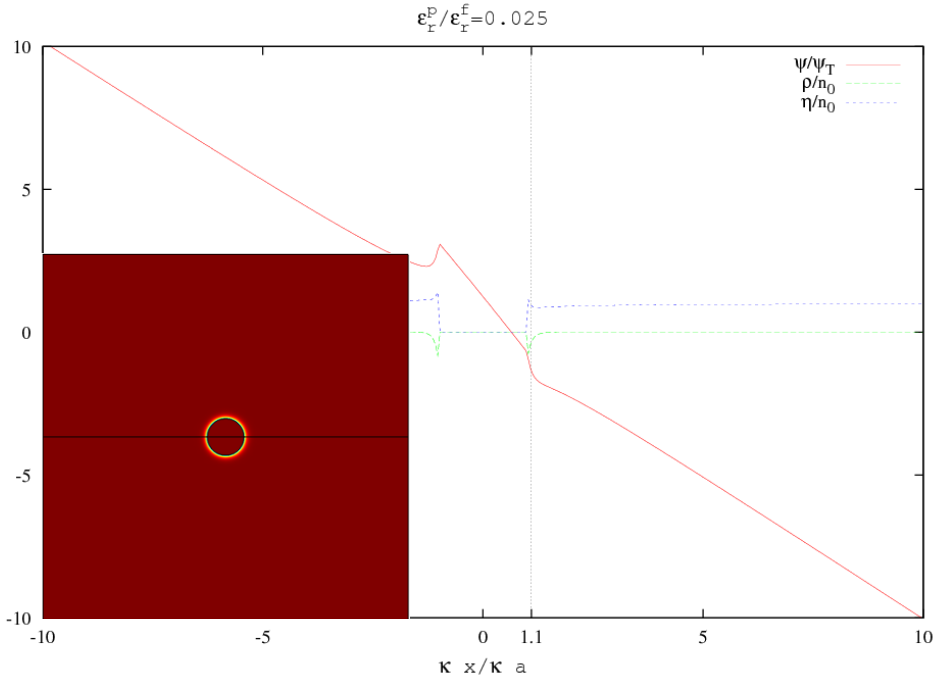

Figure 14: EDL with $\varepsilon_r^p/\varepsilon_r^f = 0.025$, $E_0/\kappa\psi_T = 0.1$, and $\kappa a = 10$

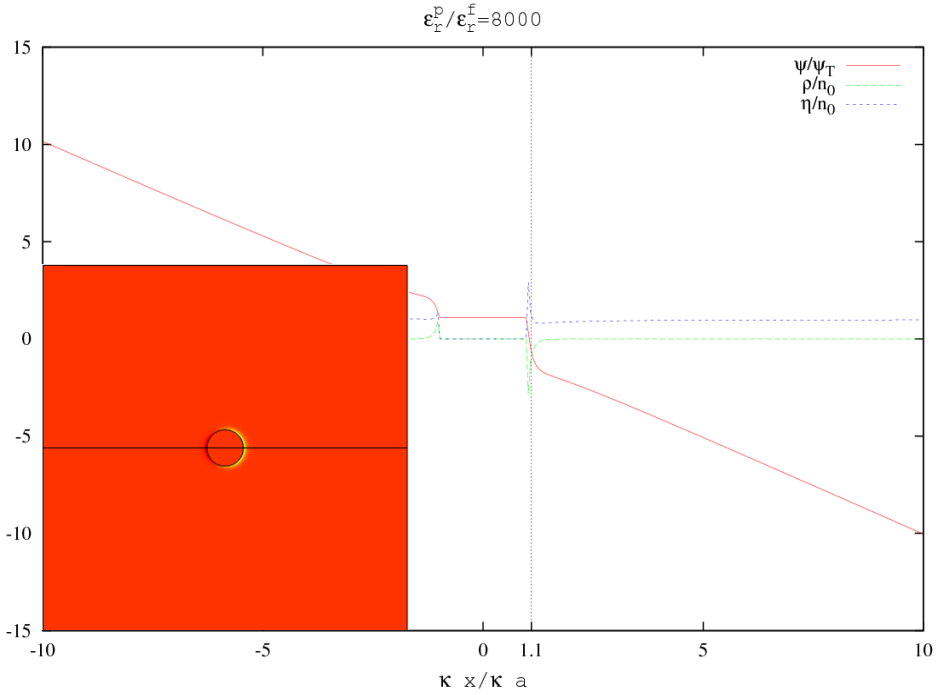

Figure 15: EDL with $\varepsilon_r^p/\varepsilon_r^f = 8000$, $E_0/\kappa\psi_T = 0.1$, and $\kappa a = 10$

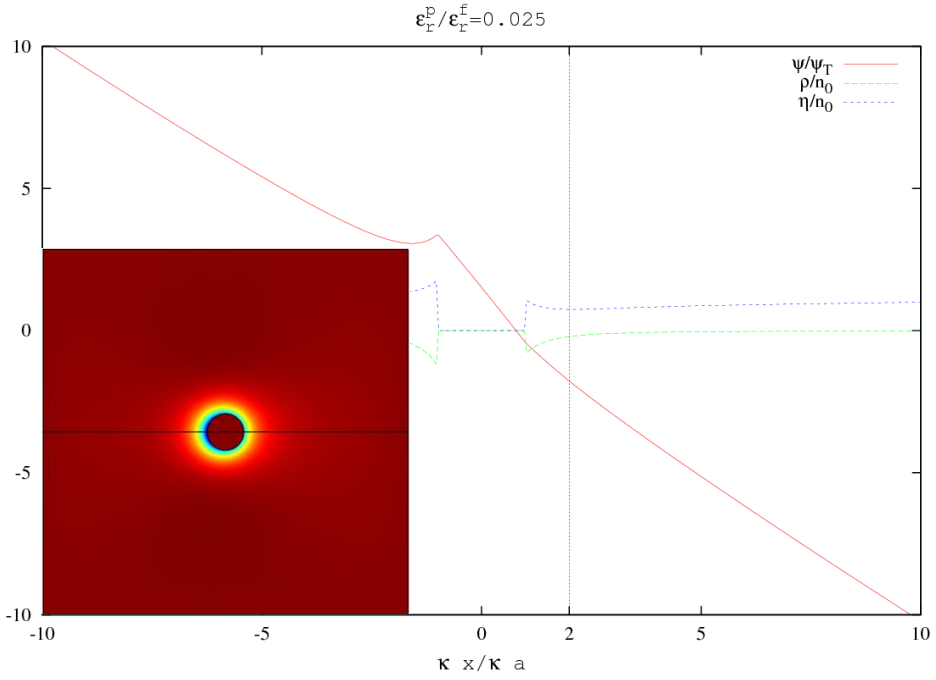

Figure 16: EDL with $\varepsilon_r^p/\varepsilon_r^f = 0.025$, $E_0/\kappa\psi_T = 1$, and $\kappa a = 1$

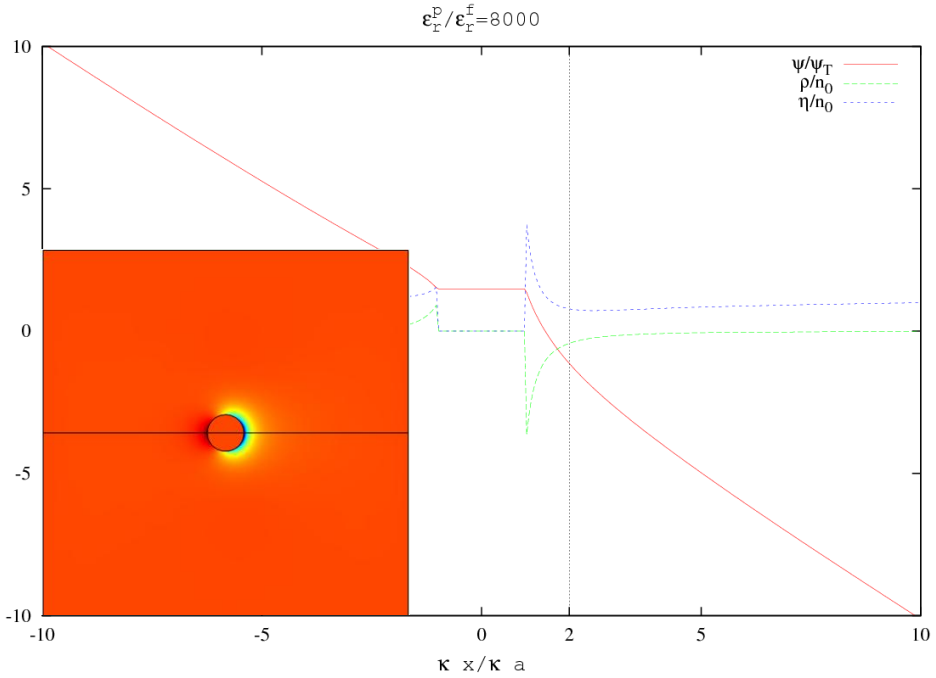

Figure 17: EDL with $\varepsilon_r^p/\varepsilon_r^f = 8000$, $E_0/\kappa\psi_T = 1$, and $\kappa a = 1$

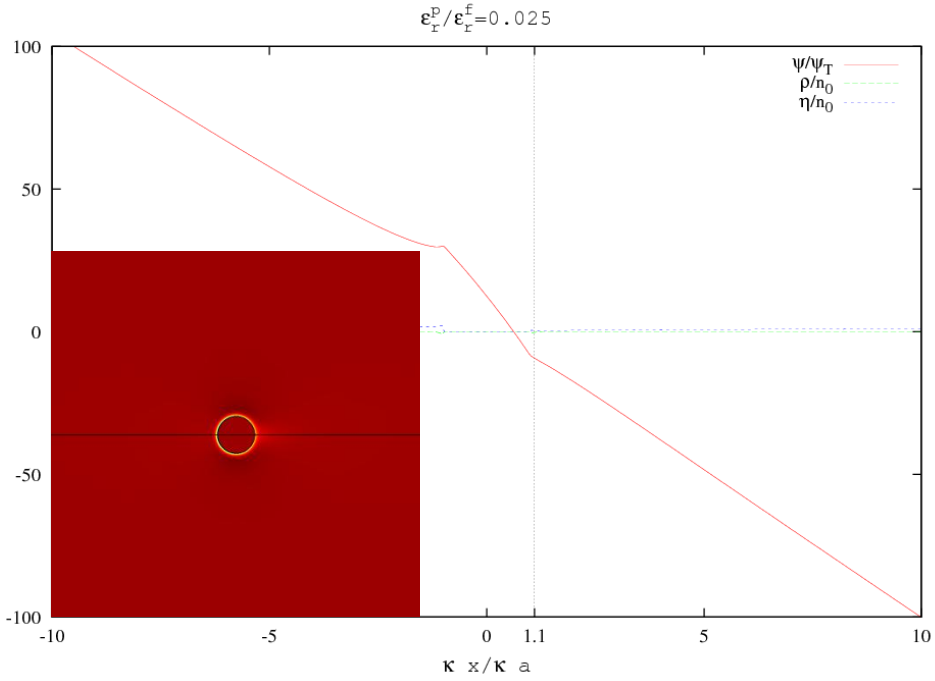

Figure 18: EDL with $\varepsilon_r^p/\varepsilon_r^f = 0.025$, $E_0/\kappa\psi_T = 1$, and $\kappa a = 10$

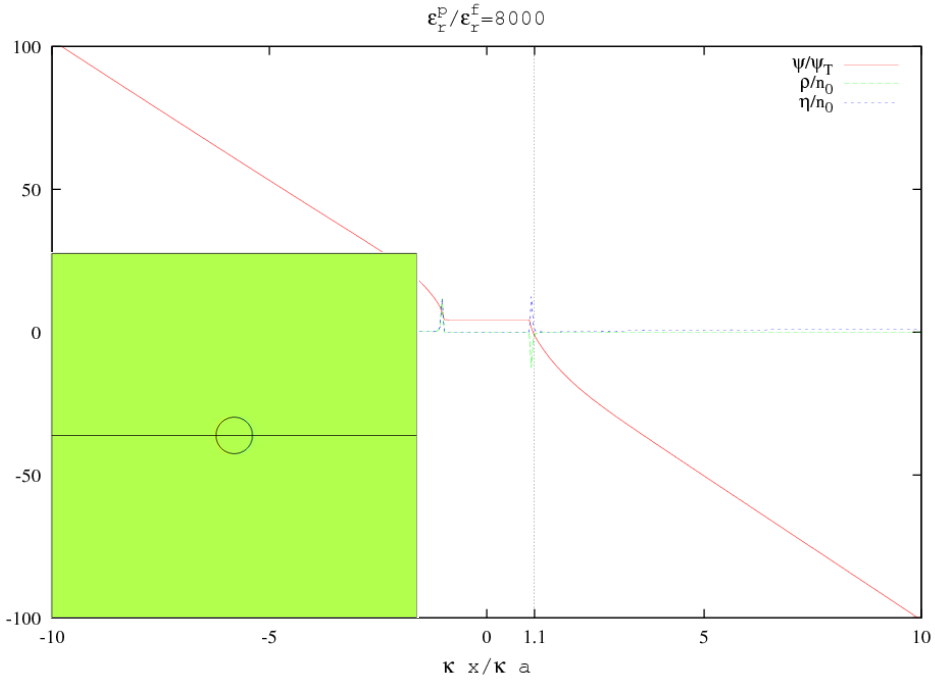

Figure 19: EDL with $\varepsilon_r^p/\varepsilon_r^f = 8000$, $E_0/\kappa\psi_T = 1$, and $\kappa a = 10$

The same process of comparing the electric potential at one Debye length (ψ_λ) used for the equilibrium EDL was used to verify the FEM solution of the EDL in an applied electric field. The analytical solution of Murtsovkin [33] is used for validation of the FEM model. This solution is valid for an uncharged cylindrical particle and small polarization. The dimensionless free charge, electric potential in the surrounding fluid, and the electric potential in the particle in polar coordinates are given by

$$\tilde{\rho} = \frac{\rho}{n_0} = -2\tilde{E}_0 \cos\theta \frac{\varepsilon_r^p}{\varepsilon_r^f} \kappa a \frac{K_1(\kappa r)}{\kappa a K_0(\kappa a) + \frac{\varepsilon_r^p}{\varepsilon_r^f} K_1(\kappa a) + K_1(\kappa a)} \tag{4.2}$$

$$\tilde{\psi}^f = \frac{\psi^f}{\psi_T} = -\tilde{E}_0 \cos\theta \frac{(\kappa a)^2}{\kappa r} - \tilde{E}_0 \cos\theta \, \kappa r + 2\tilde{E}_0 \cos\theta \frac{\varepsilon_r^p}{\varepsilon_r^f} \kappa a \frac{K_1(\kappa r)}{\kappa a K_0(\kappa a) + \frac{\varepsilon_r^p}{\varepsilon_r^f} K_1(\kappa a) + K_1(\kappa a)} \tag{4.3}$$

and

$$\tilde{\psi}^p = \frac{\psi^p}{\psi_T} = -2\tilde{E}_0 \kappa r \cos\theta \frac{\kappa a K_0(\kappa a) + K_1(\kappa a)}{\kappa a K_0(\kappa a) + \frac{\varepsilon_r^p}{\varepsilon_r^f} K_1(\kappa a) + K_1(\kappa a)} \tag{4.4}$$

where $\tilde{E}_0$ is the dimensionless applied electric field, ε_r^p is the relative permittivity of the particle, and ε_r^f is the relative permittivity of the fluid. All of these expressions contain the dimensionless parameter $\varepsilon_r^p/\varepsilon_r^f$ which has been introduced through the boundary condition on electric displacement, i.e.

$$\left(\varepsilon_r^f \varepsilon_0 \frac{\partial \psi^f}{\partial r} - \varepsilon_r^p \varepsilon_0 \frac{\partial \psi^p}{\partial r}\right)\Bigg|_{r=a} = 0 \tag{4.5}$$

or

$$\left(\frac{\partial \tilde{\psi}^f}{\partial r} - \frac{\varepsilon_r^p}{\varepsilon_r^f}\frac{\partial \tilde{\psi}^p}{\partial r}\right)\Bigg|_{r=\kappa a} = 0 \tag{4.6}$$

in dimensionless form. The right hand side of Equation 4.5 or equivalently Equation 4.6 is zero because the particles are assumed to be uncharged.

The small polarization assumption used to arrive at the analytical solution restricts the solution space to the set of solutions where the average number density of ions at any point in the EDL is approximately equal to the bulk concentration, i.e.

$$\frac{n_+ + n_-}{2} \approx n_0 \tag{4.7}$$

or

$$\frac{n_+ + n_-}{2n_0} \approx 1 \tag{4.8}$$

in dimensionless form. In Equation 4.7 and Equation 4.8 a symmetric electrolyte has been assumed for convenience.

In order to verify the FEM model with the small polarization solution, the EDL in an applied electric field was solved using the FEM model with a zero charge boundary condition and the two values of the dimensionless relative permittivity given in Table 5. For each value of dimensionless relative permittivity a constant dimensionless applied electric field of $E_0/\kappa\psi_T = 0.01$ and $E_0/\kappa\psi_T = 1$ is applied. The FEM and analytical solutions should be comparable for the weak applied electric field $(E_0/\kappa\psi_T = 0.01)$ and should demonstrate the onset of nonlinearity for a strong applied electric field $(E_0/\kappa\psi_T = 1)$.

The FEM and analytical solution for (ψ_λ/ψ_0) are compared for a dimensionless applied electric field of $E_0/\kappa\psi_T = 0.01$ and $E_0/\kappa\psi_T = 1$ in Figure 20 and Figure 21, respectively. The dimensionless electric field $(E_0/\kappa\psi_T)$ is used so that the applied electric field maintains the same proportionality to the electric field of the EDL. If $E_0/\psi_T * a$ was used, the electric field would be disproportionately stronger as κa increases making interpretation of the results difficult.

Following the comparison of the FEM solutions with analytical solutions in Figure 20 and Figure 21, some figures are presented to show the distribution and polarization of the EDL of an uncharged particle. The electric double layers surrounding an uncharged dielectric particle and an uncharged metallic particle in a weak and strong applied electric field are plotted for $\kappa a = 1$ and $ka = 10$. As a consistency check, the dimensionless average ion density which must satisfy the condition of Equation 4.8 has been plotted along the mid-plane. These figures will be utilized in the discussion presented in Section 4.3. Figure 22, Figure 23, Figure 24, and Figure 25 show the dielectric and metallic particles in a weak applied electric field. And, Figure 26, Figure 27, Figure 28, and Figure 29 show the same particles in a strong applied electric field.

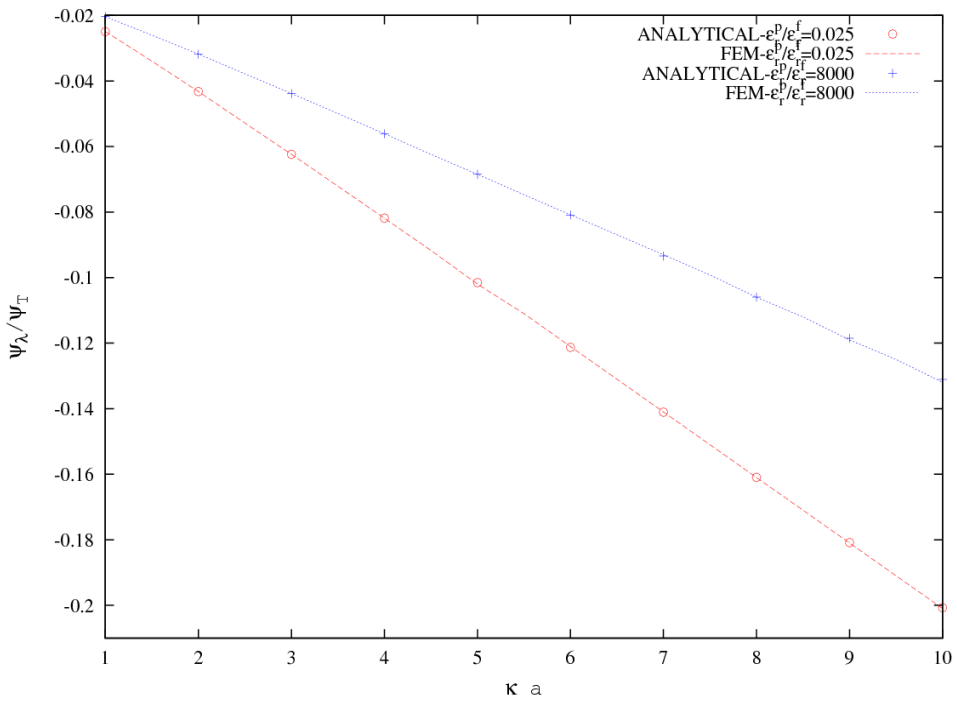

Figure 20: Electric potential at one Debye length for an uncharged particle in a weak electric field

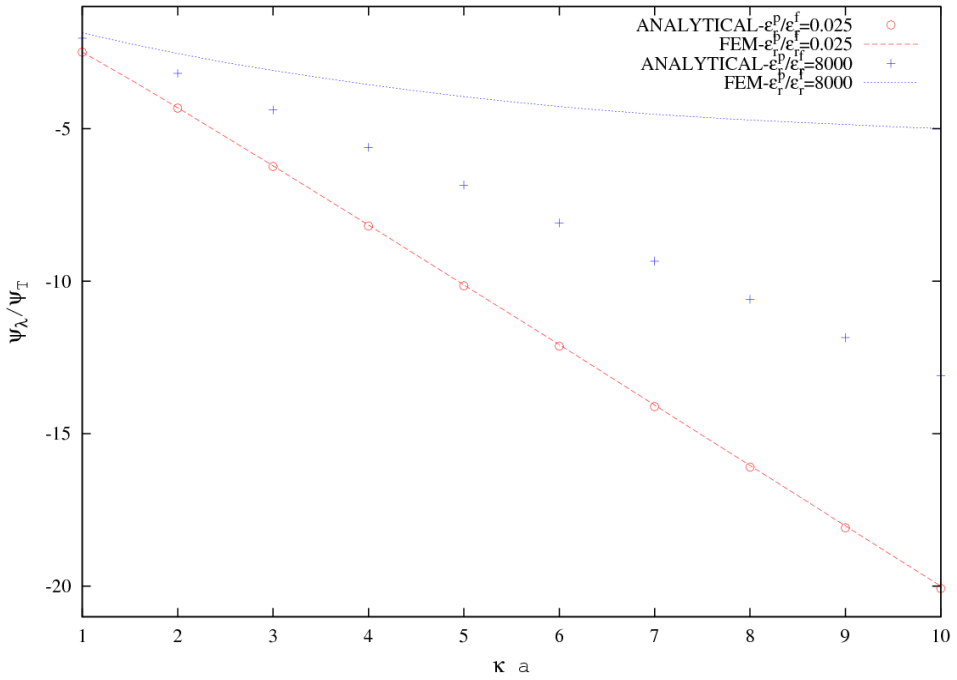

Figure 21: Electric potential at one Debye length for an uncharged particle in a strong electric field

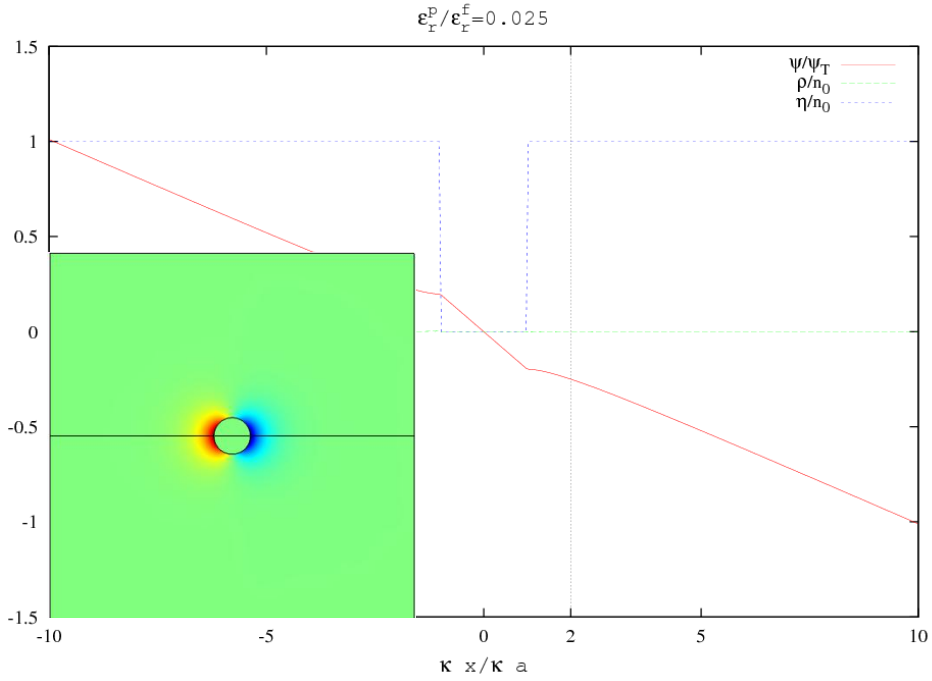

Figure 22: EDL of an uncharged particle with $\varepsilon_r^p/\varepsilon_r^f = 0.025$, $E_0/\kappa\psi_T = 0.1$, and $\kappa a = 1$

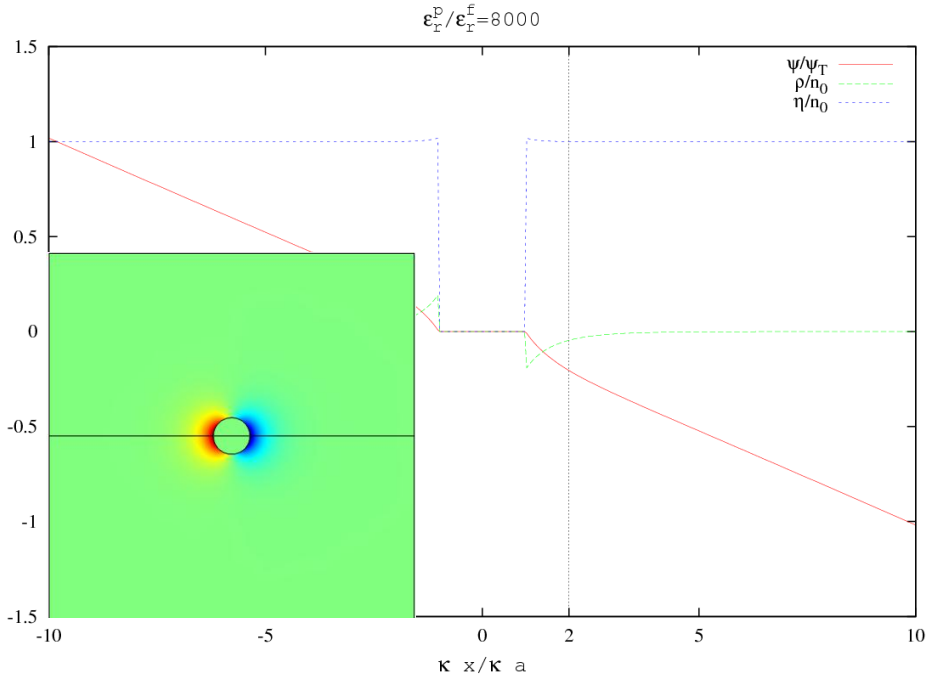

Figure 23: EDL of an uncharged particle with $\varepsilon_r^p/\varepsilon_r^f = 8000$, $E_0/\kappa\psi_T = 0.1$, and $\kappa a = 1$

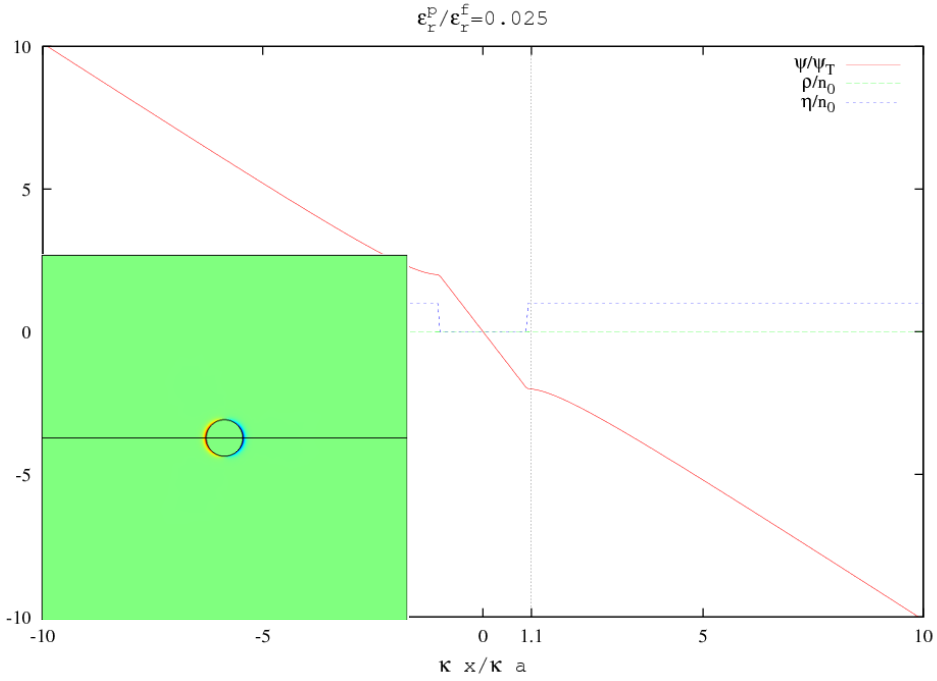

Figure 24: EDL of an uncharged particle with $\varepsilon_r^p/\varepsilon_r^f = 0.025$, $E_0/\kappa\psi_T = 0.1$, and $\kappa a = 10$

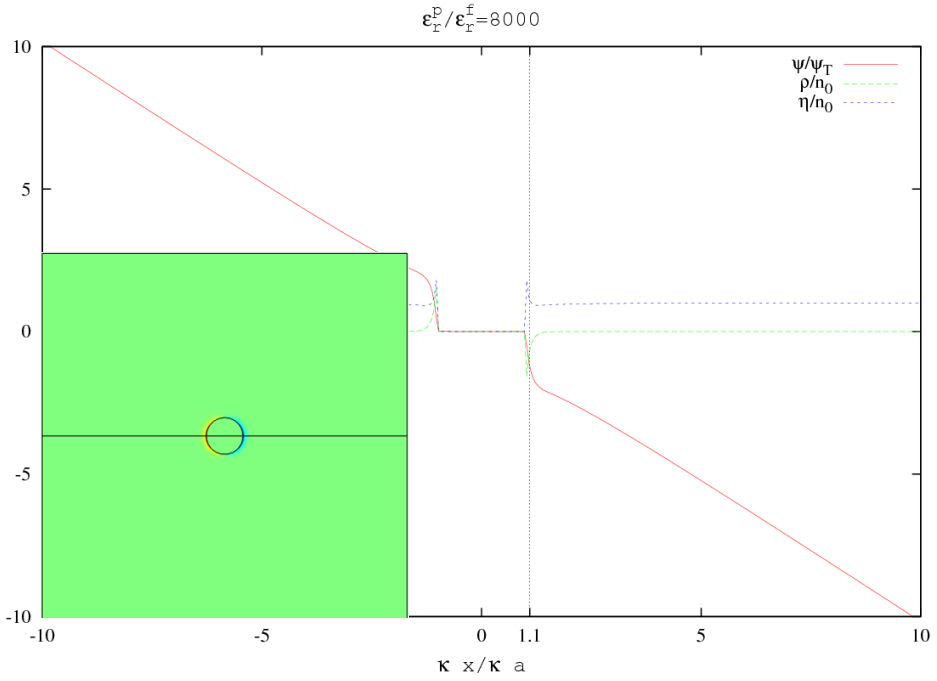

Figure 25: EDL of an uncharged particle with $\varepsilon_r^p/\varepsilon_r^f = 8000$, $E_0/\kappa\psi_T = 0.1$, and $\kappa a = 10$

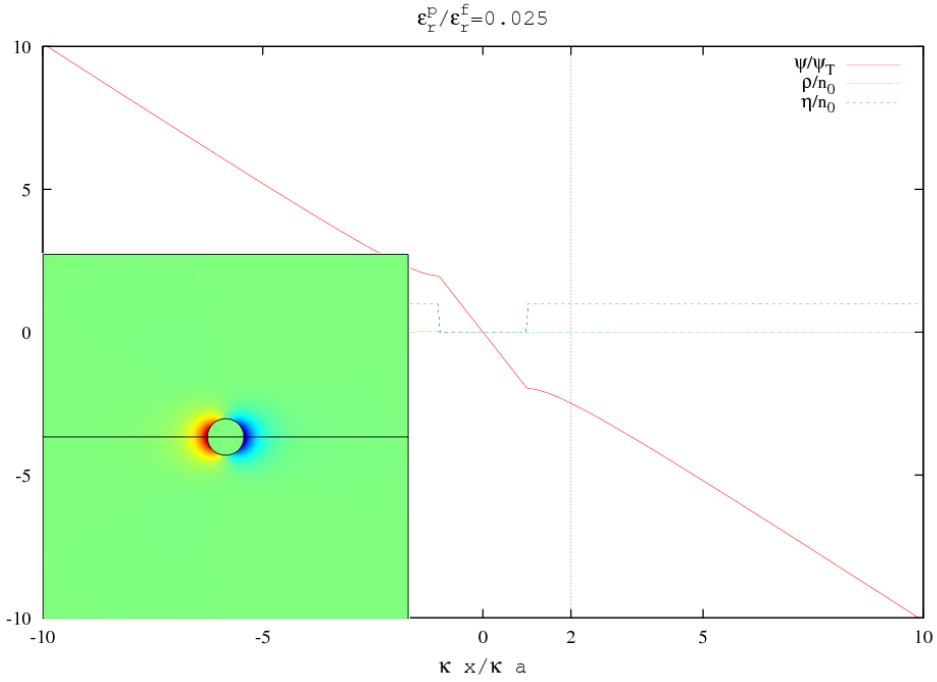

Figure 26: EDL of an uncharged particle with $\varepsilon_r^p/\varepsilon_r^f = 0.025$, $E_0/\kappa\psi_T = 1$, and $\kappa a = 1$

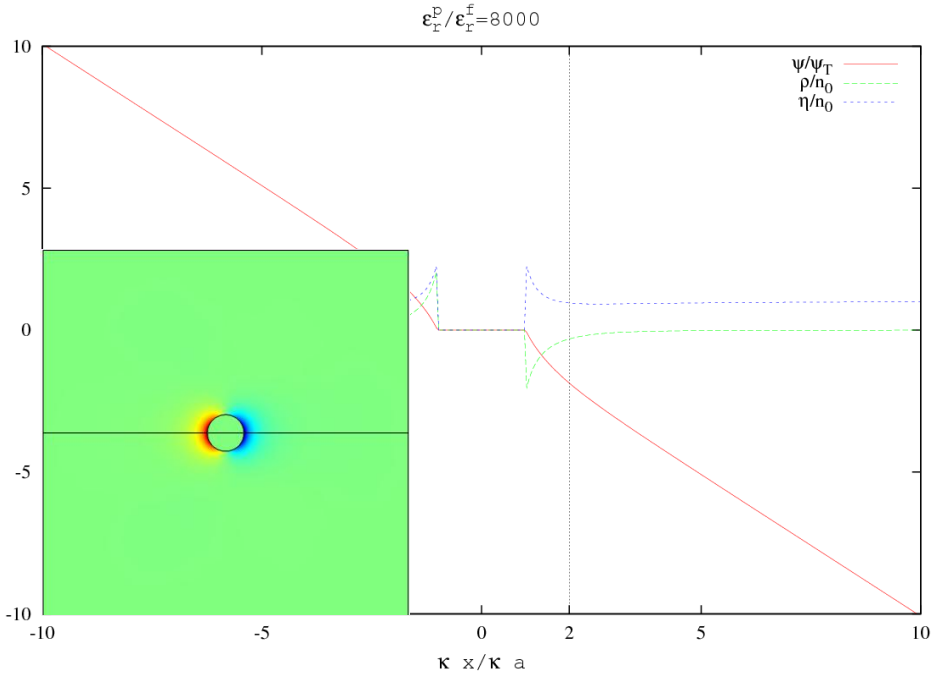

Figure 27: EDL of an uncharged particle with $\varepsilon_r^p/\varepsilon_r^f = 8000$, $E_0/\kappa\psi_T = 1$, and $\kappa a = 1$

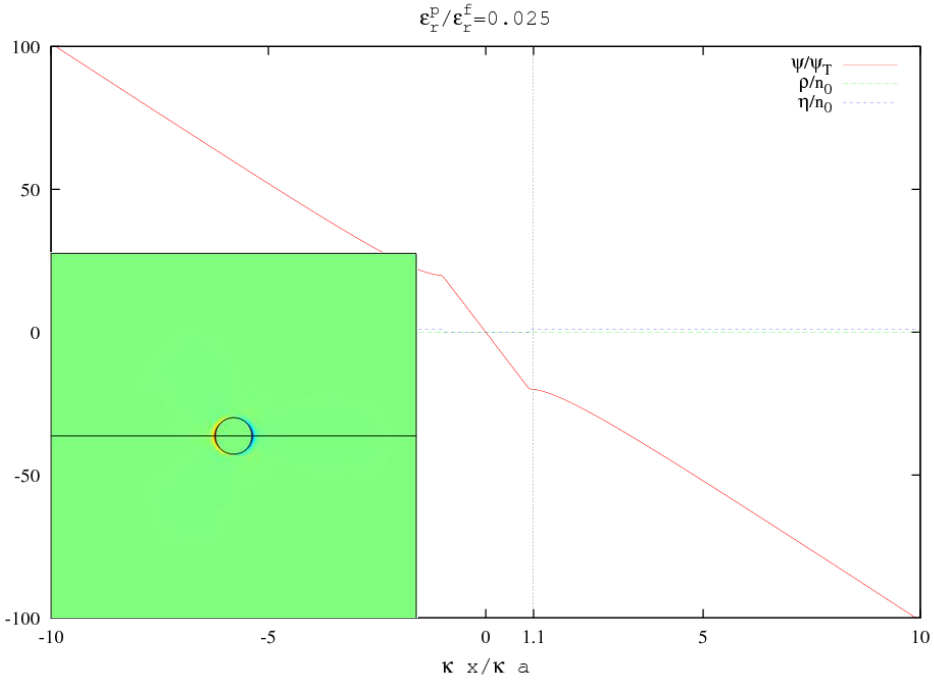

Figure 28: EDL of an uncharged particle with $\varepsilon_r^p/\varepsilon_r^f = 0.025$, $E_0/\kappa\psi_T = 1$, and **$\kappa a = 10$**

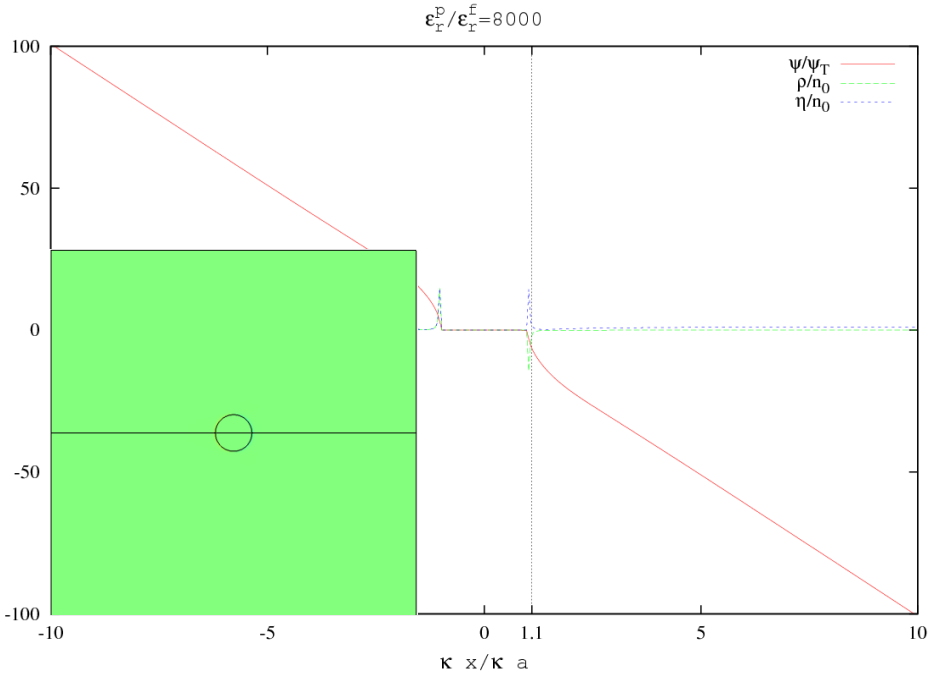

Figure 29: EDL of an uncharged particle with $\varepsilon_r^p/\varepsilon_r^f = 8000$, $E_0/\kappa\psi_T = 1$, and $\kappa a = 10$

4.3 DISCUSSION

The small surface potential results, i.e $\psi_0/\psi_T < 1$, of Figure 10 show that the finite element model is producing good results for the electric potential, ionic concentrations, and free charge of the equilibrium EDL. Also, as expected, the large surface potential results of Figure 10 show that nonlinearity becomes significant for large dimensionless surface potentials, i.e. $(\psi_0/\psi_T > 1)$. The analytical solution of Equation 4.1 over-estimates the electric potential at one Debye length for all $\psi_0/\psi_T > 1$ with an error of 0.05% at $\psi_0/\psi_T = 1$ and growing to 5% at $\psi_0/\psi_T = 4$ for $\kappa a = 10$. The error in the analytical solution is associated with the Debye-Hückel approximation of the Poisson-Boltzmann equation (Equation 2.2). Recall that the Debye-Hückel approximation uses the first term of the MacLaurin series ($\exp(-\boldsymbol{x}) \approx 1 - \boldsymbol{x}$) for the exponential term appearing in the Poisson-Boltzmann equation. While dimensionless surface potentials of equilibrium electric double layers are commonly (although not always) less than one, there is more to consider when electric fields are applied.

It is possible to induce electric potentials greater than the equilibrium surface potential when strong electric fields are applied. The concept of induce electric potentials is illustrated in Figure 26 and Figure 28. The uncharged dielectric particle would have zero surface potential at equilibrium. The results of Figure 26 and Figure 28 show that when an electric field is applied a surface potential is induced. In a strong applied electric field the dimensionless surface potential may become greater than one. The results of Figure 27 and Figure 29 for an uncharged metallic particle show a zero surface potential in an applied electric field. However, a large applied electric field will

change the surface potential of a charged metallic particle as seen in Figure 15 and Figure 17.

The results of Figure 20 validate the FEM model solution of the EDL in an applied electric field. Figure 22, Figure 23, Figure 24, and Figure 25 show that the dimensionless average ion density η/n_0 is about equal to one for a weak applied electric field regardless of particle permittivity, particle radius, or electrolyte concentration. Thus, when the electric field is small in comparison to that of the EDL and the particle is uncharged or only slightly charged the results of the small polarization model are acceptable.

The results of Figure 21 clearly demonstrate the need for a nonlinear electrokinetic model. Particularly, we have shown that the EDL surrounding a metallic particle which is uncharged or only slightly charged is easily polarized by an applied electric field and a nonlinear electrokinetic model is needed to capture the ICEP type nonlinearity. The results of Figure 17 and Figure 19 show the source of the nonlinearity is the polarization of the EDL surrounding a charged metallic particle in a large applied electric field. And the results of Figure 27 and Figure 29 show the polarization of the EDL surrounding an uncharged metallic particle in a large applied electric filed. Care should be taken when interpreting the results of the previous section concerning polarization. Polarization is a nonlinear effect of large applied electric fields; the result of a non-uniform concentration distribution on the surface of the particle. The easiest way to identify polarization is to plot the distribution of the dimensionless free charge (ρ/n_0) in the EDL. If the distribution of the free charge near the surface of the particle is non-uniform the EDL is

polarized. The magnitude of the polarization can be determined by inspecting the dimensionless average ion desity (η/n_0). If the dimensionless average ion density is greater than one, large polarization of the EDL is apparent. Any polarization of the EDL excludes the use of linearized electrokinetic models and large polarization of the EDL excludes the use of the small polarization model of Murtsovkin [33].

The linearized electrokinetic models based on the O-W model including the D-W and M-W models are not restricted to the zero charge condition. However, they assume the distribution of the EDL is unaffected or only slightly affected by the application of a weak applied electric field. Thus, there can be no polarization of the EDL. That is, the distribution of the EDL should resemble that of Figure 8 and Figure 9. The electric double layers shown in surface plots of Figure 12 and Figure 13 might at first seem to resemble that of the equilibrium EDL; if only the surface plots are considered. However, by plotting and inspecting the free charge distribution along the mid-plane as in Figure 13 it is clear that the EDL is slightly polarized. Also, the mid-plane plot of Figure 12 shows a non-uniform surface potential for the dielectric particle. So, it seems that the linearized electrokinetic models would be acceptable for dimensionless applied electric fields which are less than 0.1. A linearized electrokinetic model is clearly not applicable for the EDL shown Figure 14 even though the polarization of the EDL is quite small. As a consequence of the assumption that the EDL is basically unaffected by the presence of a weak applied electric field, linearized electrokinetic models predict that the applied electric field is not strong enough to induce a change in the electric potential at the surface of the particle. Thus, the potential distribution within the dielectric

particle shown in Figure 12 and Figure 14 could not be predicted by linearized electrokinetic models. In a strong applied electric field the EDL seldom resembles the equilibrium EDL even for a metallic particle. The results of Figure 22 through Figure 29 show that the EDL of an uncharged particle is always affected by an applied electric field regardless of strength. Thus, it is expected that the linearized electrokinetic models would not produce sufficient results for uncharged particles.

Linearized electrokinetic models use the constant surface potential boundary condition as in Equation 2.4. However, it does not make since to use the constant surface potential condition in a nonlinear electrokinetic model. First, using a constant surface boundary condition precludes the induction of surface potential in a strong applied electric field. Secondly, if the constant surface charge boundary condition is used exclusively in the nonlinear electrokinetic model the results of a linearized electrokinetic model are recovered when the applied electric field is in fact small relative to the electric field of the EDL. Thus, it is proposed that the constant surface boundary condition is the only appropriate boundary condition for a nonlinear electrokinetic model. The use of a constant potential boundary condition has a certain attraction in developing analytical solutions. However, there is no advantage in using the constant surface potential boundary condition in a numerical model such as the FEM model.

The use of a constant surface charge boundary condition is supported by a study of the electrochemistry of the interface as presented in the text of Lyklema [34]. The formation of charge on the surface of a colloid is fundamentally explained by the thermodynamics of a two phase system.

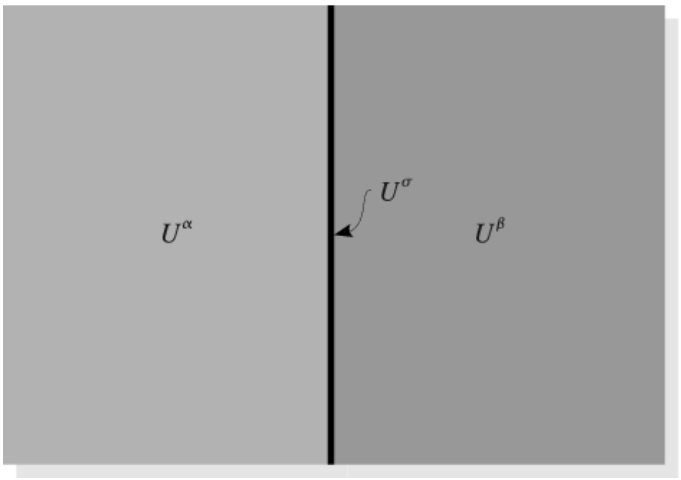

Figure 30: Two phase system with Gibbs dividing plane

The first law of thermodynamics for a two phase system with a common interface, which is idealized as a Gibbs dividing plane (Figure 30), states that at equilibrium the internal energy of the α phase, the internal energy of the interface (σ phase), and the internal energy of the β phase balance each other, i. e.

$$U^{\alpha} + U^{\sigma} + U^{\beta} = 0 \tag{4.9}$$

The second law of thermodynamics can be expressed with the Gibbs equation

$$SdT + Ad\gamma + \sum_{i} n_i \, d\tilde{\mu}_i = 0 \tag{4.10}$$

where S is the entropy, T is the temperature, A is the area of the interface, γ is the surface tension, and $\tilde{\mu}_i$ is the electrochemical potential. The surface tension is defined as the differential Gibbs free energy of the interface. It is clear, by inspecting Equation 4.10, that an initially uncharged particle when placed in a dissimilar electrolyte introduces entropy into the system. This energy is balanced at equilibrium by the

redistribution and adsorption of dissociated ions from the electrolyte solution near the surface of the particle. Interaction of adsorbed ions with the surface is electric or "coulombic" and non-electric, whatever the origin. That is, the three types of Van der Waals forces, hydrogen bonding, solvent structure originated, or real chemical bond formation. All of this interaction is at the interface and is determined locally by a balance of thermodynamic energy at the interface. Any ion that may attach to a particle will create a potential that keeps out ions of the same sign. Accumulation of a number of identical charges on a surface can then only take place if the adsorbed ions experience a non-electric affinity for the surface so that they can move against the adverse potential. Thermodynamically, this issue can be condensed into the balance of two differential Gibbs free energies by introducing the electrochemical potential

$$\tilde{\mu}_i = \mu_i + z_i e\psi \tag{4.11}$$

so that,

$$\Delta G^{\sigma}(\text{electric}) = \int_0^{\sigma_0} \psi_0' \, d\sigma_0' \tag{4.12}$$

and

$$\Delta G^{\sigma}(\text{non-electric}) = \Gamma_i \Delta_{ads} \mu_i \tag{4.13}$$

where ψ_0' and σ_0' are the electric potential during charging, Γ_i is the concentration of adsorbed ions, and $\Delta_{ads}\mu_i$ is the change in chemical energy during charging. The variable μ_i in Equation 4.11 and Equation 4.13 is often called the chemical part of the electrochemical potential. However, it really accounts for all non-electric forces including Van der Waals, etc. The system as a hole must also be in thermodynamic

equilibrium. So, to balance the Gibbs free energy of the interface, ions are redistributed in the electrolyte solution and possibly the particle if it is permeable. This redistribution of ions in the α phase and/or the β phase forms the electric double layer.

Thus, the reason an electric double layer forms is the result of the non-electric affinity of charge determining ions for a surface. The extent to which the double layer develops is determined by the non-electrostatic ↔ electrostatic interaction balance. This brings us to the fundamental problem with the constant electric potential boundary condition for a particle in a strong applied electric field. It assumes the applied electric field is so small that they do not affect the electric potential at the interface. In a strong applied electric field the surface potential is altered, i.e. an induced surface potential does exist. The induced electrochemical potential changes the electric differential Gibbs free energy (Equation 4.12) which must be balanced by adsorption of ions by Equation 4.13. This both explains the need for the GDSL theory to model adsorption and excludes the use of the constant surface potential boundary condition.

4.4 CONCLUSIONS

The finite element model solution of the equilibrium EDL and the EDL in an applied electric field has been verified by comparing the electric potential at one Debye length with that of an analytical solution of Lin, et al [32] and Murtsovkin [33], respectively. We have shown that the linearized electrokinetic models are not valid when strong electric fields are applied. Also, we have concluded that the small polarization model is valid for a dielectric particle in the weak and strong applied electric fields we considered if the particle is uncharged. However, the small

polarization assumption is violated for a metallic particle in a strong field. Finally, a nonlinear electrokinetic model is always needed to accurately calculate the distribution of the electric potential, free charge, and ion density for the general situation of a charged metallic particle in a strong applied electric field.

The constant surface boundary condition with the possible inclusion of the GDSL theory to account for Stern layer adsorption and tangential conduction within the Stern layer is proposed as the only consistent boundary condition for particles in large applied electric fields. Constant surface potentials preclude induced electric potentials or charges which are possible in applied electric fields. Stern layer adsorption models also limit the magnitude of the induced potential so that realistic electric potentials or ion concentrations are not exceeded.

The distribution of the electric double layer is an important tool to be used in the interpretation of nonlinear electrokinetic phenomena. Its accurate solution depends on the inclusion of the complete nonlinear electrokinetic theory and sufficient mesh refinement near the surface of the particle. In the following section we investigate nonlinear electrophoresis. The distribution of the EDL will be presented to identify and explain the effect of polarization on electrophoresis.

5 THE NONLINEAR ELECTROPHORETIC MOBILITY OF A DILUTE COLLOIDAL DISPERSION

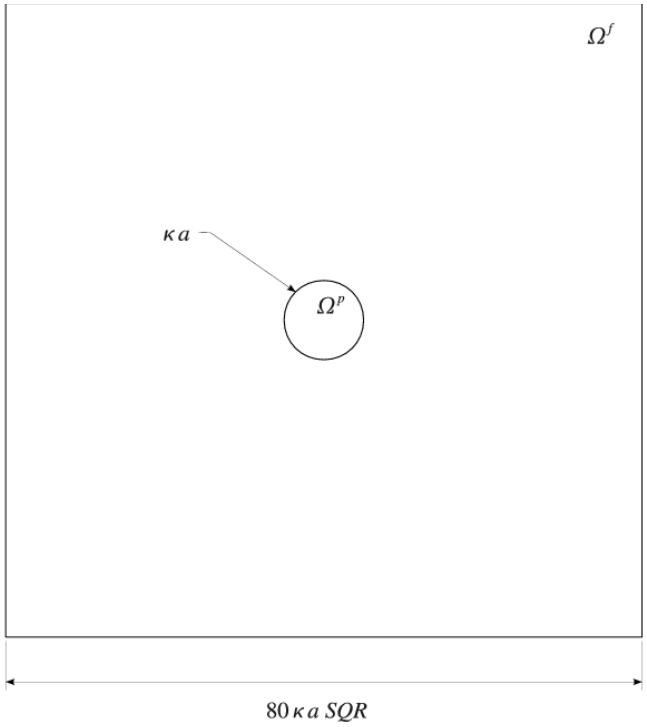

Figure 31: Single particle in a uniform electric field

5.1 PROBLEM STATEMENT

The objectives of this section are; (1) to verify the FEM solution of the electrophoretic mobility of a dilute dispersion of spherical colloidal particles and (2) to investigate the effect of large applied electric fields on the electrophoretic mobility. In the following we define the electrophoretic mobility and discuss its importance in the field of colloid and interface science, we discuss the analytical solution used in the validation of the FEM model, and we present and discuss the results of the FEM model.

When a particle is subjected to a uniform electric field $\boldsymbol{E}$ it moves with velocity $\boldsymbol{U}$. The velocity is related to the electric field by

$$U = \mu E \tag{5.1}$$

where μ is the mobility, U is the magnitude of the velocity, and E is the magnitude of the applied electric field.

This problem has been extensively studied by the colloid and interface science community because it relates the surface properties of the particle, which are not directly measurable, to the mobility of the particle. As one respected researcher in the field of colloid and interface science stated, "The measurement of electrophoretic mobility is a noninvasive probe for particle characterization. Static electrophoresis experiments, with the use of appropriate theory, for example, can be used in the determination of the zeta potential (ζ) and the surface conductance parameter (K^*). High-frequency electrophoresis experiments can yield more information than static measurements because the dynamic mobility is related not only to the electrical properties of the surface but also to the particle size a and the size distribution. The ability to carry out such a characterization rests on the availability of a stable and accurate technique to solve the standard set of electrokinetic equations."[17]

To reduce the computational cost, the problem was modeled as a single cylindrical colloidal particle in a uniform electric field applied perpendicular to the axis of the cylinder as shown in Figure 31. The FEM model also assumes the coordinate system is attached to the particle. This reduces computational cost because this model does not require the expensive remeshing associated with arbitrary Lagrangian-Eulerian finite

element based methods (ALE-FEM) first developed by Hu[35]. In this coordinate system fluid moves around a fixed domain (Ω^p in Figure 31) which represents the particle. The fluid velocity surrounding two different particles in an applied electric field is shown in Figure 32. The streamlines are traces of constant fluid velocity and the arrows represent the direction and relative magnitude of the fluid velocity. The positively charged particle is moving to the right in a positive applied electric field. So, the fluid is moving to the left relative to the particle. The surface plot shows the free charge density.

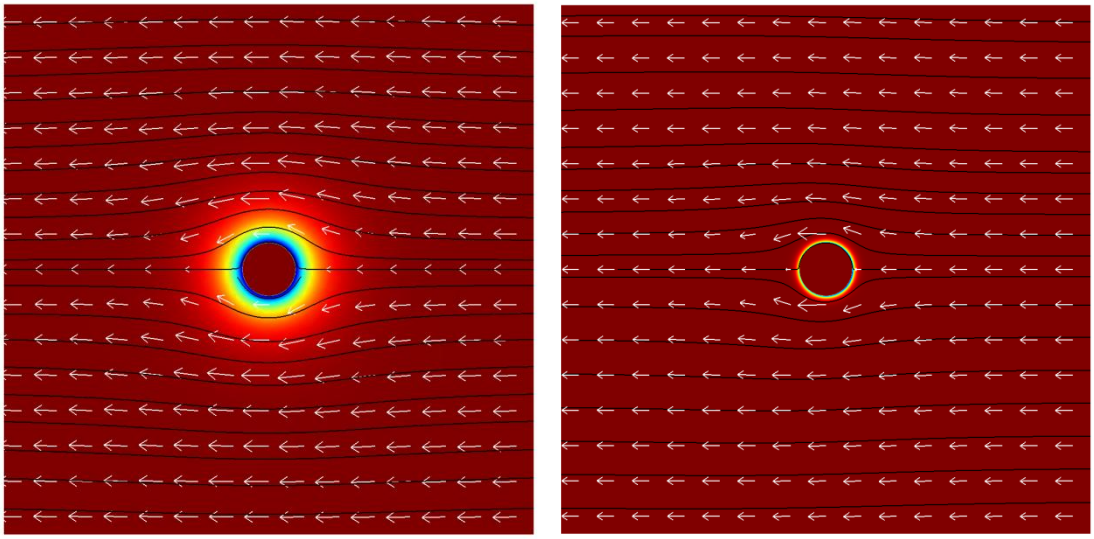

Figure 32: Free charge and fluid velocity surrounding a positively charged particle with $\kappa a = 1$ (left) and $\kappa a = 10$ (right)

The electrophoretic mobility in this coordinate system is simply the fluid velocity at an infinite distance from the particle. In the FEM model the average fluid velocity on the boundary of the fluid domain is taken as the electrophoretic mobility since some variation in the fluid velocity will exist when the domain is finite. However, as the

domain is increased the variation becomes negligible. In addition to a mesh refinement study, the size of the domain needed to approximate an infinite domain was also performed.

Ohshima has developed analytical solutions for the static mobility $\mu(\kappa a)$ and the dynamic mobility $\mu(\kappa a, \omega)$ based on the Debye-Hückel approximation which are valid for all κa and low zeta potentials. Separate expressions are given for the mobility of a cylindrical particle oriented perpendicular to the applied field $\mu_{\perp}$ and parallel to the applied field $\mu_{\parallel}$ [36, 37]. Ohshima[37] has also shown that the mobility of a cylinder averaged over a random distribution of orientation of the cylinder axis is roughly equal to the mobility of a sphere with a radius of 1.5 times the cylinder radius. However, no attempt is made here to compare the results of the finite element model with that of a spherical particle. Instead, the results of the FEM model are compared with the analytical solutions for $\mu_{\perp}$.

5.2 RESULTS

The results of this section illustrate the steps taken to verify the FEM solution for electrophoretic mobility using the analytical solution from Ohshima [36, 37] and demonstrate the nonlinear effects of large applied electric fields on electrophoretic mobility. The section is divided into two sub-sections. In the first sub-section we present solutions for the static electrophoretic mobility of a single particle in a weak applied electric field to validate the FEM model and a single particle in a strong applied electric field to investigate nonlinear effects. In the next sub-section we present and discuss the effect of the applied electric field frequency on the dynamic electrophoretic

mobility of a single particle. The presentation of these results is followed by a discussion in Section 5.3 and some conclusions in Section 5.3.

5.2.1 Static electrophoretic mobility

The validation of the FEM solution for the static electrophoretic mobility using the analytical solution from Ohshima [36] is presented in Figure 33. Then, the effect of strong applied electric fields on the mobility is presented for different surface boundary conditions and dimensionless particle permittivities in the figures on pages 78, 82, 94, and 101. The mobility presented in the figures that follow has been scaled by Smoluchowski's formula which is given by

$$\mu_S = \varepsilon_r^f \varepsilon_0 \zeta / \eta_0 \tag{5.2}$$

which is the mobility of an infinitely large particle or equivalently the mobility of a cylindrical particle with its axis oriented parallel to the applied electric field.

The analytical result of Ohshima [36] for the static electrophoretic mobility is given as

$$\mu = \frac{\varepsilon_r^f \varepsilon_0}{\eta_0} \zeta \, f(\kappa a) \tag{5.3}$$

where $f(\kappa a)$ is the Henry function. Ohshima [36] has determined the Henry function of a cylindrical particle with a small zeta potential. It is given as

$$f(\kappa a) = 1 - \frac{4(\kappa a)^4}{K_0(\kappa a)} \int_{\kappa a}^{\infty} \frac{K_0(t)}{t^5} dt + \frac{(\kappa a)^2}{K_0(\kappa a)} \int_{\kappa a}^{\infty} \frac{K_0(t)}{t^3} dt \tag{5.4}$$

where $K_0(t)$ is the zeroth-order Bessel function of the second kind evaluated at t.

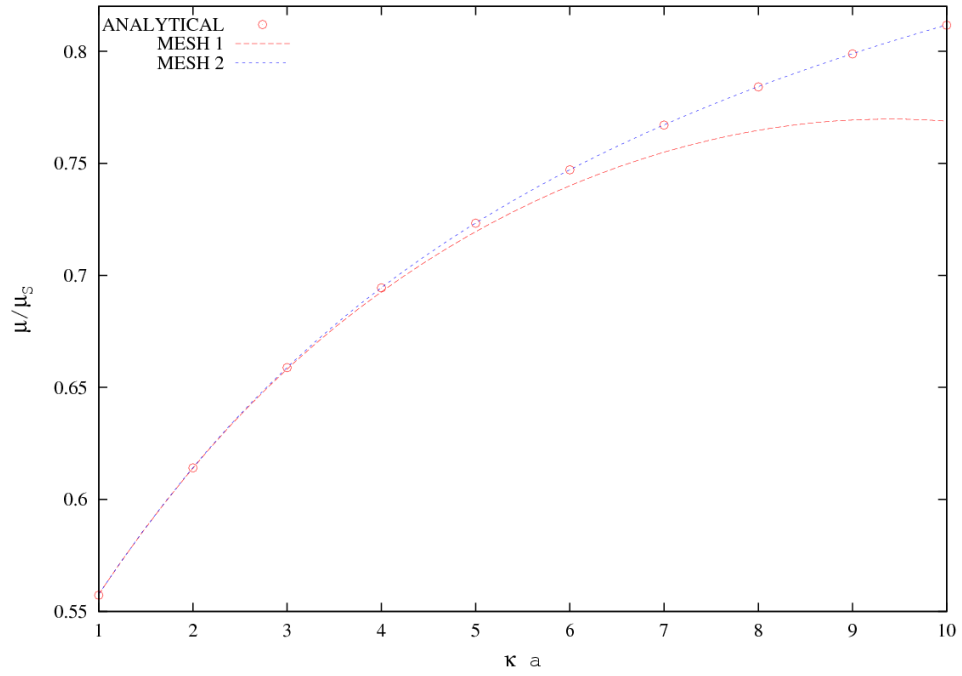

Figure 33: Scaled mobility as a function of dimensionless particle radius

The results of the FEM model and the analytical solution (Equation 5.3 and Equation 5.4) are compared in Figure 33 for several values of κa. The constant surface potential boundary condition $(\psi_0/\psi_T = -0.1)$ was used with a small dimensionless applied electric field $(E_0/\kappa\psi_T = 1 \times 10^{-2})$. The result in Figure 33 labeled Mesh #1 was calculated using a mesh of 1429 elements for the half domain model. This results in 14705 degrees of freedom. The second result shown, labeled Mesh #2, is from a mesh with 6438 elements for 61300 degrees of freedom. The two meshes are shown to illustrate the necessary process of mesh refinement to produce acceptable results.

To investigate the nonlinear effects of large applied electric fields the static electrophoretic mobility was computed as a function of dimensionless applied electric field $(E_0/\kappa\psi_T)$ for different surface boundary conditions. Three different surface

boundary conditions were considered (1) constant surface potential, (2) constant surface charge, and (3) the Stern layer boundary condition of the GDSL theory. In each case, four different values for the boundary condition are considered which represent particles with zeta potentials of -2.57, -25.7, -38.6, and -51.4 mV. The FEM solutions for the scaled nonlinear electrophoretic mobility (μ/μ_S) using the constant surface potential boundary condition are presented Figure 34.

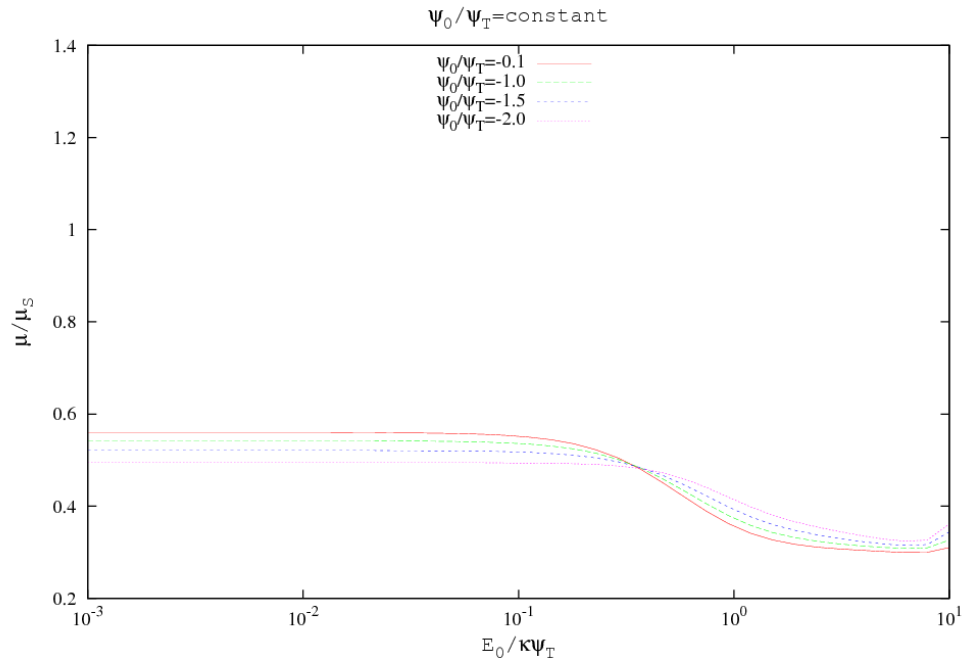

Figure 34: Scaled mobility as a function of applied electric field for constant surface potential

The results of Figure 34 show that when using the constant surface potential boundary condition: The scaled mobility decreases with increasing surface potential. The scaled mobility decreases with increasing dimensionless applied electric field strength. A minimum mobility exists with respect to dimensionless applied electric field

strength. The nonlinear effect of a large dimensionless applied field is reduced with increasing surface potential.

To explain the change in the mobility observed in Figure 34, the distribution of the EDL for the constant surface potential boundary condition is plotted in Figure 35, Figure 36, and Figure 37 for dimensionless applied electric fields of $E_0/\kappa\psi_T = 10^{-2}$, $E_0/\kappa\psi_T = 10^0$, and $E_0/\kappa\psi_T = 10^1$. The surface plot included in each figure shows the dimensionless free charge and the streamlines and the arrows show the direction and relative magnitude of the fluid velocity.

The results of Figure 35, Figure 36, and Figure 37 show that as the strength of the applied electric field is increased the EDL is polarized with the maximum free charge occurring at the left portion of the particle being positive. The results of Figure 35 show that for the dimensionless surface potential presented, $\psi_0/\psi_T = -0.1$, the EDL is slightly polarized at $E_0/\kappa\psi_T = 10^{-2}$. The dimensionless average ion density plotted in Figure 36 shows that as the applied electric field is increase to $E_0/\kappa\psi_T = 10^0$ the polarization becomes large. As the applied electric field is increased beyond $E_0/\kappa\psi_T = 10^0$ the average ion density and free charge become very large and the EDL is condensed, as shown in Figure 37.

Further discussion concerning the nonlinear effects observed in Figure 34 and the results of Figure 35, Figure 36, and Figure 37 is deferred to Section 5.3 after the results for different boundary conditions have been presented. In this way the effect of the surface boundary condition and dimensionless particle permittivity can be fully understood.

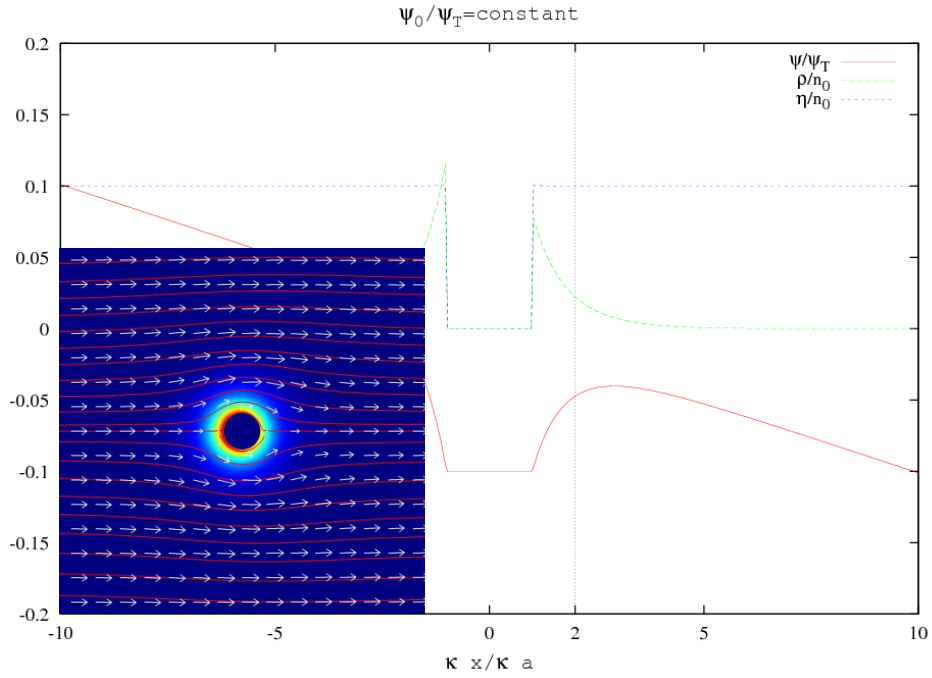

Figure 35: EDL of a particle with; $\psi_0/\psi_T = -0.1$, $E_0/\kappa\psi_T = 0.01$

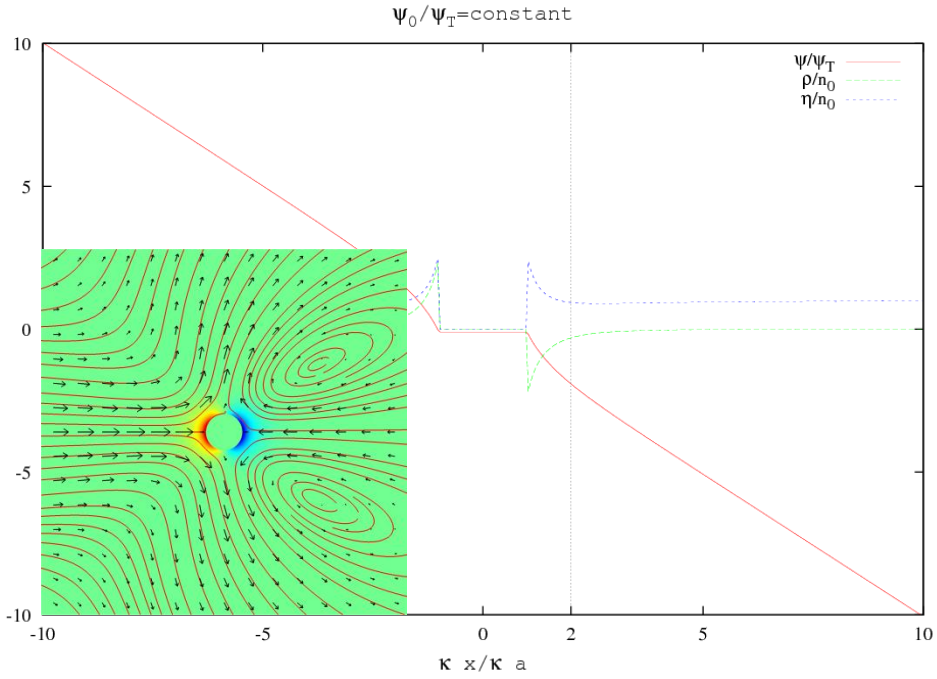

Figure 36: EDL of a particle with; $\psi_0/\psi_T = -0.1$, $E_0/\kappa\psi_T = 1$

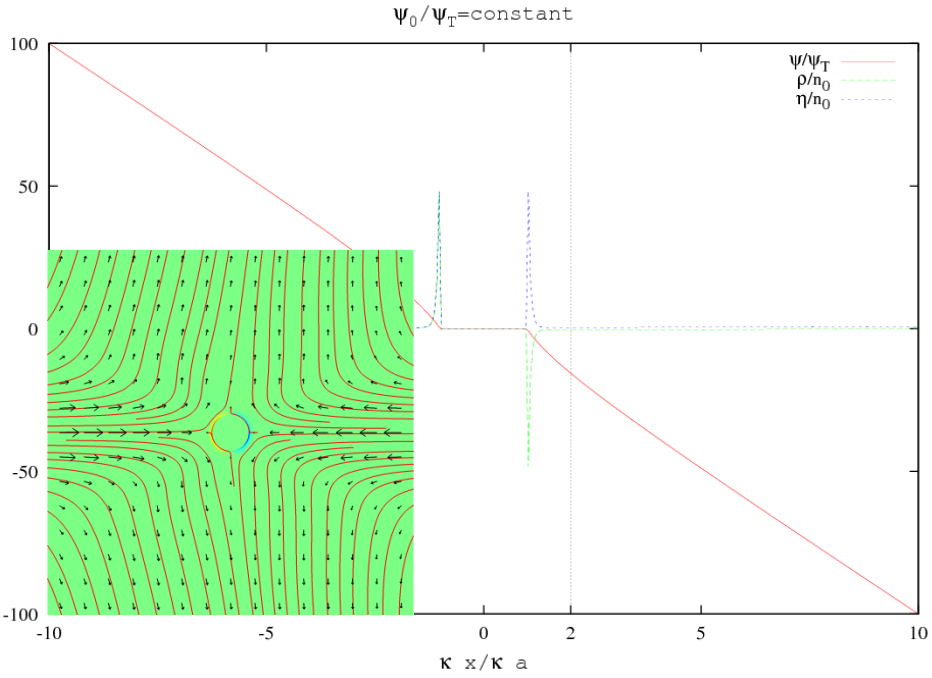

Figure 37: EDL of a particle with; $\psi_0/\psi_T = -0.1$, $E_0/\kappa\psi_T = 10$

The FEM solutions for the scaled nonlinear electrophoretic mobility (μ/μ_S) using the constant surface charge boundary condition are presented Figure 38. The results of Figure 38 are directly comparable to the results of Figure 34 as the dimensionless surface charges used in Figure 38 correspond to the equilibrium surface potentials used in Figure 34. Since the electrophoretic mobility using different boundary conditions is the same for weak applied electric fields, a comparison of Figure 34 and Figure 38 reveals nonlinear effects due to the strength of the applied electric field. The effect of the particle permittivity was included by considering each of the values of $\varepsilon_r^p/\varepsilon_r^f$ listed in Table 5.

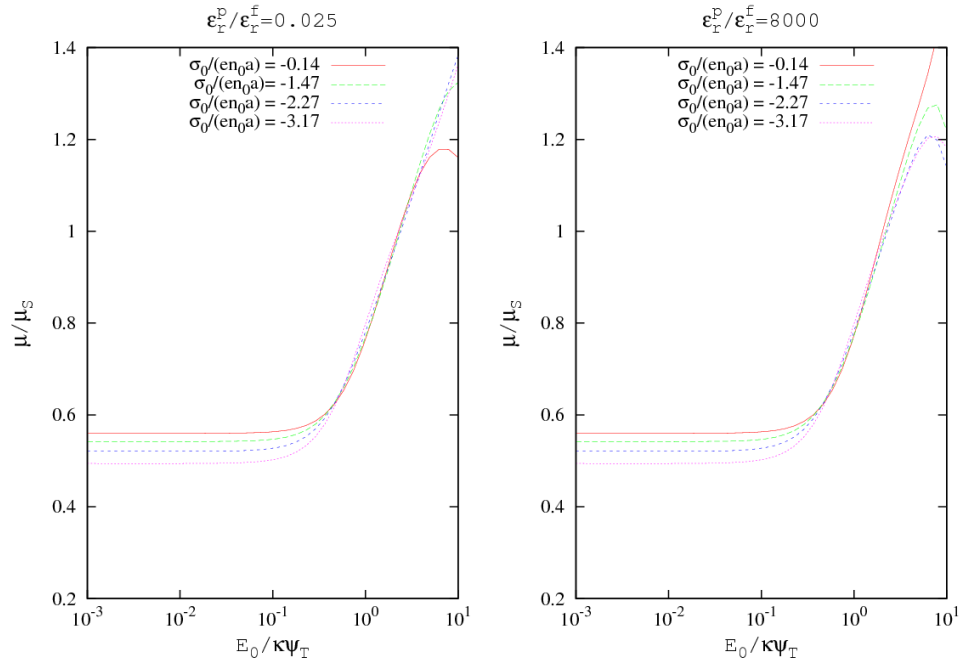

Figure 38: Scaled mobility as a function of dimensionless applied electric field for constant surface charge boundary condition

The results of Figure 38 show that for the constant surface boundary condition: electrophoretic mobility increases. A maximum electrophoretic mobility exists. As the charge of the particle is increased the maximum electrophoretic mobility increases for $\varepsilon_r^p/\varepsilon_r^f = 0.025$ and decreases for $\varepsilon_r^p/\varepsilon_r^f = 8000$. And, nonlinear electrokinetic effects begin to be observed above $E_0/\kappa\psi_T = 0.1$ for $\varepsilon_r^p/\varepsilon_r^f = 0.025$ and $\varepsilon_r^p/\varepsilon_r^f = 8000$.

These observations are explained by plotting the distribution of the EDL, the surface plot of the free charge, and the velocity of the fluid for the results of Figure 38. Three different dimensionless parameters are represented in Figure 38; the dimensionless charge (σ_0/en_0a), the dimensionless permittivity of the particle $(\varepsilon_r^p/\varepsilon_r^f)$, and the dimensionless applied electric field strength $(E_0/\kappa\psi_T)$. So, to completely explain the

results of Figure 38 at least 3^2 combinations must be considered. That is, at least two values of the three dimensionless parameters must be considered.

The values of dimensionless surface charge selected to explain the results of Figure 38 are $\sigma_0/en_0a = -0.14$ and $\sigma_0/en_0a = -3.17$. These values of dimensionless surface charge have been selected from the results of Figure 38 with the objective of explaining why the maximum mobility increases with increasing charge for the dielectric particle and decreases with increasing charge for the metallic particle. The values of dimensionless applied electric field strength selected to explain the results of Figure 38 are $E_0/\kappa\psi_T = 10^{-2}$, $E_0/\kappa\psi_T = 10^0$, and $E_0/\kappa\psi_T = 10^1$. These values of dimensionless applied electric field strength have been selected from the results of Figure 38 to explain the observation of a mobility maximum. The smaller surface charge boundary condition $(\sigma_0/en_0a = -0.14)$ is presented first which corresponds to a constant dimensionless surface potential of $\psi_0/\psi_T = -0.1$. The results are compared for a slightly charged dielectric particle and a slightly charged metallic particle in Figure 39, Figure 40, Figure 41, Figure 42, Figure 43, and Figure 44 for dimensionless applied electric field strengths of $E_0/\kappa\psi_T = 10^{-2}$, $E_0/\kappa\psi_T = 10^0$, and $E_0/\kappa\psi_T = 10^1$. Then, the same is done for the highly charged particles in Figure 45, Figure 46, Figure 47, Figure 48, Figure 49, Figure 50 where conveniently the even numbered figures are for the dielectric particle and the odd numbered figures are for the metallic particle. This presentation is followed by the results for the Stern layer boundary condition.

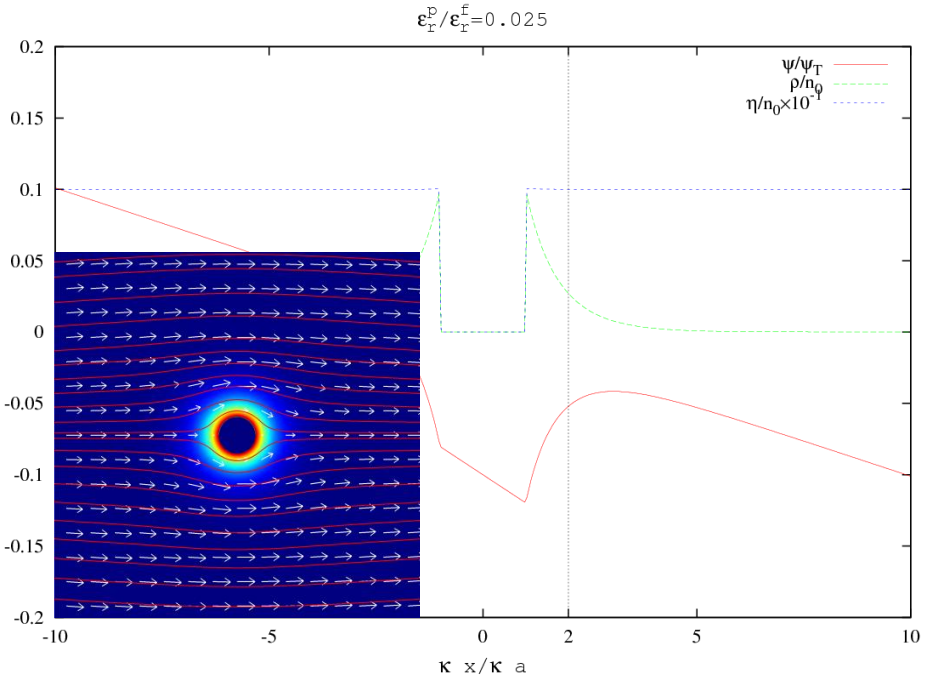

Figure 39: EDL of a dielectric particle with; $\sigma_0/en_0a = -0.14$, $E_0/\kappa\psi_T = 0.01$

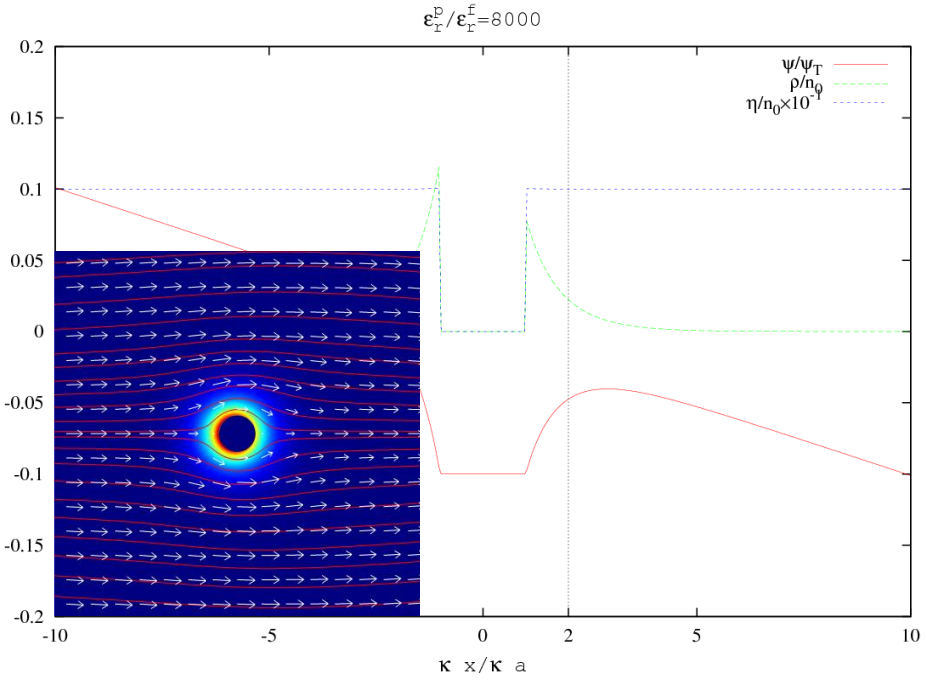

Figure 40: EDL of a metallic particle with; $\sigma_0/en_0a = -0.14$, $E_0/\kappa\psi_T = 0.01$

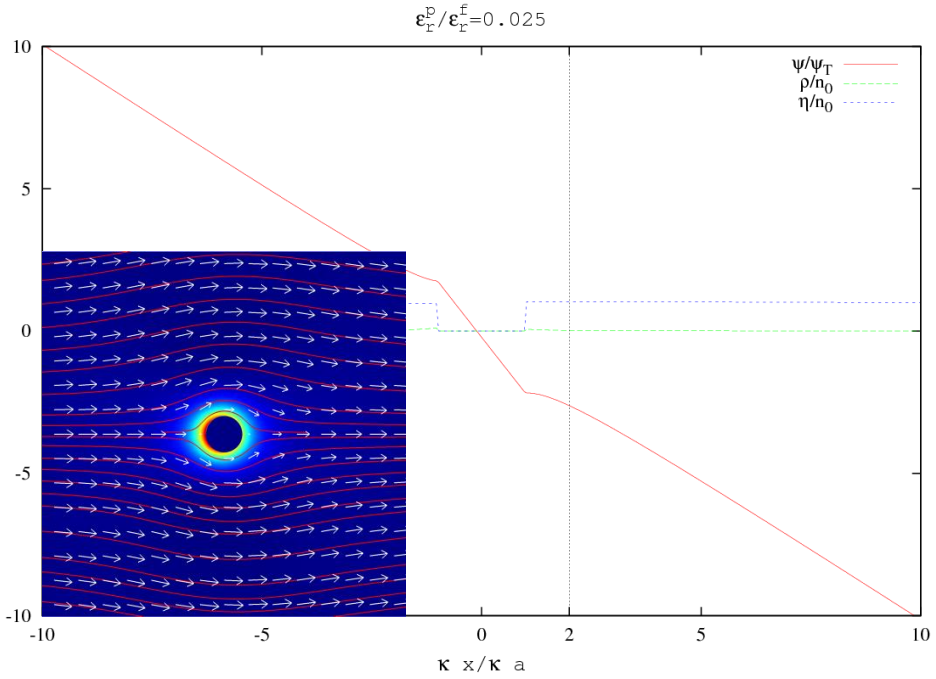

Figure 41: EDL of a dielectric particle with; $\sigma_0/en_0a = -0.14$, $E_0/\kappa\psi_T = 1$

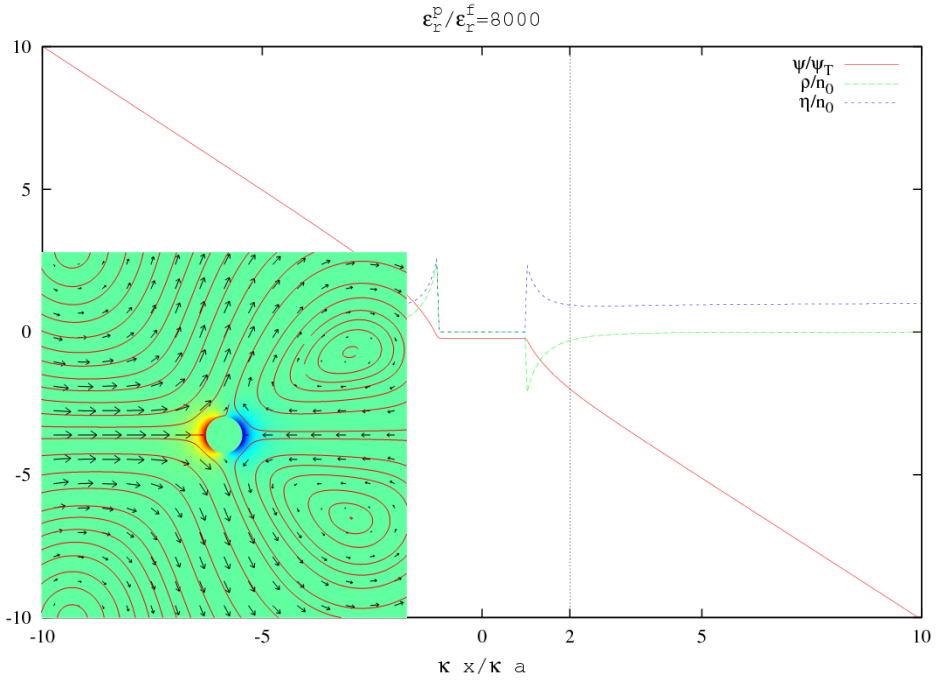

Figure 42: EDL of a metallic particle with; $\sigma_0/en_0a = -0.14$, $E_0/\kappa\psi_T = 1$

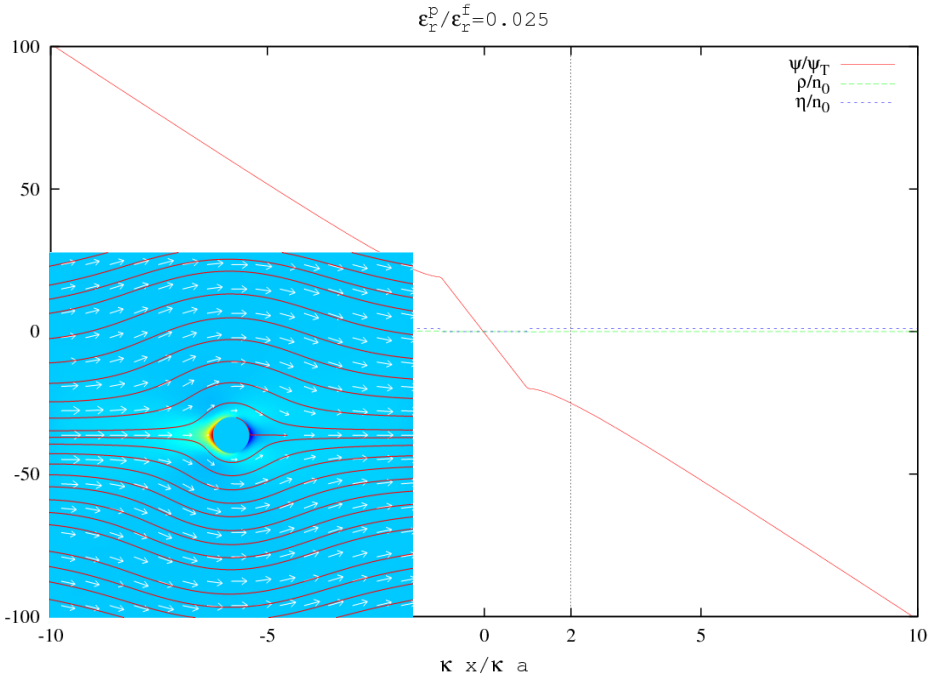

Figure 43: EDL of a dielectric particle with; $\sigma_0/en_0a = -0.14$, $E_0/\kappa\psi_T = 10$

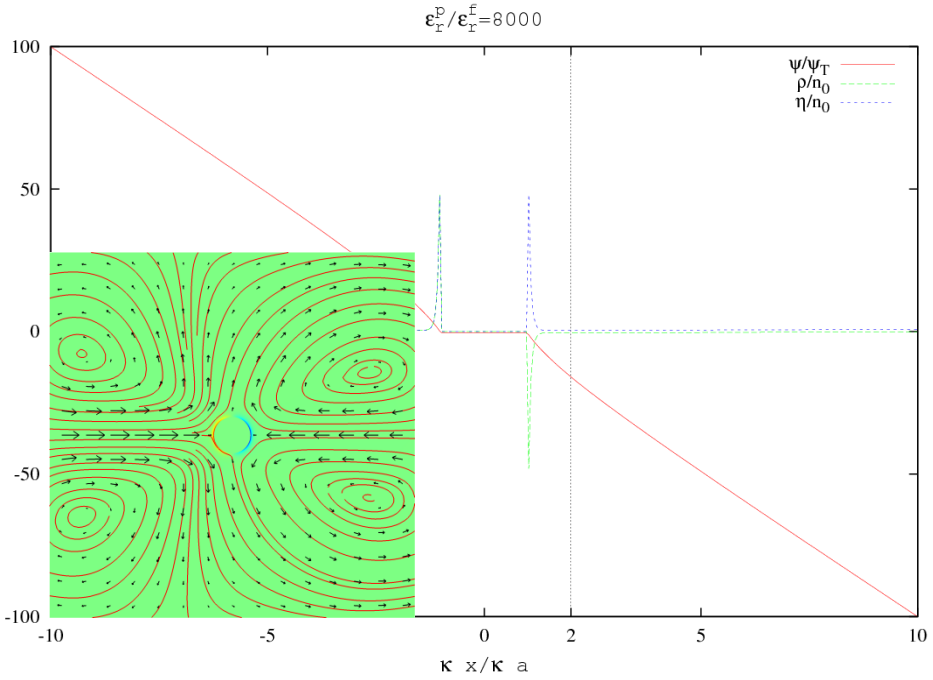

Figure 44: EDL of a metallic particle with; $\sigma_0/en_0a = -0.14$, $E_0/\kappa\psi_T = 10$

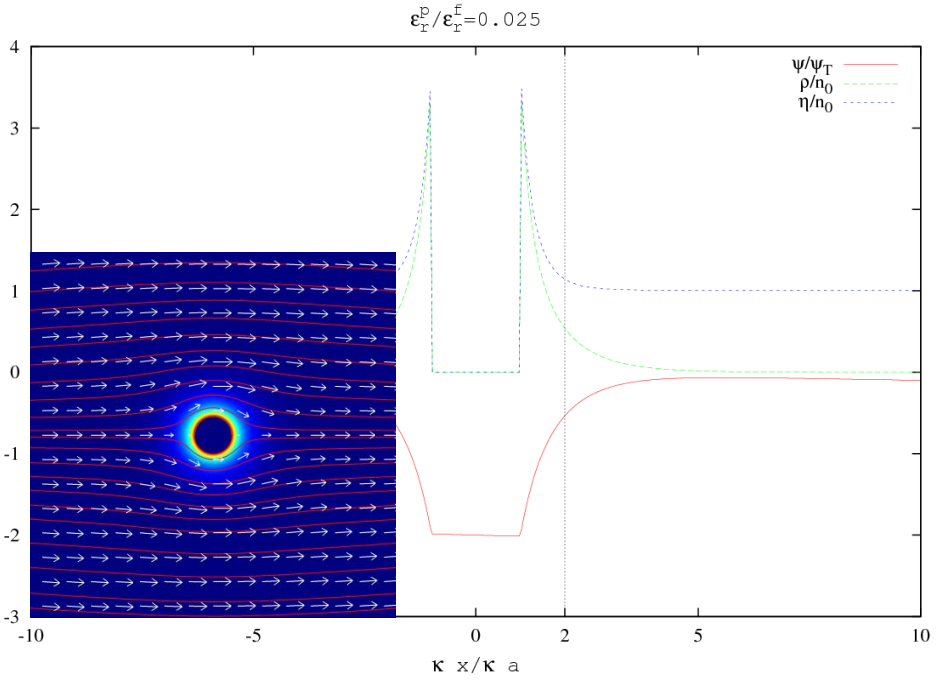

Figure 45: EDL of a dielectric particle with; $\sigma_0/en_0a = -3.17$, $E_0/\kappa\psi_T = 0.01$

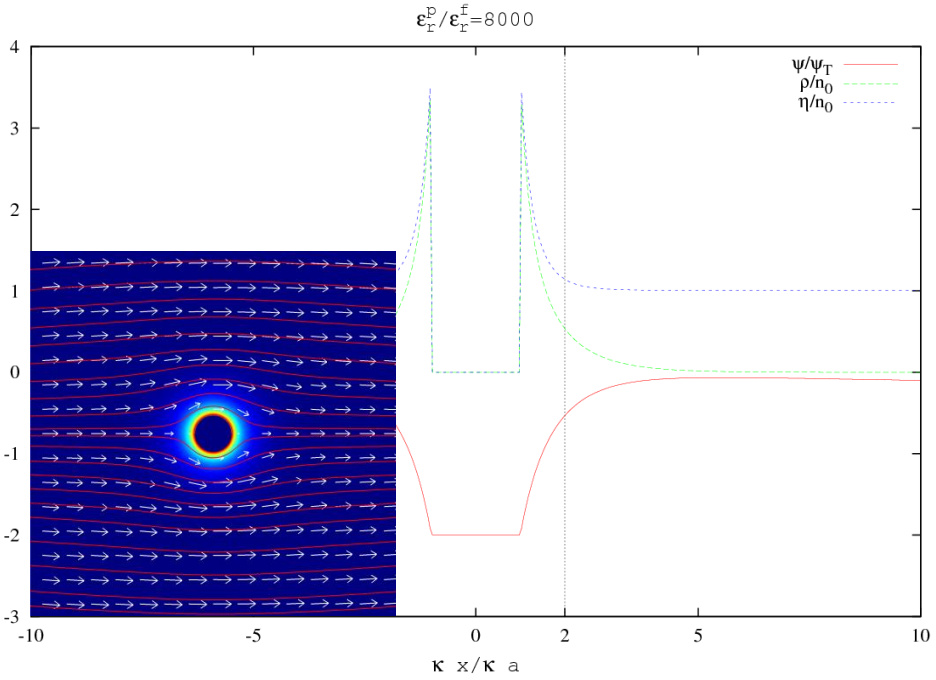

Figure 46: EDL of a metallic particle with; $\sigma_0/en_0a = -3.17$, $E_0/\kappa\psi_T = 0.01$

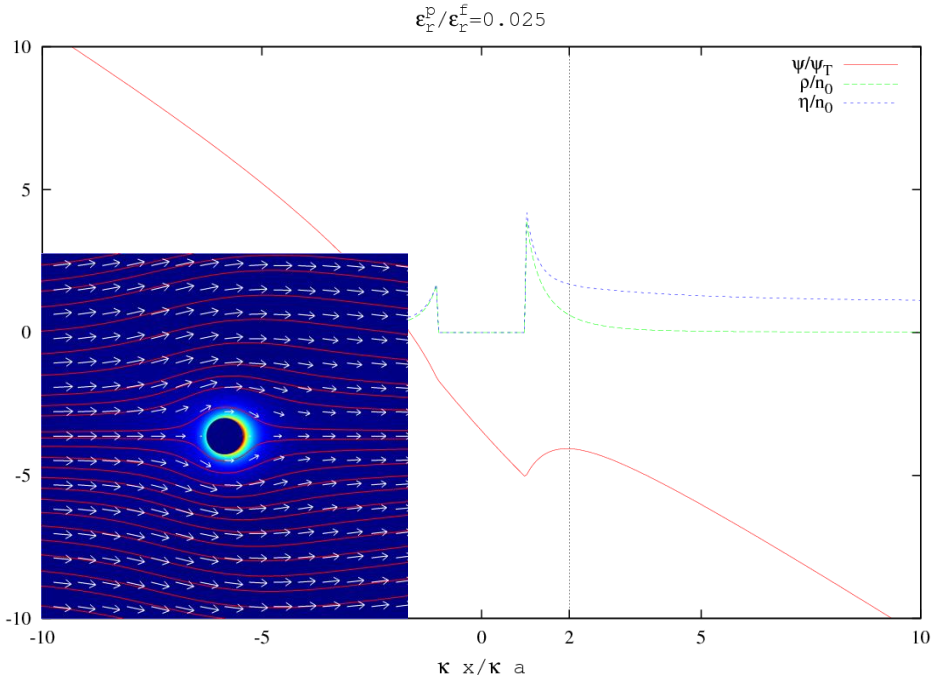

Figure 47: EDL of a dielectric particle with; $\sigma_0/en_0a = -3.17$, $E_0/\kappa\psi_T = 1$

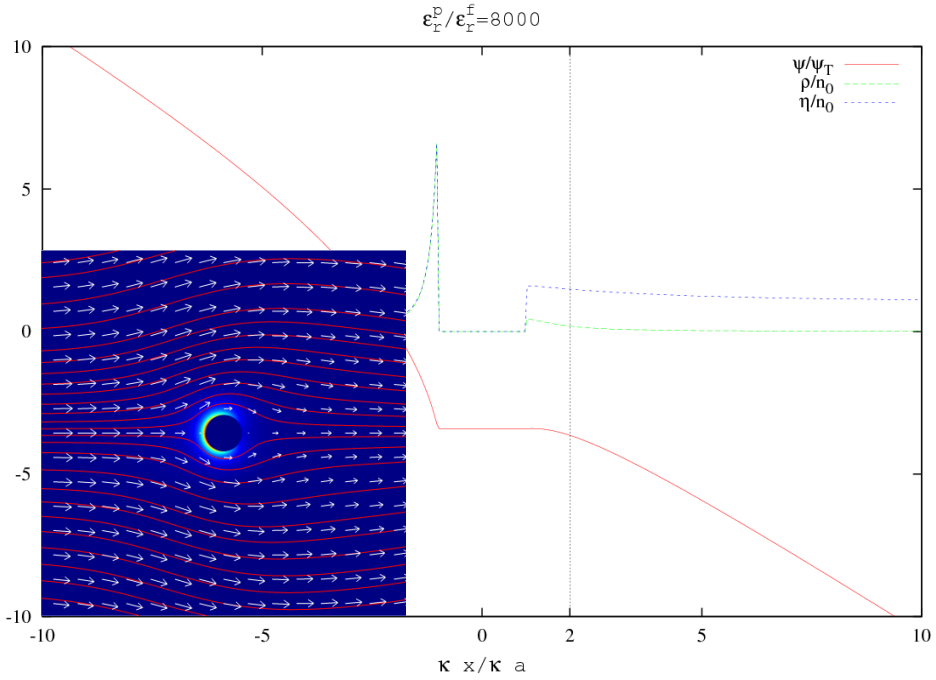

Figure 48: EDL of a metallic particle with; $\sigma_0/en_0a = -3.17$, $E_0/\kappa\psi_T = 1$

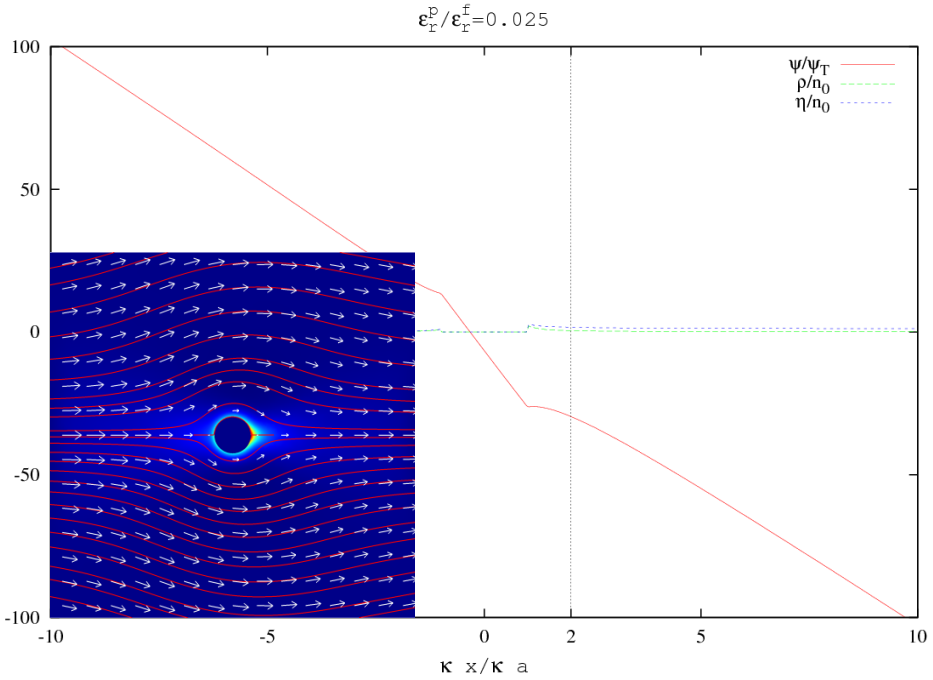

Figure 49: EDL of a dielectric particle with; $\sigma_0/en_0a = -3.17$, $E_0/\kappa\psi_T = 10$

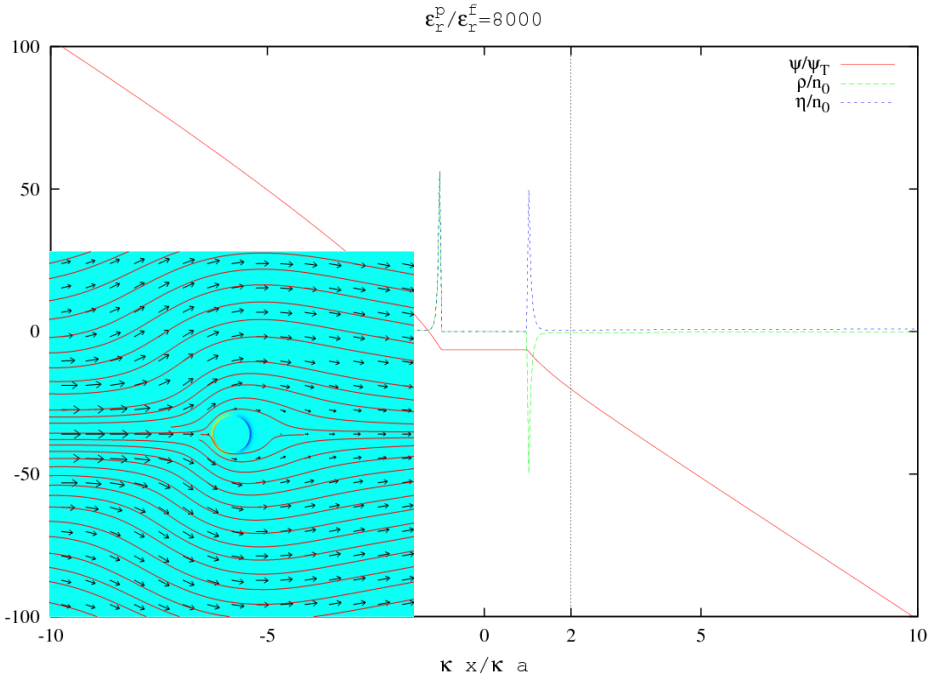

Figure 50: EDL of a metallic particle with; $\sigma_0/en_0a = -3.17$, $E_0/\kappa\psi_T = 10$

A few summary observations can be made from the results of Figure 39 through Figure 50: First, the electric displacement field within the latex particle is easily relaxed due to its low dimensionless permittivity. This leads to large induced potentials at the surface of the particle when strong electric fields are applied. Secondly, the electric displacement field within the metallic particle is not easily relaxed due to its high dimensionless permittivity. This leads to somewhat smaller induced surface potentials that are uniform on the surface of the particle. These observations are verified by plotting the surface potential as a function of applied electric field strength for the dielectric particle, shown in Figure 51, and the metallic particle, shown in Figure 52.

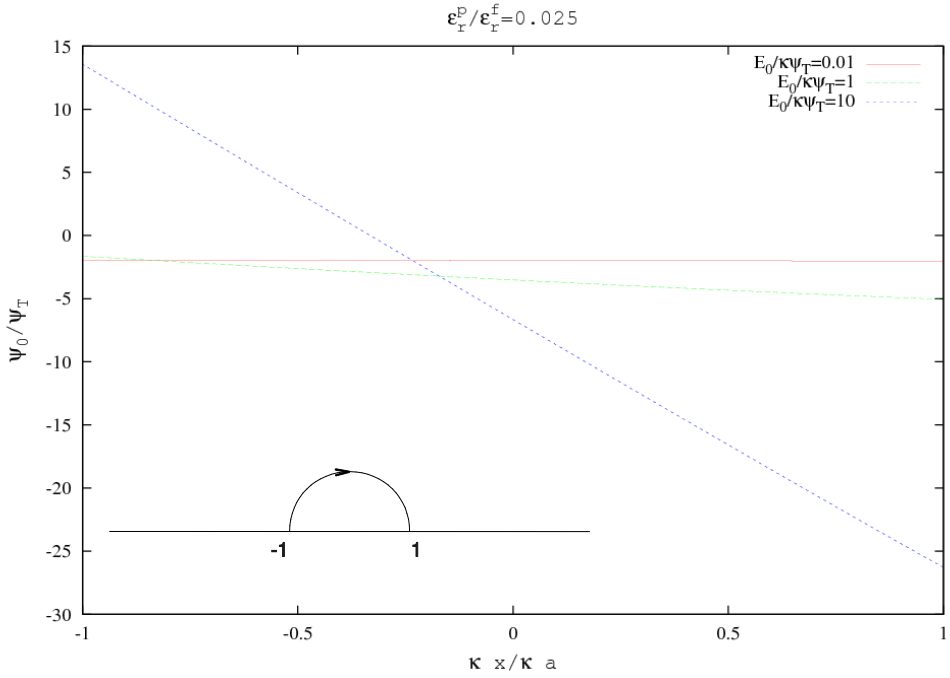

Figure 51: Dimensionless surface potential of a dielectric particle with constant surface charge ($\sigma_0/en_0a = -3.17$) as the applied electric field is increased

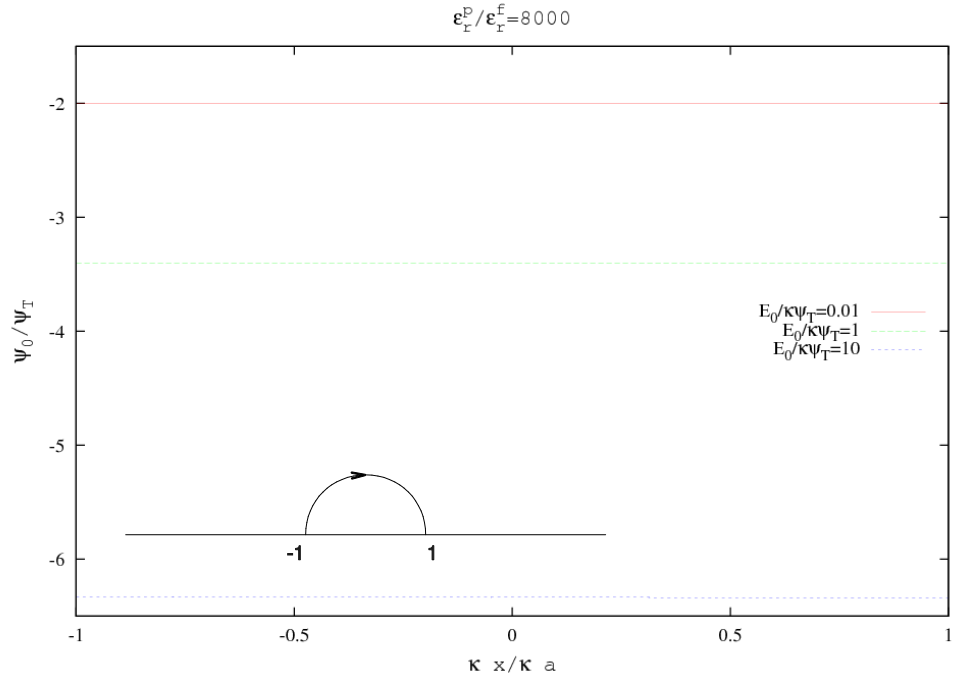

Figure 52: Dimensionless surface potential of a metallic particle with constant surface charge ($\sigma_0/en_0a = -3.17$) as the applied electric field is increased

The results of Figure 52 show that the surface potential of a metallic particle is nearly uniform for $E_0/\kappa\psi_T \leq 10$. To show the effect of stronger surface charge on the induced potential, the scaled average surface potential is plotted for all values of surface charge. The results for a dielectric particle are shown in Figure 53 and the results for a metallic particle are shown in Figure 54. The average surface potential of a dielectric particle can be interpreted as the constant portion of the induced potential which has superimposed upon it a linearly varying portion.

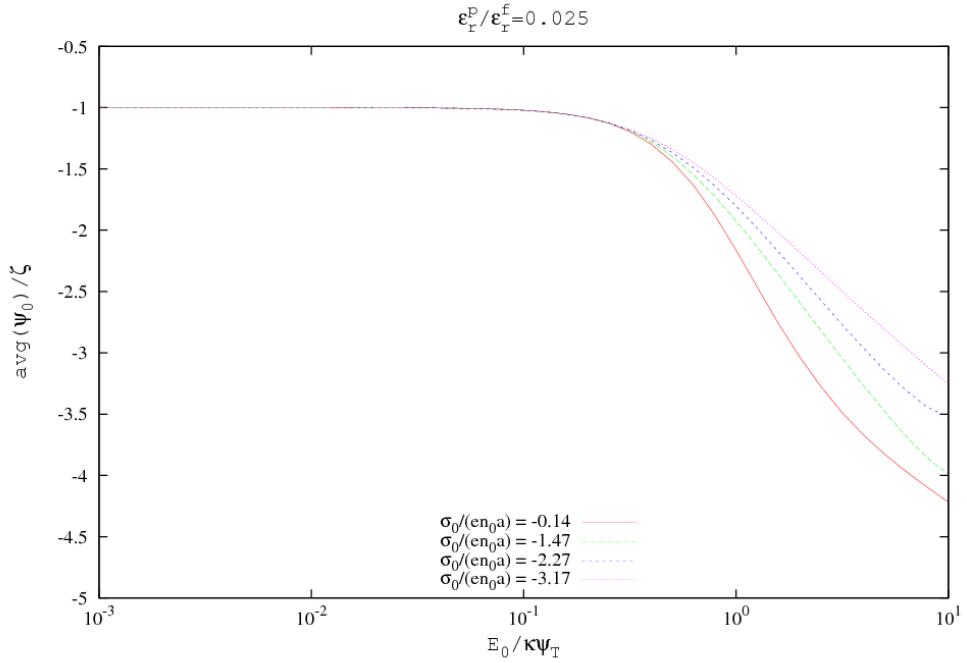

Figure 53: Average scaled surface potential of a dielectric particle as the applied electric field is increased

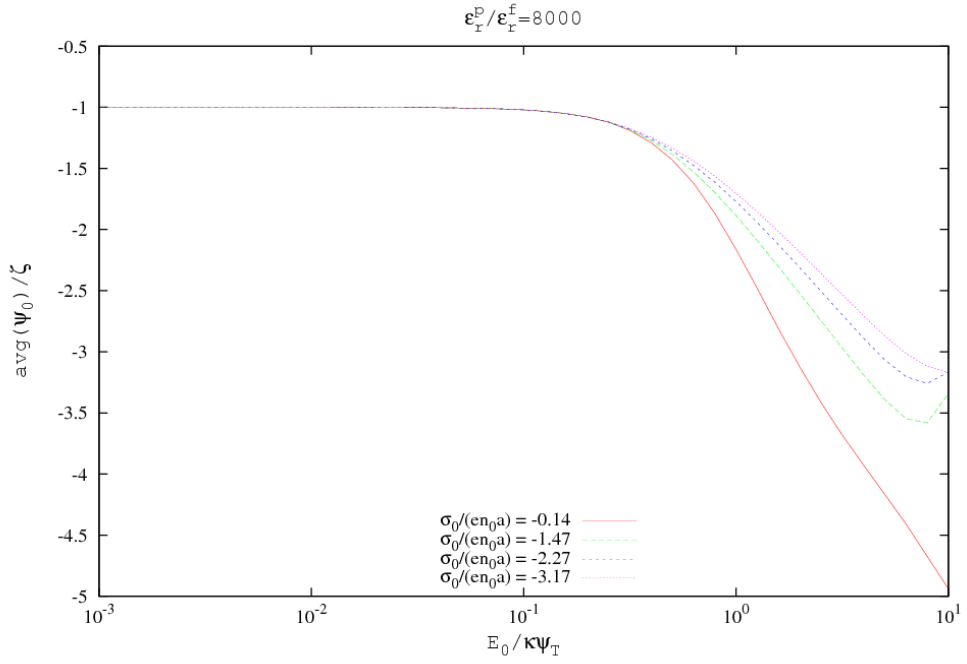

Figure 54: Average scaled surface potential of a metallic particle as the applied electric field is increased

Figure 53 and Figure 54 show that the magnitude of the average scaled surface potential of a dielectric particle is about the same as the metallic particle. Further, both the dielectric particle and the metallic particle show the same trend of decreasing average scaled induced potential when the surface charge is increased. Therefore, the reason the maximum mobility increases with increasing charge for the dielectric particle and decreases with increasing charge for metallic particle, as shown in Figure 38, must primarily be the effect of the relaxation of the electric displacement field in dielectric particle versus the polarization of the EDL of the metallic particle.

The FEM solutions for the scaled nonlinear electrophoretic mobility (μ/μ_S) using the Stern layer boundary condition (GDSL model) are presented in the figures on pages 94 and 101. The scaled mobility for the Stern layer model presented in these figures is directly comparable with that in Figure 38 for the constant surface charge boundary condition as the equilibrium surface potentials are the same. The same process of investigation used for the constant surface charge boundary condition is repeated for the Stern layer model.

There is an additional parameter, the dimensionless number of Stern layer sites available (θ_S), introduced with the Stern layer model whose effect must also be considered. Values for this parameter were selected from those used by White, et al [23, 24] in developing the GDSL theory. The values used in the parametric study are listed in Table 6. In addition to the parameter θ_S, the rate constants of the reaction must also be selected. The rate of association (or adsorption), k_1, and the rate of dissociation (or desorption), k_2, used are also given by White, et al [23].

Table 6: Stern layer parameters

Small Stern layer charge	$\theta_S = 0.187$
Large Stern layer charge	$\theta_S = 1.87$
Dimensionless rate of adsorption	$k_1 = 0.511$
Dimensionless rate of desorption	$k_2 = 0.0511$

The FEM solutions for the scaled nonlinear electrophoretic mobility (μ/μ_S) using the small Stern layer charge boundary condition ($\theta_S = 0.187$) are presented in Figure 55.

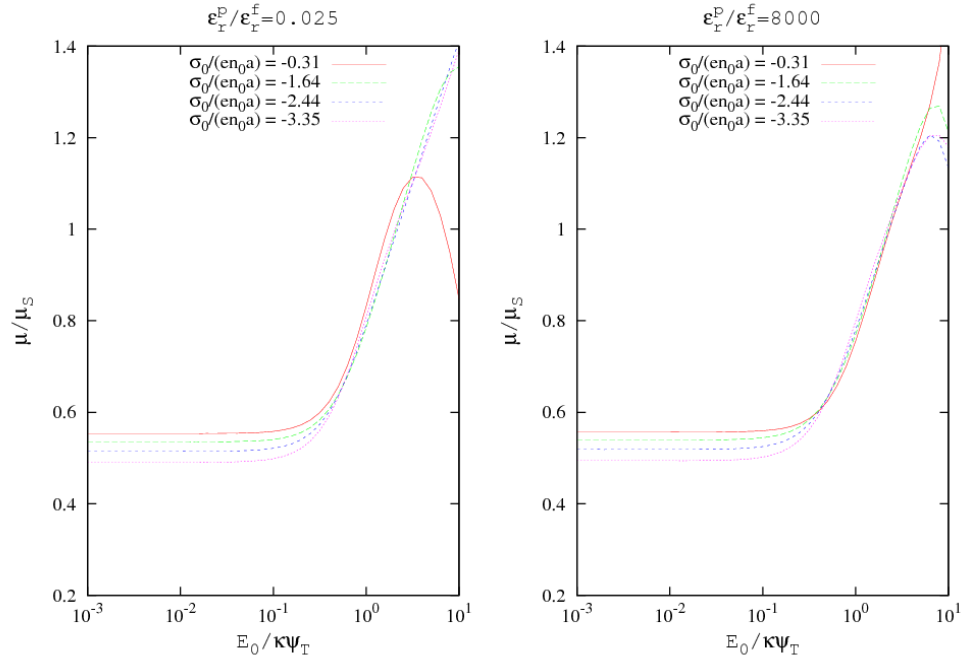

Figure 55: Scaled mobility as a function of dimensionless applied electric field for Stern layer boundary condition with $\theta_s = 0.1873$

The results of Figure 55 show the same trends as that for the constant surface boundary condition presented in Figure 38: The electrophoretic mobility increases. A maximum electrophoretic mobility exists. As the charge of the particle is increased the maximum electrophoretic mobility increases for $\varepsilon_r^p/\varepsilon_r^f = 0.025$ and decreases for $\varepsilon_r^p/\varepsilon_r^f = 8000$. And, nonlinear electrokinetic effects begin to be observed above $E_0/\kappa\psi_T = 0.1$ for $\varepsilon_r^p/\varepsilon_r^f = 0.025$ and $\varepsilon_r^p/\varepsilon_r^f = 8000$.

The following observations are made when comparing the results for the Stern layer boundary condition (Figure 55) and the constant surface charge boundary condition (Figure 38): First, the maximum scaled electrophoretic mobility of the slightly charged dielectric particle when using the Stern layer boundary condition is significantly less than that of the constant surface charge boundary condition. Second, there is no significant difference in the results for a metallic particle. And finally, the differences observed for a slightly charged particle are mitigated as the surface charge is increased.

To explain the differences observed in Figure 55, the EDL of a slightly charged dielectric particle is plotted for $E_0/\kappa\psi_T = 1$ and $E_0/\kappa\psi_T = 10$ in Figure 56 and Figure 57, respectively. The dimensionless surface potential and density of adsorbed ions of a slightly charged dielectric particle are also plotted in Figure 58 and Figure 59 to confirm the observations concerning the results of Figure 56 and Figure 57. The dimensionless surface potential and density of adsorbed ions of a highly charged dielectric particle are then presented to explain why the effects of the Stern layer boundary condition are reduced. The reason there is no significant difference in the results for a metallic particle will be deduced from the analysis for dielectric particles.

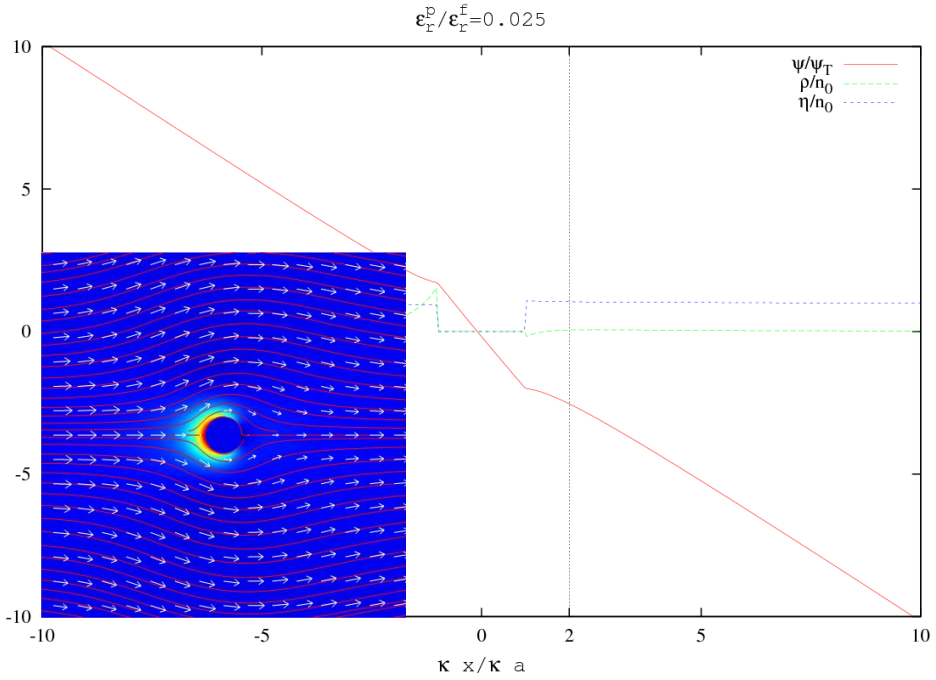

Figure 56: Stern layer model of dielectric particle with; $\theta_S = 0.187$, $\sigma_0/en_0a = -0.31$, $E_0/\kappa\psi_T = 1$

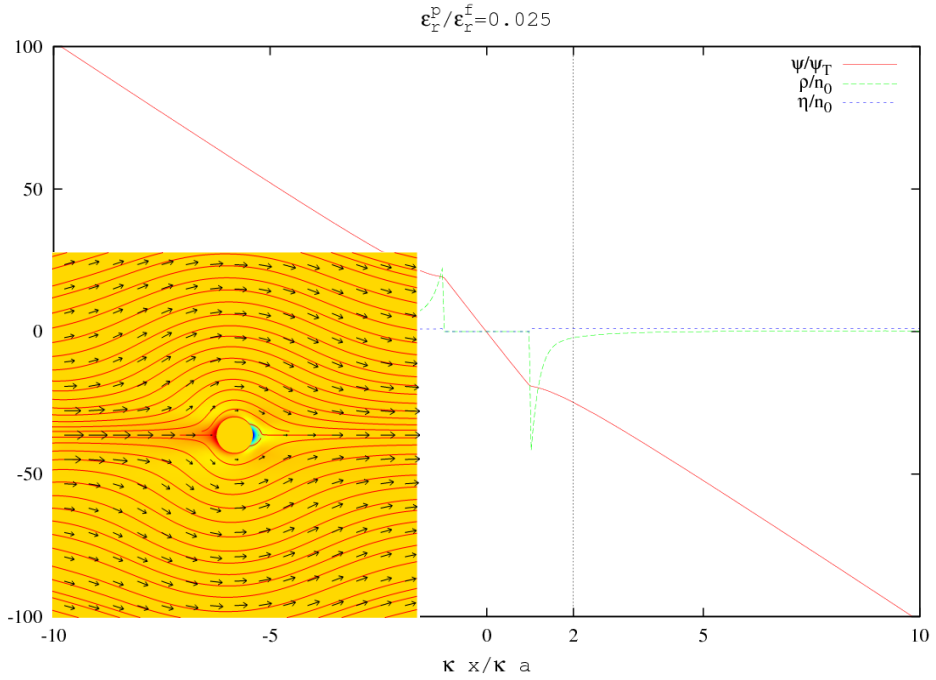

Figure 57: Stern layer model of dielectric particle with; $\theta_S = 0.187$, $\sigma_0/en_0a = -0.31$, $E_0/\kappa\psi_T = 10$

When compared with Figure 41 and Figure 43, Figure 56 and Figure 57 show that there is significantly more polarization of the EDL for a slightly charged dielectric particle when the Stern layer model is included. The reason must be associated with adsorption of positive ions onto the surface when the displacement electric field in the particle is relaxed. When the displacement electric field is relaxed in a strong applied electric field the potential at one side of the slightly charged dielectric particle becomes negative while that on the other becomes positive as shown in Figure 58.

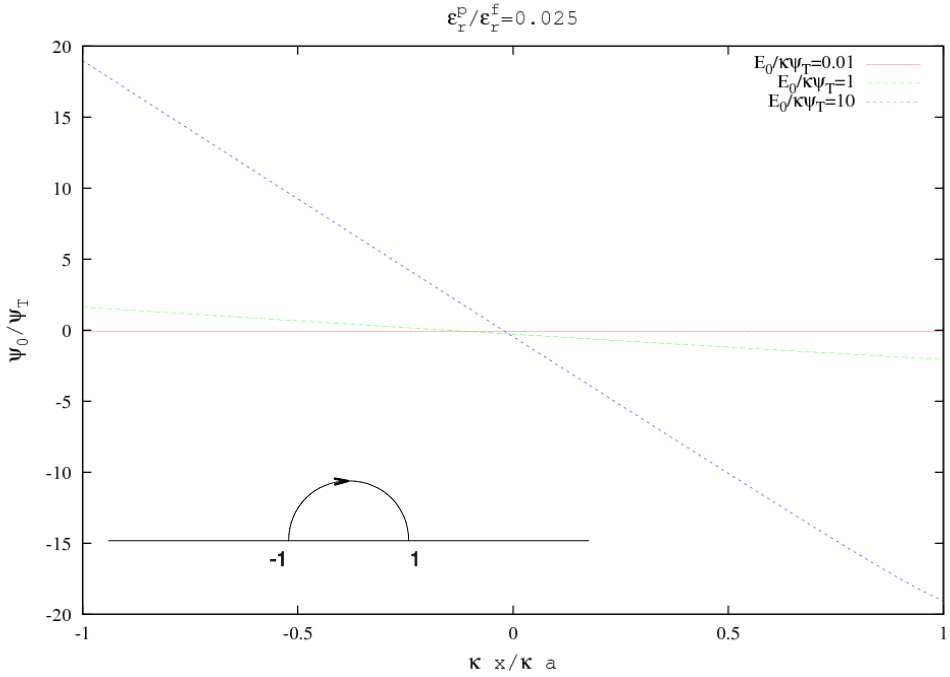

Figure 58: Dimensionless surface potential of a dielectric particle with $\theta_S = 0.1873$ and $\sigma_0/en_0a = -0.31$ as the applied electric field is increased

In the proposed Stern layer FEM model only positive ions are absorbed and desorbed in the Stern layer. The rate of adsorption is ten times as fast as the rate of desorption, as shown in Table 6, thus more ions would be adsorbed onto one side of the dielectric

particle as the applied electric field induces surface potential than are desorbed from the other side. This is confirmed by plotting the concentration of adsorbed ions as a function of the applied electric field along the surface of the dielectric particle as shown in Figure 59.

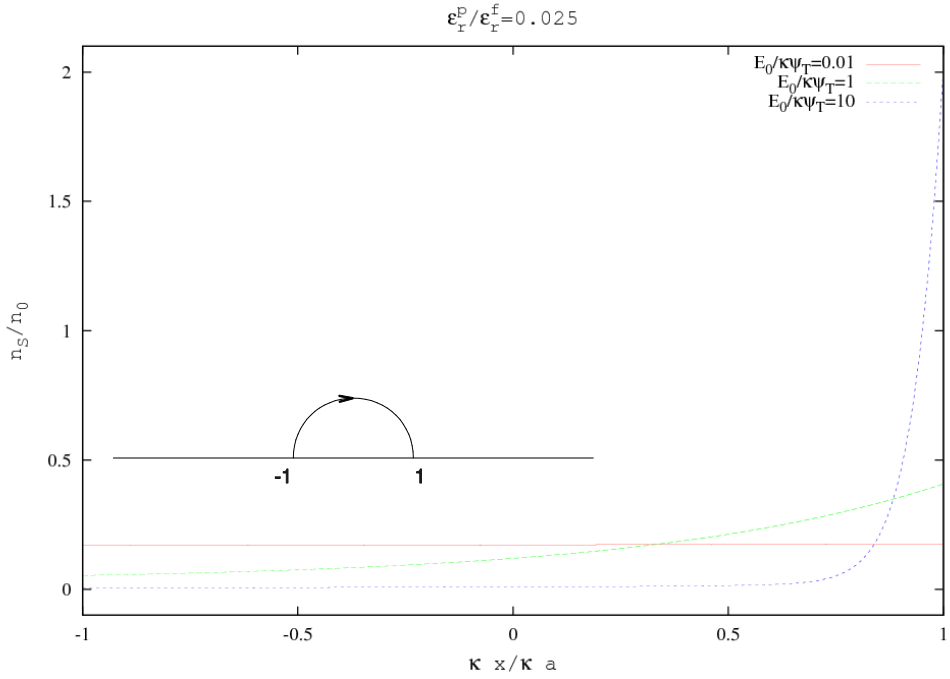

Figure 59: Dimensionless number density of adsorbed ions for a dielectric particle with $\theta_S = 0.1873$ and $\sigma_0/en_0a = -0.31$ as the applied electric field is increased

Figure 59 shows that for the dielectric particle: The concentration of adsorbed ions is uniform for weak electric fields. As the electric field is increased Stern layer ions are desorbed from the positive side of the particle and adsorbed on the negative side of the particle. The Stern layer ions are completely depleted on the positive side of the particle and have a high concentration at $\kappa x/\kappa a = 1$ for $E_0/\kappa\psi_T = 10$.

The surface potential and number density of adsorbed ions of a highly charged dielectric particle are now presented in Figure 60 and Figure 61, respectively, to explain why the effect of Stern layer adsorption is reduced as the charge of the particle is increased. Figure 60 shows that the dimensionless surface potential induced in an electric field is skewed toward the negative due to the high negative charge of the particle. The results presented for $E_0/\kappa\psi_T = 1$ show that the entire surface is still negative. So, adsorption of positive ions into the Stern layer occurs over the whole surface resulting in less polarization. This trend is also observed for $E_0/\kappa\psi_T = 10$, but a portion of the particle surface is now positive.

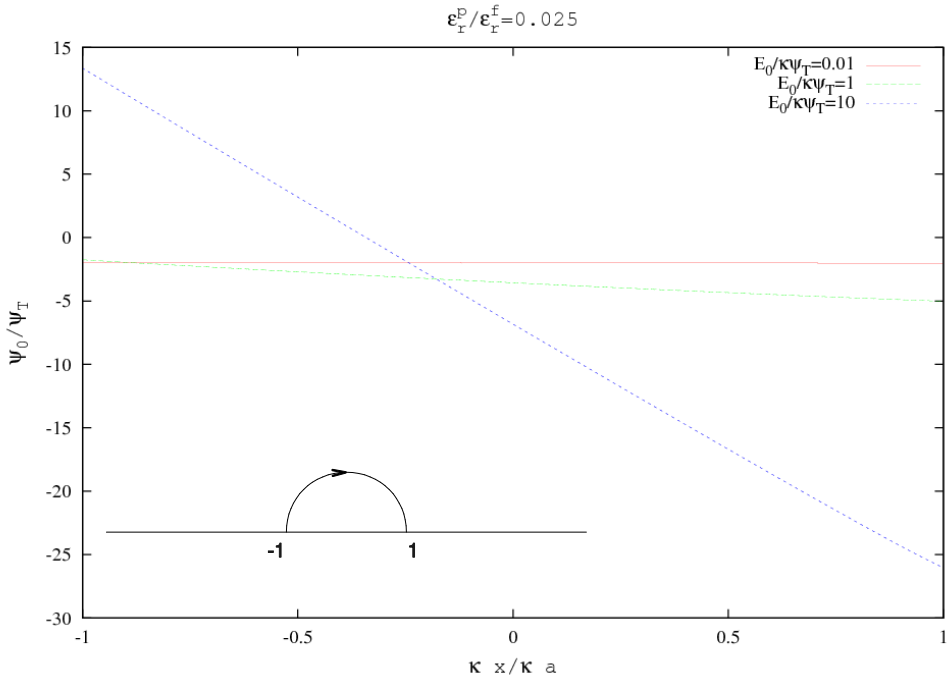

Figure 60: Dimensionless surface potential of a dielectric particle with $\theta_S = 0.1873$ and $\sigma_0/en_0a = -3.35$ as the applied electric field is increased

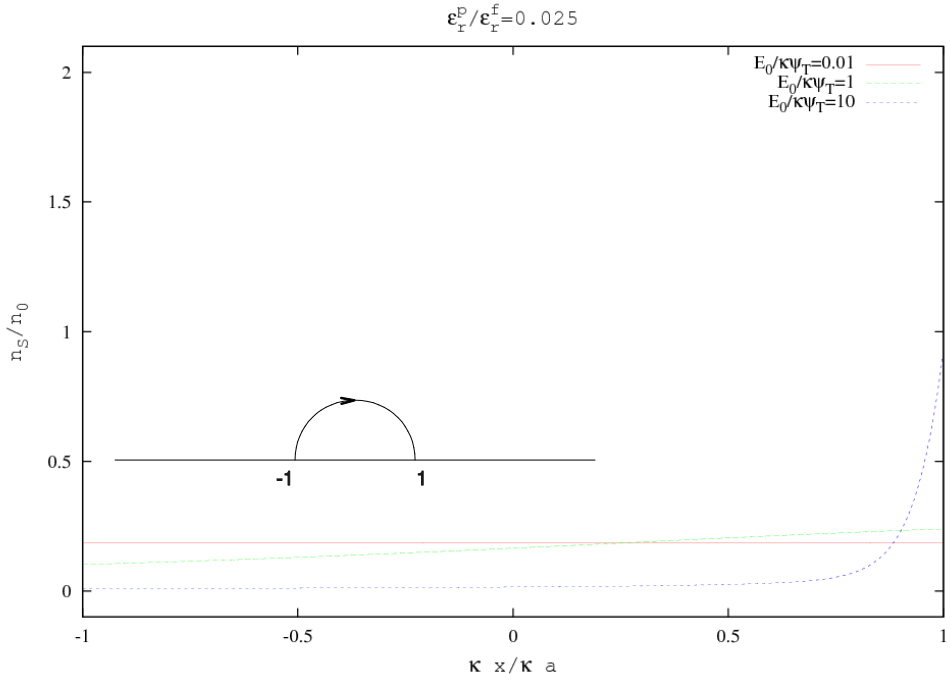

Figure 61: Dimensionless number density of adsorbed ions for a dielectric particle with $\theta_S = 0.1873$ and $\sigma_0/en_0a = -3.35$ as the applied electric field is increased

Figure 61 shows that the concentration of adsorbed ions on the surface of the highly charged dielectric particle is more evenly distributed than that of a slightly charged dielectric particle, shown in Figure 59. We can also deduce from the results of Figure 59 and Figure 61 the reason the differences observed for the metallic particle with the Stern layer boundary condition were not significant.

A metallic particle adsorbing ions onto its Stern layer would decrease the induced potential due to the applied electric field. However, since the surface potential of the metallic particle is uniform, this would not lead to polarization of the EDL because there is not preferential adsorption on one side. If there were a larger number of Stern layer sites available the electrophoretic mobility of a metallic particle would be reduced.

The FEM solutions for the scaled nonlinear electrophoretic mobility (μ/μ_S) using the large Stern layer charge boundary condition ($\theta_S = 1.873$) are presented in Figure 62. The following observations are made when comparing the results for the Stern layer boundary condition with ($\theta_S = 0.1873$) in Figure 55 and that for ($\theta_S = 1.873$) in Figure 62. First, the maximum scaled electrophoretic mobility of the slightly charged metallic particle when using $\theta_S = 1.873$ is significantly less than that for $\theta_S = 0.1873$. Second, there is no significant difference in the results for a highly charged metallic particle. And finally, the mobility of a dielectric particle decreases drastically above $E_0/\kappa\psi_T = 1$. The EDL's for the Stern layer boundary condition are presented in Figure 63, Figure 64, Figure 65, and Figure 66.

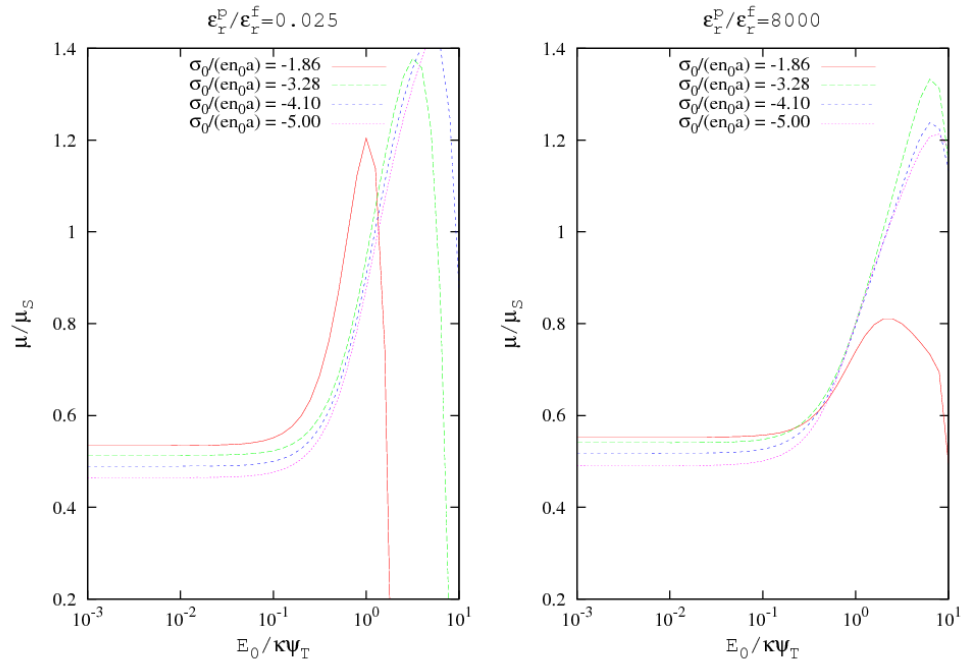

Figure 62: Scaled mobility as a function of dimensionless applied electric field for Stern layer boundary condition with $\theta_s = 1.87$

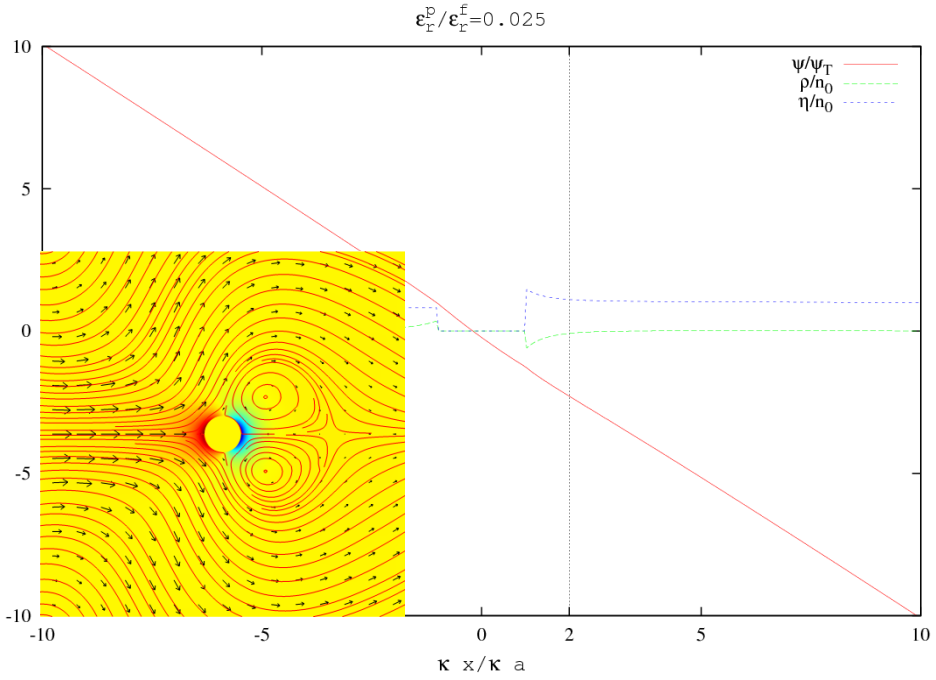

Figure 63: Stern layer model of dielectric particle with; $\theta_S = 1.87$, $\sigma_0/en_0a = -1.86$, $E_0/\kappa\psi_T = 1$

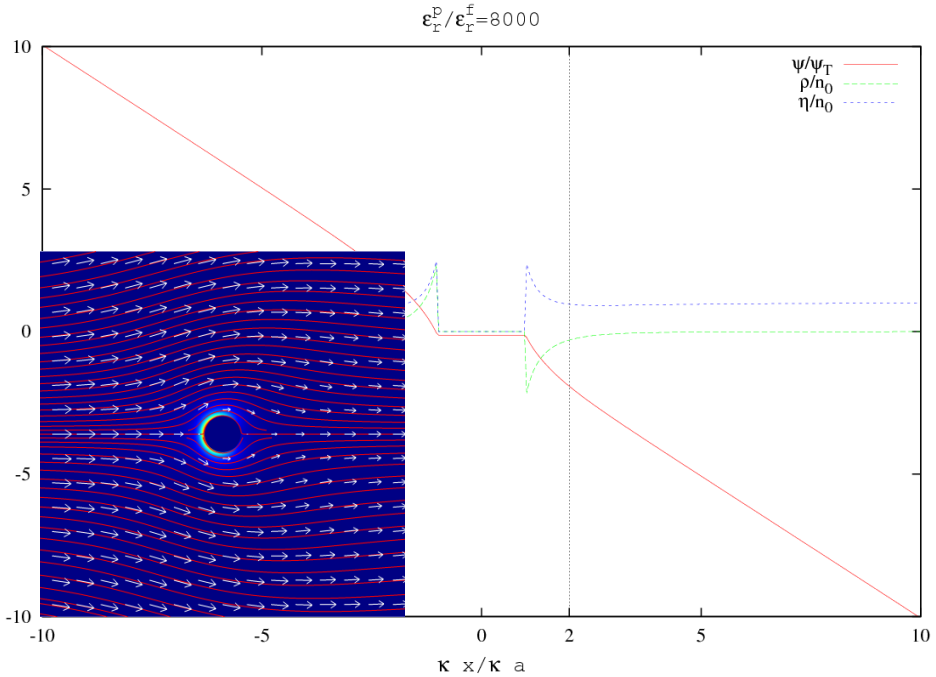

Figure 64: Stern layer model of metallic particle with; $\theta_S = 1.87$, $\sigma_0/en_0a = -1.86$, $E_0/\kappa\psi_T = 1$

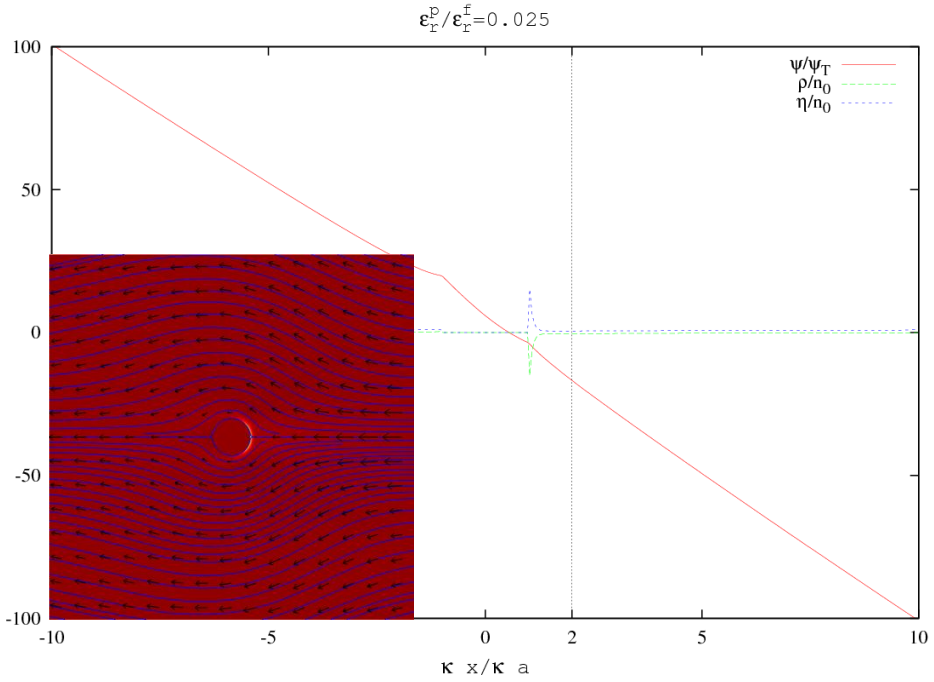

Figure 65: Stern layer model of dielectric particle with; $\theta_S = 1.87$, $\sigma_0/en_0a = -1.86$, $E_0/\kappa\psi_T = 10$

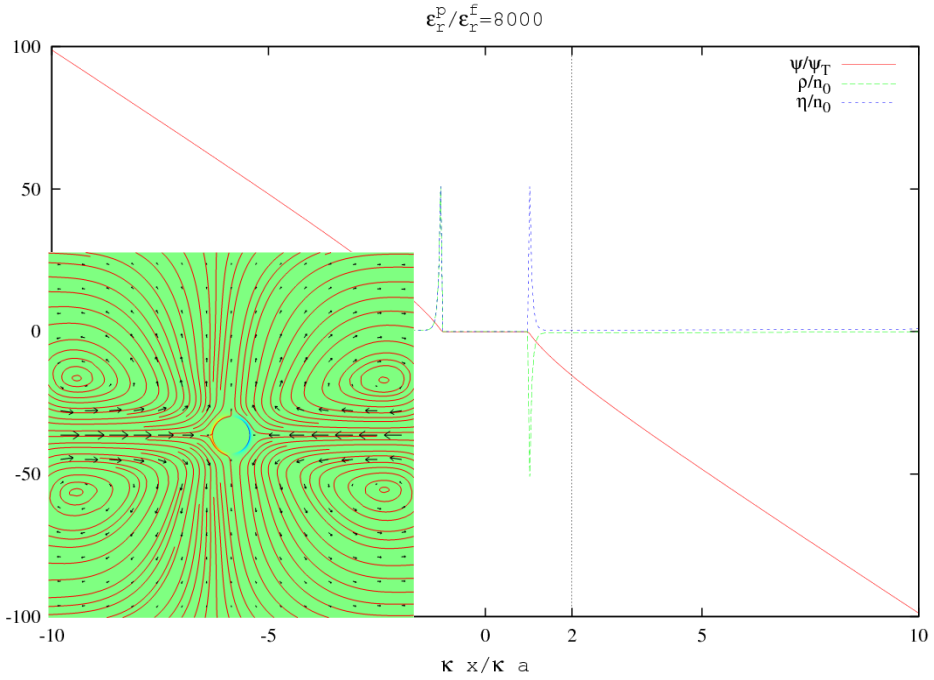

Figure 66: Stern layer model of metallic particle with; $\theta_S = 1.87$, $\sigma_0/en_0a = -1.86$, $E_0/\kappa\psi_T = 10$

The results of Figure 63 explain why the mobility decreases so drastically for the dielectric particle above $E_0/\kappa\psi_T = 1$. The electric displacement field is completely relaxed in both the particle and the EDL for the dielectric particle with $\theta_S = 1.873$ and $E_0/\kappa\psi_T = 1$ shown in Figure 63. Thus, there is no net force on the particle. The results of Figure 65 show that if the applied electric field is increased beyond $E_0/\kappa\psi_T = 1$ the force changes direction and the particle begins to move in the opposite direction. This reversal of the force on the particle is explained in Figure 67 and Figure 68. Figure 67 shows the dimensionless surface potential of the slightly charged dielectric particle with $\theta_S = 1.873$ as the applied electric field is increased. And, Figure 68 shows the resulting dimensionless adsorbed ion density.

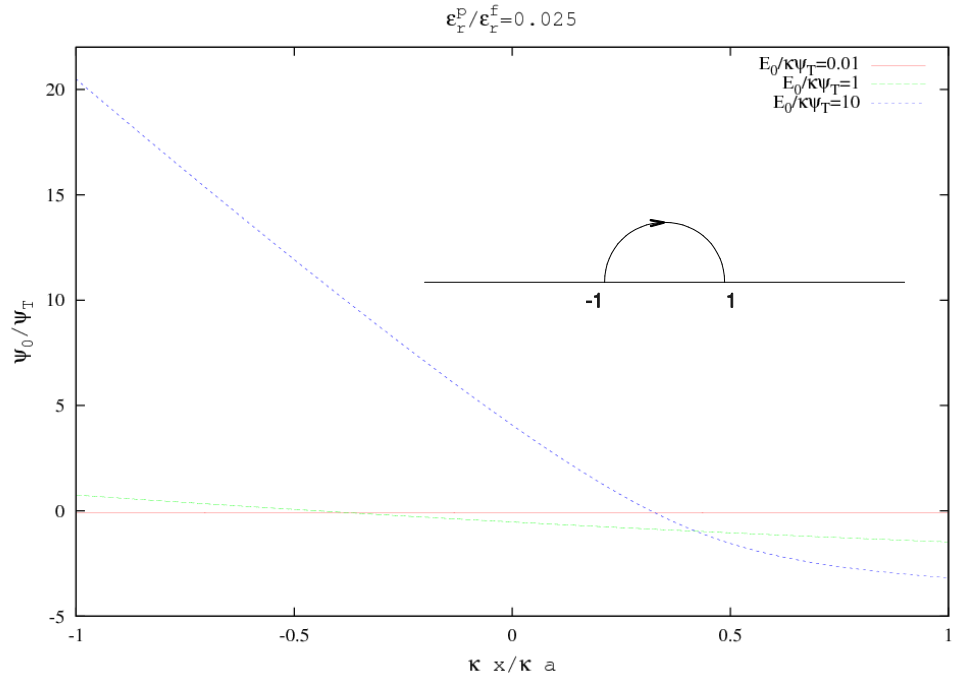

Figure 67: Dimensionless surface potential for a dielectric particle with $\theta_S = 1.873$ and $\sigma_0/en_0a = -1.86$ as the applied electric field is increased

The results of Figure 67 show that the originally negatively charged particle has a surface potential which is mostly positive when $E_0/\kappa\psi_T = 10$. Also, when compared with Figure 58 and Figure 60 for $\theta_S = 0.1873$, Figure 67 reveals that the x-component of the tangential electric field is not constant when $\theta_S = 1.873$. The dimensionless adsorbed ion density, shown in Figure 68, has a maximum value of 20 (positive) on the right portion of the particle for $E_0/\kappa\psi_T = 10$. Thus, the originally positive free charge surrounding a slightly negative charged dielectric particle is negative near the right portion of the particle and zero on left portion of the particle. This is confirmed by the plot of the dimensionless free charge shown in Figure 65.

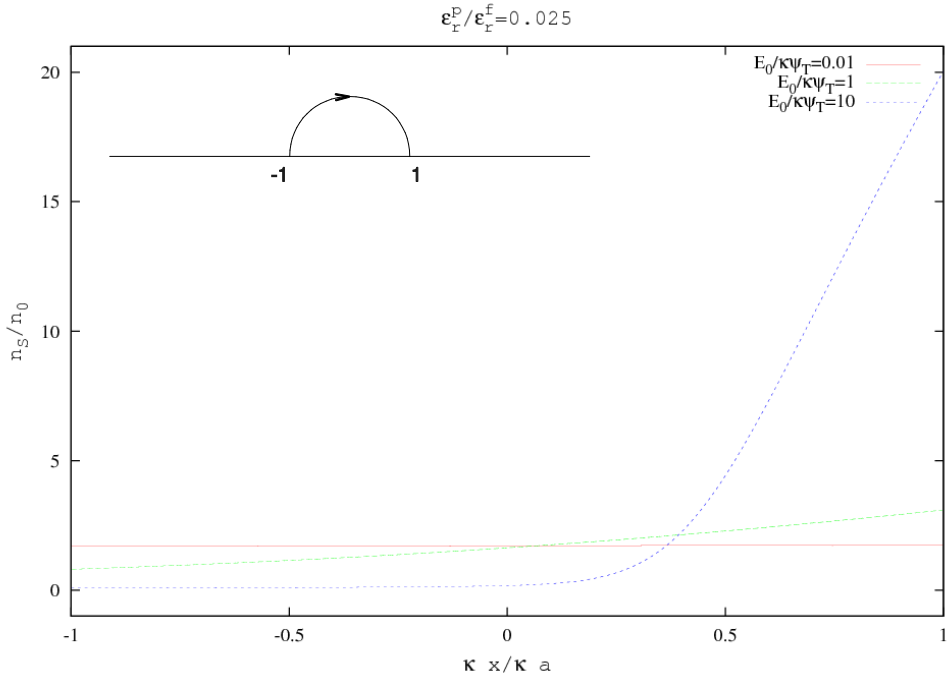

Figure 68: Dimensionless adsorbed ion density for dielectric particle with $\theta_S = 1.873$ and $\sigma_0/en_0a = -1.86$ as the applied electric field is increased

The reason the maximum electrophoretic mobility of a slightly charged metallic particle is significantly reduced when the Stern layer model is included with $\theta_S = 1.873$ can be determined by comparing the EDL figures for the Stern layer model presented in Figure 64 and Figure 66 with that of the constant surface charge boundary condition presented in Figure 42 and Figure 44. The distribution of the dimensionless free charge in the EDL is about the same. However, a close inspection of the dimensionless electric potential reveals the magnitude of the induced surface potential of the metallic particle is reduced by the Stern layer boundary condition. This observation is confirmed by plotting the dimensionless surface potential for $E_0/\kappa\psi_T = 0.01, 1, \text{and } 10$ in Figure 69.

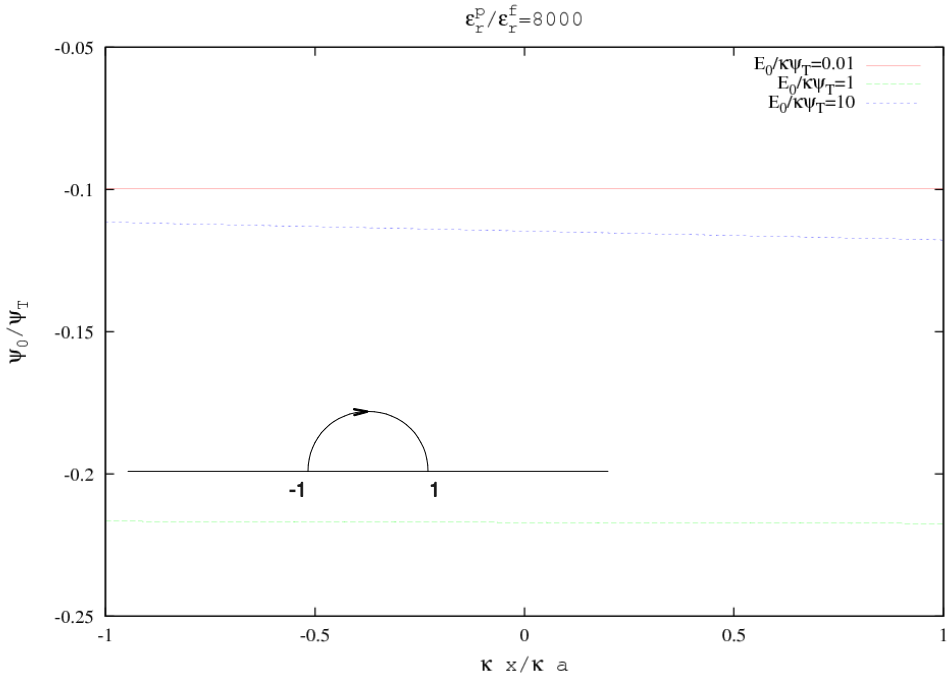

Figure 69: Dimensionless surface potential for a metallic particle with $\theta_S = 1.873$ and $\sigma_0/en_0a = -1.86$ as the applied electric field is increased

The surface potential of the metallic particle is increased as the applied electric field is increased to $E_0/\kappa\psi_T = 1$, then as the applied electric field is increased beyond one the adsorption of positive ions begins to decrease the surface potential until at $E_0/\kappa\psi_T = 10$ the average surface potential of the metallic particle is about reduced to the original equilibrium potential.

The last observation concerning the results of Figure 62 to be explained is the reduced effect of the Stern layer boundary condition for both the dielectric and metallic particle as the surface charge is increased. The EDLs surrounding highly charged dielectric particles are compared with those of highly charged metallic particles in Figure 70, Figure 71, Figure 72, and Figure 73. The results of Figure 70 and Figure 72 show that the EDL of a highly charged dielectric particle is strong enough to keep the applied electric field and the resulting adsorption from inducing potentials which cause the force to change direction. The distribution of free charge surrounding a highly charged metallic particle, shown in Figure 71 and Figure 73, remains essentially the same as that of the constant surface charge boundary condition. However, the increased strength of the EDL decreased the induction of surface potential by the applied electric field of the metallic particle. Since, the electric field is not able to induce large surface potentials the adsorption is not as strong. Thus, the effect is mitigated.

The results of Figure 74 confirm that the surface potential of a highly charged dielectric particle remains essentially negative. And, the results of Figure 75 confirm that because the EDL of the highly charge particle is not relaxed the adsorption of ions is not strong enough to reverse the induction of surface potential by the applied electric field.

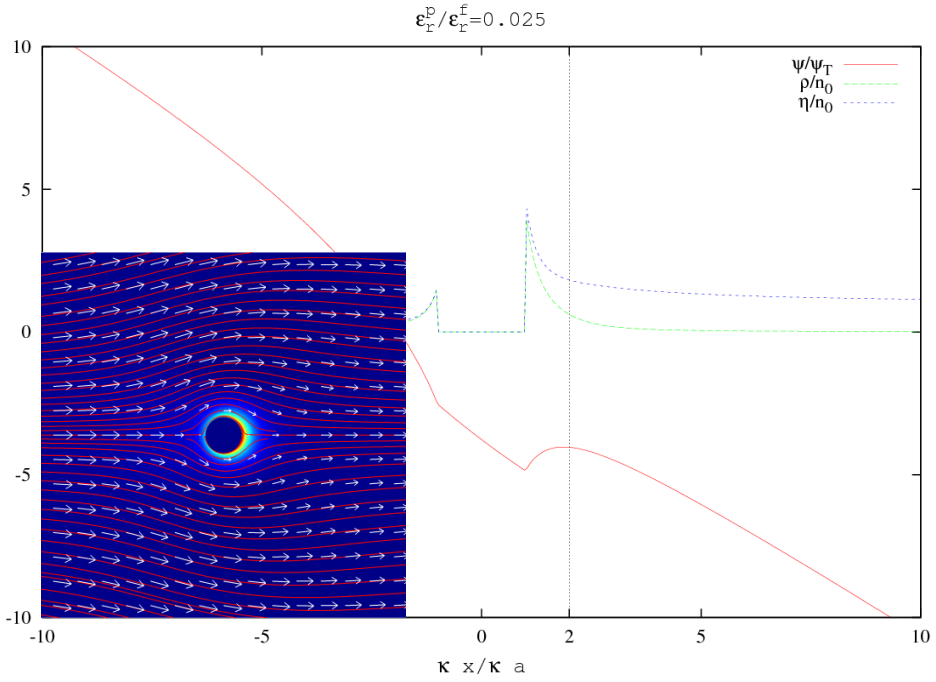

Figure 70: Stern layer model of dielectric particle with; $\theta_S = 1.87$, $\sigma_0/en_0a = -5$, $E_0/\kappa\psi_T = 1$

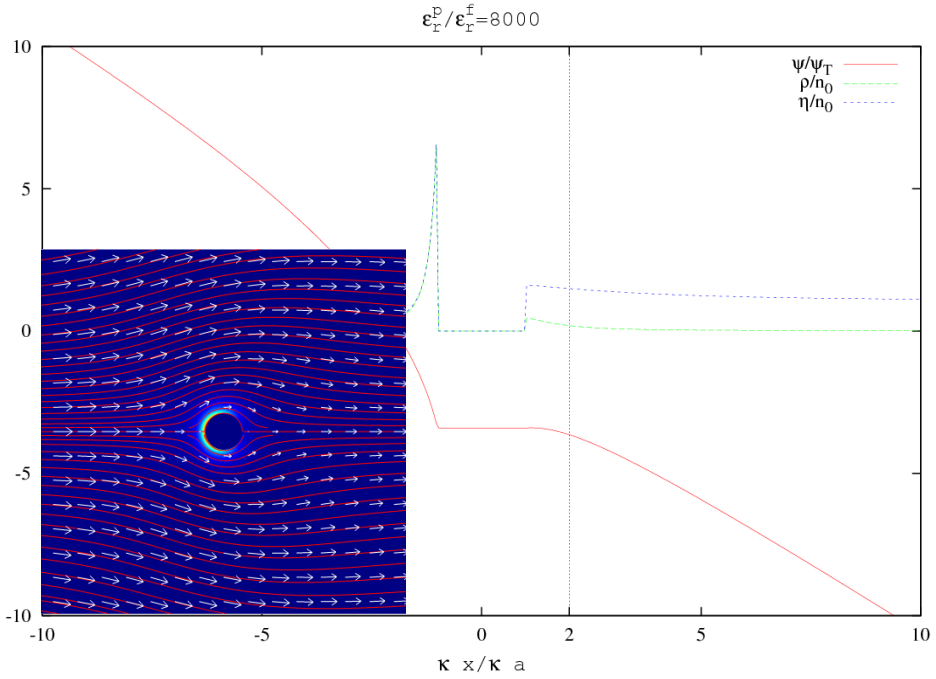

Figure 71: Stern layer model of metallic particle with; $\theta_S = 1.87$, $\sigma_0/en_0a = -5$, $E_0/\kappa\psi_T = 1$

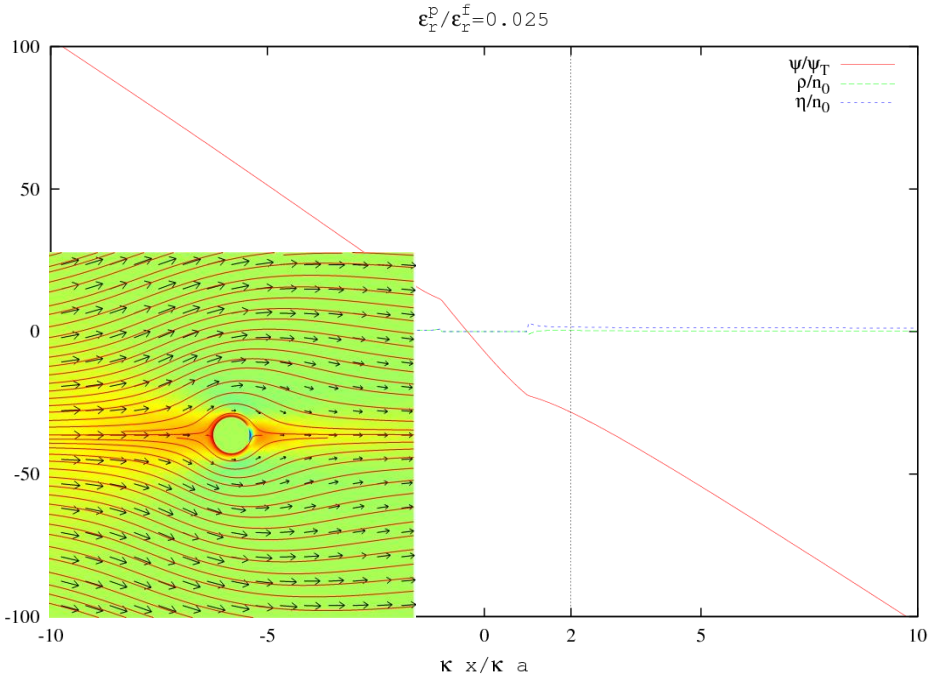

Figure 72: Stern layer model of dielectric particle with; $\theta_S = 1.87$, $\sigma_0/en_0a = -5$, $E_0/\kappa\psi_T = 10$

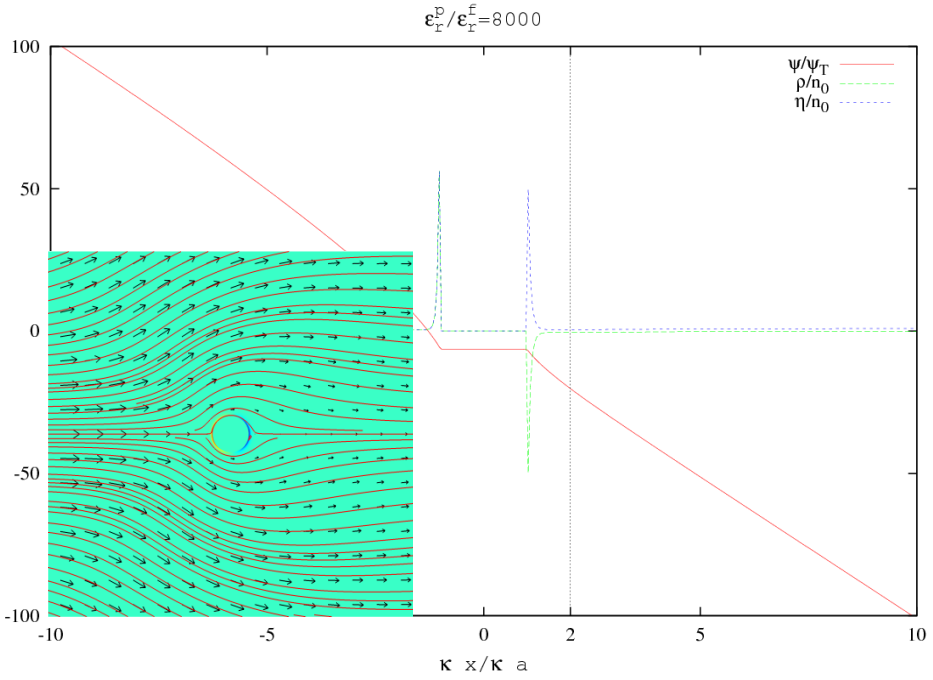

Figure 73: Stern layer model of metallic particle with; $\theta_S = 1.87$, $\sigma_0/en_0a = -5$, $E_0/\kappa\psi_T = 10$

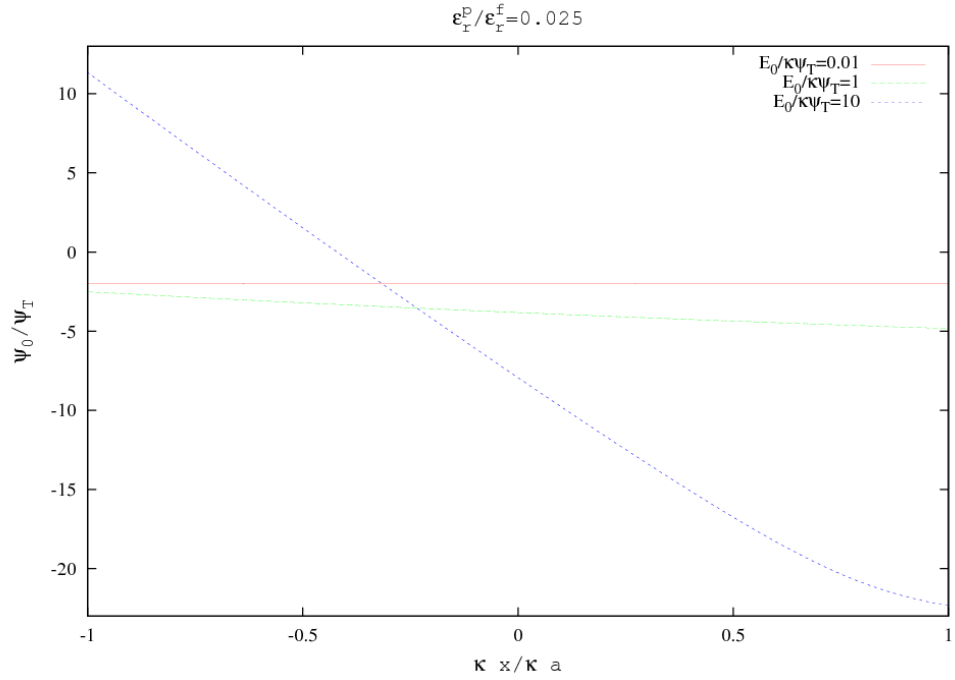

Figure 74: Dimensionless surface potential for a dielectric particle with $\theta_S = 1.873$ and $\sigma_0/en_0a = -5$

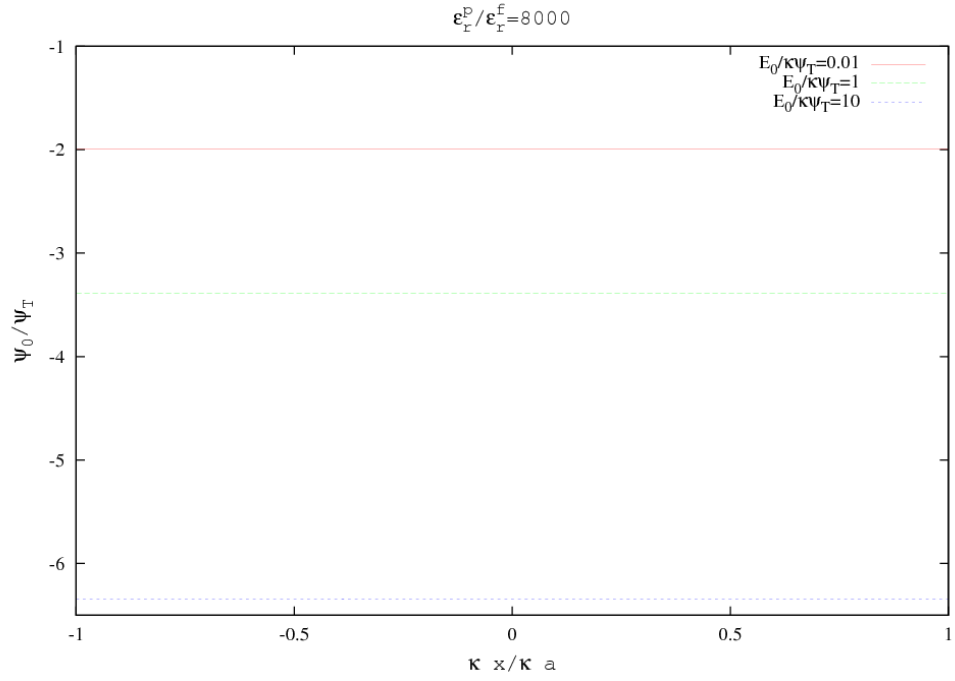

Figure 75: Dimensionless surface potential for a metallic particle with $\theta_S = 1.873$ and $\sigma_0/en_0a = -5$

5.2.2 Dynamic electrophoretic mobility

The FEM solution for dynamic electrophoretic mobility is compared with that of the analytical solution by Ohshima [37], which is valid for arbitrary particle size, small surface potentials, and applied frequency, in Figure 76. The mobility is plotted as a function of the dimensionless applied frequency $(\rho_0 a^2 \omega/\eta_0)$ where the applied frequency has been scaled by τ_f, the characteristic diffusion time for fluid motion, as defined by Equation 3.12.

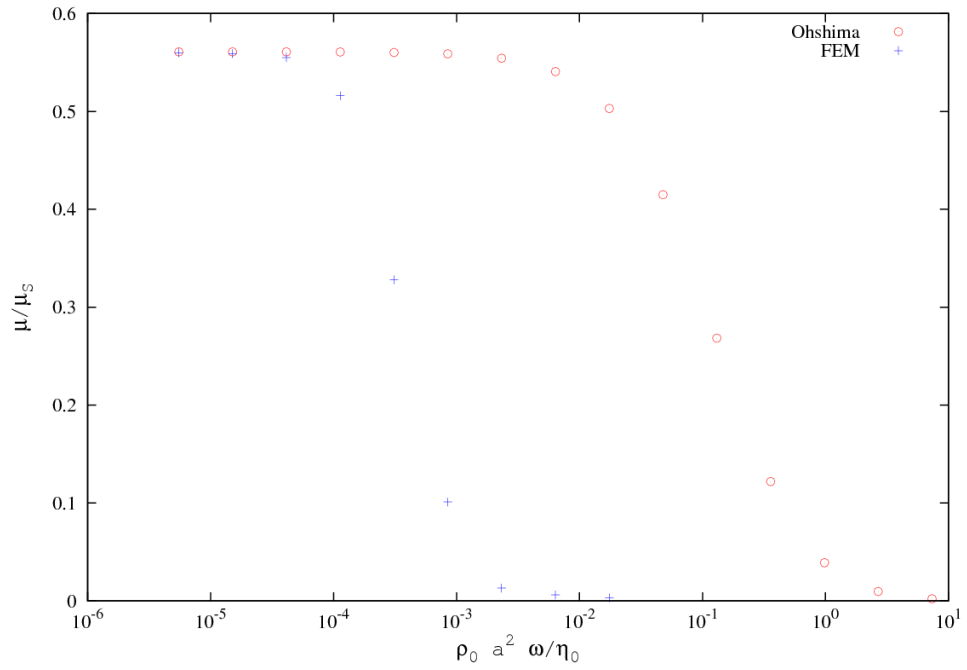

Figure 76: Dynamic electrophoretic mobility

At low frequencies the solutions are in agreement. However, large errors exist for higher frequencies with the FEM solution underestimating the mobility. The source of the error is the coordinate system used to reduce computational cost. A coordinate

system which is fixed to the particle is a non-inertial frame of reference. So, accelerations and inertial forces or impulses and momentums are neglected. However, the FEM model would give good solutions for a particle which is fixed as in ICEO flows or a particle moving at constant velocity as in DC electrophoresis or AC electrophoresis at low frequencies.

5.3 DISCUSSION

In the following we summarize the observed nonlinear effects of large applied electric fields for the three different boundary conditions considered. Then, the explanations for these observations are reviewed and comparisons are made between the different boundary conditions. The effects of the permittivity of the particle and the number of available Stern layer sites are reviewed as well.

When the constant surface potential boundary condition was used the scaled electrophoretic mobility decreases as the applied electric field is increased reaching a minimum between $E_0/\kappa\psi_T = 10^0$ and $E_0/\kappa\psi_T = 10^1$. By plotting the distribution of the EDL, polarization of the EDL was identified as the mechanism for the reduction in mobility. As the applied electric field is increase to $E_0/\kappa\psi_T = 10^0$ the polarization of the EDL becomes large reducing the mobility of the particle. As the applied electric field is increased beyond $E_0/\kappa\psi_T = 10^0$ the average ion density and free charge become very large and the EDL is condensed. A condensed EDL increases the mobility as the particle behaves as if it has a larger value of κa. And, Figure 33 confirms that this would begin to increase the mobility. As the surface potential is increased the electric field of the EDL is stronger and the ability of the applied electric field to relax and thus

condense the EDL is diminished resulting in a mitigation of the nonlinear effects observed at smaller surface potentials.

In stark contrast to the constant surface potential boundary condition, the electrophoretic mobility increases as the applied electric field is increased when the constant surface charge boundary condition or the Stern layer boundary condition is used. The induction of surface potential by was identified as the principle cause of the observed increase in mobility by plotting the EDL and dimensionless surface potential of the dielectric and metallic particle as the electric field is increased. Even though the mobility of both the dielectric particle and the metallic particle increased as a result of induced surface potential, an inspection of the dimensionless surface potential revealed very different nonlinear effects.

The displacement electric field in a dielectric particle is easily relaxed as the electric field in the EDL is relaxed at higher applied electric fields. The resulting electric field in the particle produces large surface potentials one either side of the particle which are of opposite sign. The average scale surface potential of a dielectric particle, presented in Figure 53, explains why the mobility increases as the applied electric field is increased. The decrease in electrophoretic mobility above $E_0/\kappa\psi_T = 10^0$ is a result of increasing polarization of the EDL.

The displacement electric field in a metallic particle is not easily relaxed resulting in a uniform surface potential. As with the dielectric particle, the induced surface potential increased as the applied electric field which increases the mobility of the metallic

particle. However, for metallic particles the polarization of the EDL begins to reduce the surface potential above $E_0/\kappa\psi_T = 10^0$ which begins to reduce the mobility.

The differences mechanisms of polarization and induction of surface potential for dielectric and metallic particles is also the reason that as the surface charge is increased the maximum electrophoretic mobility increases for $\varepsilon_r^p/\varepsilon_r^f = 0.025$ and decreases for $\varepsilon_r^p/\varepsilon_r^f = 8000$. The displacement electric field of a dielectric particle of higher charge is harder to relax and will maintain a negative surface potential which decreases the effect of polarization which is responsible for the reduction in mobility observed above $E_0/\kappa\psi_T = 10^0$. As the charge of the metallic particle is increased the electric field of the EDL becomes strong enough to reduce the effect of the applied electric field on the induced potential. Thus, reducing the mobility as the charge is increased.

The effects of the Stern layer boundary condition were different depending on the value of dimensionless number of Stern layer sites available. When using the Stern layer boundary condition with $\theta_S = 0.1873$, the maximum scaled electrophoretic mobility of the slightly charged dielectric particle is significantly less than that of the constant surface charge boundary condition. However, there is no significant difference in the results for a metallic particle. When using the Stern layer boundary condition with $\theta_S = 1.873$, the maximum scaled electrophoretic mobility of the slightly charged metallic particle is significantly less than that of the constant surface charge boundary condition. And, the mobility of a dielectric particle decreases drastically above $E_0/\kappa\psi_T = 10^0$.

The EDL, dimensionless surface potential, and dimensionless adsorbed ion density were plotted for a dielectric particle and a metallic particle to explain the effect of Stern

layer adsorption. The relaxation of the displacement electric field in a dielectric particle at higher applied electric fields leads to adsorption on one side of the particle and desorption on the other. This leads to extreme concentration polarization on the surface of a dielectric particle which causes the force on the particle to change sign. As the electric field is increased beyond $E_0/\kappa\psi_T = 10^0$ for a metallic particle the adsorption of Stern layer ion begins to reduce the potential of the particle, thus mitigating the effect of the applied electric field and reducing the mobility.

5.4 CONCLUSIONS

Recall that linearized electrokinetic theories are based on the assumption that the applied electric field is much smaller than that of the EDL. While this is normally the case for interface science, where the objective is the determination of surface properties from the dynamic mobility and dielectric response of dilute colloidal dispersions, the motivation of this research is in the application of colloidal microfluidics; specifically, in the application of colloidal assembly where the applied electric fields can be quite large. An EDL with a zeta potential of $10\,mV$ and a Debye length of $10\,nm$ has an electric field of about $1\ V/\mu m$. A microfluidic device with a $1\,V$ potential difference across a $1\,\mu m$ electrode gap would have an applied electric field on the order of the EDL. Therefore, the linearized electrokinetic theories are not adequate. Further, linear electrokinetic models neglect the ion convection term of Equation 3.13. However, a quick calculation reveals that the value of the Peclet number is approximately 0.25 for an $0.1\ mM$ electrolyte solution so it should not be neglected in most cases. When the ion convection term is included with $Pe = 0.25$, the ion distribution is perturbed by the

moving fluid and a comparison of the electric potential at one Debye length with that from the FEM model without the convection term is slightly different. Several nonlinear electrokinetic phenomena including the induced electro-osmotic backflow in microfluidic channels shown in Figure 6 could not be explained without the inclusion of this term.

The results of Section 5.2 and the discussion presented in Section 5.3 have shown that the constant surface potential boundary condition is inappropriate for nonlinear electrokinetic models. The inclusion of the Stern layer boundary condition is needed for small surface charges especially if the number of Stern layer sites available is large. However, it is proposed that the Stern layer boundary condition is the most general and thus the appropriate boundary condition for a nonlinear electrokinetic model. The electrophoretic mobility results presented in Figure 55 and Figure 62 for a Stern layer boundary condition with $\theta_S = 0.1873$ and $\theta_S = 1.873$, respectively, do not completely reveal the influence of Stern layer adsorption on the properties of the surface. The dielectric response of a dispersion of particles, which has not been presented here, is greatly affected by Stern layer adsorption. Also, the dependence of the electrophoretic mobility on applied electric field strength was only presented for $\kappa a = 1$. The effect of Stern layer adsorption on the electrophoretic mobility may increase with increasing values of κa.

Finally, the proposed FEM model does not do a good job of calculating the dynamic electrophoretic mobility of particles at high frequencies. In the brief discussion presented in Section 5.2.2 the source of the error was revealed as the coordinate system

used in the FEM model. A coordinate system which is fixed to the particle is a non-inertial frame of reference. Thus, it cannot be used unless the particle is fixed or moving at constant velocity. Some improvements to the finite element model that will allow the accurate calculation of the dynamic electrophoretic mobility will be suggested in Section 8 following the presentation of particle-particle interaction in Section 6 and a single particle in a non-uniform electric field in Section 7. However, the proposed model is an efficient way to calculate the static electrophoretic mobility as the particle travels at constant velocity in a constant applied electric field. And, the FEM model is very useful in the calculation of ICEO flows around fixed particles or surfaces. In fact, a significant advantage of the FEM model even when electric fields are small enough to use the linearized electrokinetic models is the calculation of ICEO flows surrounding non-spherical particles as in the triangular shaped particle of Figure 5 as linearized electrokinetic models use spherical symmetry to derive their semi-analytical expressions.

6 PARTICLE-PARTICLE INTERACTION

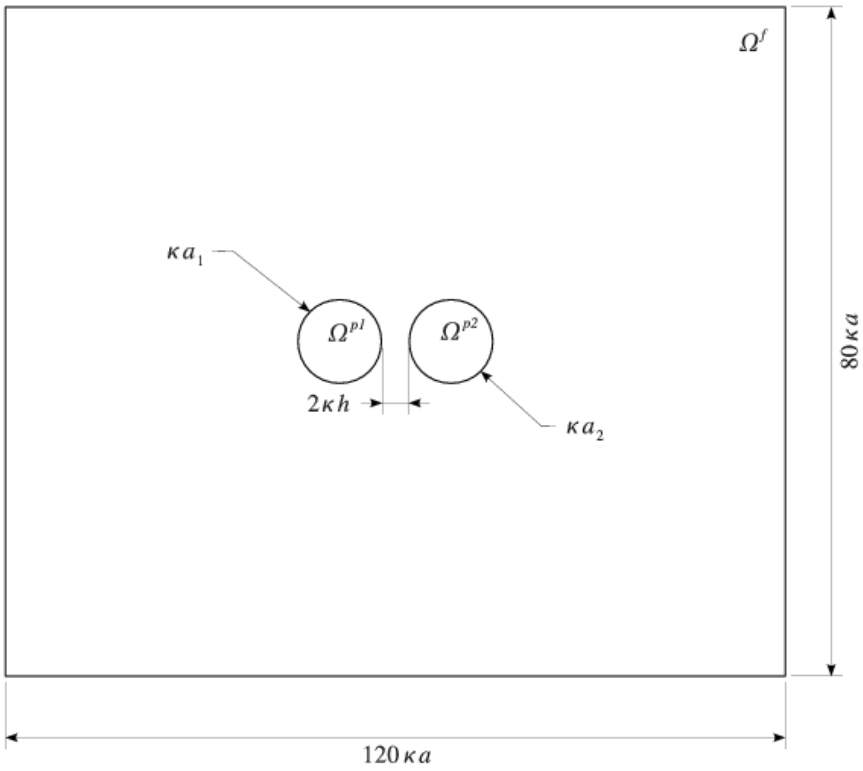

Figure 77: Particle-particle interaction

6.1 PROBLEM STATEMENT

The objectives of this section are; (1) the validation of the FEM model for interacting particles in the absence of an applied electric field, (2) the characterization of hydrodynamic and electric particle-particle interaction forces for particles in an applied electric field, and (3) investigation of nonlinear effects associated with electric field strength. In the following the theory developed by Derjaguin, Landau, Verwey and Overbeek commonly called the DLVO theory [10] is described, the significance of interacting particles to colloidal science reviewed, and the results of the FEM model are presented and discussed. The computational domain used is shown in Figure 77.

Characterization of the distribution of the electric double layers surrounding interacting particles in the absence of an electric field is important in stability of colloidal solutions. Colloidal stability is maintained if the electrostatic repulsion of the EDL is strong enough to resist coagulation. The DLVO theory obtained potential energy curves for two particles (or plates), including Van der Waals attraction and the electrostatic repulsion of the EDL as in Figure 78. The electrostatic energy was calculated using the Gouy-Chapman theory reviewed in Section 2.1.

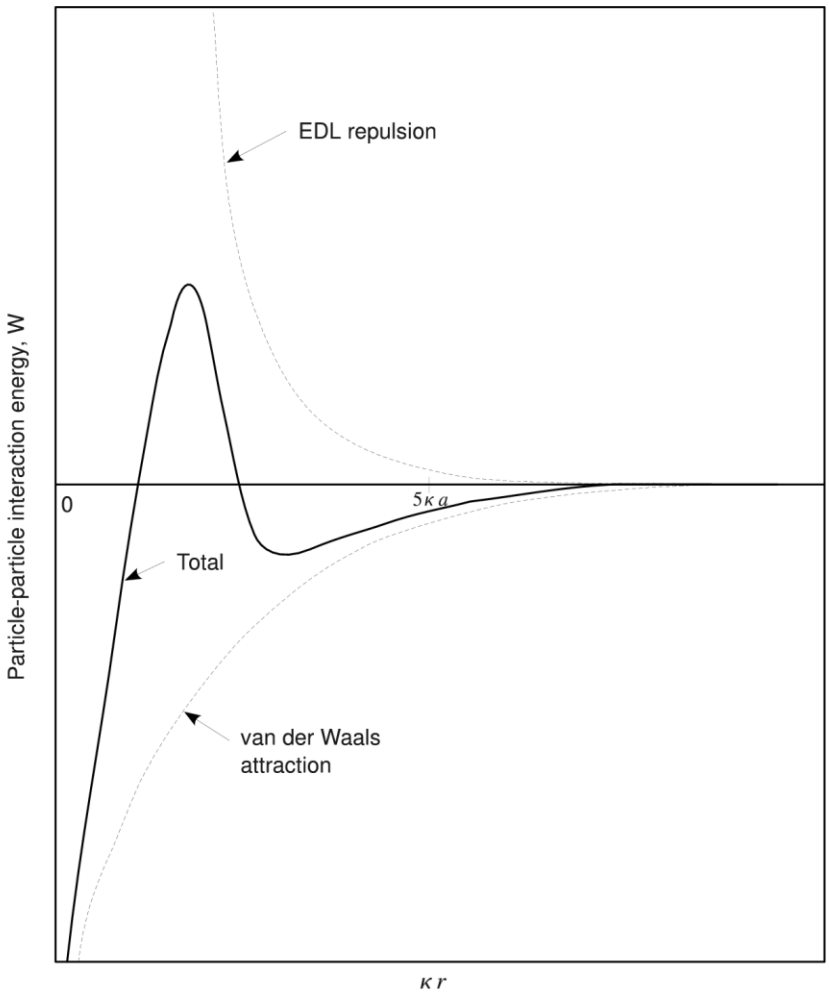

Figure 78: Schematic of the variation of free energy with particle separation according to DLVO theory

Figure 79 summarizes the results of the DLVO theory. A stable colloidal dispersion can be made unstable with the addition of salt to the solution or by decreasing the surface potential, (ψ_0). Adding salt decreases the length of the EDL and decreasing the surface potential decreased the electrostatic repulsion. More importantly, if one desires to disperse a given colloid in a solution, e.g. ψ_0 is given, the DLVO theory can predict the critical electrolyte concentration for stability.

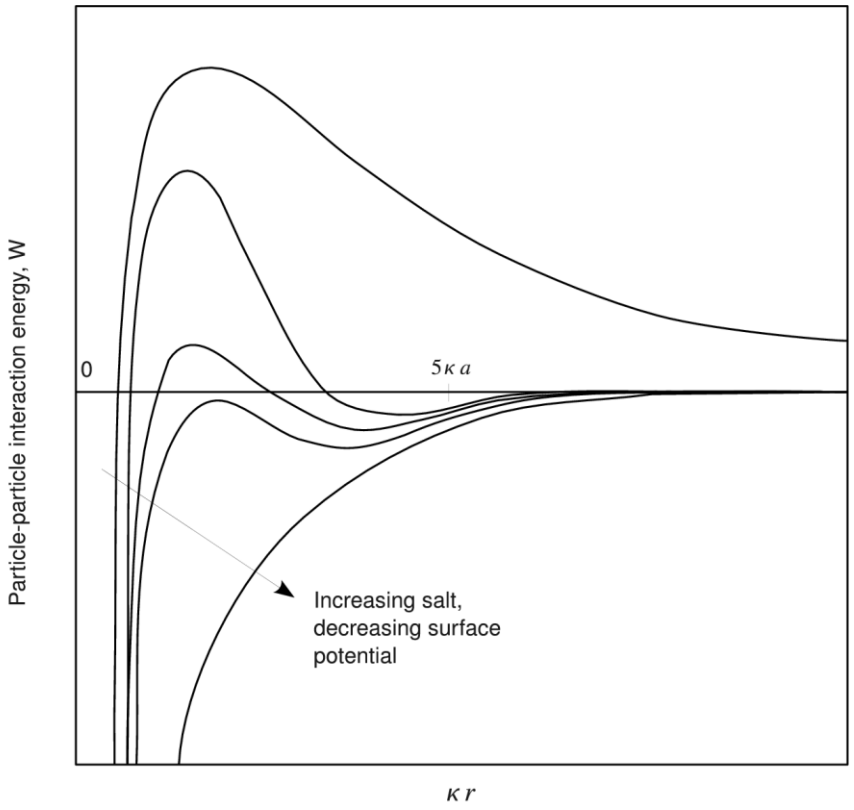

Figure 79: Summary of DLVO theory

The DLVO theory has also been extended to the dynamic interaction of two particles in solution. This dynamic DLVO theory[38, 39] is useful in the interaction of EDL's in AC electric fields. Essentially, at higher frequencies the EDL is relaxed,

reducing the electrostatic repulsion so that coagulation occurs. This relaxation is useful in directed assembly of colloids because under the right conditions the assembly is reversible, i.e. the colloids can be re-dispersed upon reduction of the frequency.

6.2 RESULTS

The results presented in this section validate the FEM model and demonstrate the combined effects of particle-particle interaction and applied electric fields. First, the analytical solutions used for model verification are presented. Then, the results which verify the FEM model are presented and discussed. Having verified the accurate solution of the electric double layers surrounding interacting particles, some results are presented to demonstrate the effect of an applied electric field on the interaction of particles. This is followed by a discussion in Section 6.3 and the presentation the conclusions in Section 6.4.

The results presented in Figure 80, Figure 81, Figure 82 and Figure 83 verify the accurate calculation of electric field and charge distribution in the equilibrium EDL. A parametric study of the dimensionless particle radius (κa), the dimensionless minimum half-separation distance $\kappa h/\kappa a$, and the dimensionless Stern potential (ψ_0/ψ_T) was performed using the proposed FEM model. Results were verified with two different analytic solutions based on DLVO theory. $DLVO_1$ is the nonlinear parallel plate model which is valid for arbitrary Stern potential[10]. The error associated with the $DLVO_1$ model of order κa. $DLVO_2$ is a linear cylinder-cylinder model valid for arbitrary particle radius [40]. The error associated with this solution is of order ψ_0/ψ_T. So, in every case the FEM solution should have the following limiting behavior:

$$\lim_{\kappa a \to \infty} \psi_{\mathrm{FEM}} = \psi_{\mathrm{DLVO}_1} \tag{6.1}$$

$$\lim_{\psi_0 \to 0} \psi_{\mathrm{FEM}} = \psi_{\mathrm{DLVO}_2} \tag{6.2}$$

which may be verified in Figure 82 and Figure 83.

The finite element results presented in Figure 82 and Figure 83 were generated by solving the 2-D nonlinear electrokinetic equations using the finite element method and extracting the potential at the point in between the two particles at the mid-plane which is called ψ_C. The intermediate results are shown in Figure 80 and Figure 81 which show the distribution of the EDL surrounding interacting particles. Figure 80 is a surface plot of the electric potential when the dimensionless surface potential is one and the dimensionless half separation is one. Then, in Figure 81 the dimensionless electric potential is plotted along the mid-plane to show the position of ψ_C. The results of Figure 80 and Figure 81 also show slight polarization of the EDL as the particles start to interact.

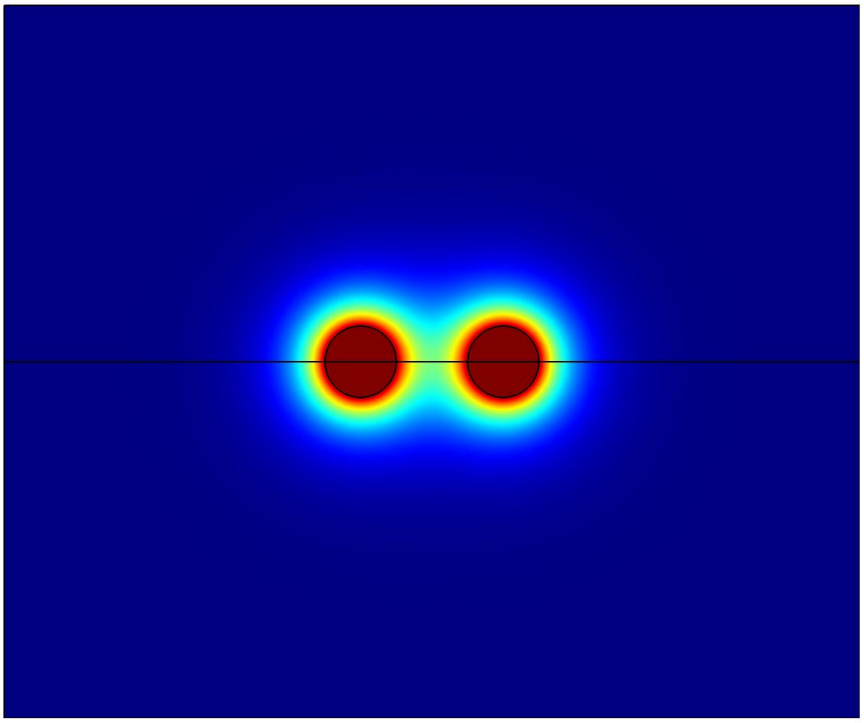

Figure 80: Electric potential around interacting particles

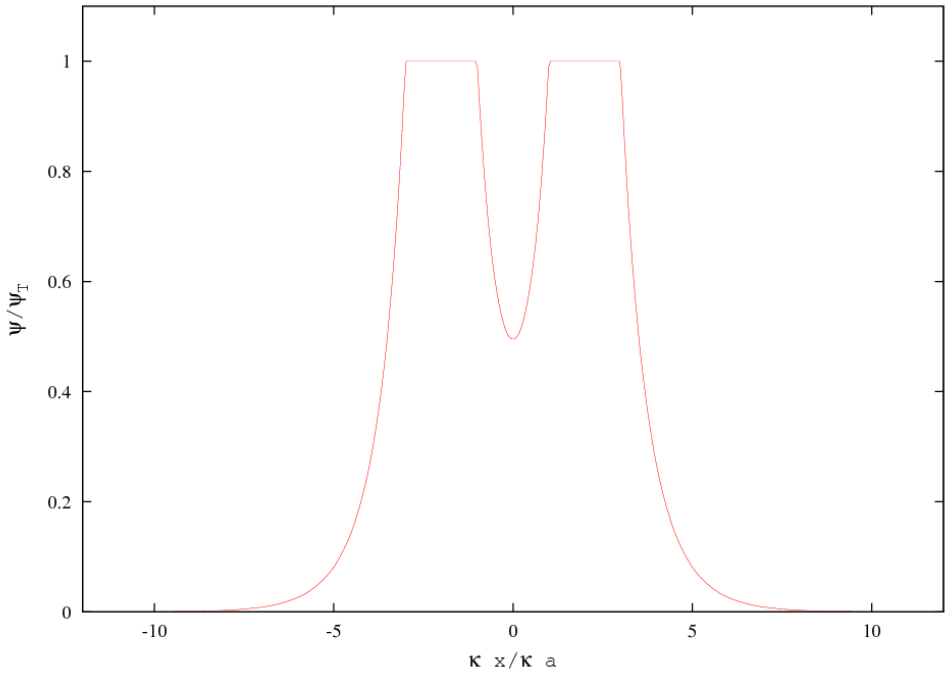

Figure 81: Electric potential along mid-plane

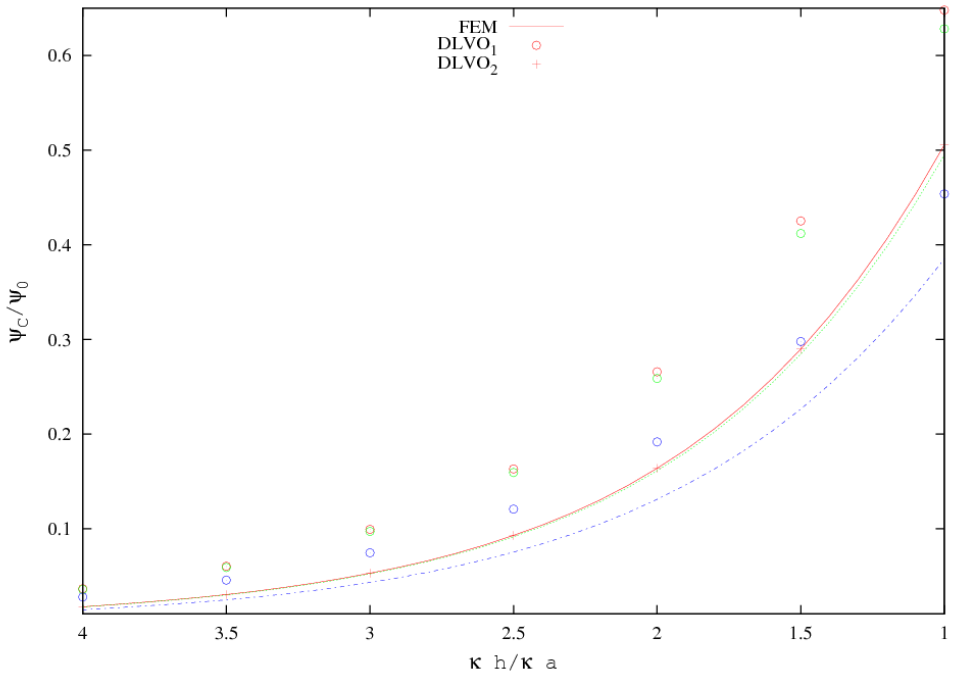

Figure 82: Particle-particle interaction ($\kappa a = 1$)

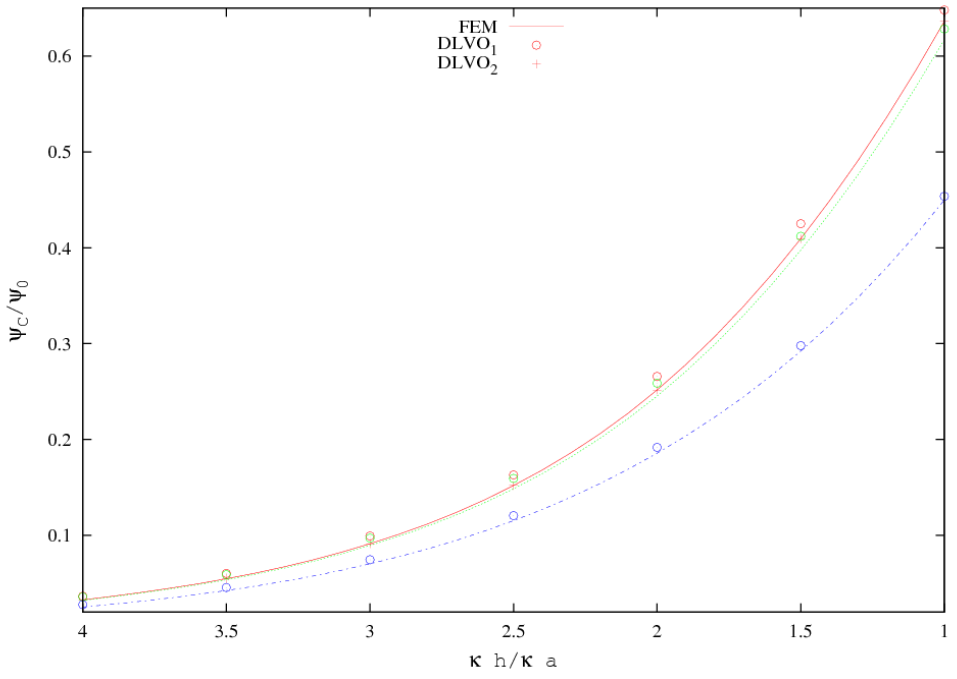

Figure 83: Particle-particle interaction ($\kappa a = 16$)

red – $\psi_0/\psi_T \to 0$, green – $\psi_0/\psi_T = 1$, blue – $\psi_0/\psi_T = 4$

The results for $\kappa a = 1$ shown in Figure 82 show that: The FEM solution is in agreement with the $DLVO_2$ model for small surface potentials. The error in the $DLVO_2$ model becomes significant for dimensionless surface potentials greater than one. And, the errors in the $DLVO_1$ (flat plate) model are significant when $\kappa a = 1$.

The results for $\kappa a = 16$ shown in Figure 83 show that: The same errors in the $DLVO_2$ model exist as they are associated with the surface potential regardless of the dimensionless particle radius. And the FEM model is in approximate agreement with the $DLVO_1$ model for $\kappa a = 16$ at all surface potentials.

Having verified the FEM model for interacting particles in the absence of an applied electric field, we now present results which demonstrate the effect of an applied electric field. As shown in Section 4 and Section 5, the effect of the applied electric field depends on the surface boundary condition and the dimensionless particle permittivity. As in the previous sections we first consider the constant surface potential boundary condition, followed by the constant surface charge boundary condition, and then the Stern layer boundary condition. However, the effect of the particle charge is not included as only surface boundary conditions which result in a dimensionless surface potential of one when no electric field is applied is used. The value of dimensionless number of Stern layer sites used with the Stern layer boundary condition was $\theta_S = 1.873$. Results for each of the boundary conditions are presented for the dimensionless particle permittivities of the dielectric particle and metallic particle used in the previous sections and recorded in Table 5. Also, only a dimensionless particle size of $\kappa a = 1$ is considered, as this results in a large distance of interaction.

Primarily, two sets of results will be used to characterize the effect of applied electric field strength and particle-particle interaction with additional results included as needed. First, surface plots of the electric potential surrounding interacting particles in a weak applied electric field will be presented for dimensionless separations of $\kappa h/\kappa a = 1$ and $\kappa h/\kappa a = 0.5$. Also, streamlines and arrows will be included in the fluid domain of the surface plots to show the fluid flow as well as arrows on the boundary of the particles to show the sum of the Maxwell traction and the hydrodynamic traction. Next, to better quantify the interaction, we will present section plots of the dimensionless electric potential and dimensionless free charge along the mid-plane for different particle separations. Then, to investigate the effect of electric field strength, the surface plots and section plots will be presented for interacting particles in a strong applied electric field and comparisons will be made. Finally, to investigate the effect of the surface boundary condition, the process is repeated for the constant surface boundary condition (Section 6.2.1), the constant surface charge boundary condition (Section 6.2.2) , and the Stern layer boundary condition (Section 6.2.3).

6.2.1 Constant surface potential boundary condition

The objective of this section is to present and describe the results for the constant surface potential boundary condition. First, the weak applied electric field results will be presented. Then, the strong applied electric field results are presented for comparison. The surface plots for interacting particles in a weak applied electric field are shown in Figure 84 and Figure 85. And, the section plots of dimensionless electric potential and dimensionless free charge are presented in Figure 86 and Figure 87.

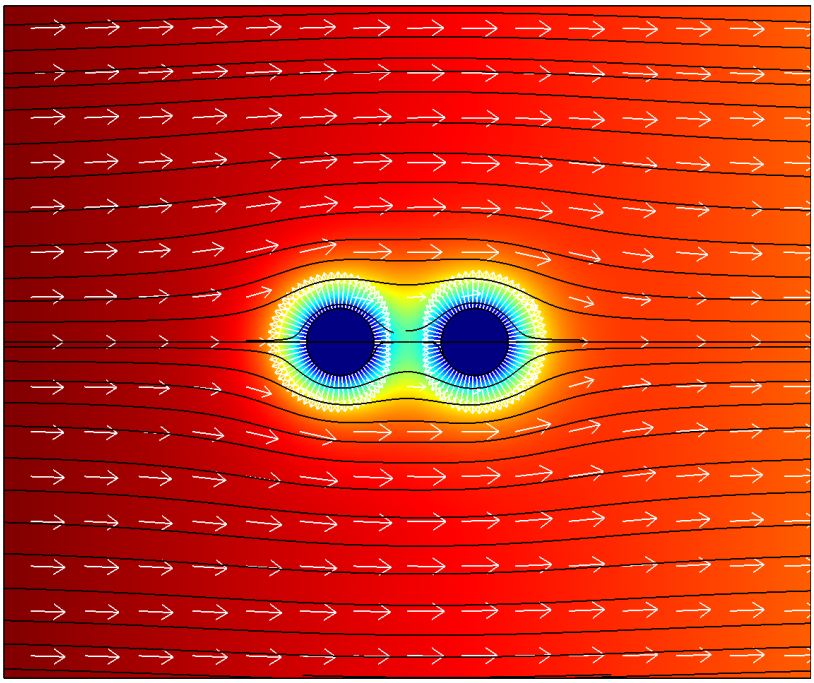

Figure 84: Interacting particles with; $\psi_0/\psi_T = -1$, $E_0/\kappa\psi_T = 10^{-2}$, and $\kappa h/\kappa a = 1$

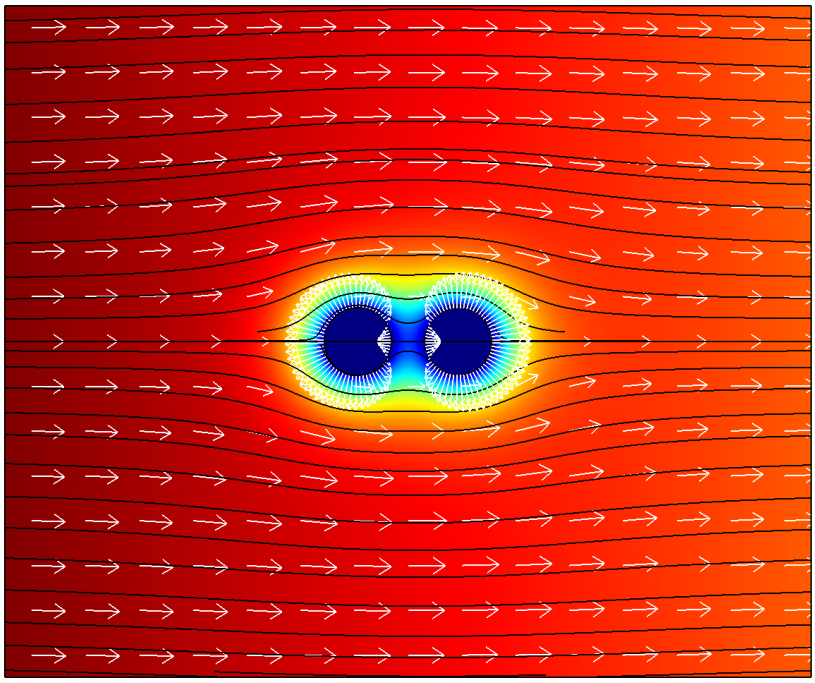

Figure 85: Interacting particles with; $\psi_0/\psi_T = -1$, $E_0/\kappa\psi_T = 10^{-2}$, and $\kappa h/\kappa a = 0.5$

The results of Figure 84 and Figure 85 show that in a weak applied electric field: The fluid flow is not significantly affected by the presence of the interacting particles, i.e. no large regions of circulation exist. The EDL of a particle is only slightly polarized by the interaction with the other particle and the applied electric field. And, the distribution of the traction on the surface is altered as the particles become closer resulting in an increase in the repulsive force.

The dimensionless electric potential between the particles, shown in Figure 86, appears to be unaffected by the weak applied electric field. However, it should be noted that Figure 87 shows that the dimensionless free charge at the surface of the particle on the left, hereafter particle one, is slightly higher than the particle on the right (particle two).

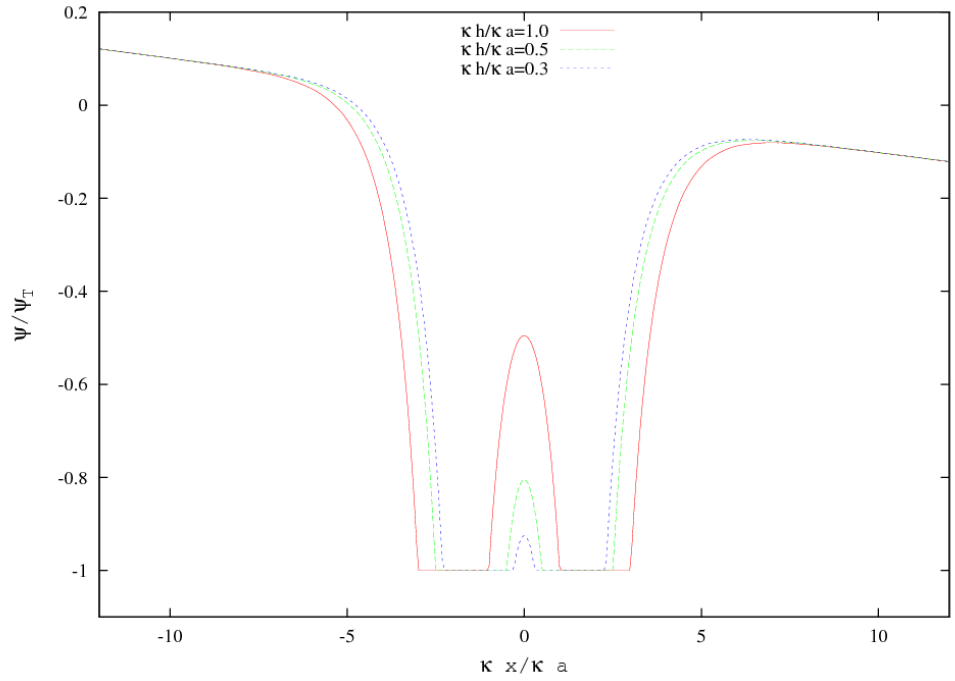

Figure 86: ψ/ψ_T for interacting particles with constant surface potential in a weak applied electric field

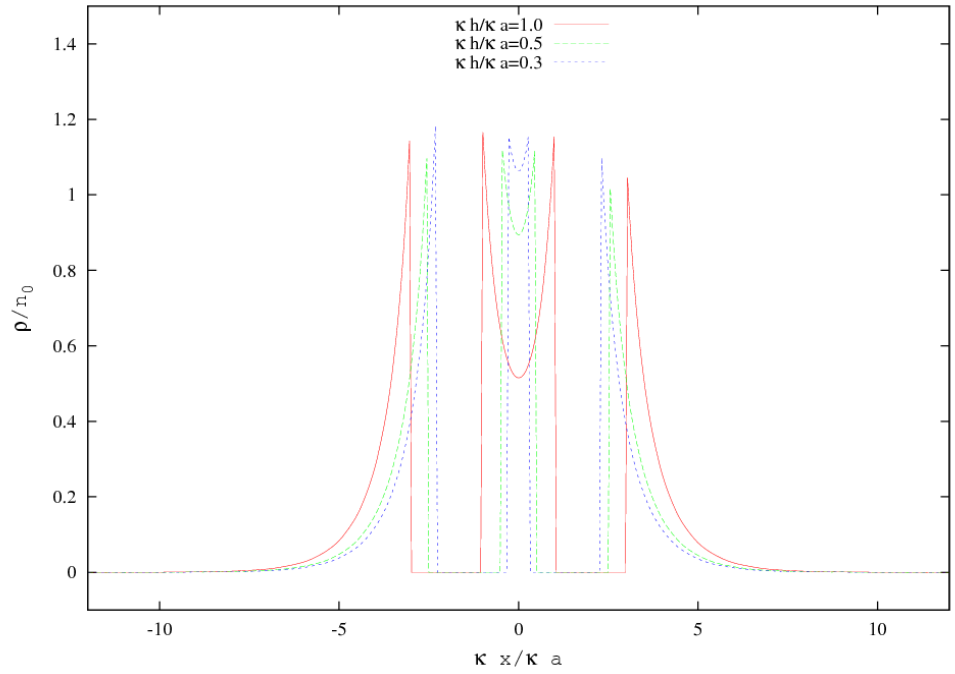

Figure 87: ρ/n_o for interacting particles with constant surface potential in a weak applied electric field

The results for interacting particles in a strong applied electric field using the constant surface potential boundary condition will now be presented. The surface plots are shown in Figure 88 and Figure 89. And, the dimensionless electric potential and dimensionless free charge along the mid-plane are shown in Figure 90 and Figure 91. Following the presentation of these results, comparisons will be made with the weak applied electric field results. Then, the process outlined in this section will be repeated for the constant surface boundary condition in Section 6.2.2. Some attempt is made to keep discussion short in this section and the following sections. A complete discussion and conclusions will follow the presentation the results for all the surface boundary conditions so that the dependence of the applied electric field strength on the surface boundary condition can be demonstrated.

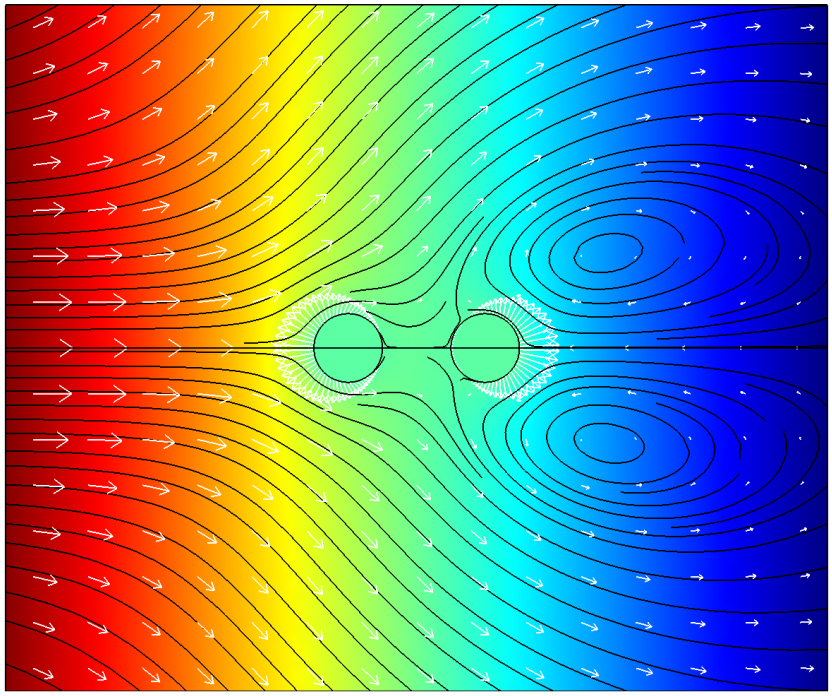

Figure 88: Interacting particles with; $\psi_0/\psi_T = -1$, $E_0/\kappa\psi_T = 10^0$, and $\kappa h/\kappa a = 1$

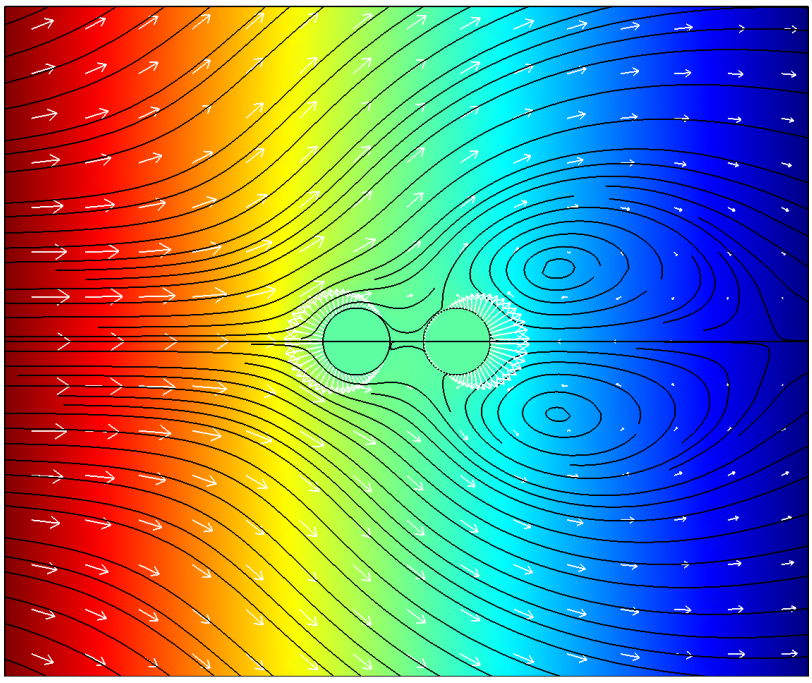

Figure 89: Interacting particles with; $\psi_0/\psi_T = -1$, $E_0/\kappa\psi_T = 10^0$, and $\kappa h/\kappa a = 0.5$

The streamlines of the fluid velocity shown in Figure 88 and Figure 89 show that the fluid flow surrounding interacting particles with a constant surface potential is affected by the strong applied electric field. Large circulation zones appear on the leeward side of the flow. From the arrows showing the traction on the boundary of the particles, it appears that the repulsive force between the particles is stronger than that of the same particles in a weak applied electric field. Some insight into why the repulsive force increases with applied electric field strength can be revealed by plotting the dimensionless electric potential and dimensionless free charge for different particle separations as shown in Figure 90 and Figure 91.

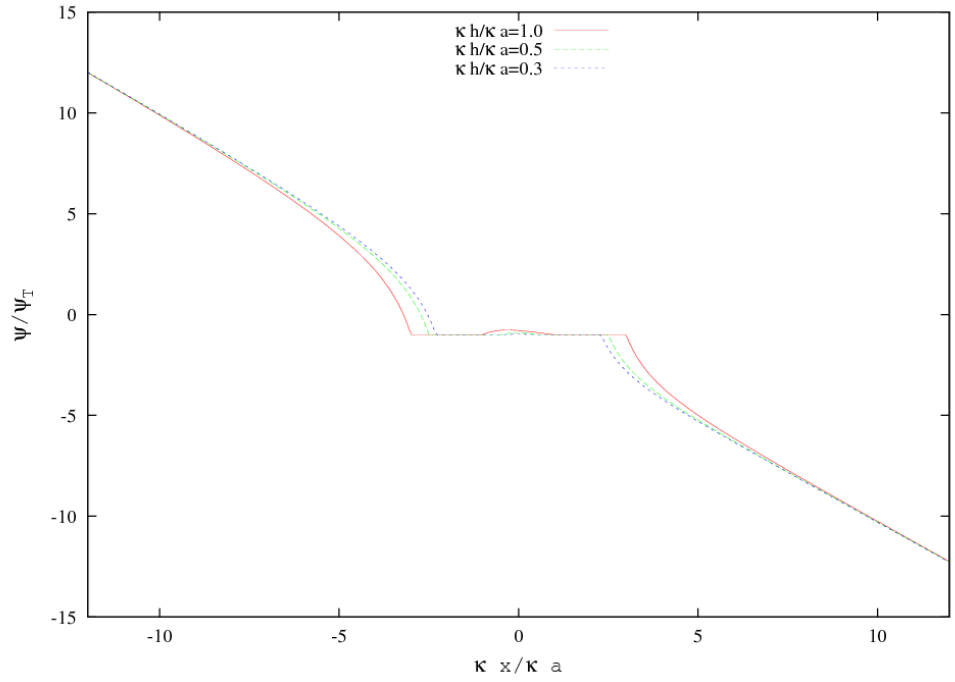

Figure 90: ψ/ψ_T for interacting particles with constant surface potential in a strong applied electric field

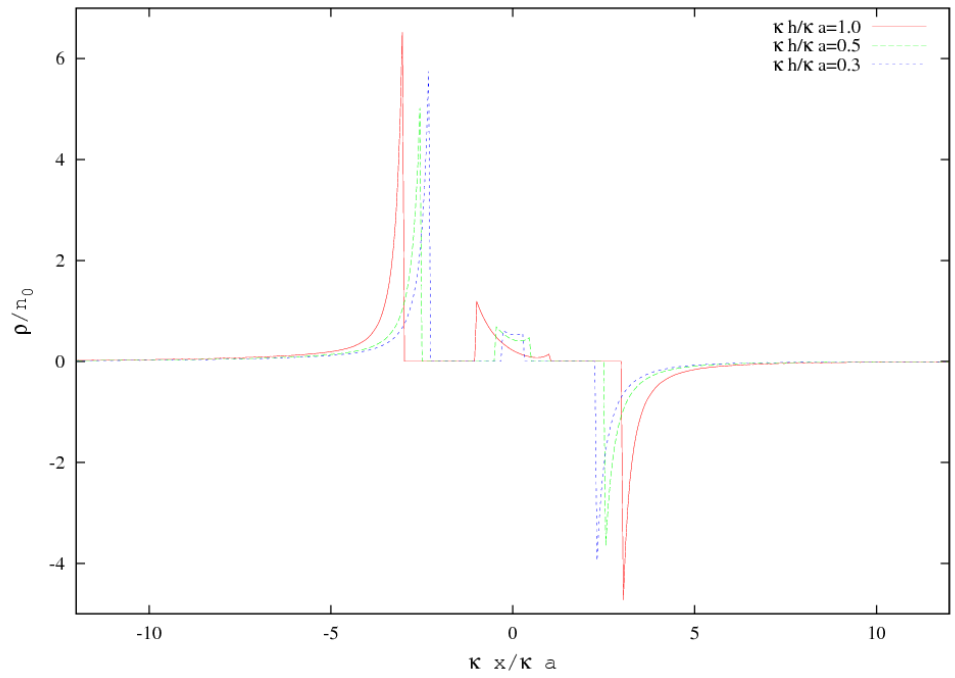

Figure 91: ρ/n_o for interacting particles with constant surface potential in a strong applied electric field

The distribution of potential and free charge between interacting particles in a large applied electric field (Figure 90 and Figure 91) is quite different than that between interacting particles in a weak applied electric field (Figure 86 and Figure 87). The maximum electric potential and free charge occurs in the center for weak applied electric fields and is skewed in large applied electric fields as shown in Figure 90 and more clearly in the detail of Figure 92. The direction of the skew corresponds to the opposite sign of the free charge between the particles in a positive electric applied electric field (for the constant surface potential boundary condition). That is,

$$\text{direction of skew} = -sign(E_0) \times sign(\rho). \tag{6.3}$$

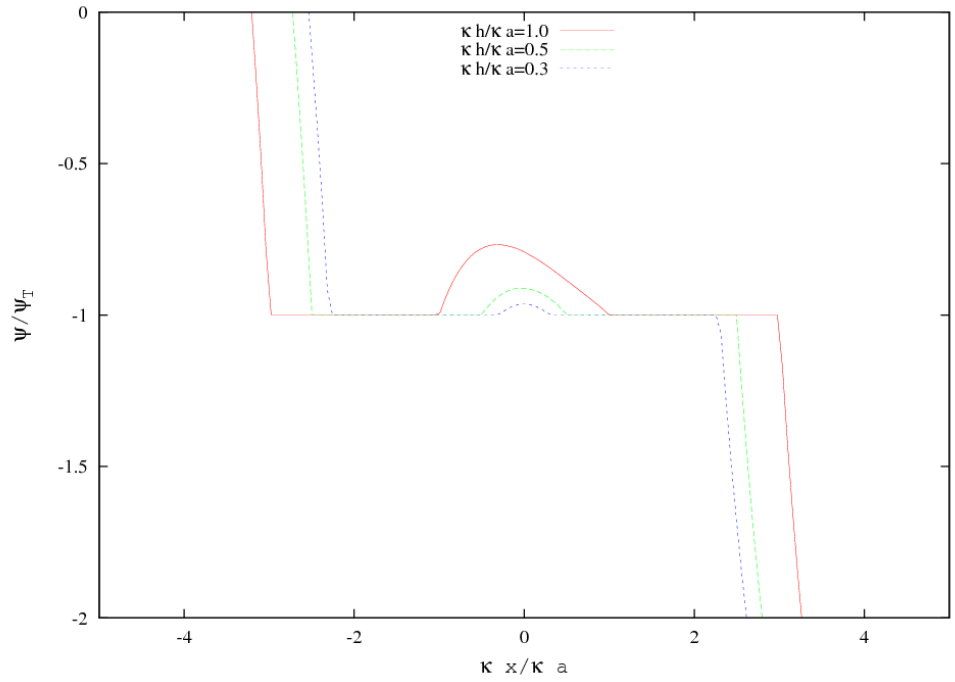

Figure 92: Detail of ψ/ψ_T between interacting particles with; $\psi_o/\psi_T = -1$ & $E_0/\kappa\psi_T = 10^0$

The results of Figure 92 reveal a deviation from assumptions made in the development of DLVO based theories. DLVO theories assume the applied electric field is small. So, the maximum electric potential is at the mid-point and they use a symmetry boundary condition at the mid-plane to determine the distribution of the EDL for interacting particles from the Poisson-Boltzmann equation (Equation 2.2). Obviously, this is not the case for interacting particles in large applied electric fields. The results of Figure 93 show that; (1) a DLVO theory (labeled $E/\kappa\,\psi_T = 0$) would accurately predict the electric potential between two interacting particles in a weak applied electric field, and (2) when the applied electric field is strong, the DLVO theory would not produce sufficient results.

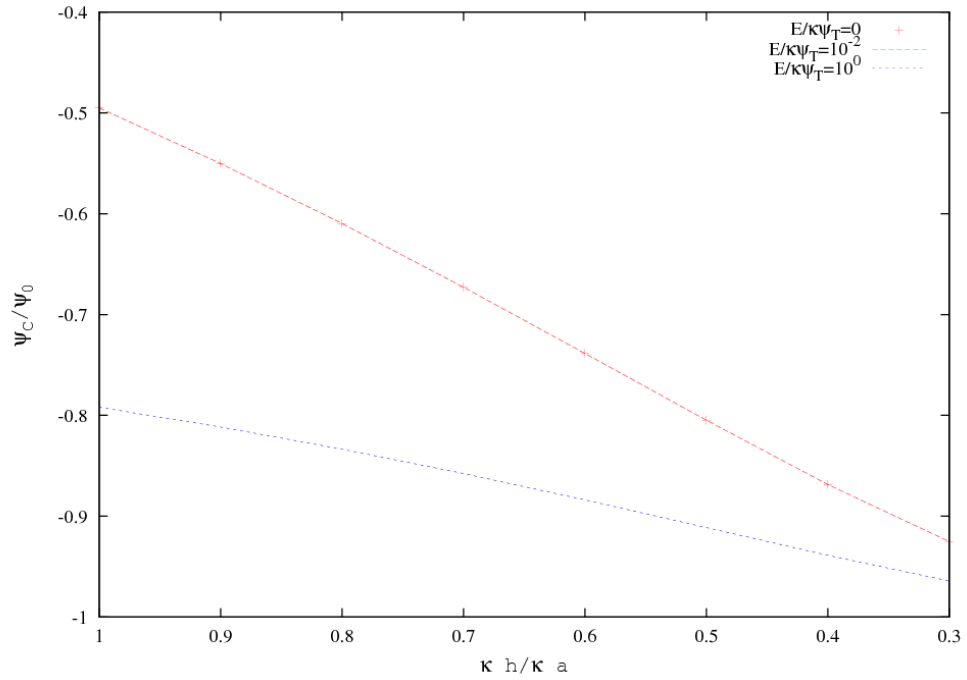

Figure 93: Dimensionless mid-point potential for constant surface potential boundary condition

The results of Figure 93 also illustrate two competing nonlinear electrokinetic phenomena; (1) particle-particle interaction and (2) distortion of the electric double layers by the applied electric field. When the dimensionless half-separation of the particles is on the order of one the effect of electric field strength on mid-plane potential is dominant, but as the separation is decreased the effect of particle interaction takes over. This is illustrated in Figure 93 where the difference in the $E/\kappa\psi_T = 10^{-2}$ solution and the $E/\kappa\psi_T = 10^{0}$ solution is larger for $\kappa h/ka = 1$ than it is for $\kappa h/ka = 0.3$. These observations are supported by the results of Figure 92, which shows that as the particles move closer together the shift due to the applied electric field is nullified. Therefore, the results of Figure 93 indicate that the repulsive force between the particles will be greater for strong applied electric fields than for weak applied electric fields and

that the difference between the strong and weak electric field forces will decrease as the particles approach one another. This is verified by plotting the dimensionless force on particle one as a function of dimensionless particle separation for a weak applied electric field and a strong applied electric field as shown in Figure 94.

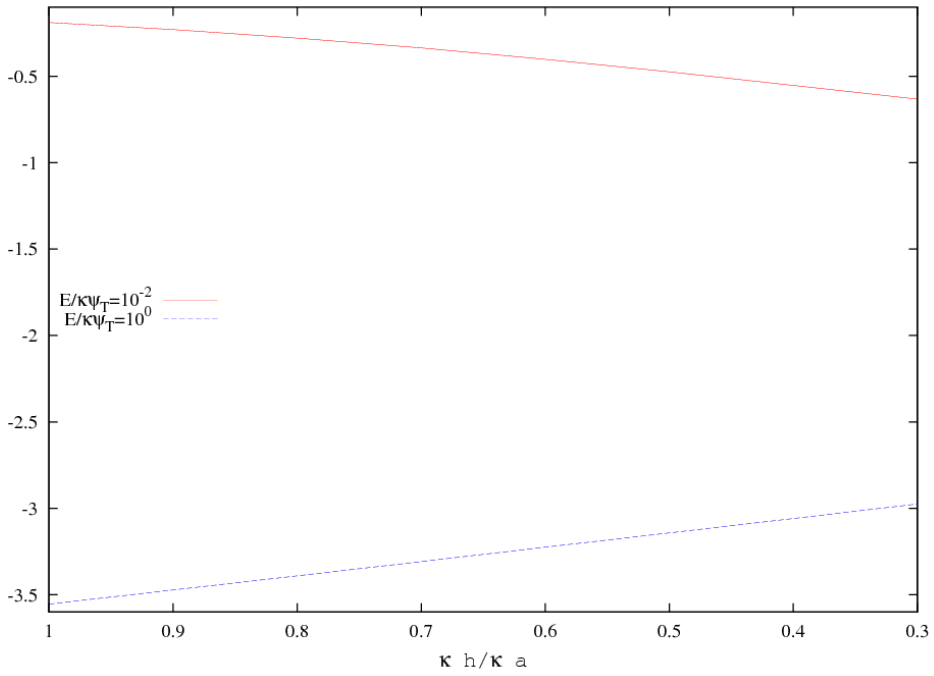

Figure 94: Dimensionless force on particle one for constant surface potential boundary condition

6.2.2 Constant surface charge boundary condition

The objective of this section is to present and describe the results for the constant surface charge boundary condition. The process outlined in Section 6.2.1 is repeated in this section for interacting dielectric particles, interacting metallic particles, and a dielectric particle interacting with a metallic particle with the dimensionless particle permittivities of Table 5 using the constant surface boundary condition. Then, in Section 6.2.3 the same combinations are repeated, but the Stern layer boundary condition is used.

The surface plots for interacting dielectric particles in a weak applied electric field are presented in Figure 95 and Figure 96. And, the section plots of the dimensionless electric potential and dimensionless free charge along the mid-plane are presented in Figure 97 and Figure 98. Then, without discussion, the results for a strong applied electric field are presented in Figure 99, Figure 100, Figure 101, and Figure 102 for comparison.

A comparison of the fluid velocity streamlines and boundary traction vectors shown in Figure 95 and Figure 96 for interacting dielectric particles using the constant surface boundary condition with those of the constant surface potential boundary condition presented in Figure 84 and Figure 85 reveals some differences resulting from the boundary conditions used. First, the velocity streamlines for the constant surface potential results seem to be more distorted than the dielectric-constant charge results. Secondly, the distribution of the traction vectors is quite different. This is particularly true for small particle separations.

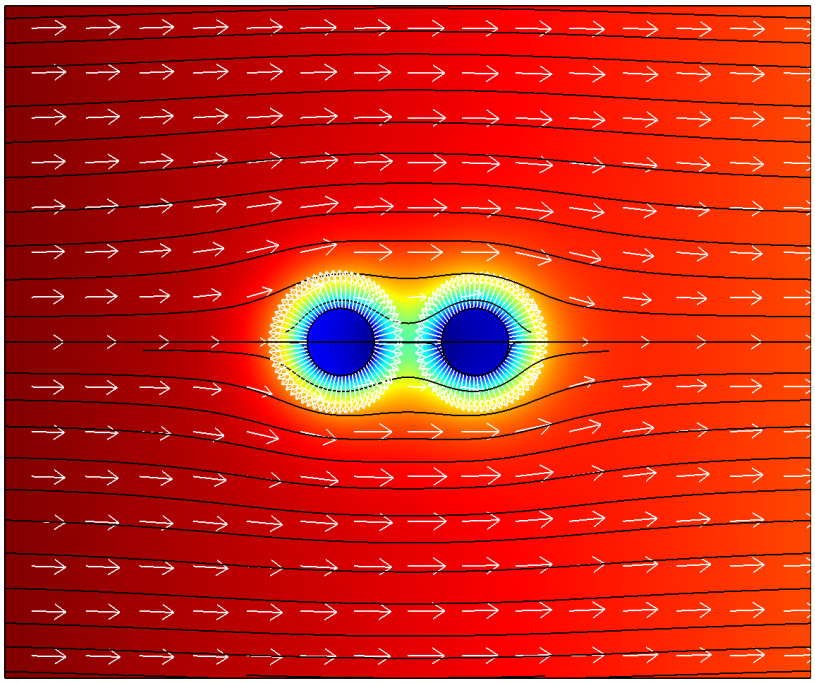

Figure 95: Interacting dielectric particles with; $\sigma_0/en_0a = -1.47$, $E_0/\kappa\psi_T = 10^{-2}$, and $\kappa h/\kappa a = 1$

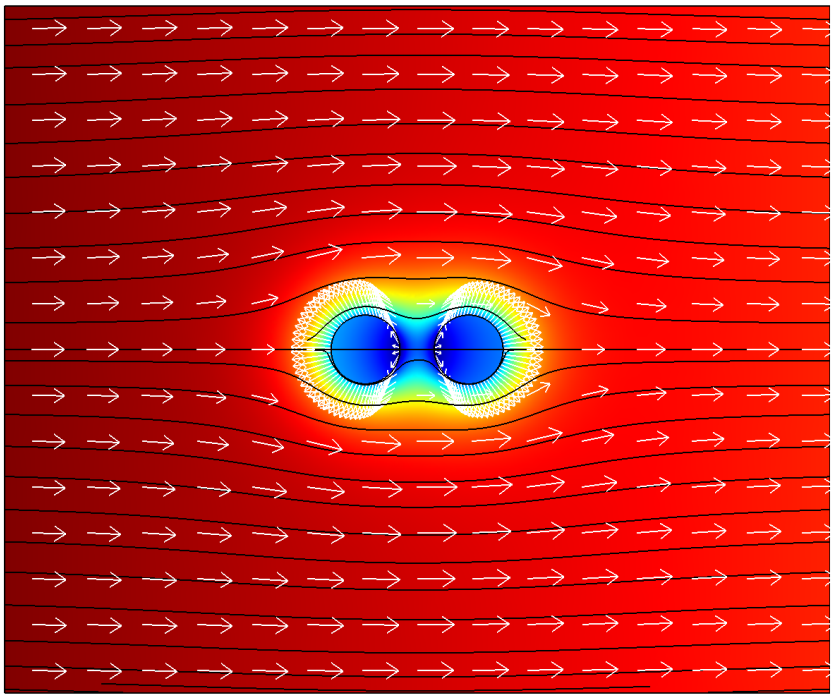

Figure 96: Interacting dielectric particles with; $\sigma_0/en_0a = -1.47$, $E_0/\kappa\psi_T = 10^{-2}$, and $\kappa h/\kappa a = 0.5$

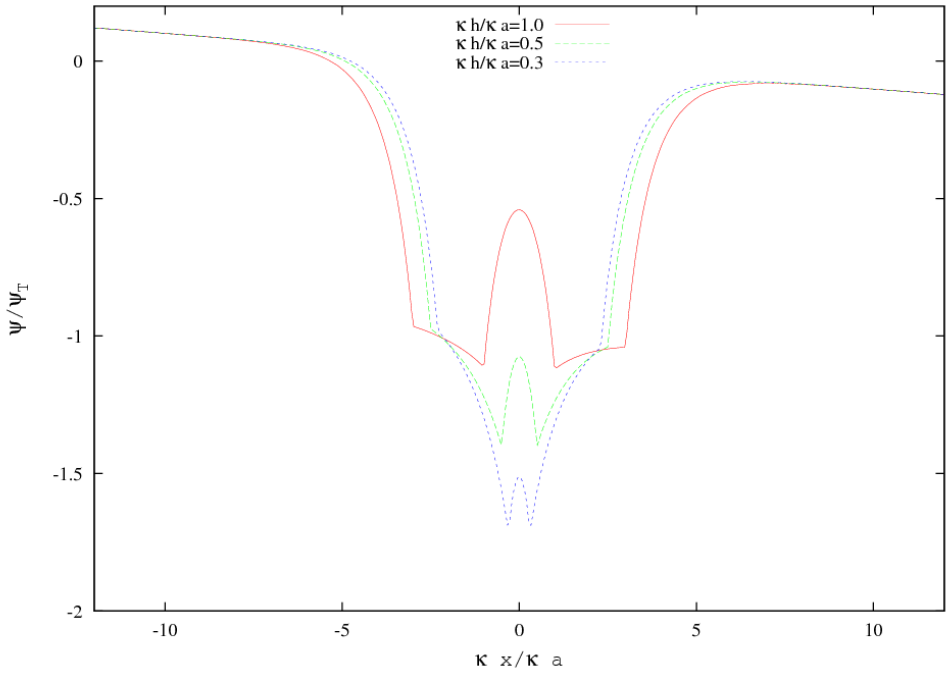

Figure 97: ψ/ψ_T for interacting dielectric particles in a weak applied electric field

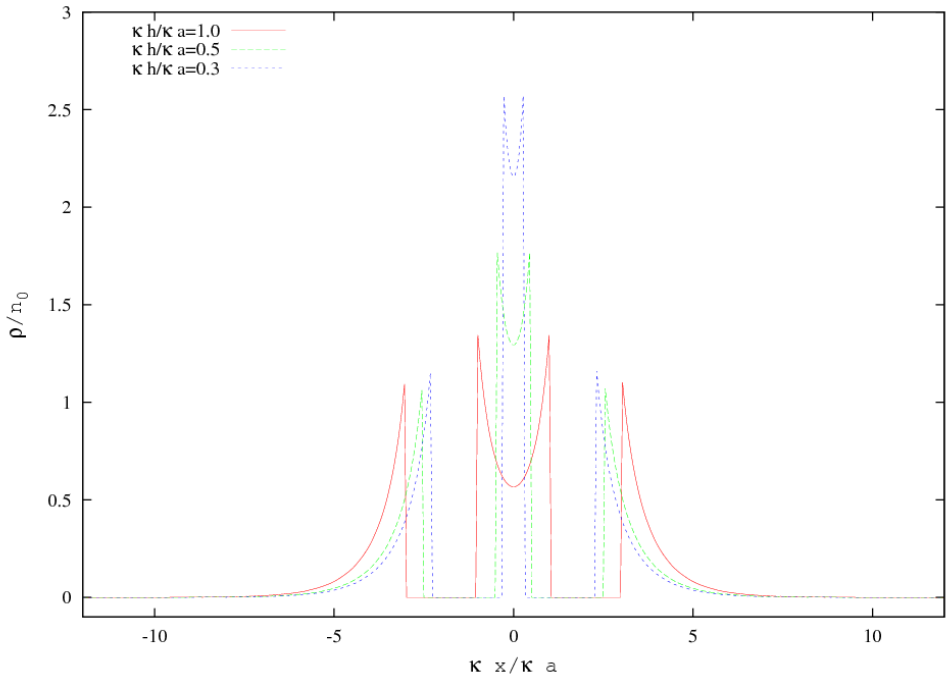

Figure 98: ρ/n_0 for interacting dielectric particles in a weak applied electric field

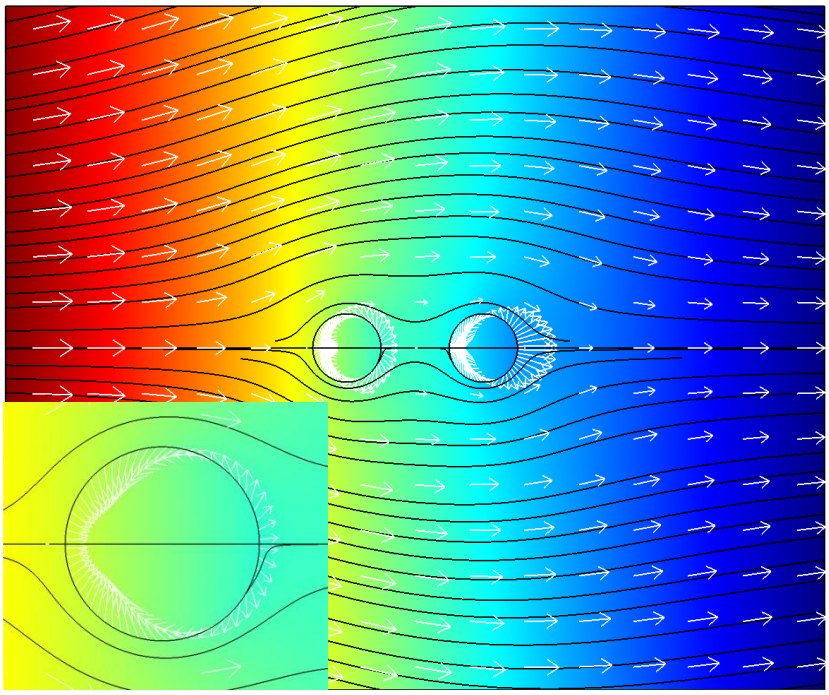

Figure 99: Interacting dielectric particles with; $\sigma_0/en_0a = -1.47$, $E_0/\kappa\psi_T = 10^0$, and $\kappa h/\kappa a = 1$

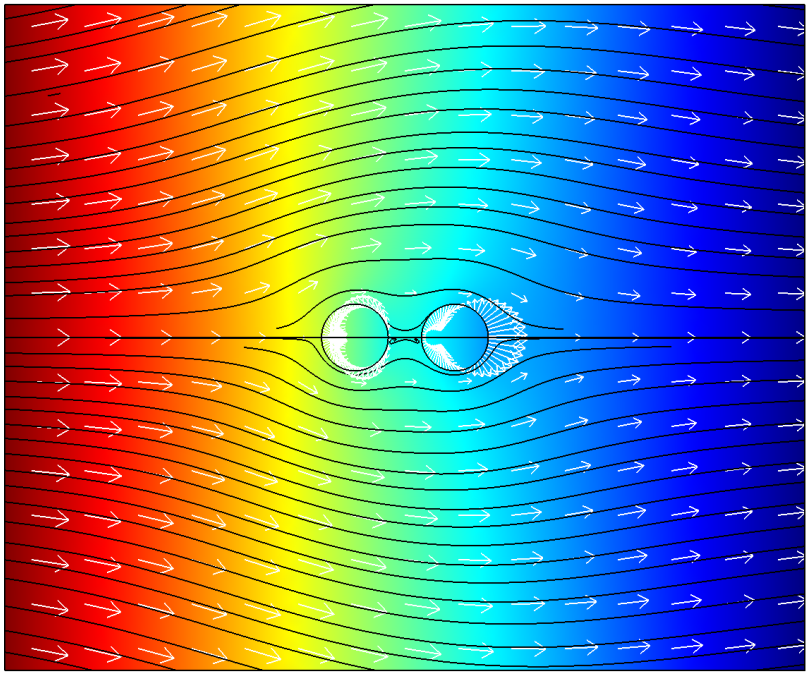

Figure 100: Interacting dielectric particles with; $\sigma_0/en_0a = -1.47$, $E_0/\kappa\psi_T = 10^0$, and $\kappa h/\kappa a = 0.5$

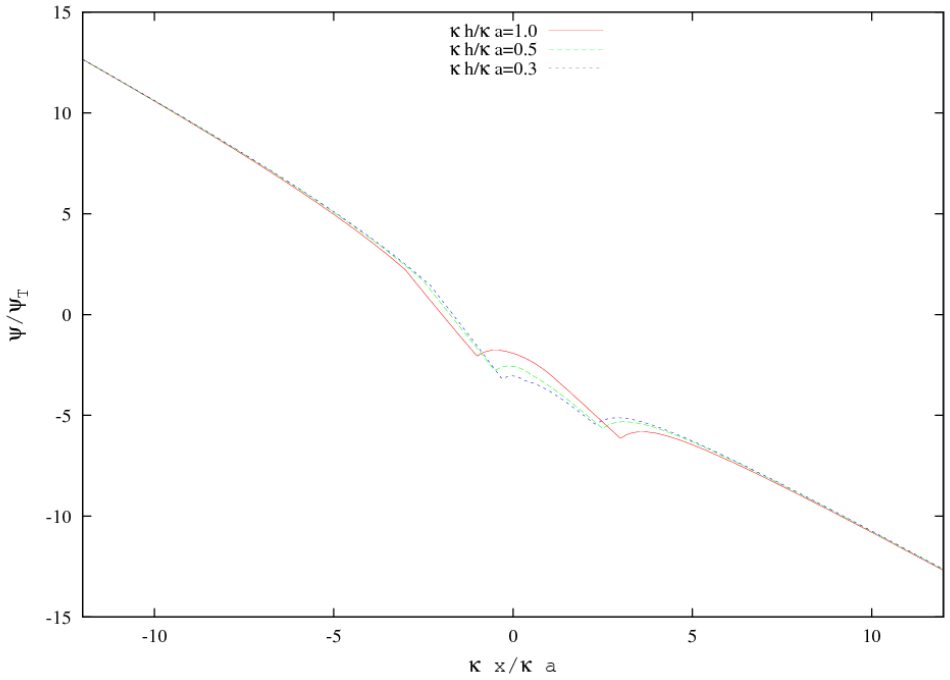

Figure 101: ψ/ψ_T for interacting dielectric particles in a strong applied electric field

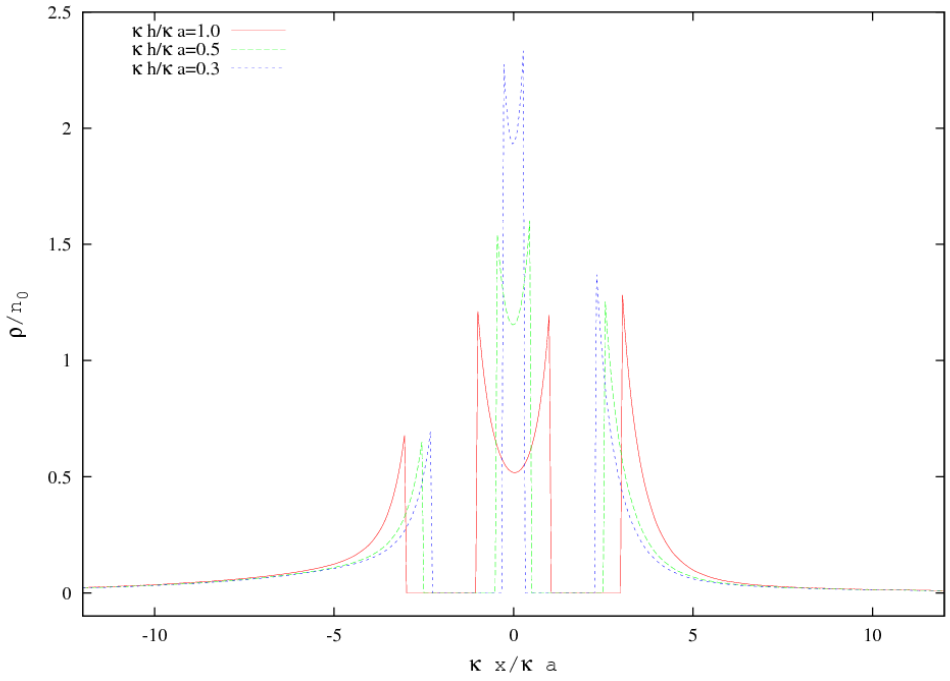

Figure 102: ρ/n_0 for interacting dielectric particles in a strong applied electric field

The distribution of the electric potential for interacting dielectric particles with the constant surface charge boundary condition in a weak applied electric field is similar to that of the constant surface potential boundary condition in that the maximum electric potential is at the mid-point between the particles. Thus, a linearized electrokinetic model like the small polarization model presented in Section 4 that included DLVO theory for particle-particle interaction would produce sufficient results if the applied electric field was weak. As with the constant surface potential boundary condition, the maximum electric potential between interacting particles is shifted in a strong applied electric field albeit the direction of the shift is in the opposite direction due to the relaxation of the weakly dielectric particle.

The electric displacement field in the latex particles is relaxed in a strong applied electric field as shown in Figure 101 and large electric potentials are induced due to a combination of the large applied electric field and the interaction with the other particle. It appears as though the interaction of the particles is dominant as the induced surface potential is much larger on the inside portion of the particles. The results of Figure 102 show that the EDL surrounding the composite of both particles is polarized in a strong applied electric field. That is, the free charge on the surface of particle two at the side opposite particle one is significantly higher than the free charge on the surface of particle one at the side opposite particle two. However, the distribution of the free charge between the particles is not shifted significantly by the strong applied electric field as it was with the constant surface potential boundary condition. Thus, the effect of the applied electric field will not be as strong and there should not be a significant change as

the separation decreases. This postulate is verified by plotting dimensionless force on particle one, shown in Figure 103. That is, the difference between the weak electric field ($E/\kappa\psi_T = 10^{-2}$) result and the strong electric field ($E/\kappa\psi_T = 10^{0}$) result is small at $\kappa h/\kappa a = 1$ and there is not much change in the difference as the separation decreases.

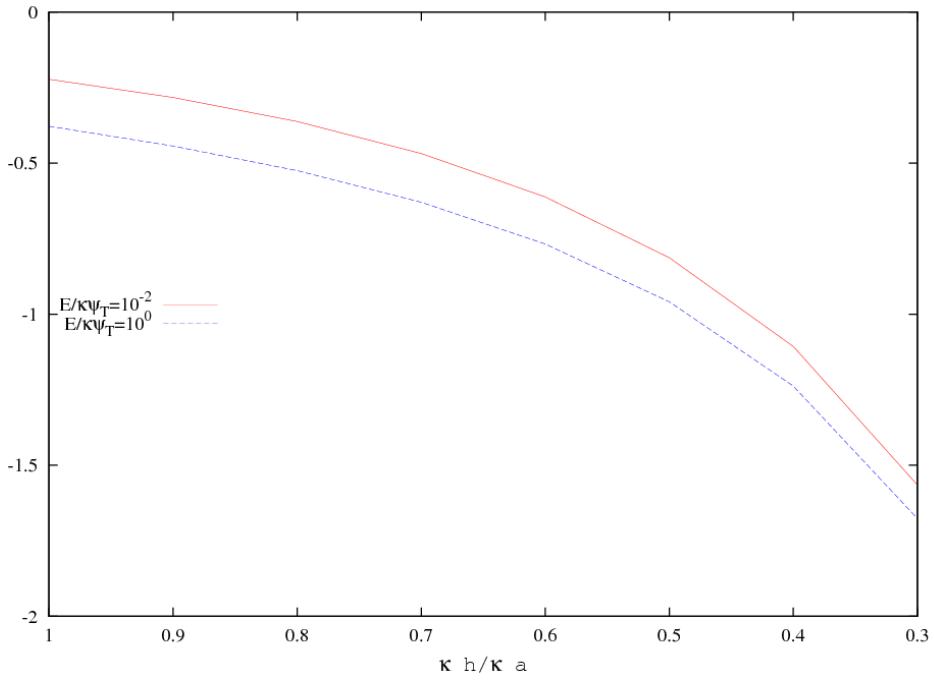

Figure 103: Dimensionless force on particle one for interacting dielectric particles with constant surface charge

Next, the results for metallic particles using a constant surface charge boundary condition are presented. The surface plots for a weak applied electric field are presented in Figure 104 and Figure 105 followed by the section plots of dimensionless electric potential and dimensionless free charge in Figure 106 and Figure 107. Some observations are made following the presentation of the weak applied electric field results. Then, the results for a strong applied electric field are presented in Figure 108, Figure 109, Figure 110, and Figure 111 for comparison.

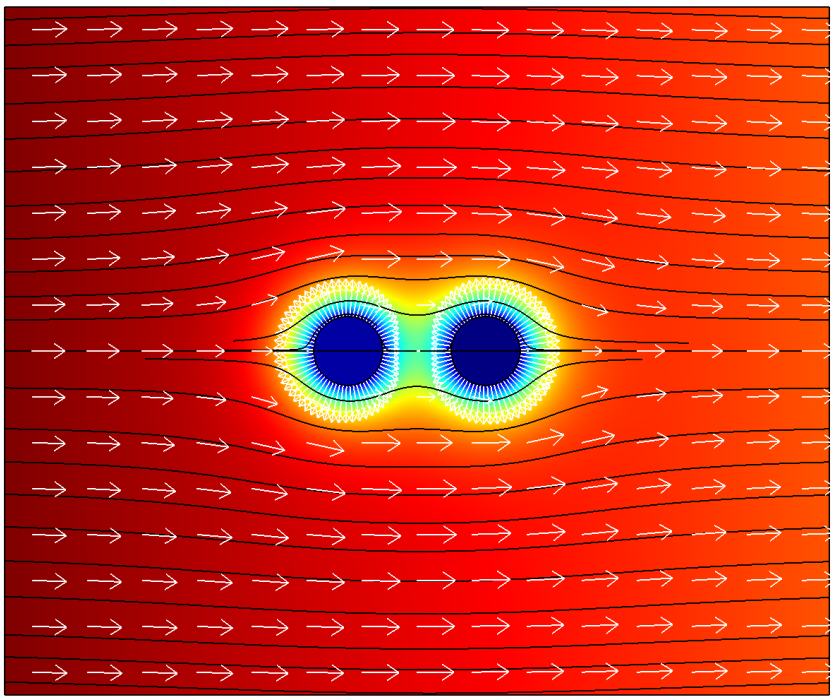

Figure 104: Interacting metallic particles with; $\sigma_0/en_0a = -1.47$, $E_0/\kappa\psi_T = 10^{-2}$, and $\kappa h/\kappa a = 1$

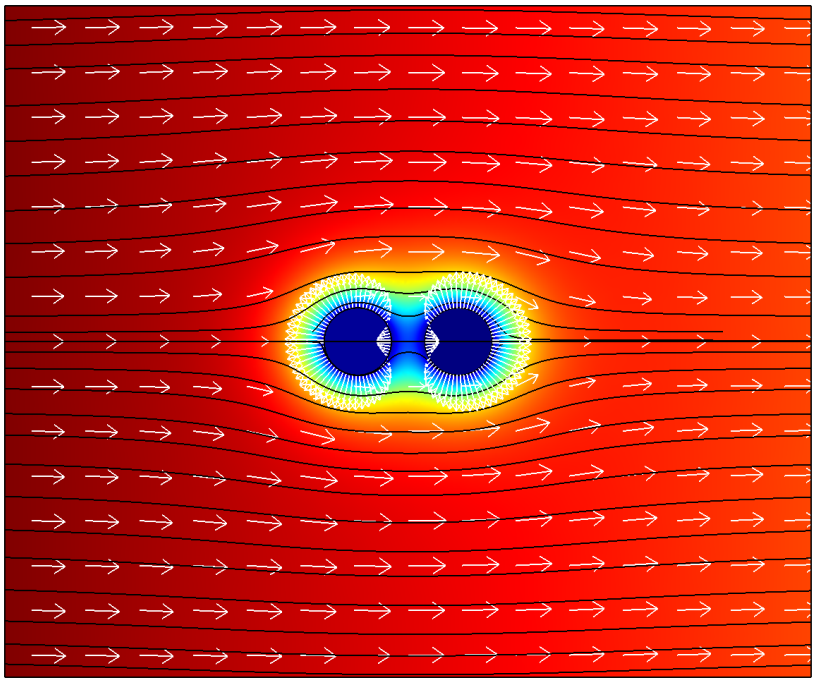

Figure 105: Interacting metallic particles with; $\sigma_0/en_0a = -1.47$, $E_0/\kappa\psi_T = 10^{-2}$, and $\kappa h/\kappa a = 0.5$

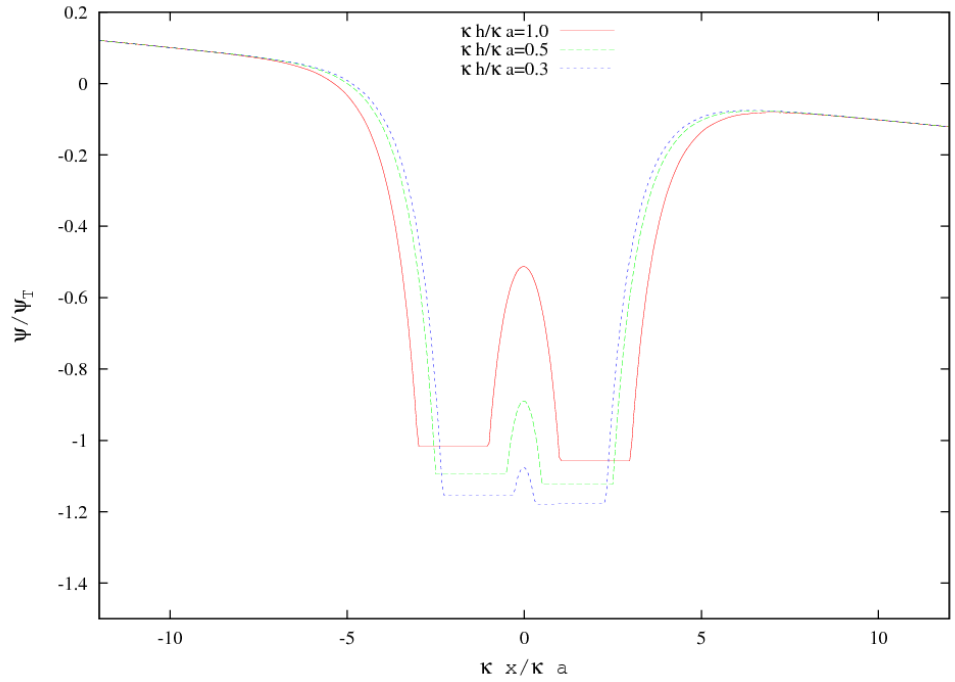

Figure 106: ψ/ψ_T for interacting metallic particles in a weak applied electric field

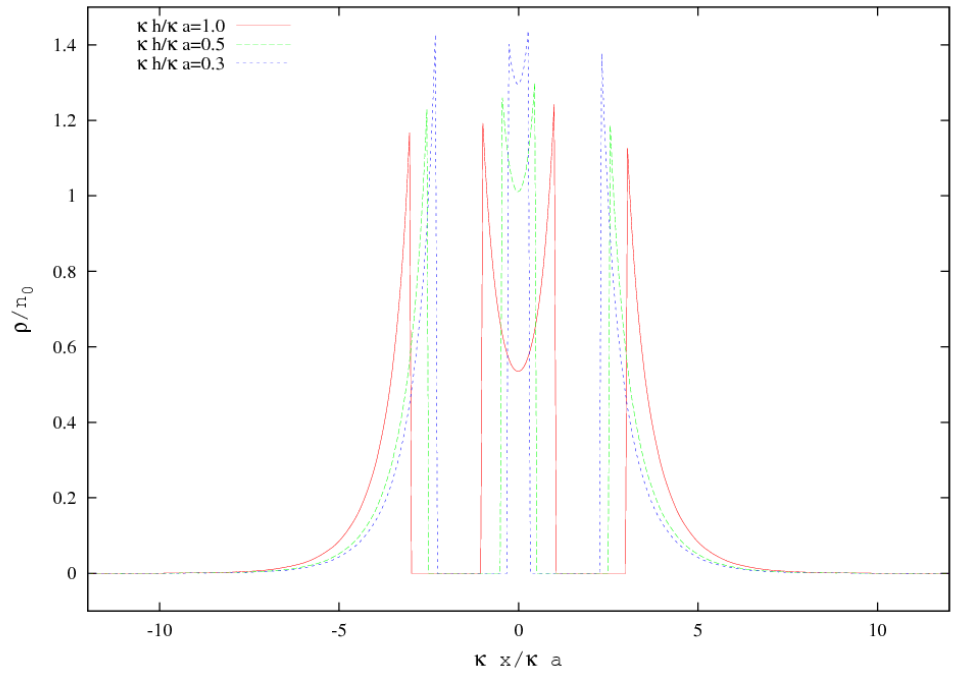

Figure 107: ρ/n_0 for interacting metallic particles in a weak applied electric field

The results of Figure 106 show that surface potential is induced by both the applied electric field and particle-particle interaction. Particle-particle interaction in the absence of an applied electric field would increase magnitude of the surface potential equally (as long as the particles are of the same charge). Thus, the fact that the particles have different electric surface potentials in Figure 106 is a result of the applied electric field. The difference in the potentials is relatively small, but noticeable, for the weak applied electric field results of Figure 106 and Figure 107. The difference should be even more significant in a strong applied electric field. The fact that interacting particles have different surface potentials in an applied electric field leads to the high conductivity of assembled particles. If the constant surface potential boundary condition is used this effect is not revealed. Therefore, as the results of the previous sections have also demonstrated, the constant surface potential boundary condition is not valid for particles in strong applied electric fields. Further, the results of the present section have shown that the constant surface potential is not valid when particle concentration is high.

Even though the surface potentials are not the same when an electric field is applied, the potential at the mid-point for a metallic particle in a weak applied electric field is essentially the same as for no applied electric field. Therefore, a linearized electrokinetic model with DLVO theory included might produce sufficient results when the electric field is weak. However, the following results demonstrate the effect of a strong applied electric field. An effect which is not captured by linearized electrokinetic models particularly for metallic particles.

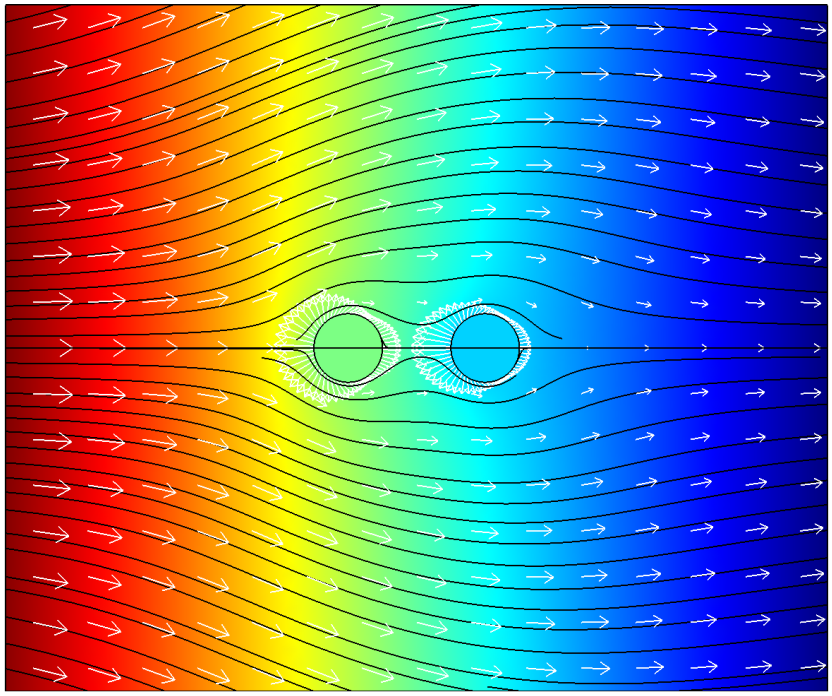

Figure 108: Interacting metallic particles with; $\sigma_0/en_0a = -1.47$, $E_0/\kappa\psi_T = 10^0$, and $\kappa h/\kappa a = 1$

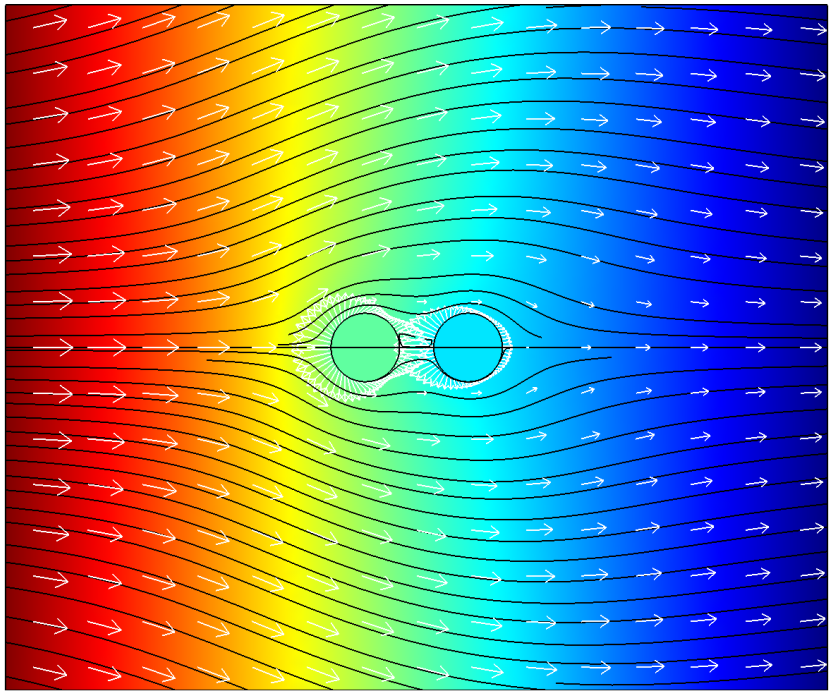

Figure 109: Interacting metallic particles with; $\sigma_0/en_0a = -1.47$, $E_0/\kappa\psi_T = 10^0$, and $\kappa h/\kappa a = 0.5$

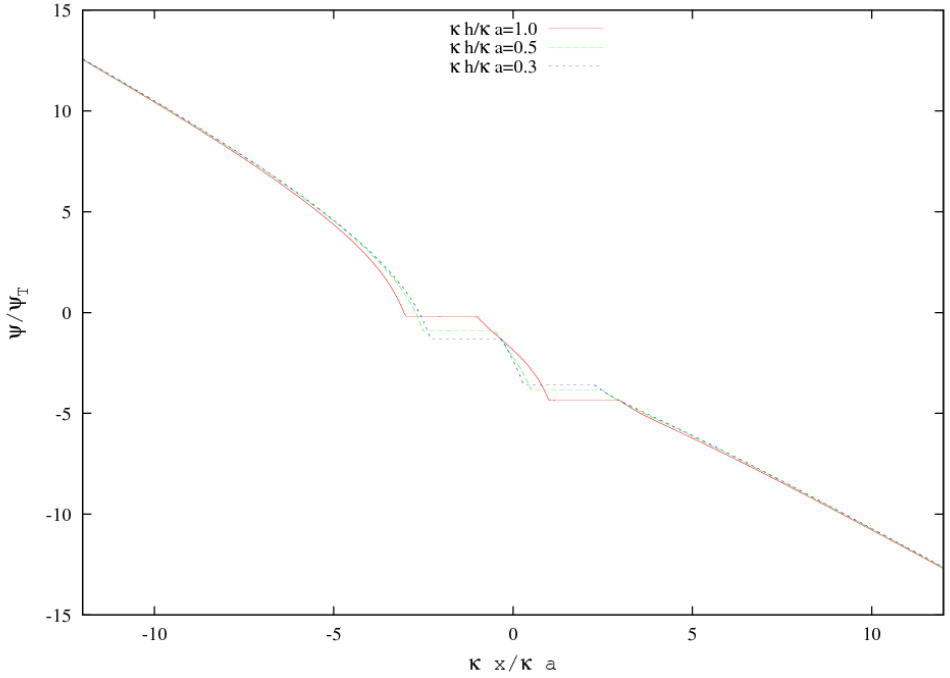

Figure 110: ψ/ψ_T for interacting metallic particles in a strong applied electric field

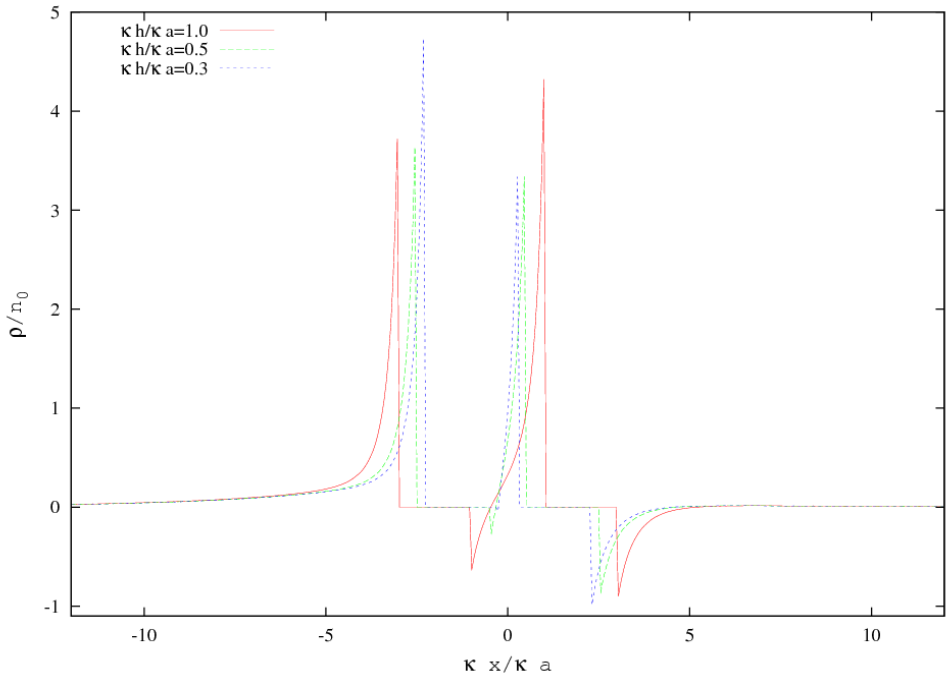

Figure 111: ρ/n_0 for interacting metallic particles in a strong applied electric field

The results of Figure 110 show that the induced surface potential due to the applied electric field is increased as the strength of the applied electric field increases. That is, the difference in the surface potentials is larger. Figure 112 shows that the surface potential is nearly zero for particle one and is about four for particle two. Thus, the induced electric potential is on the order of the equilibrium potential when strong electric fields are applied. The effect of the applied electric field on interacting metallic particles may be separated from the effect of particle interaction by considering that in the absence of an applied electric field interaction would increase the induced surface potential equally. So, the results of Figure 112 also demonstrate the competing effects of particle-particle interaction and applied electric field strength. When interaction is weak the difference in the surface potentials is large for particle interacting in a strong applied electric field, but the difference in the surface potentials decreases as the particle move closer together.

The results of Figure 113 show that even though these two nonlinear phenomena are competing the applied electric field is dominant as the difference in the mid-plane potential is about the same for all dimensionless particle separations. However, it is clear from these results that the mid-point potential is not a complete indication of these two nonlinear effects. Inspection of the dimensionless free charge surrounding interacting metallic particles, shown in Figure 111, reveals that the EDL surrounding the interacting metallic particles is polarized by a strong applied electric field. This polarization is not completely captured by the electric potential at the mid-plane and it leads to perhaps the most interesting result for interacting metallic particles.

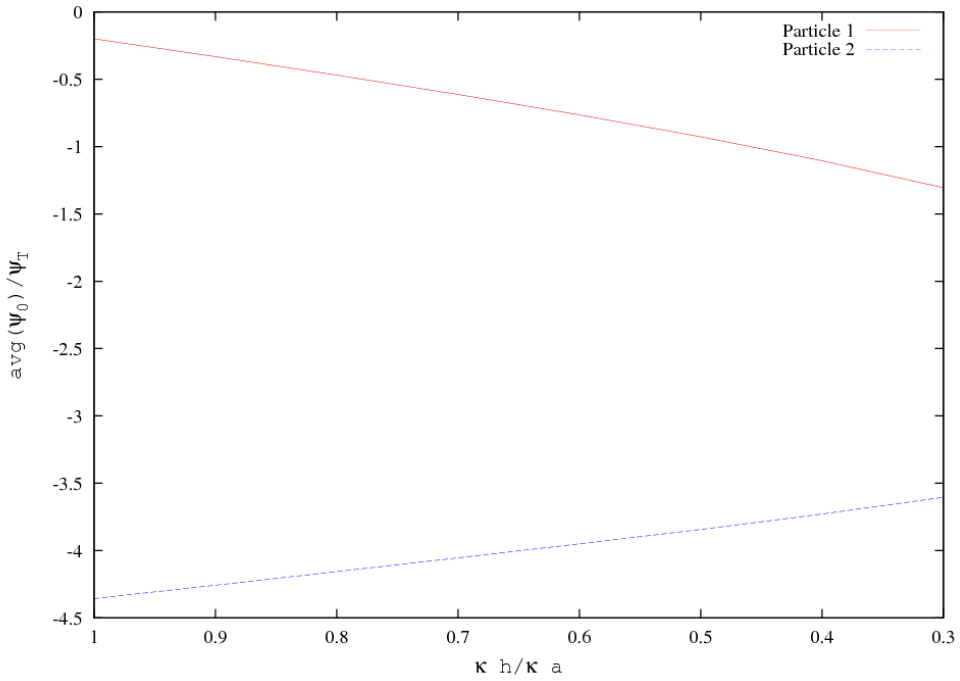

Figure 112: Average dimensionless surface potential for interacting metallic particles in a strong applied electric field

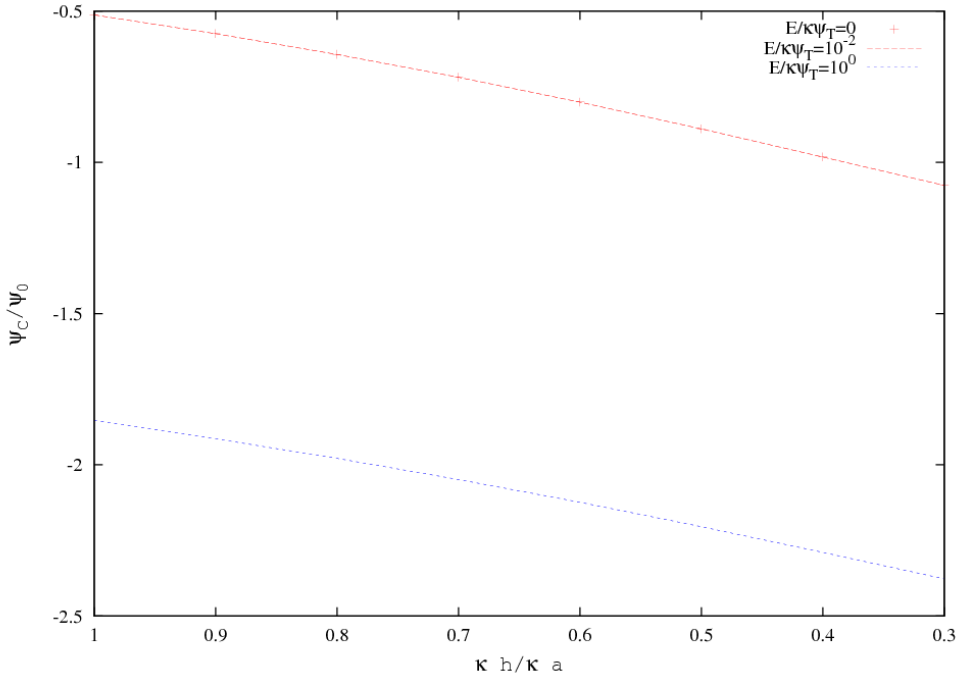

Figure 113: Dimensionless mid-point potential for interacting metallic particles with constant surface charge

The effect of a strong applied electric field on interacting metallic particles, which is at least in part a result of polarization of the EDL, is revealed by the distribution of the boundary tractions shown in Figure 108 and Figure 109. When compared with the boundary tractions in a weak applied electric field, it is clear that they are drastically different. The difference is quantified by plotting the resultant force on particle one for a weak applied electric field and a strong applied electric field which is shown in Figure 114. Figure 114 shows that as the strength of the applied electric field is increased the resultant force changes direction. This is a result of the induced potential driving the surface potential to nearly zero for particle one and the polarization of the EDL.

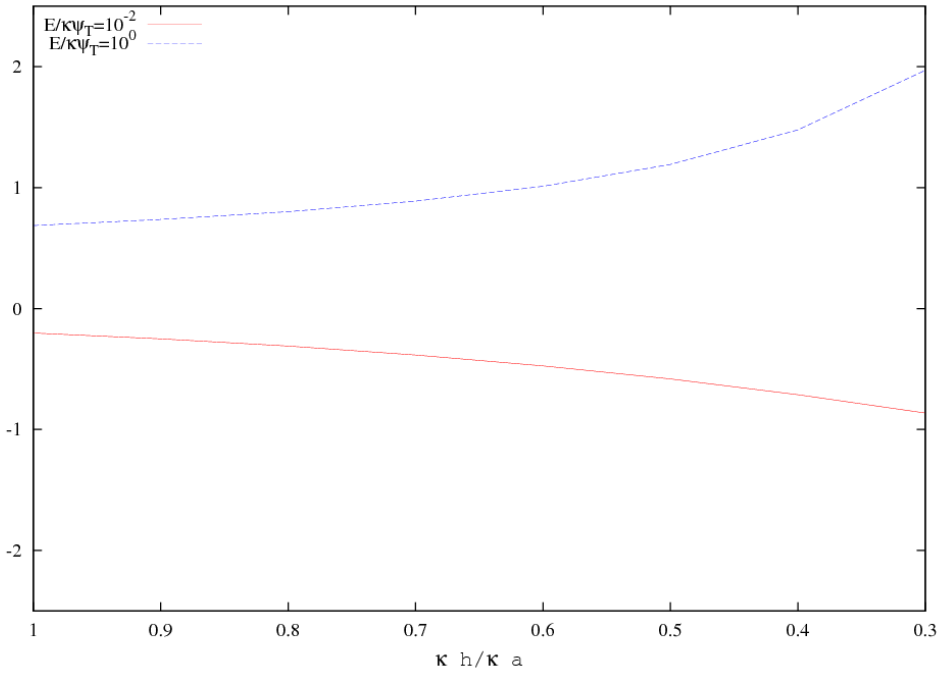

Figure 114: Dimensionless force on particle one for interacting metallic particles with constant surface charge

To complete the analysis of the constant surface charge boundary condition we present results for a dielectric particle interacting with a metallic particle. On the outset

it can be said that the DLVO theory would not be valid for such a situation as the different particle permittivities lead to a shift in the maximum potential between the interacting particles which violates the symmetry boundary condition. However, it should be noted that approximate solutions using the linearized Poisson-Boltzmann equation have been developed for interacting dissimilar particles which do not use the symmetry boundary condition [9, 40]. However, the method relies on superposition so it is not valid for nonlinear electrokinetics.

The surface plots for interacting dissimilar particles in a weak applied electric field are presented in Figure 115 and Figure 116 followed by the section plots of dimensionless electric potential and dimensionless free charge in Figure 117 and Figure 118. Then, in Figure 119, Figure 120, Figure 121, and Figure 122, the results for a strong applied electric field are presented for comparison. Then, to quantify the effect of the interaction and the applied electric field, the dimensionless mid-plane potential is plotted as a function of particle separation for a weak applied electric field and a strong applied electric field. Finally, the dimensionless force on each particle is plotted as a function of particle separation for a weak applied electric field and a strong applied electric field.

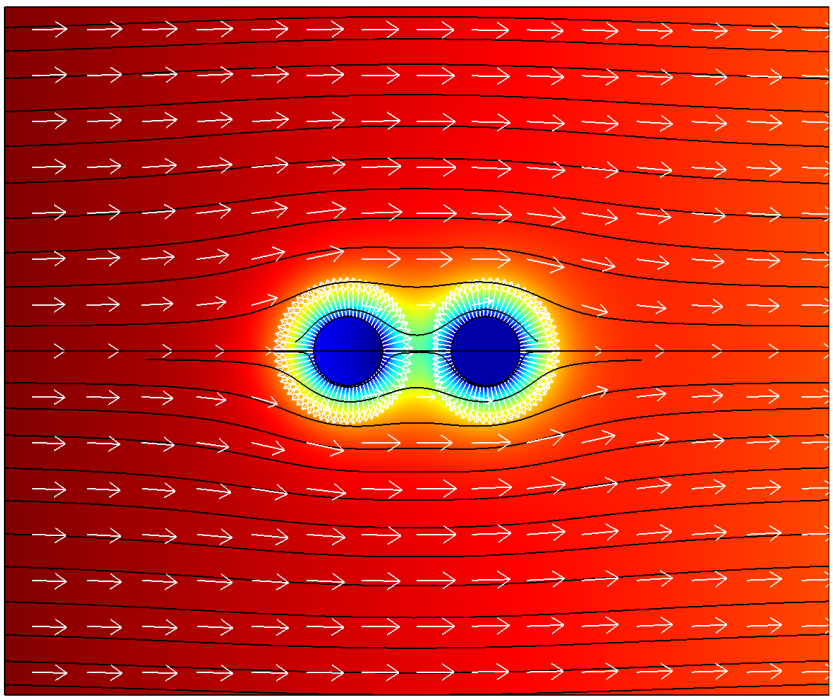

Figure 115: Particles with; different permittivities, $\sigma_0/en_0a = -1.47$, $E_0/\kappa\psi_T = 10^{-2}$, and $\kappa h/\kappa a = 1$

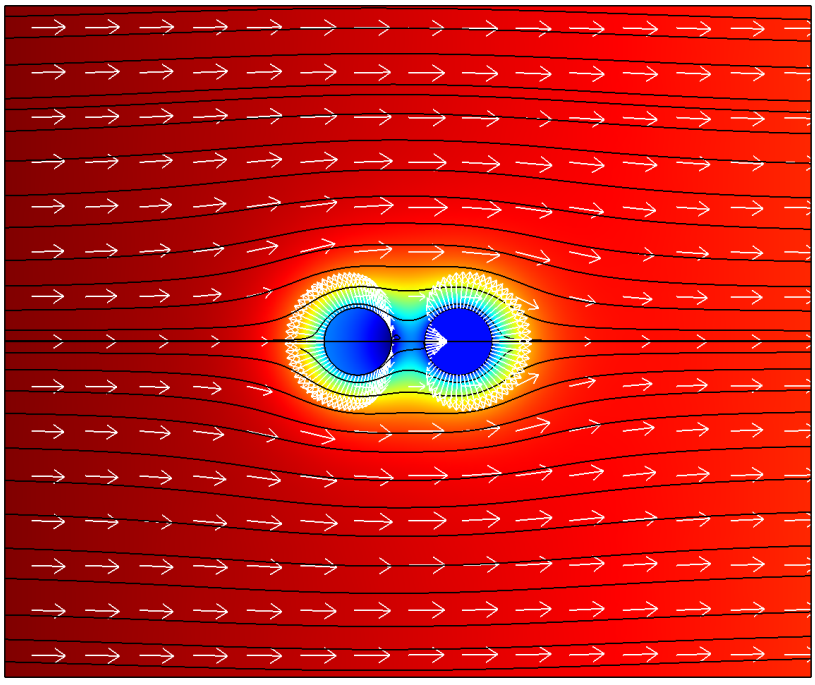

Figure 116: Particles with; different permittivities, $\sigma_0/en_0a = -1.47$, $E_0/\kappa\psi_T = 10^{-2}$, and $\kappa h/\kappa a = 0.5$

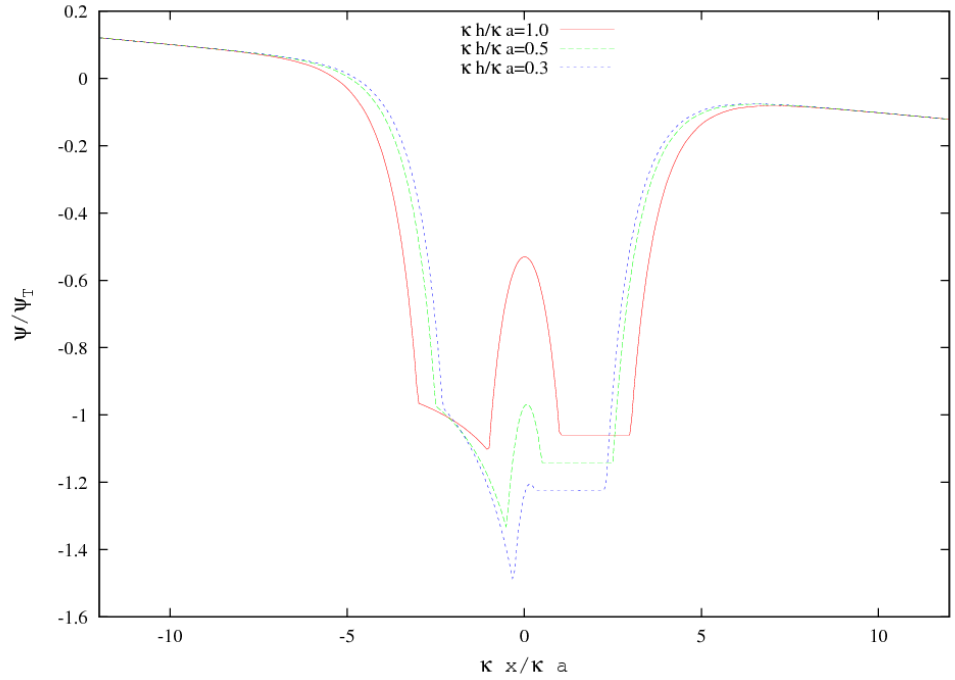

Figure 117: ψ/ψ_T for interacting particles with different permittivities in a weak applied electric field

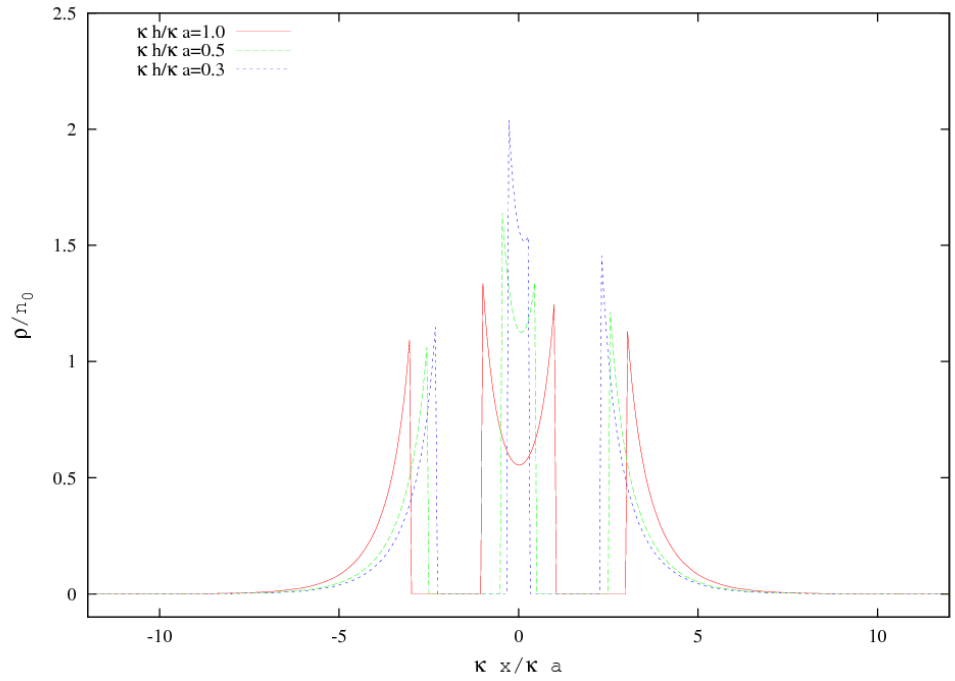

Figure 118: ρ/n_0 for interacting particles with different permittivities in a weak applied electric field

A comparison of the results for interacting dissimilar particles presented in Figure 115, Figure 116, Figure 117, and Figure 118 for a weak applied electric field with those from the constant surface potential and constant surface charge-dielectric particles and constant surface charge-metallic particles reveals some differences which seem to be primarily associated with a shift in the mid-plane potential and free charge. This shift is not associated with the applied electric field (because the applied electric field is weak); rather it is because the particles have different permittivities. Therefore, it may be difficult to separate the effects of particle-particle interaction from the effects of the applied electric field as they have similar effects on the mid-plane potential and free charge.

The results for a strong applied electric field are now presented and comparisons are made with the weak applied electric field results. The surface plots are presented in Figure 119 and Figure 120 and the section plots of dimensionless electric potential and dimensionless free charge are presented in Figure 121 and Figure 122. In some cases a detail of the surface tractions is included in the surface plot for clarity. The surface tractions on the dielectric particle are particularly difficult to interpret as the strong applied electric field relaxes the weakly dielectric particle and large differences in the surface potential exist.

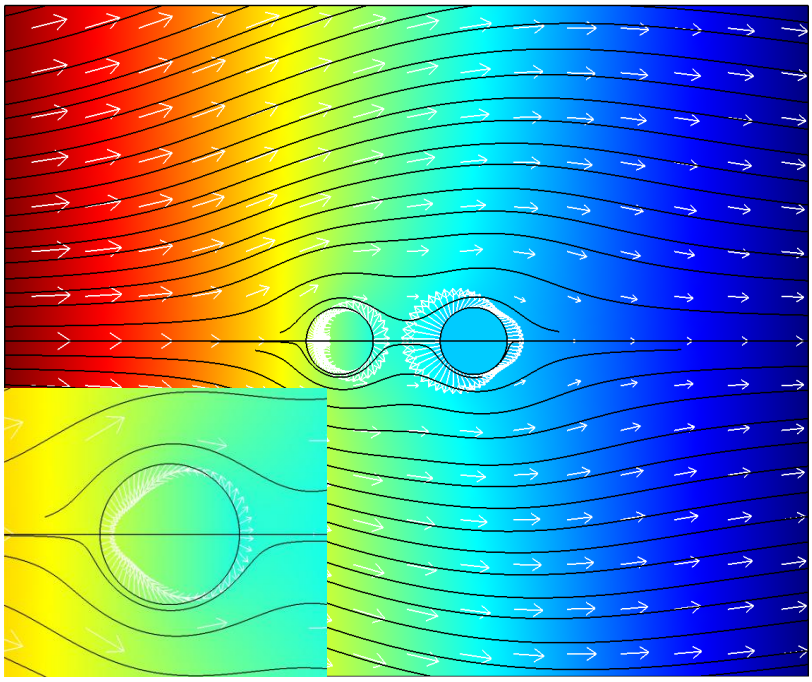

Figure 119: Particles with; different permittivities, $\sigma_0/en_0a = -1.47$, $E_0/\kappa\psi_T = 10^0$, and $\kappa h/\kappa a = 1$

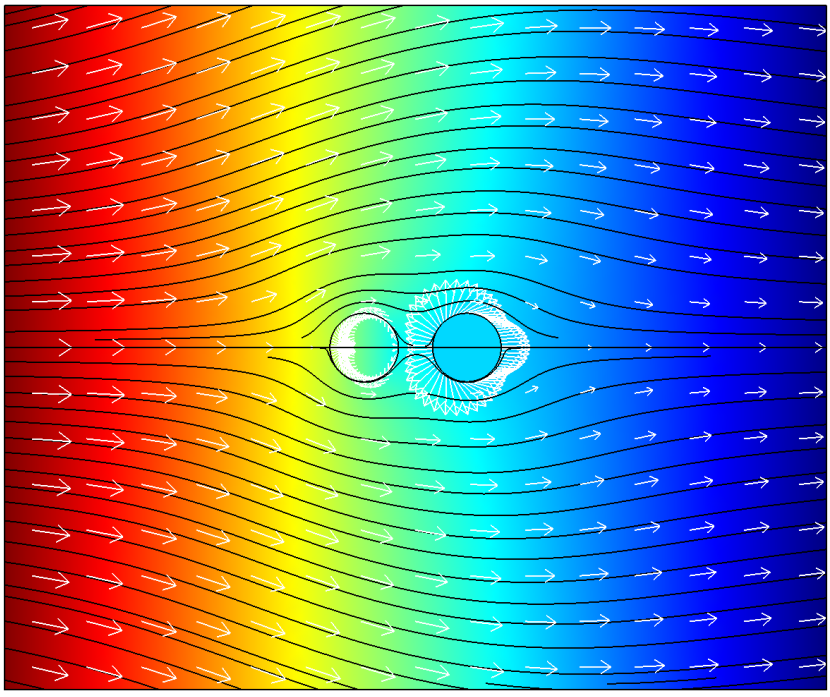

Figure 120: Particles with; different permittivities, $\sigma_0/en_0a = -1.47$, $E_0/\kappa\psi_T = 10^0$, and $\kappa h/\kappa a = 0.5$

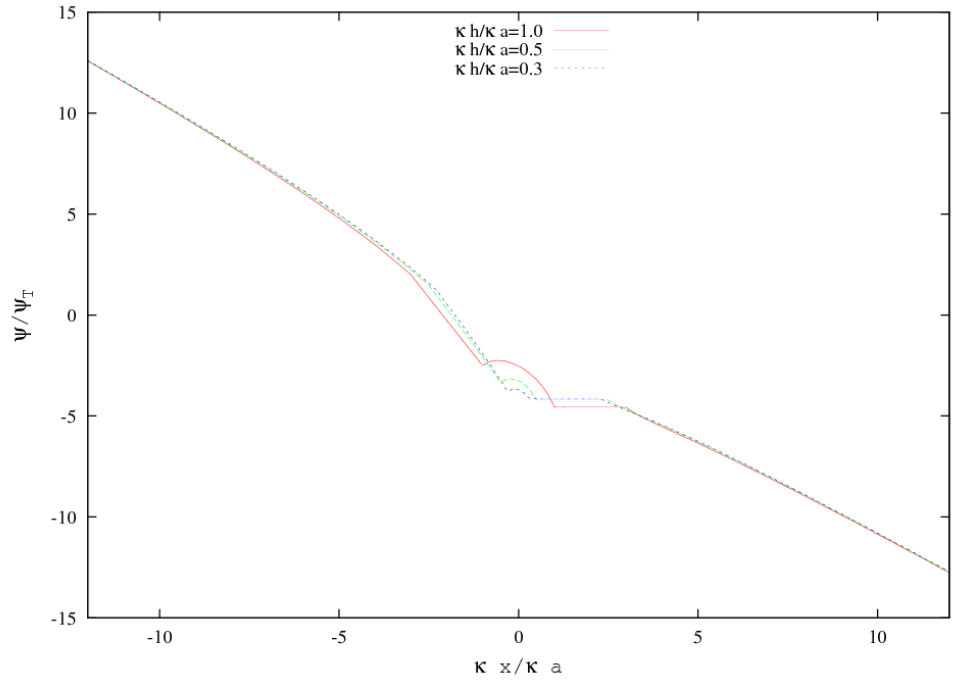

Figure 121: ψ/ψ_T for interacting particle with different permittivities in a strong applied electric field

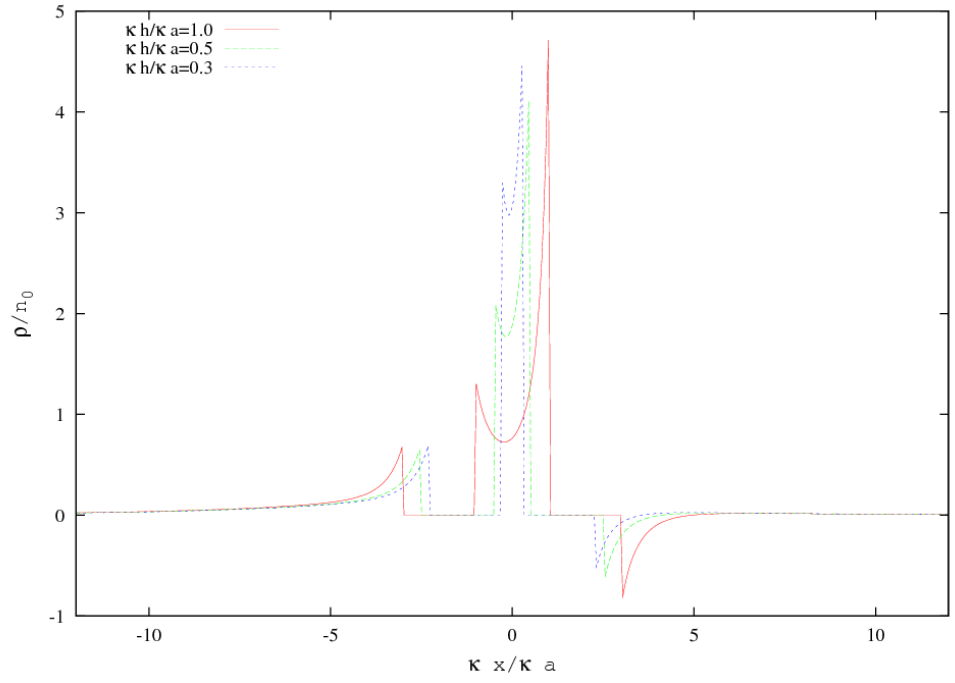

Figure 122: ρ/n_0 for interacting particles with different permittivities in a strong applied electric field

In an attempt to separate the effects of the particle-particle interaction and applied electric field strength on the distribution of electric potential between the particles (which both shift the distribution) we compare the results of Figure 117 with the results of Figure 121. The results of Figure 117 show that interaction in a weak applied field (shift due to interaction) shifts the maximum potential to the right. Whereas, the results of Figure 121 show that interaction in a strong applied electric field shifts the maximum potential to the left. The same trend is observed in the shift of the free charge between the particles which is revealed by comparing Figure 118 and Figure 122. Thus, even though particle-particle interaction and the applied electric field both shift the distributions of electric potential and free charge between the two particles, the directions of the shift in this case are opposite. The results of Figure 123 show that the difference in the mid-plane electric potential of the weak applied electric field and strong applied electric field remains essentially the same as the particle separation decreases. The results of Figure 124 and Figure 125 reveal that the interaction force is repulsive and that it increases with electric field strength and decreasing separation.

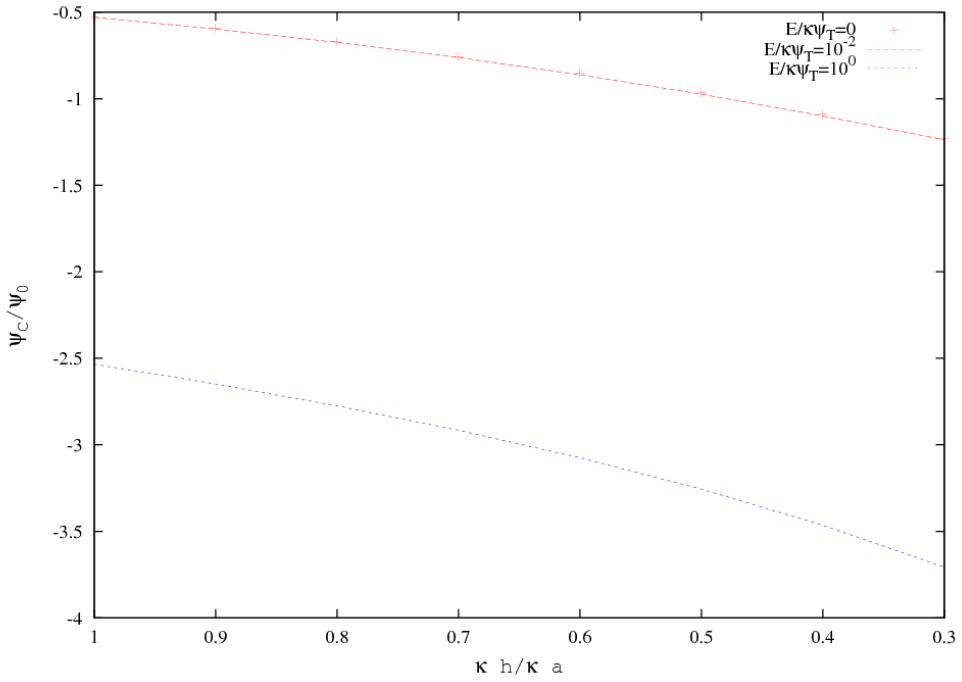

Figure 123: Scaled mid-point potential for interacting particles with different permittivities

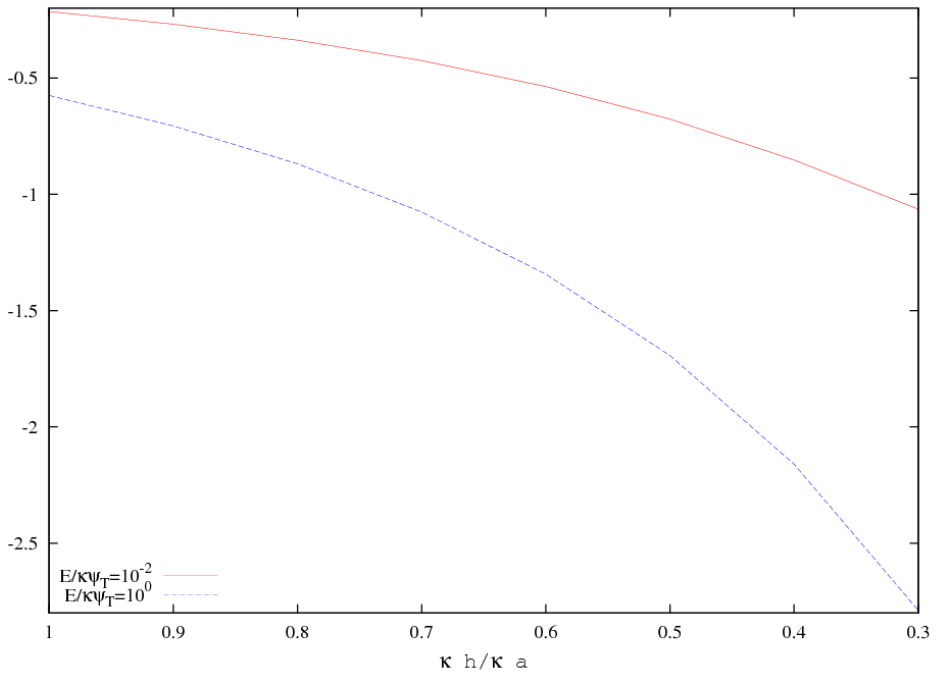

Figure 124: Dimensionless force on the dielectric particle as a function of dimensionless separation

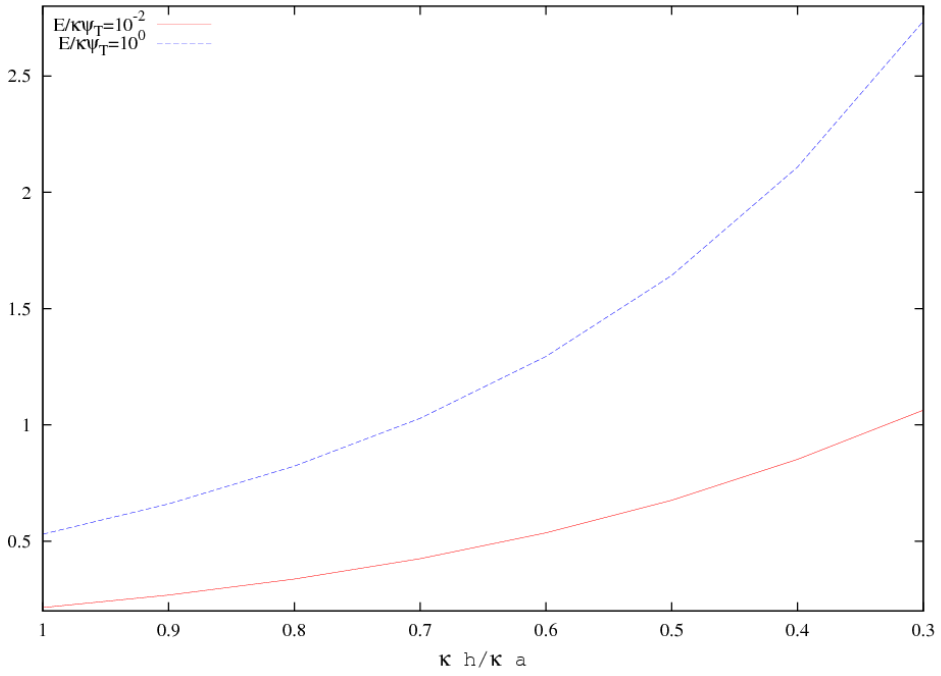

Figure 125: Dimensionless force on the metallic particle as a function of particle separation

6.2.3 Stern layer surface boundary condition

The objective of this section is to investigate the effect of the Stern layer boundary condition when particles are interacting and large electric fields are applied. In the following the Stern layer boundary condition are presented and compared with the results of Section 6.2.2 for the constant surface charge boundary condition. Results are presented for interacting dielectric particles and interacting metallic particles in weak and strong applied electric fields using the Stern layer boundary condition. Interacting dissimilar particles are not considered in this section. The surface plots for interacting dielectric particles in a weak applied electric field are presented in Figure 126 and Figure 127. And, the section plots of dimensionless electric potential and dimensionless free charge are presented in Figure 128 and Figure 129.

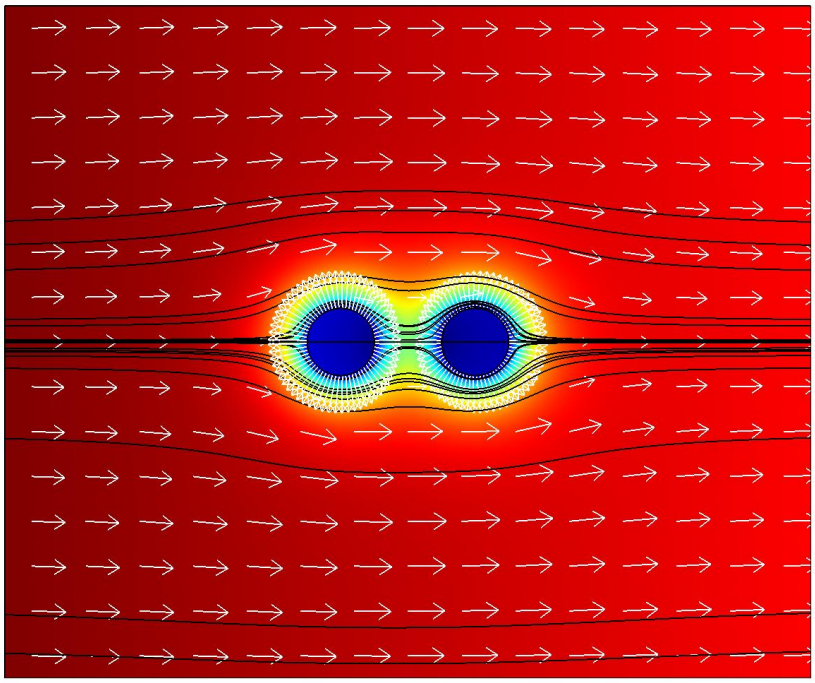

Figure 126: Dielectric particles with; GDSL model, $\sigma_0/en_0a = -3.28$, $E_0/\kappa\psi_T = 10^{-2}$, and $\kappa h/\kappa a = 1$

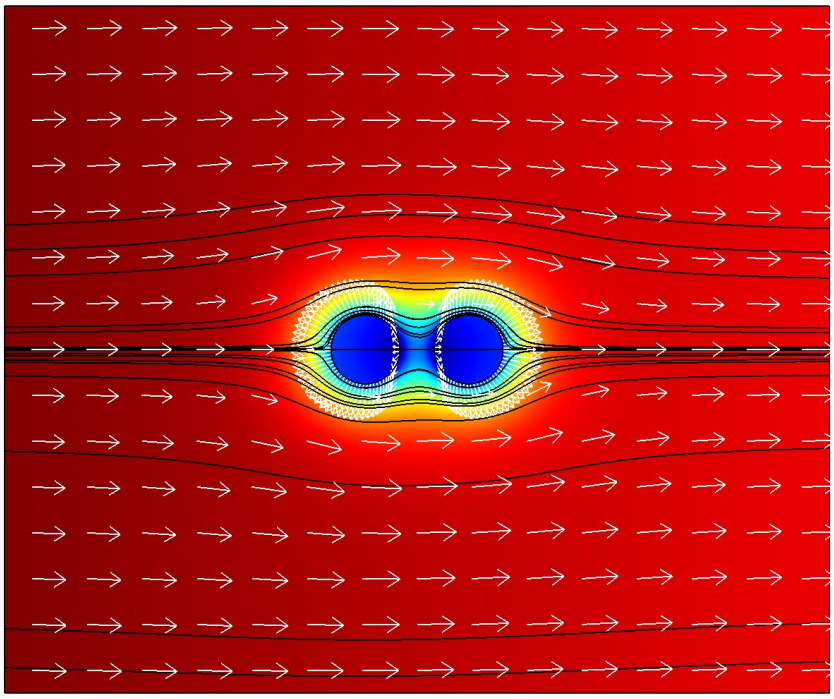

Figure 127: Dielectric particles with; GDSL model, $\sigma_0/en_0a = -3.28$, $E_0/\kappa\psi_T = 10^{-2}$, and $\kappa h/\kappa a = 0.5$

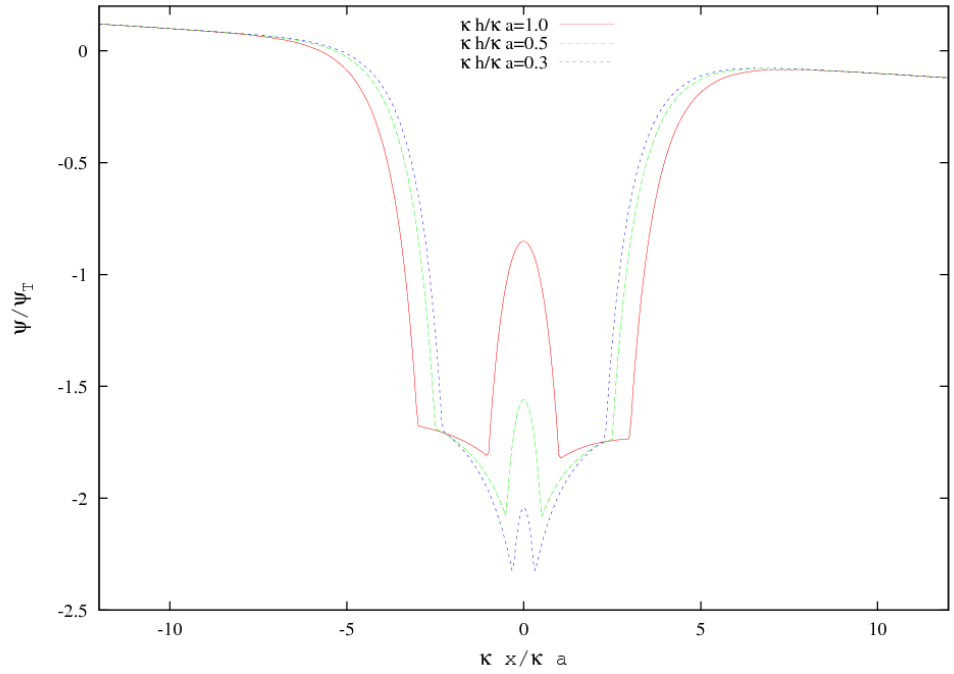

Figure 128: ψ/ψ_T for interacting dielectric particles with GDSL model in a weak applied electric field

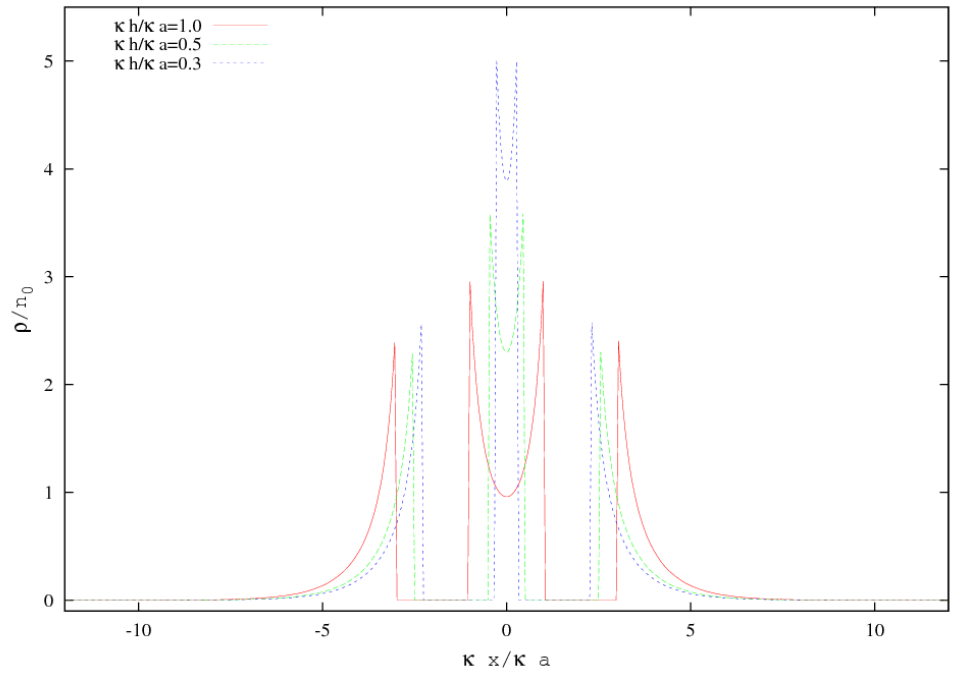

Figure 129: ρ/n_0 for interacting dielectric particles with GDSL model in a weak applied electric field

The distribution of the boundary surface tractions shown in Figure 126 and Figure 127 are slightly different than that for the constant surface charge boundary condition (Figure 95 and Figure 96), however these surface plots do not reveal the extent to which the Stern layer results differ from the constant surface boundary condition results for weak applied electric fields. The difference is revealed by comparing the dimensionless electric potential and dimensionless free charge for the constant charge (Figure 97 and Figure 98) and the GDSL model (Figure 128 and Figure 129). The following observations are made: (1) The magnitude of the electric potential and free charge between the particles is much larger for the GDSL model. And, (2) the displacement electric field in the dielectric particle is more relaxed by the particle-particle interaction when the constant surface charge boundary condition is used.

Next, the results for interacting dielectric particles in a strong applied electric field with the Stern layer boundary condition are presented and comparisons are made with the results for a weak applied electric field and the constant surface charge boundary condition results are made. The surface plots for a strong applied electric field are presented in Figure 130 and Figure 131. And, the section plots of dimensionless electric potential and dimensionless free charge are presented in Figure 132 and Figure 133.

The fluid velocity streamlines shown in Figure 130 and Figure 131 are similar to the constant surface charge results of Figure 99 and Figure 100. However, the boundary traction vectors on the particles have a different distribution. Therefore, the resultant forces on the particles are expected to be different when the Stern layer boundary condition is used.

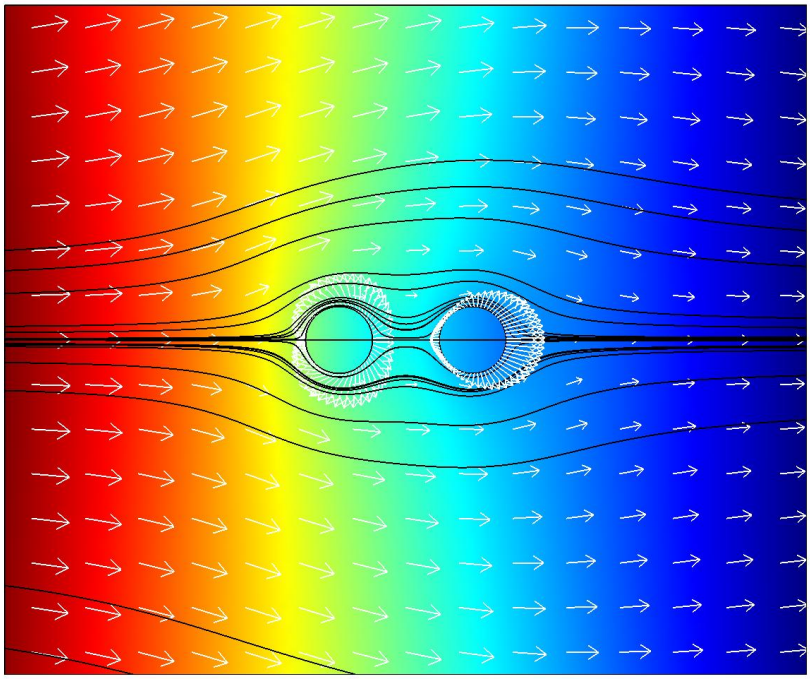

Figure 130: Dielectric particles with; GDSL model, $\sigma_0/en_0a = -3.28$, $E_0/\kappa\psi_T = 10^0$, and $\kappa h/\kappa a = 1$

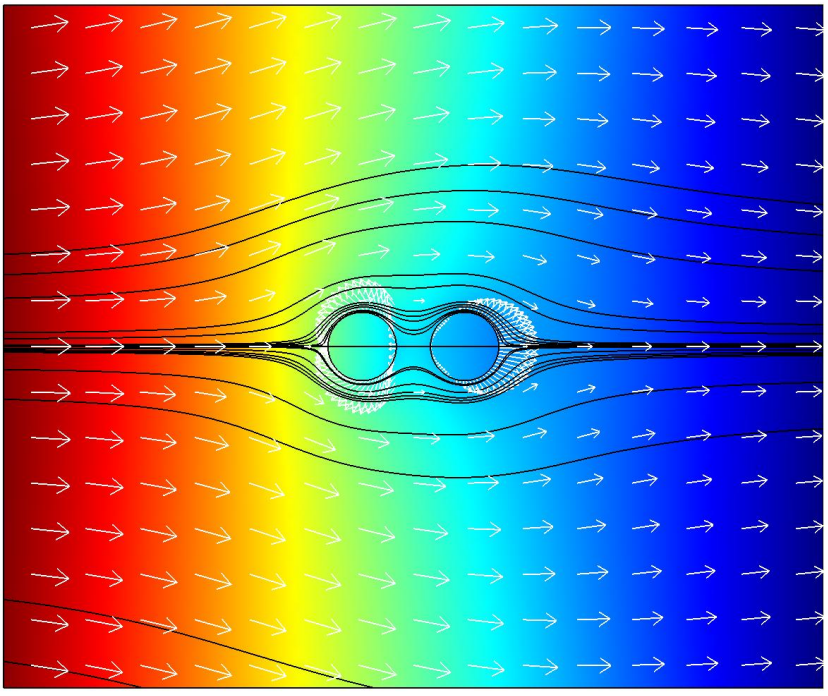

Figure 131: Dielectric particles with; GDSL model, $\sigma_0/en_0a = -3.28$, $E_0/\kappa\psi_T = 10^0$, and $\kappa h/\kappa a = 0.5$

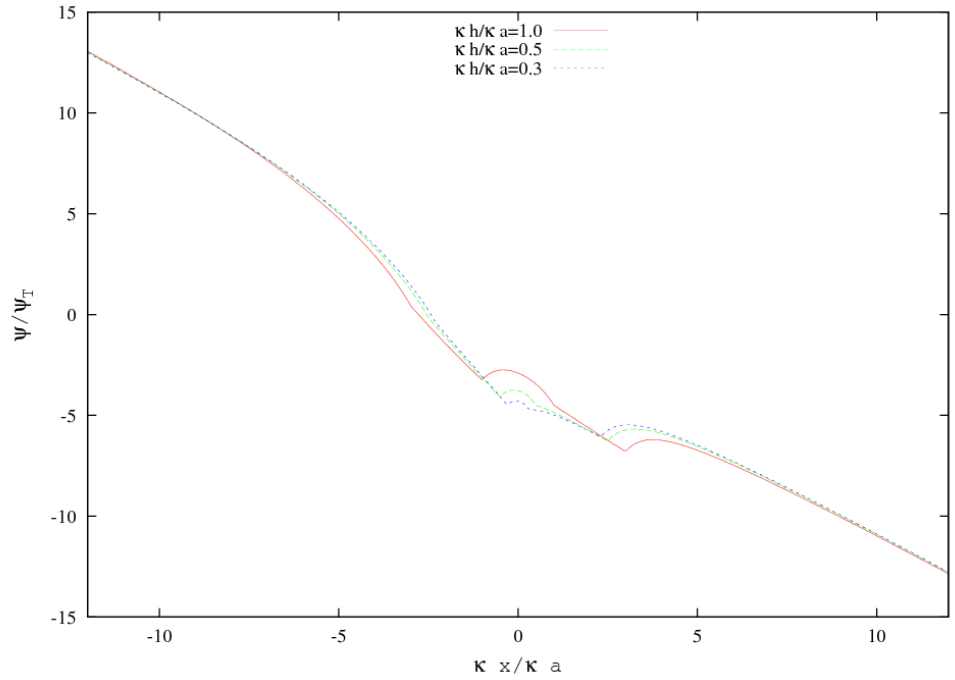

Figure 132: ψ/ψ_T for interacting dielectric particles with GDSL model in a strong applied electric field

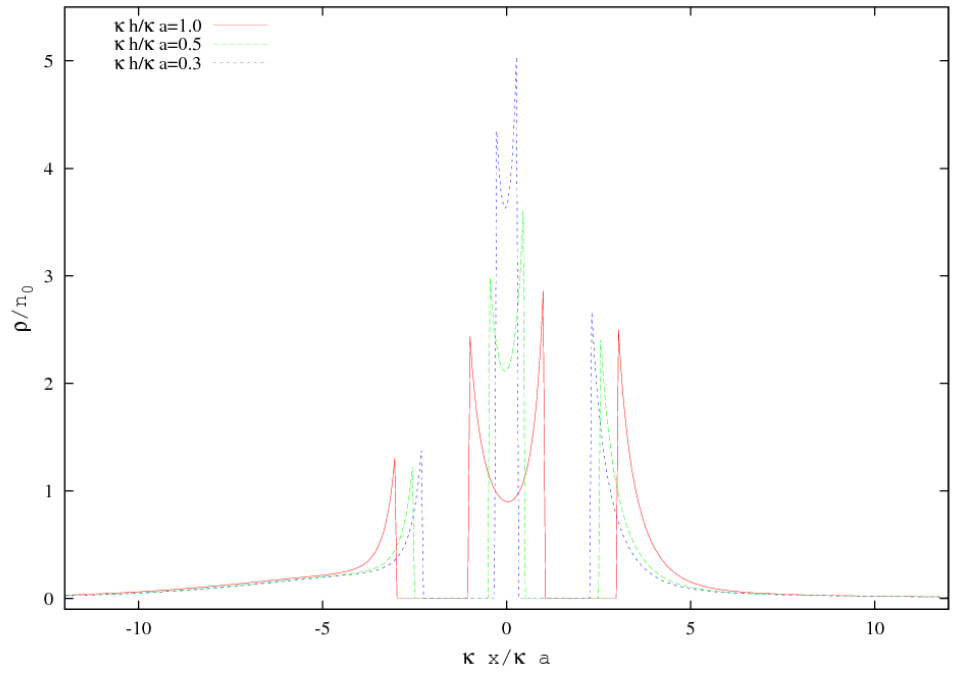

Figure 133: ρ/n_0 for interacting dielectric particles with GDSL model in a strong applied electric field

The following observations are made when comparing the section plots of dimensionless electric potential and dimensionless free charge of Figure 132 and Figure 133 (strong field – Stern layer) with those of Figure 101 and Figure 102 (strong field - constant charge): (1) The induced electric potential on particle two is considerably larger for the Stern layer boundary condition. (2) The free charge near the surface in between the particles is about twice as high for the Stern layer boundary condition. And, (3) the distribution of the free charge between the particles is more affected by the applied electric field for the Stern layer boundary condition.

The observations described above only serve to explain the change in the forces on the particles. The net dimensionless force on particle one is plotted in Figure 134 and compared with the result for the constant surface charge boundary condition shown in Figure 103. The following observations are made when comparing the dimensionless force on particle one of Figure 134 with that of Figure 103: (1) the force is larger for the Stern layer boundary condition regardless of applied electric field strength. And, (2) the difference in the weak electric field result and the strong electric field result is the same for all values of $\kappa h/\kappa a$ considered.

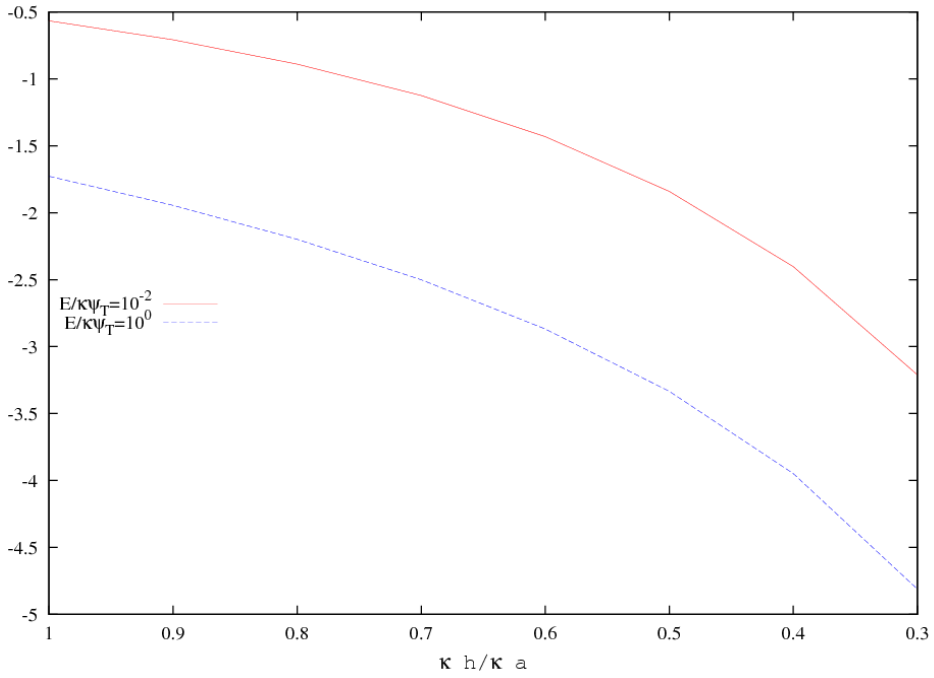

Figure 134: Dimensionless force on particle one for interacting dielectric particles with GDSL model

The Stern layer boundary condition results for interacting metallic particles are presented and described in the following. The surface plots for a weak applied electric field are presented in Figure 135 and Figure 136. The surface plots of Figure 135 and Figure 136 are very similar to the constant surface charge boundary condition results in Figure 104 and Figure 105. Therefore, any difference due to the surface boundary condition must be reveal through the section plots of the dimensionless electric potential and dimensionless free charge in Figure 137 and Figure 138.

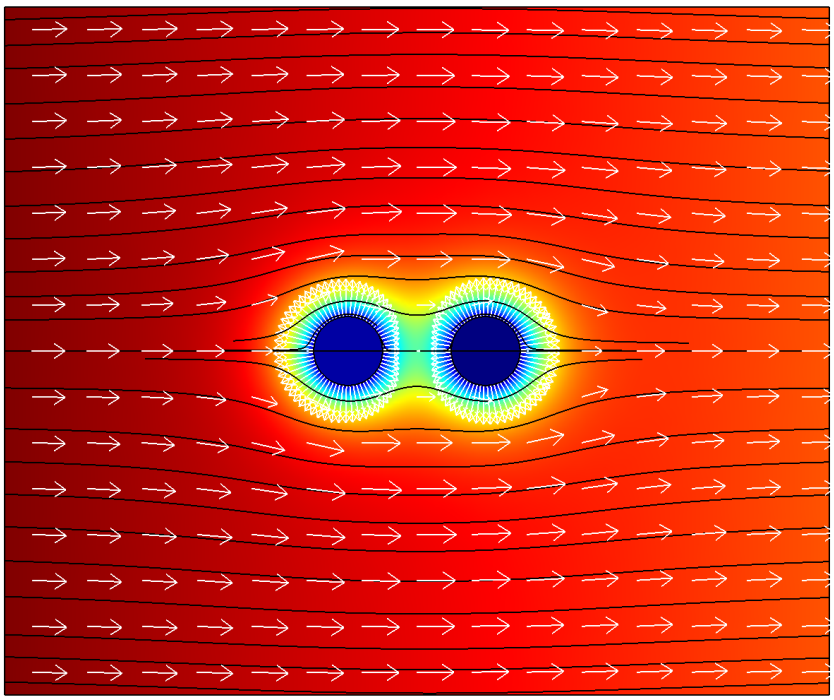

Figure 135: Metallic particles with; GDSL model, $\sigma_0/en_0a = -3.28$, $E_0/\kappa\psi_T = 10^{-2}$, and $\kappa h/\kappa a = 1$

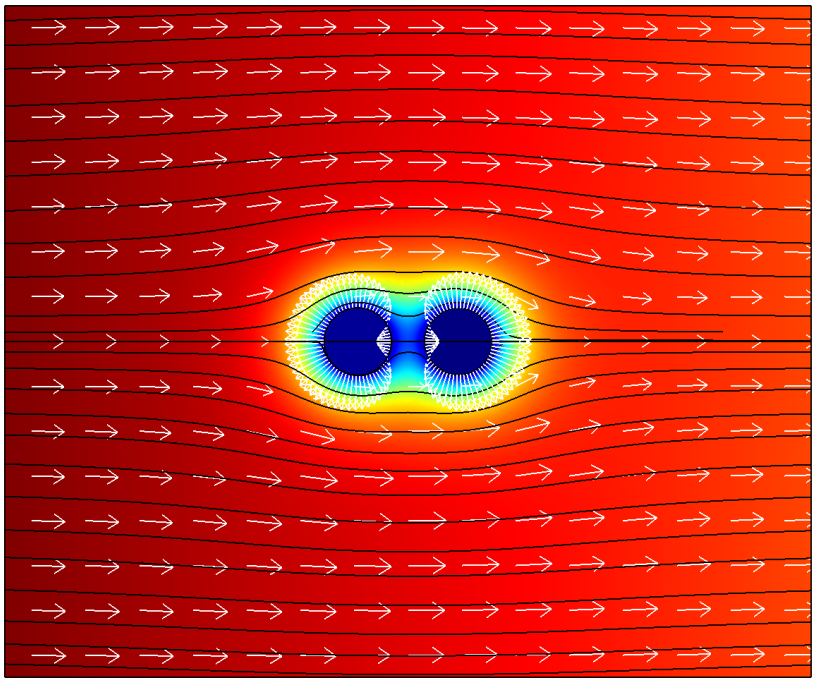

Figure 136: Metallic particles with; GDSL model, $\sigma_0/en_0a = -3.28$, $E_0/\kappa\psi_T = 10^{-2}$, and $\kappa h/\kappa a = 0.5$

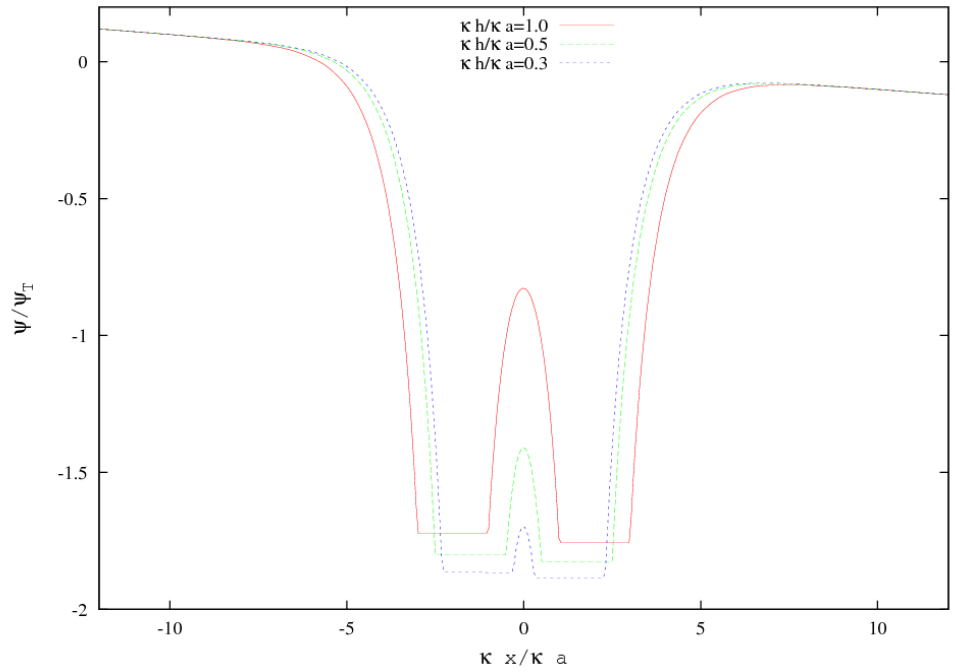

Figure 137: ψ/ψ_T for interacting metallic particles with GDSL model in a weak applied electric field

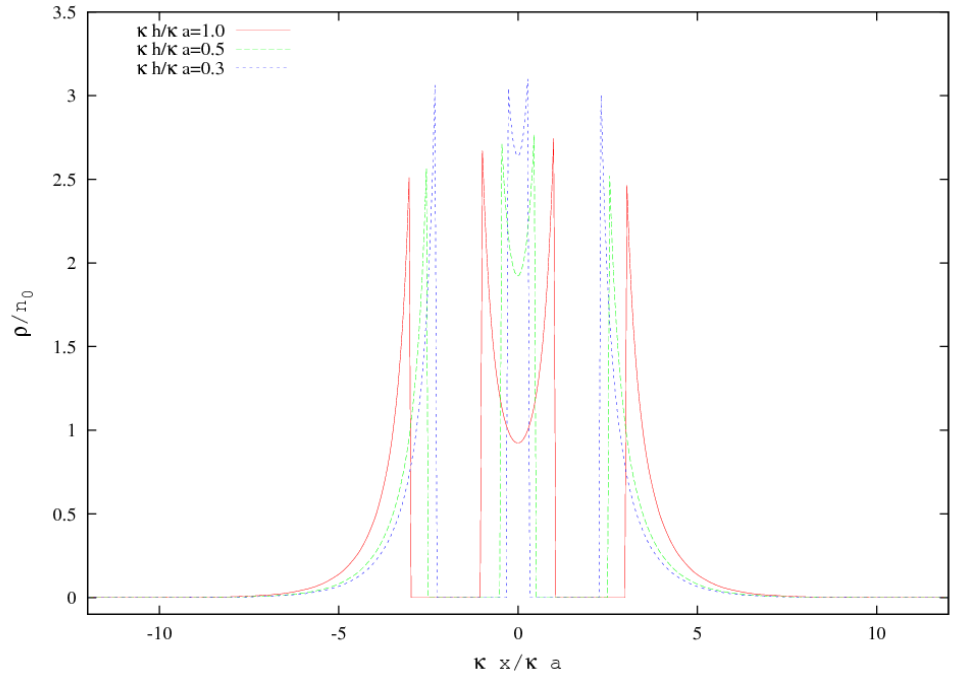

Figure 138: ρ/n_0 for interacting metallic particles with GDSL model in a weak applied electric field

The following observations are made when comparing the weak applied electric field results of Figure 137 and Figure 138 with those of Figure 106 and Figure 107: (1) The difference in the surface potentials of the two particles due to the applied electric field is about the same for the two boundary conditions. And (2) the induced electric potential and free charge between the particles is larger for the Stern layer boundary condition.

The results for interacting metallic particles in a strong applied electric field are presented in the following. The surface plots presented in Figure 139 and Figure 140 are again very similar to the results for interacting metallic particles with the constant surface charge boundary condition presented in Section 6.2.2. However, the section plots shown in Figure 141 and Figure 142 reveal the effect of the Stern layer boundary condition for interacting metallic particles.

A comparison of the dimensionless electric potentials along the mid-plane for the two boundary conditions shows that the two metallic particles have slightly more negative surface potentials for the Stern layer boundary condition. And, perhaps more importantly, Figure 142 shows that the free charge is much higher on the left portion of both particles when Stern layer adsorption is included and that the free charge does not become negative as it did with the constant surface charge boundary condition.

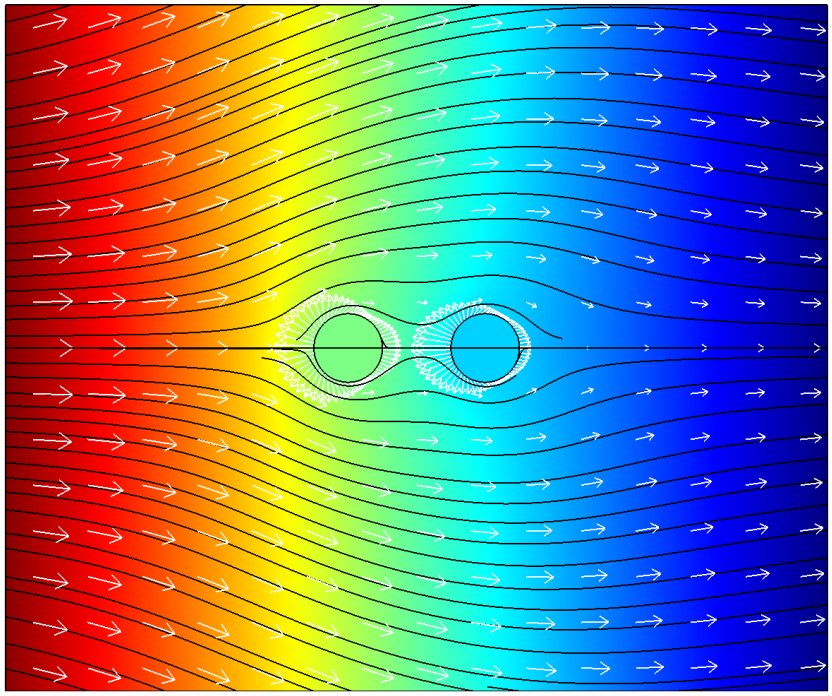

Figure 139: Metallic particles with; GDSL model, $\sigma_0/en_0a = -3.28$, $E_0/\kappa\psi_T = 10^0$, and $\kappa h/\kappa a = 1$

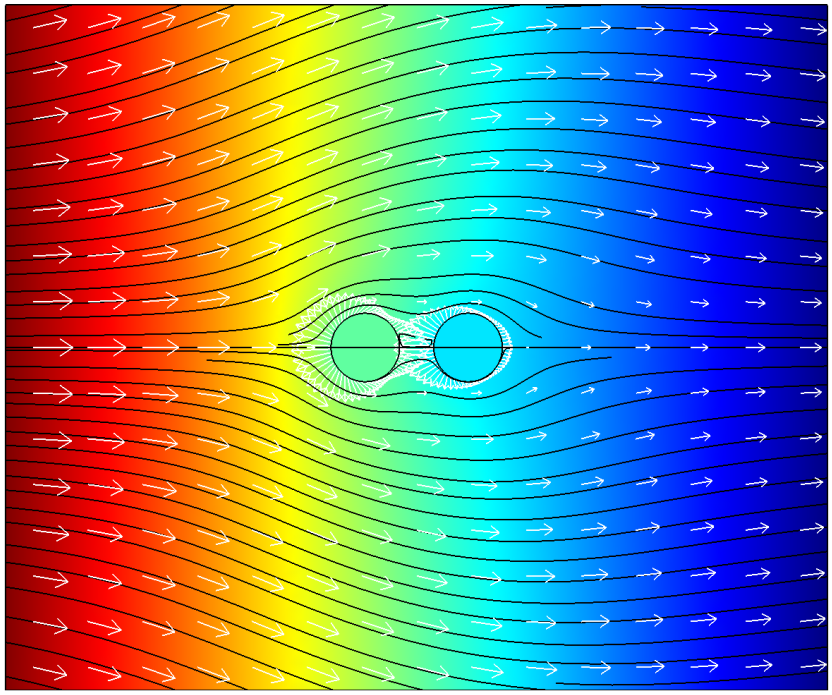

Figure 140: Metallic particles with; GDSL model, $\sigma_0/en_0a = -3.28$, $E_0/\kappa\psi_T = 10^0$, and $\kappa h/\kappa a = 0.5$

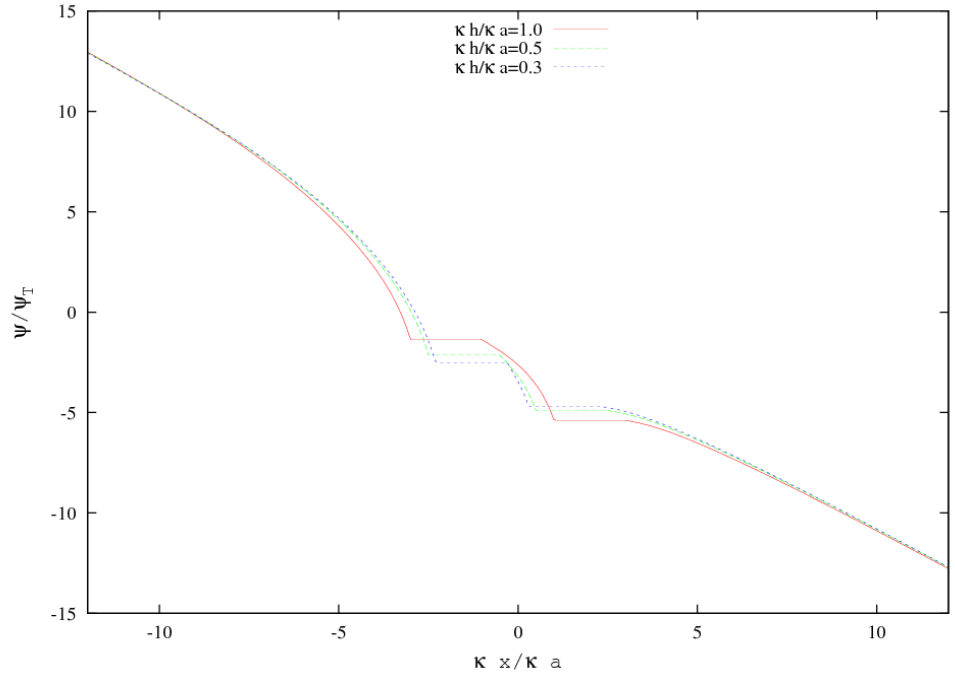

Figure 141: ψ/ψ_T for interacting metallic particles with GDSL model in a strong applied electric field

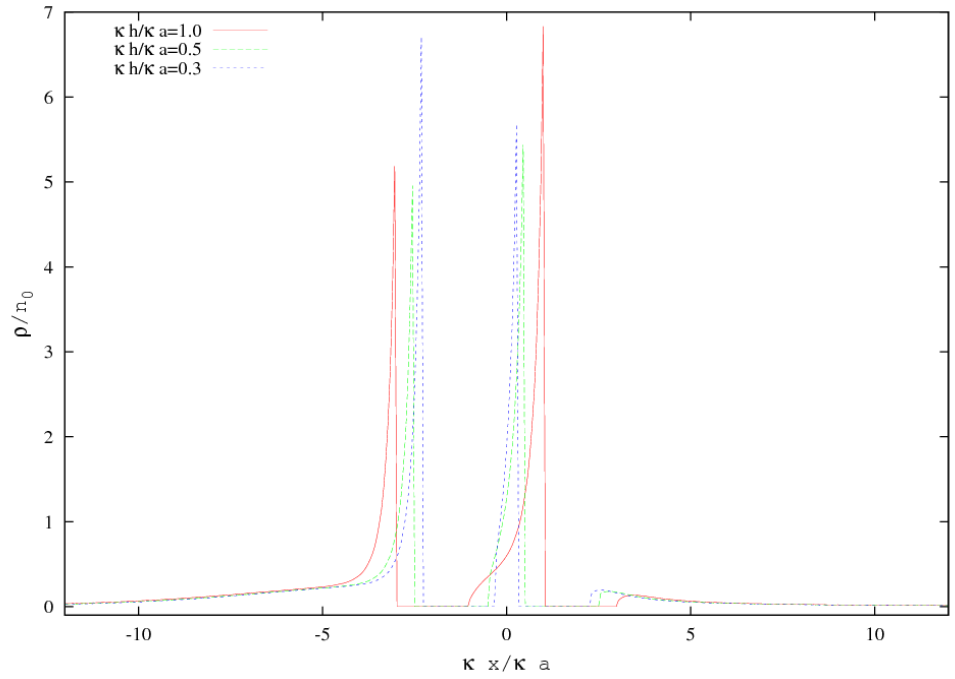

Figure 142: ρ/n_0 for interacting metallic particles with GDSL model in a strong applied electric field

A comparison of the dimensionless mid-plane potential for the Stern layer boundary condition presented in Figure 143 and for the constant surface boundary condition presented in Figure 113 reveals that the mid-plane potential is larger for the Stern layer boundary condition regardless of applied electric field strength. However, the most significant difference in the two boundary conditions arises from the results of Figure 142. The results of Figure 144 show that, because the free charge does not become negative on the right side of both particles when large electric fields are applied, the force on the particle does not change directions.

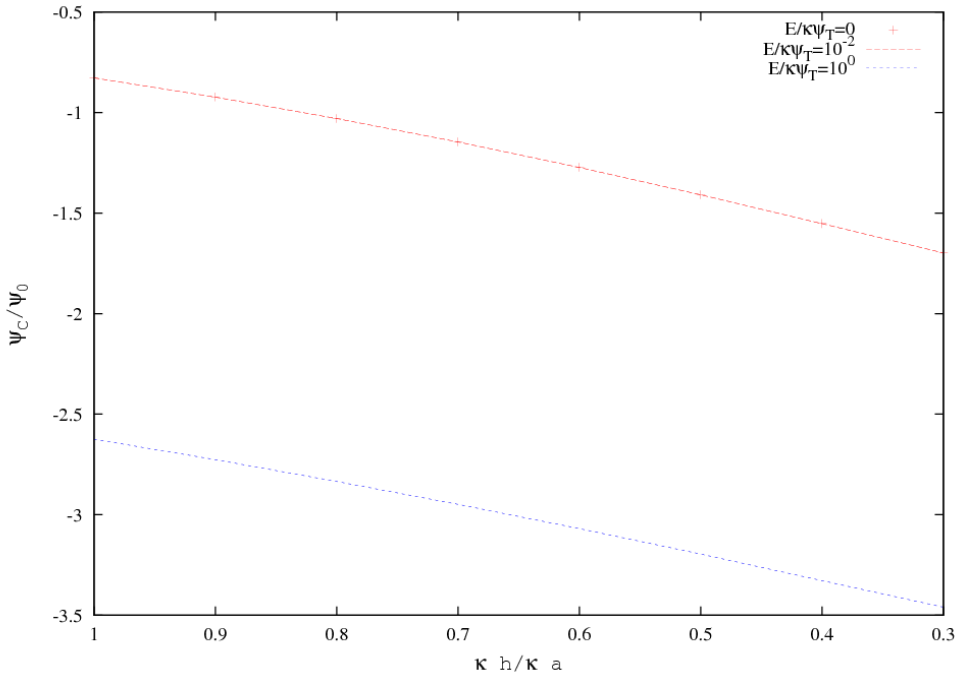

Figure 143: Scaled mid-point potential for interacting metallic particles with GDSL model

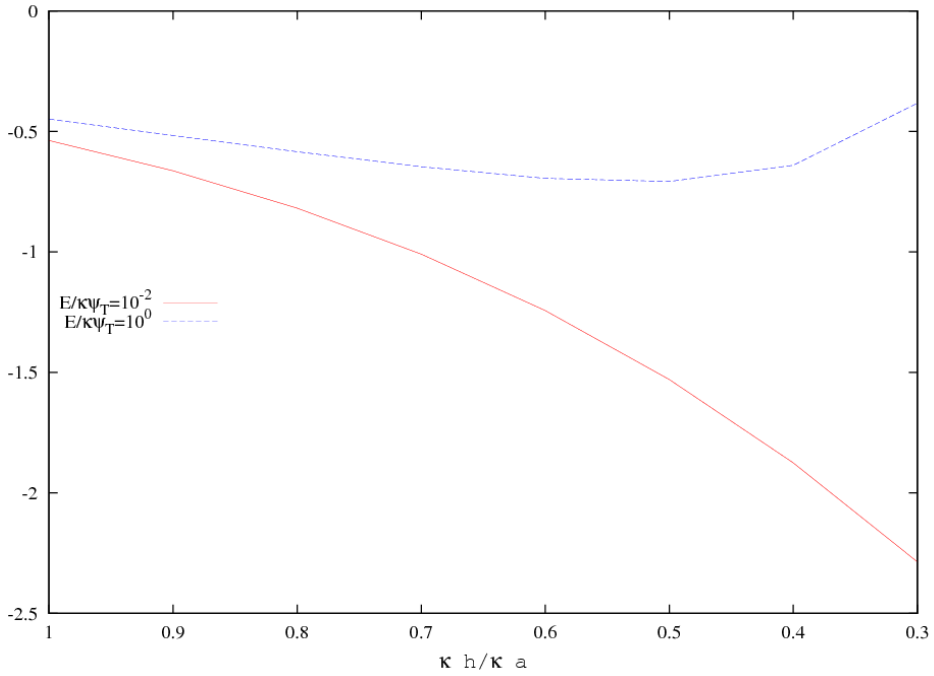

Figure 144: Dimensionless force on particle one for interacting metallic particles with GDSL model

6.3 DISCUSSION

In this section we summarize the steps taken to; (1) verify the FEM model, (2) characterize hydrodynamic and electric particle-particle interaction forces for particles in an applied electric field, and (3) identify the nonlinear effect of applied electric field strength. Then, the observations made in Section 6.2 are reviewed and discussed.

First, the finite element model was verified by comparing the scaled electric potential (ψ_C/ψ_0) at the mid-plane between the two particles interacting in the absence of an applied electric field with solutions available in the literature [10, 40]. The comparison, which was presented in Figure 82 and Figure 83, validated the FEM model. These results also showed that: (1) The error in the linearized DLVO model becomes significant for dimensionless surface potentials greater than one. And, (2) the error in

the flat plate model is significant when $\kappa a = 1$. Having verified the accurate solution of the electric double layers surrounding interacting particles in the absence of an applied electric field we preceded in Sections 6.2.1, 6.2.2, and 6.2.3 to demonstrate the effect of an applied electric field on the interaction of particles for the constant surface potential boundary condition, the constant surface charge boundary condition, and the Stern layer boundary condition, respectively. Also, proposed in Section 6.2 was a method of characterizing the hydrodynamic and electric particle-particle interaction forces for particles in an applied electric field. This method, which is summarized below, was used for each of the boundary conditions considered.

The method used in Section 6.2 to characterize hydrodynamic and electric particle-particle interaction forces is a combination of the methods used by the authors of the DLVO theory [10] and the MST method [27]. In [10] the authors used the mid-plane potential to compare solutions of two different models for the EDL between interacting particles. A model for weakly interacting particles, which used linearized equations and superposition, was compared with a model for strongly interacting particles, which used the nonlinear Poisson-Boltzmann equation and the symmetry boundary condition. A thesis of this work is that in an applied electric field the symmetry boundary condition is violated. Therefore, in Section 6.2 the mid-plane potential was presented for interacting particles in a weak applied electric field and a strong applied electric field and compared with that of the DLVO theory. The idea being that one should determine when and if the method of using the mid-plane potential could be used to characterize particle interaction when applied electric fields are present. The MST method was used to characterize

particle-particle interaction by plotting both the distribution of the boundary tractions and the resultant force on particles for different electric field strengths and particle separations. This method, when used with the appropriate nonlinear electrokinetic theory, does not introduce additional assumptions. In the following, we summarize the observations made at the conclusion of the process for each of the boundary conditions.

The results of Section 6.2.1 showed that when the constant surface potential boundary condition is used the forces on the particles are repulsive. That is, the particles would separate if not held by some (imaginary) external force. This repulsive force increases as larger electric fields are applied. However, the difference in the weak applied electric field result and the strong electric field result becomes smaller as the separation between the particles is decreased. An interesting nonlinear phenomenon observed for the constant surface potential boundary condition that is not seen with the other boundary conditions is shown in Figure 88 and Figure 89. The fluid velocity streamlines show large areas of circulation on the leeward side of the particles. The existence of this zone of circulation would be intriguing to those who would like to mix two liquids or disperse solids in liquids in microfluidics because conventional convective mixing is not possible due to the typically small Reynolds of mircofluidic devices. The results of Section 6.2.1 also show that, if charged conducting islands fixed in a microfluidic device are used to disperse charged solids which have surface chemistry which is consistent with the constant surface boundary condition, one can be relatively sure that the dispersed particles will not collect on the island. We emphasis relative assurance because van-Der Waals forces are not modeled here. However, they are

relatively short range. So, the strongly repulsive electric particle-particle interaction force observed for the constant surface potential boundary condition indicates that the particle should not attach to the island.

In Section 6.2.2 results were presented for interacting dielectric, interacting metallic, and dissimilar interacting particles with the constant surface charge boundary condition. When the constant surface boundary condition was used for interacting dielectric particles, the applied electric field had very little effect on the force of interaction. This result is summarized by the plot of the dimensionless force on particle one as a function of particle separation presented in Figure 103. Figure 103 shows that the dimensionless force on particle one is not significantly increased by a strong applied electric field. However, the results of Figure 101 and Figure 102 show that when the weakly dielectric latex particles interact in a strong applied electric field the displacement electric field in the particles is relaxed and the charge in the EDL's is increased as large surface potentials are induced. Thus, an assembly of latex particles is likely to have a higher conductivity than that of the bulk fluid even though the first order effect would be to decrease the conductivity of the system. That is, to first order in the particle concentration, the relatively high conducting solution is replaced with a particle with low conductivity. The situation for interacting metallic particles using the constant surface charge boundary condition was quite different than that for interacting dielectric particles. The results of Figure 114 show that the force on the particles changes direction in a large applied electric field. That is, the originally repulsive particle-particle interaction force becomes attractive. This important result implies that metallic

particles may be assembled by large applied electric fields. This is not completely surprising although it has not been shown in any other work. It is not surprising because it has been shown by experiment, by Velev [41] for example, that metallic particles which do not spontaneously assembly in the absence of applied electric fields may be assembled by high frequency applied electric fields. And, that when the frequency is reduced the particles disassemble. This reversible assembly of metallic particles by high frequency applied electric fields is analogous to assembly by high strength applied electric fields because the mechanism is similar. At high frequencies, the EDL is relaxed because free charges have finite mobility and cannot move fast enough to resist the applied electric field. In a strong applied electric field the EDL which has a charge equal to the charge of the particle surface is not strong enough to resist the applied electric field. The results of Figure 110 show that interacting metallic particles can have very different surface potentials when the constant surface charge boundary condition is used; a result that would lead to a highly conductive colloidal structure. Since, the electric field may be reduced the assembly is likely to be reversible. Thus, one can change the conductivity of the solution at will by manipulating the particles with applied electric fields. Either by applied electric field strength or by applied electric field frequency. The model problem of interacting dissimilar particles was posed to describe a microfluidics device filled with a dispersion of dielectric particles which incorporates a (fixed) charged conducting island. Velev [41] incorporated uncharged conducting islands into a microfluidics device designed to assemble metallic colloidal wires. These islands induce a non-uniform electric field which ultimately leads to assembly in AC

electric fields. The results of Figure 124 and Figure 125 show that when a weakly dielectric particle interacts with a charge conducting island the interaction force is always repulsive. Thus, the combination of dimensionless permittivity used for the particle and island does not lead to assembly.

Finally, in Section 6.2.3 results were presented for interacting dielectric and interacting metallic particles using the Stern layer boundary condition. The results of Section 6.2.3 can be summarized by noting that use of the Stern layer boundary condition increased the force on particle one for both dielectric and metallic particles. The following observations were made from plots of the dimensionless electric potential and dimensionless free charge: (1) The magnitude of the electric potential and free charge between interacting dielectric particles and interacting metallic particles in a weak applied electric field is much larger for the Stern layer boundary condition. (2) The displacement electric field in the dielectric particle is more relaxed by the particle-particle interaction when the constant surface charge boundary condition is used. And, (3) The difference in the dimensionless surface potentials for metallic particles interacting in a weak applied electric field are about the same for the Stern layer or constant surface charge boundary condition. These observations explain the increase in the force on particle one. First, an increase in surface potential would increase the dimensionless force on particle one as shown in Equation 5.4. Second, the electric (Maxwell) force on a completely relaxed dielectric particle would be zero. Since the displacement electric field in the dielectric particle was more relaxed for the constant surface charge boundary condition, the force on the dielectric particle is greater for the

Stern layer boundary condition. Finally, the fact that the surface potential of a metallic particle is significantly larger for particles interacting in a weak applied electric field combined with the fact that the difference in the surface potentials of the particles is about the same for the Stern layer and constant charge boundary conditions means that the surface potentials are primarily increased by particle-particle interaction when applied electric fields are weak. The increase in surface potential due to particle interaction leads to a nonlinear increase in the repulsive force between the particles as the separation is decreased. This is observed in Figure 134 where it is shown that although the dimensionless force on the dielectric particles in a weak applied electric field are about the same as the constant surface charge boundary condition when the dimensionless separation is $\kappa h/ka = 1$ the dimensionless force increases much faster as the separation decreases when the Stern layer boundary condition is used. However, the most significant difference in the two boundary conditions arises from the results of Figure 142. The results of Figure 144 show that, because the free charge does not become negative on the right side of both particles when large electric fields are applied, the force on the particle does not change directions. Therefore, when the Stern layer boundary condition is used the interaction forces would lead to separation of the particles; not assembly.

6.4 CONCLUSIONS

The interaction of two particles in applied electric field was posed in this section to demonstrate the capabilities of the proposed finite element model in determining the conditions and parameters which lead to reversible particle assembly. In the following,

we present some conclusions which are based on the results of the model problem and suggest some improvements to improve the reliability of the FEM model results.

First, the results of Section 6.2.1 showed that the use of the constant electric potential boundary condition results in large areas of fluid circulation and large repulsive forces which increased as the electric field strength increased. Based on the results presented in Section 6.2.1 and the discussion that followed we make the following conclusions: (1) Large applied electric fields could not be used to assemble particles which have surface conditions which are accurately described by the constant surface potential boundary condition. (2) One could use such a particle as a fixed conducting island to promote circulation as described by Bazant, et al [20-22, 42]. And, (3) an assembly of particles which are accurately described by the constant potential boundary condition would have a low conductivity because the surface potentials are the same. Based on the third conclusion above and the conclusion of Section 4, which was that the constant surface potential should not be used for particles in a large applied electric field, we abandon the use of the constant surface potential boundary condition. The desirable fluid circulation zones shown in Section 6.2.1 can be achieved with the constant surface charge boundary condition if the right combination of surface charge and applied electric field strength are used. Thus, the existence of such a zone of fluid circulation as shown by experiment does not validate the used of the constant surface potential boundary condition. However, it does indicate that the particle behaves as if it has a constant surface potential.

Next, the results of Section 6.2.2 showed that the effect of a strong applied electric field depends of the permittivity of the interacting particles. Based on the results of Section 6.2.2 and the discussion that followed we make the following conclusions: (1) the assembly of dielectric particles by strong applied electric fields is not likely and would result in only a moderate change in the conductivity of the colloidal dispersion. (2) The assembly of metallic particles by strong applied electric fields is likely and the resulting assembly would have a significantly different conductivity. And, (3) the use of a charged conducting island does not promote the assembly of dielectric particles by strong applied electric fields.

Finally, the results of Section 6.2.3 showed that the effect of Stern layer adsorption on the interaction of particles is significant regardless of applied electric field strength or particle permittivity. The large differences in the Stern layer boundary condition results for a weak applied electric field implies that particle-particle interaction forces are significantly affected by the presence of a Stern layer. And, larger differences between the weak field results and strong field results imply that the effect of applied electric fields is also stronger when the Stern layer boundary condition is used. Most importantly, the forces acting on interacting particles do not change direction when large applied electric fields are applied when the Stern layer boundary condition is used. Rather, the repulsive forces decrease as strong electric field are applied which leads to assembly that is reversible.

7 A SINGLE PARTICLE IN A NON-UNIFORM ELECTRIC FIELD

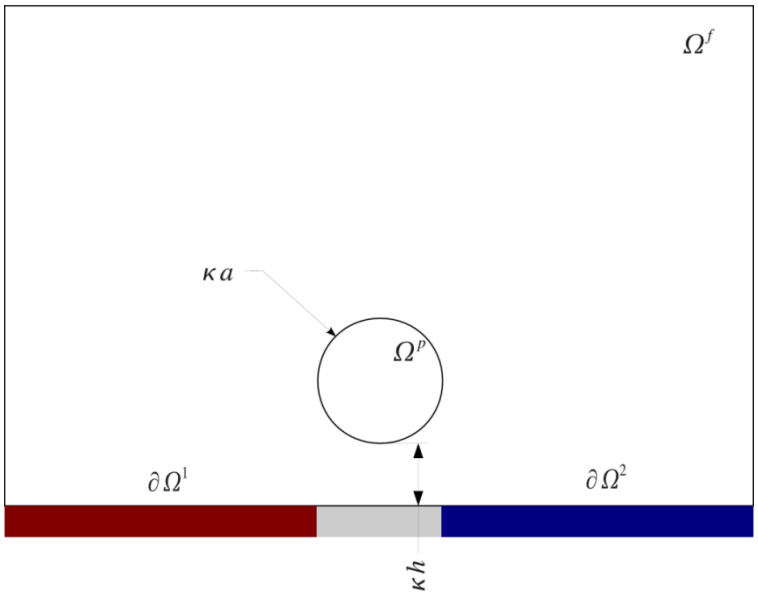

Figure 145: A single particle in a non-uniform AC field

7.1 PROBLEM STATEMENT

The objective of this section is to demonstrate the capabilities of the FEM model by determining the forces of interaction between a single particle and a planar electrode surface which results from the application of a non-uniform AC electric field (as shown schematically in Figure 145). The calculation of forces in non-uniform AC electric field is of great importance to AC electrokinetic because they lead to non-zero time average particle and fluid velocities. Problems similar to the problem discussed in this section have been presented by other authors. In a series of papers, Green, et al [43-45] analyzed the fluid flow induced by non-uniform AC electric fields on micro-electrode arrays. They subsequently used the linearized electrokinetic finite element model with a simple Stern layer model to determine the magnitude of the electric field and gradient of

the electric field norm [46] to be used in the determination of the dielectrophoretic (DEP) force. However, the presence of the particle and its effect on the electric field was not included. Thus, interaction of the particle with the electrode is not included and their solution is only valid when the dimensionless separation is greater than about four. The model domain and boundary conditions used by Green, Ramos, and Morgan [46] to calculate the electric field and fluid flow are presented in Figure 146. Obviously, when a particle is present the boundary condition at the right $(\tilde{\psi} = 0)$ is violated. Thus the effect of the EDL surrounding the particle is not included. The effect of the particle and its EDL are not negligible. In fact, Velev and others [4, 41, 47] have described how a previously deposited particle increases the DEP force leading to assembly of on-chip colloidal wires.

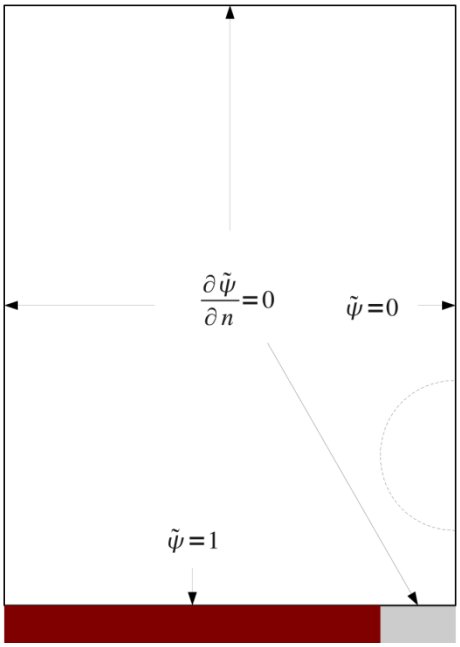

Figure 146: Model domain and boundary conditions used by Green, Ramos, and Morgan

7.2 RESULTS

In the following section we present and discuss the electric field, fluid flow, and dielectrophoretic forces acting on a stationary particle in a non-uniform applied electric field for the constant surface charge boundary conditions. The problem is modeled using the domain of Figure 145 where the dimensionless particle radius, the dimensionless particle-electrode separation, and the dimensionless electrode gap are taken as one. The (red) electrode on the left has an electric potential of one and the (blue) electrode on the right has an electric potential of minus one. However, the constant surface potential boundary condition is not used as it is inconsistent with the results presented by Green et al [43-45]. Instead the electrodes are included in the model domain and the zero charge boundary condition is used at the interface while specifying the electric potential on the bottom boundary. The gap between the electrodes is modeled using a zero charge boundary condition. Having already presented the effect of the strength of the surface charge on the polarization and relaxation of the EDL, only particle surface boundary conditions which result in equilibrium surface potentials of minus one are presented. Symmetry boundary conditions are used on the left and right portions of the domain for all the variables. And, bulk boundary conditions are used for the boundary on the top.

In the following we present steady state results of the transient solution to the problem described above. In a DC applied field an EDL forms near the electrode surface which blocks the applied electric field and no net flow develops. As the

frequency of the applied electric field is increased the EDL relaxes and the nonlinear electric field induces fluid flow.

The results of Figure 147 and Figure 148 show the dimensionless free charge and fluid flow surrounding a stationary dielectric particle (left) and metallic particle (right) for applied electric field frequencies of $\omega/2\pi = 1 \times 10^2\ Hz$ and $\omega/2\pi = 1 \times 10^3\ Hz$, respectively. The surface plot shows the dimensionless free charge and the streamlines and arrow show the fluid flow. These steady state results and those that follow are taken at the instant the maximum electric field is applied. The width of the computational domain is also shown in Figure 147 and Figure 148 although the height of the figures has been reduced. In the figures that follow details are presented which focus on the electric field, fluid flow, and surface tractions near the particle. It is important to note that the computational domain is the same. These results are only details of the same results.

Figure 149 and Figure 150 show the electric field, fluid flow, and total traction on a dielectric particle $\left(\varepsilon_r^p/\varepsilon_r^f = 0.025\right)$ for applied electric field frequencies of $\omega/2\pi = 1 \times 10^2\ Hz$ and $\omega/2\pi = 1 \times 10^5\ Hz$, respectively. The surface plot shows the dimensionless electric potential, the streamlines and black arrows show the fluid flow, and the white arrows on the surface of the particle show the distribution of the total traction (electric plus hydraulic) acting on the particle at that particular particle location.

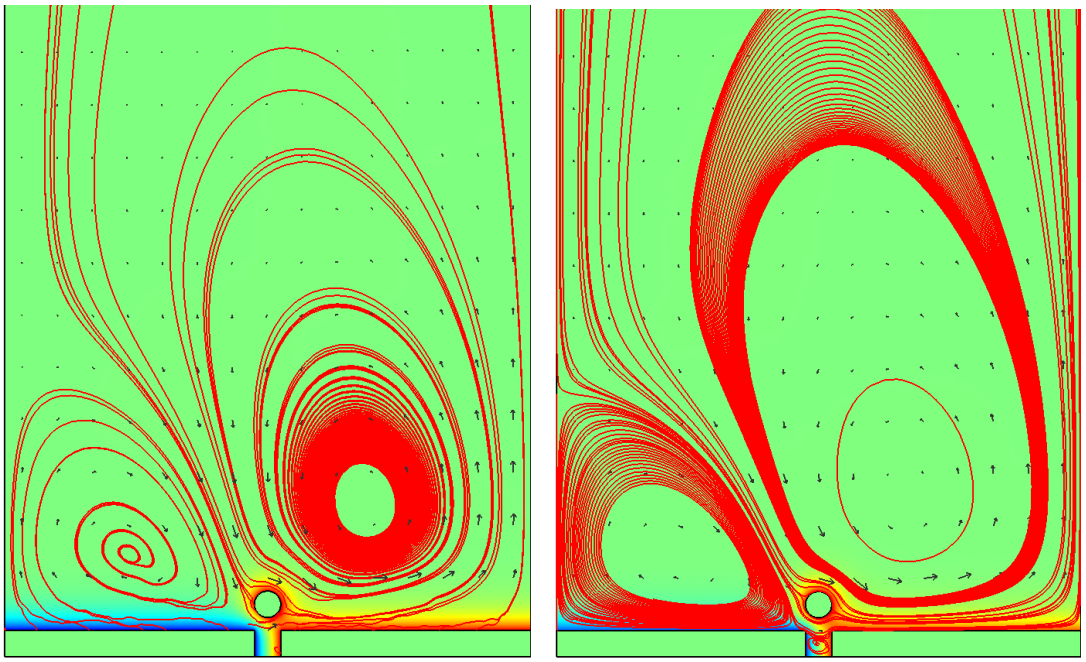

Figure 147: Dimensionless free charge and fluid flow surrounding a dielectric particle (left) and a metallic particle (right) – $\kappa h/\kappa a = 1$ & $\omega/2\pi = 1 \times 10^2\ Hz$

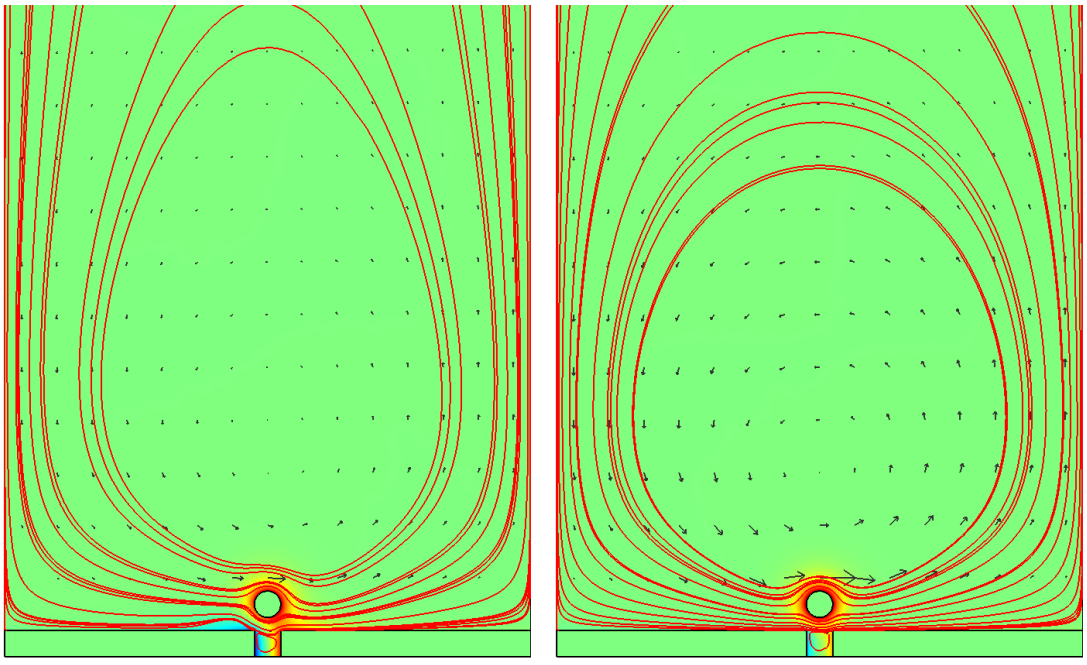

Figure 148: Dimensionless free charge and fluid flow surrounding a dielectric particle (left) and a metallic particle (right) – $\kappa h/\kappa a = 1$ & $\omega/2\pi = 1 \times 10^3\ Hz$

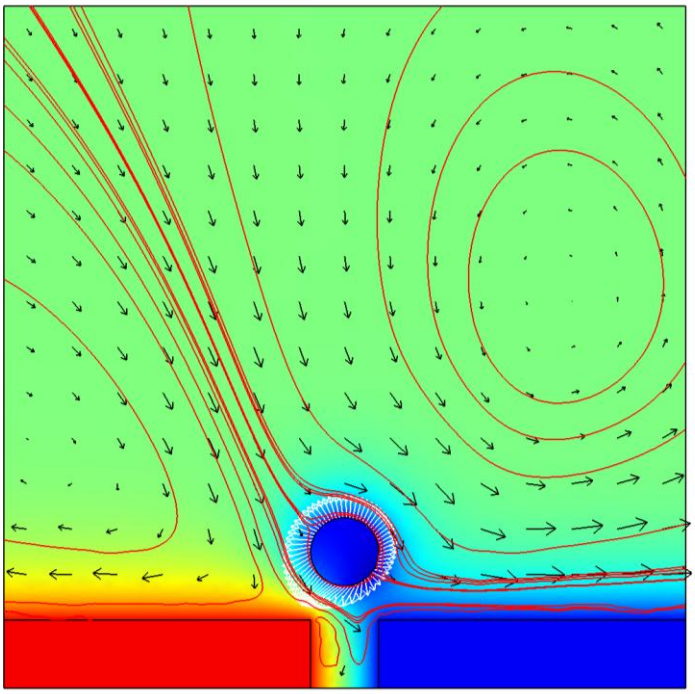

Figure 149: Dielectric particle in a non-uniform electric field - $\kappa h/\kappa a = 1$ & $\omega/2\pi = 1 \times 10^2\ Hz$

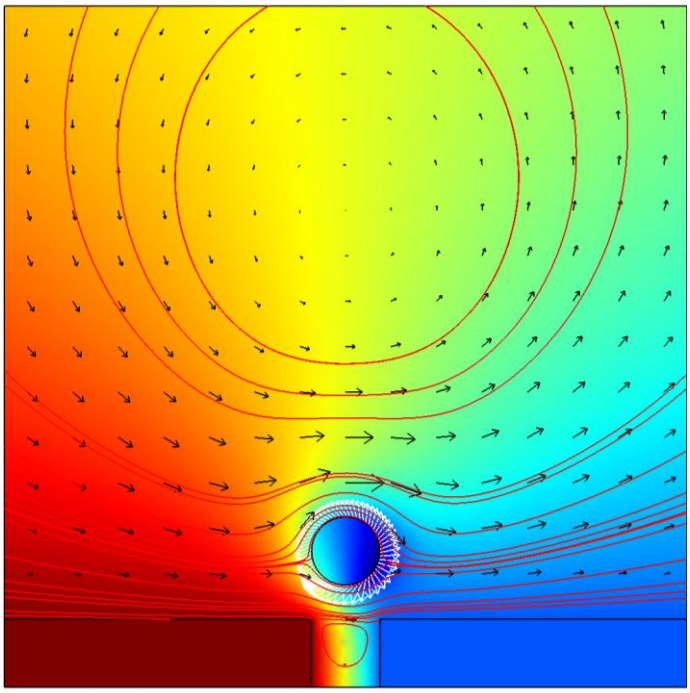

Figure 150: Dielectric particle in a non-uniform electric field - $\kappa h/\kappa a = 1$ & $\omega/2\pi = 1 \times 10^5\ Hz$

The results of Figure 147 show that two opposing zones of circulation exist at $\omega/2\pi = 1 \times 10^2$. One zone of circulation is smaller and clockwise and the larger is counterclockwise. Where the results of Figure 148 for $\omega/2\pi = 1 \times 10^3$ show that there is only one counterclockwise zone of circulation and that the distribution of free charge near the electrode surface is concentrated near the electrode gap.

The results of Figure 149 and Figure 150 show that the negatively charged particle is attracted to the positive electrode and repelled from the negative electrode. And, that the symmetry assumed by Green, et al is destroyed by the inclusion of the charged particle. This is evident by the distortion of the fluid streamlines from the mid-plane and the distribution of the electric potential near the particle. The distribution of the traction on the particle (not shown here) also shows that the forces which act on the particle increase as the particle approaches the electrode. This is confirmed integrating the surface traction and plotting the components of the dimensionless force acting on the particle as a function of the dimensionless particle-electrode separation. The results for a low frequency applied electric field ($\omega/2\pi = 1 \times 10^2$) are presented in Figure 151. Results for higher frequency applied electric fields are similar however the force components are large at higher frequencies because the electrode EDL is relaxed.

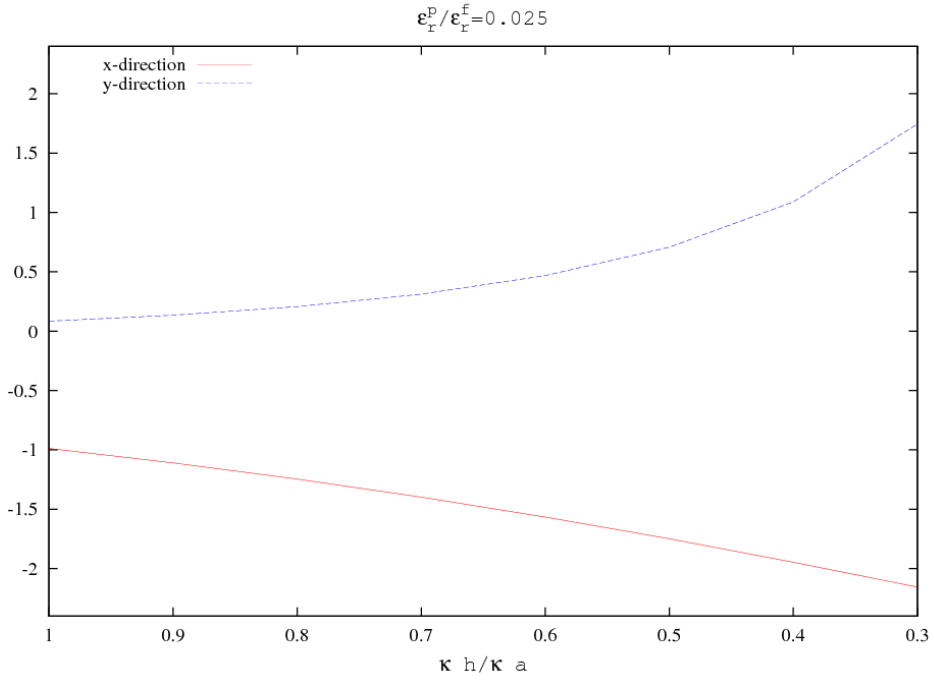

Figure 151: Dimensionless force components for a dielectric particle in a non-uniform electric field

The results of Figure 151 show that the forces on the particle would tend to move the dielectric particle to the left and away from the electrode surfaces. This tendency increases nonlinearly as the particle is moved closer to the electrode surface. However, these results are only the force at some instant. In order to have a net movement of the particle the time average force must be nonzero. Therefore, the dimensionless force components are plotted as a function of time in Figure 152 and Figure 153 to determine if the electric field results in nonzero time-averaged forces on the particle.

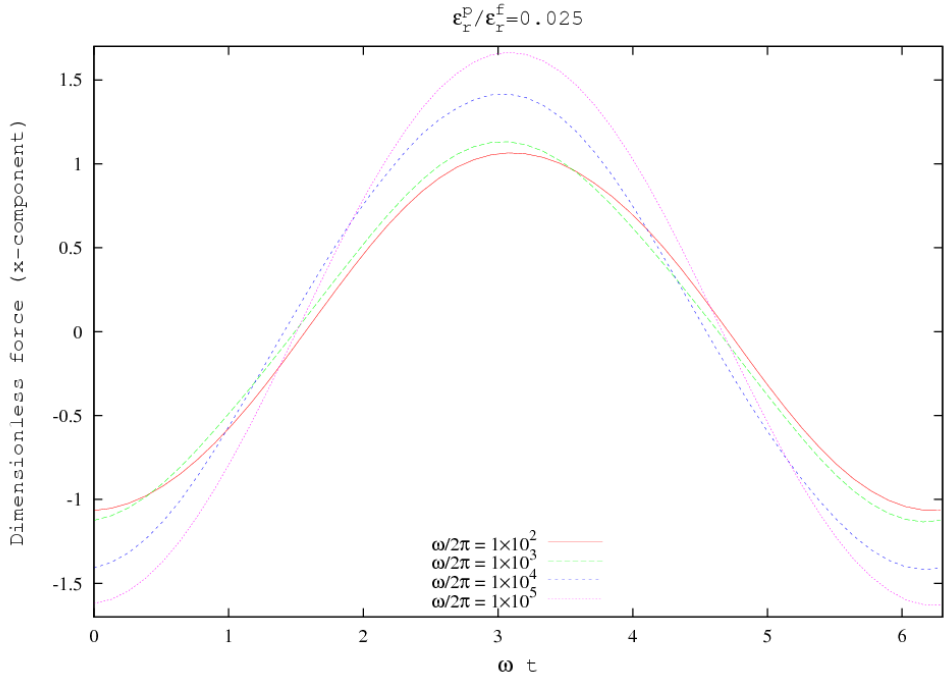

Figure 152: Dimensionless force in the x-direction as a function of dimensionless time – dielectric particle

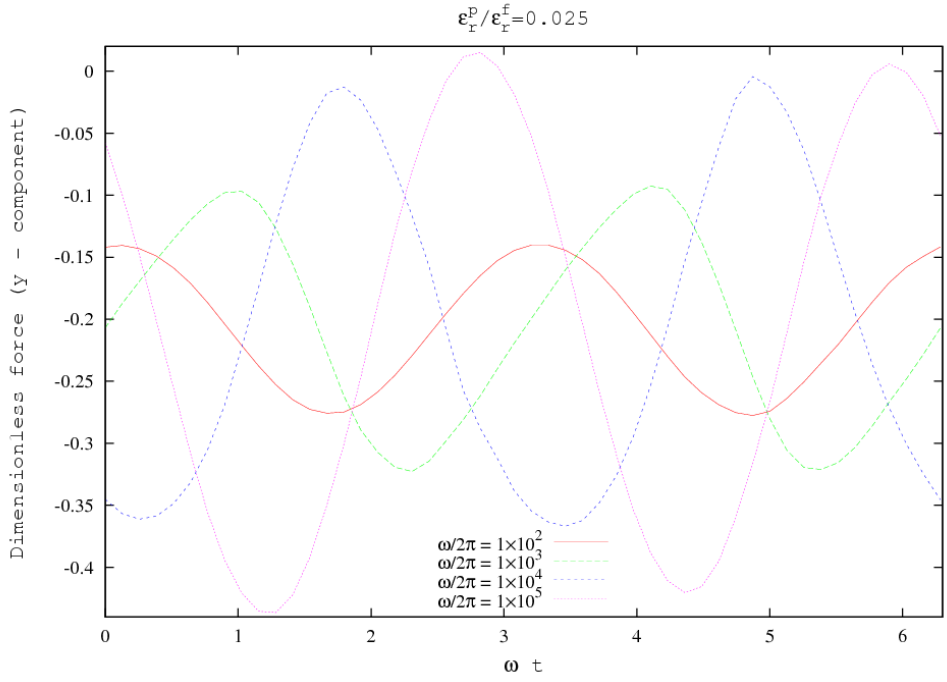

Figure 153: Dimensionless force in the y-direction as a function of dimensionless time – dielectric particle

The results of Figure 152 and Figure 153 show that time-average of the x-component is essentially zero and that the time-average of the y-component is negative for the dimensionless particle-electrode separation considered, i.e. $(\kappa h/\kappa a = 1)$. This leads one to the conclusion that the dielectric particle will be deposited onto the positive electrode. However, it is clear from the results of Section 6 that assembly will not be possible because the previously deposited dielectric particle will repeal another dielectric particle of the same charge.

Figure 154 and Figure 155 show the electric field, fluid flow, and total traction on a metallic particle $\left(\varepsilon_r^p/\varepsilon_r^f = 8000\right)$ for applied electric field frequencies of $\omega/2\pi = 1 \times 10^2\ Hz$ and $\omega/2\pi = 1 \times 10^5\ Hz$, respectively. The surface plot shows the dimensionless electric potential, the streamlines and black arrows show the fluid flow, and the white arrows on the surface of the particle show the distribution of the total traction acting on a metallic particle at that particular particle location. These results are quantified by integrating the surface traction and plotting the results as a function of particle-electrode separation. The results for a low frequency applied electric field are presented in Figure 156.

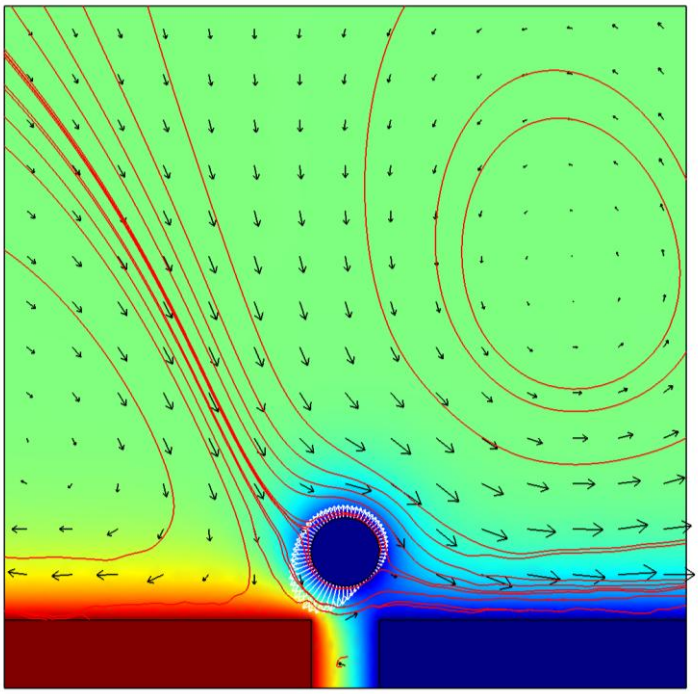

Figure 154: Metallic particle in a non-uniform electric field - $\kappa h/\kappa a = 1$ & $\omega/2\pi = 1 \times 10^2\ Hz$

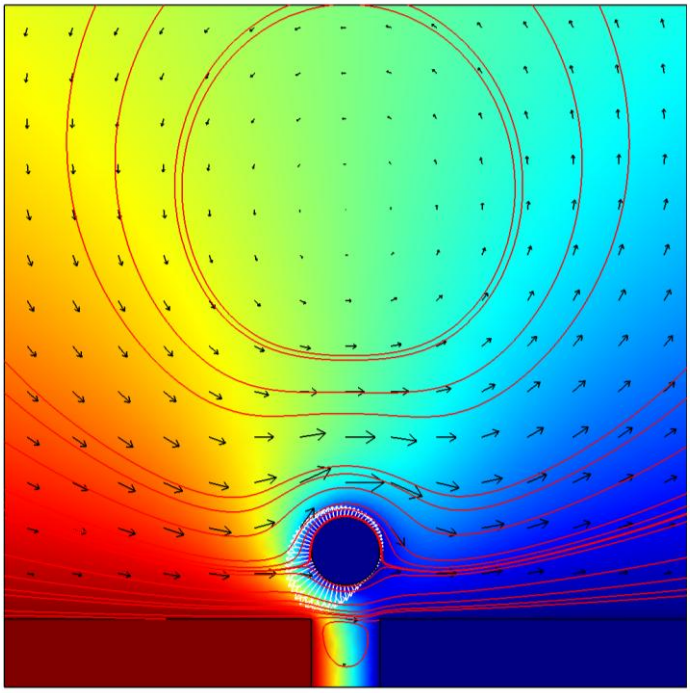

Figure 155: Metallic particle in a non-uniform electric field - $\kappa h/\kappa a = 1$ & $\omega/2\pi = 1 \times 10^5\ Hz$

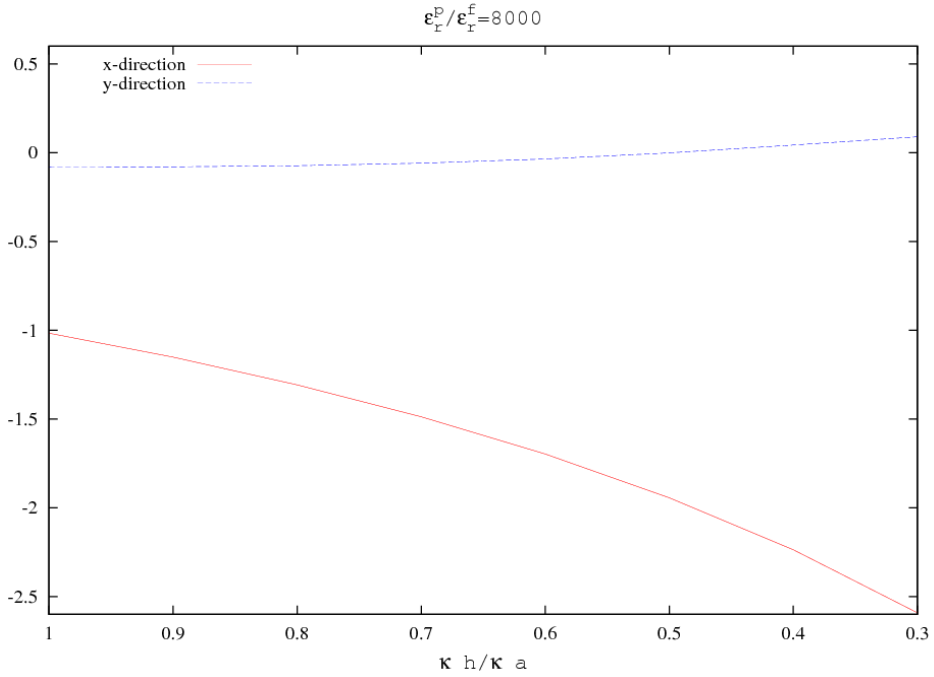

Figure 156: Dimensionless force components for a metallic particle in a non-uniform electric field

The results of Figure 156 show that the force in the y-direction is quite small for the particle-electrode at the particle locations considered. In fact, the y-component of the dimensionless force passes through zero at about $\kappa h/\kappa a = 0.6$. However, the x-component of the force is very strong and its magnitude increases as the separation decreases. However, as with the dielectric particle the only force that is important is the time average of the force components. The results of Figure 157 show that, even though the instantaneous force in the x-direction is strong, its time average is approximately zero. And, the results of Figure 158 show that the time average of the y-component is nonzero.

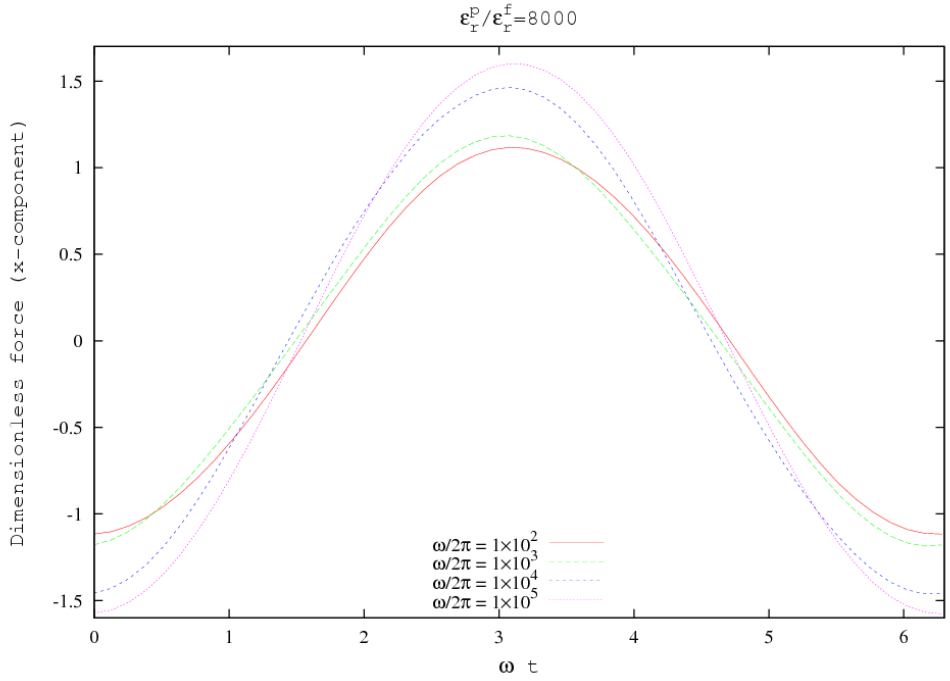

Figure 157: Dimensionless force in the x-direction as a function of dimensionless time – metallic particle

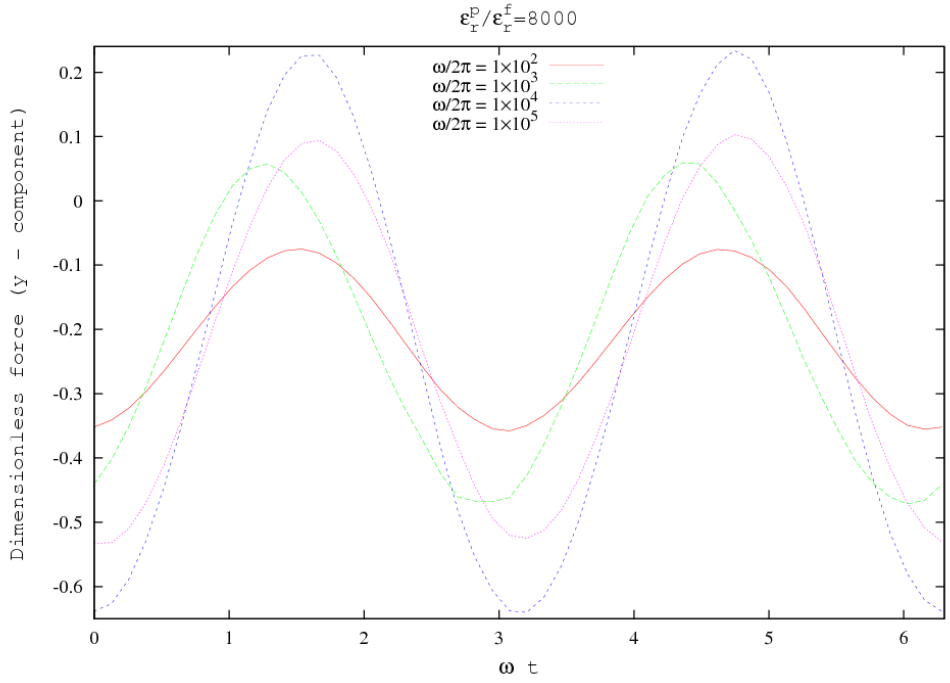

Figure 158: Dimensionless force in the y-direction as a function of dimensionless time – metallic particle

7.3 DISCUSSION

The results of the previous section show that the proposed finite element model is capable of accurately determining the electrokinetic forces on particles in non-uniform electric fields. These results also show that a non-uniform AC electric field produces nonzero time average forces on a particle near the electrode.

The time averaged y-component of the force on the particle was negative for both the dielectric and metallic particle which would imply deposition of these particles onto the positively charged electrode. However, based on the observations made in Section 6, we know that when the constant surface charge boundary condition is used surface potentials are induced by interactions in dielectric and metallic particles. These induced surface potentials eventually cause the interaction between the particle and the electrode to be repulsive. Thus, particles do not irreversibly attach to the oppositely charged electrode.

7.4 CONCLUSIONS

The results of this section illustrate the ability of the FEM model to characterize electrokinetic forces which lead to assembly. However, the model cannot accurately predict the strength and frequency of the applied electric field that would result in the deposition of a particle onto an electrode and the subsequent assembly of additional particles. The following improvements to the FEM model would result in a robust model capable of predicting assembly. (1) One must include a model for the attractive van Der Waals forces. And, (2) a moving mesh FEM model must be developed to include the effect of the particles mass.

8 SUMMARY AND CONCLUSIONS

8.1 SUMMARY

In the preceding sections we have presented the development of a new finite element model to describe the electrokinetics of electric field guided assembly of colloids. The model was developed from the nonlinear electrokinetic equations as presented by White, et al [13, 15, 16]. A model based on this theory cannot be found in the literature as the applications up to the present time have been of dilute dispersions of particles in small applied electric fields. The FEM model was also developed to include Stern layer adsorption using the GDSL theory. The importance of Stern layer conduction and its effect on the mobility and dielectric response of colloidal dispersion has been reported by several researchers [14, 23-26]. The inclusion of the GDSL theory is novel in more than one way. First, no other FEM model can be found which implements the GDSL theory. Secondly, the equilibrium reaction assumption introduced in the GSDL theory was relaxed in the development of the FEM model so that the adsorption model is valid for very high frequencies ($\omega/2\pi > 1\ MHz$). Finally, the Maxwell stress tensor method was used in determining the forces on the particles.

In Section 4 through Section 7 four model problems were posed to validate the FEM model and investigate the effect of applied electric field strength. In Section 4 analytical solutions were used to validate the FEM model solution of the equilibrium EDL and the EDL in an applied electric field. After validating the solution of the EDL

for different dimensionless particle sizes (κa) the effect of the applied electric field strength was considered.

The solution of the nonlinear electrophoretic mobility of a dilute dispersion of colloidal particles was presented and discussed in Section 5. Weak applied electric field results of the static electrophoretic mobility compared well with published analytical solutions. And, for the first time, plots showing the dependence of the electrophoretic mobility on applied electric field strength were presented for different boundary conditions and particle permittivities. The dependence of the electrophoretic mobility was found to be a function of; (1) the strength of the surface charge, (2) the surface boundary condition, and (3) the particle permittivity. The mechanisms of the observed differences were described as being related to the relaxation and polarization of the EDL and the particle. Solutions of the dynamic electrophoretic mobility and its dependence on applied electric field frequency revealed significant errors in the FEM model. It was explained in Section 5 that the coordinate system used, i.e. fixed to the moving particle, resulted in a model which neglected the inertia of the particle. This assumption is not valid at high frequencies.

The results of Section 6 showed that the effect of a strong applied electric field on the forces acting on interacting particles is highly dependent on the boundary condition used. The results of Section 6.2.1 showed that when the constant surface potential boundary condition is used: (1) The repulsive force between the particles increases when strong electric fields are applied. And (2), large fluid circulation zones are observed for strong applied electric fields. The results of Section 6.2.2 showed that

when the constant surface charge boundary condition is used: (1) the force acting on interacting dielectric particles is not significantly increased by strong applied electric fields. And, (2) the forces acting on interacting metallic particles changes direction when strong applied electric fields are applied. The results of Section 6.2.3 showed that when the Stern layer boundary condition is used the force acting on interacting particles increases regardless of electric field strength, boundary condition, or particle permittivity. Also, the force acting on interacting metallic particles does not change direction when the Stern layer boundary condition is used.

The results of Section 7 demonstrated that the FEM model is capable of characterizing the electrokinetic forces acting on a particle interacting with a planar electrode which produces a non-uniform electric field. The ability to determine the force on a particle near an electrode is an important step in determining the applied electric field strength and frequency that causes assembly of colloidal structures. However, to accurately determine the AC electric field that would cause assembly improvements must be made. Important improvements to the FEM model are discussed in the following section.

8.2 CONCLUSIONS

Electric field guided assembly of colloids represents a new area in colloidal microfluidics where large AC electric fields are used to assemble colloidal structures. The ability to determine the applied electric field strength and frequency required to assembly colloidal structures and determine the dielectric response of these structures requires the use of the nonlinear electrokinetic equations (Section 2.2). In the preceding

sections we have presented the development, validation, and results of a robust finite element model which is based on the full nonlinear electrokinetic equations, uses and improves the GDSL theory to include the effect of Stern layer adsorption, and accurately determines the electrokinetic forces acting on a particle by using the MST method. In the following we review the conclusions of this work.

First, the constant surface potential boundary condition should not be used for particles in a strong applied electric field. The use of the constant surface potential boundary condition has continued to be used in the literature as a matter of legacy. Early electrophoretic models like the Smoluchowski's formula (Equation 4.2) related the electrophoretic mobility to the zeta potential, which is the constant potential at the slip plane, so it is difficult for researchers to abandon the idea the mobility is strictly a function of fictitiously constant surface potential. The mobility is a strong function of the zeta potential only when κa is quite large. Colloidal science is booming. Smaller and smaller particles are being produced and larger and larger electric fields are being applied.

Second, the use of a fixed coordinate system in the FEM model which is attached to the particle results in large errors at high frequencies because the particles inertia is neglected. That is, such a coordinate system is not an inertial frame of reference because it has nonzero acceleration. The solution to this problem is not trivial. There are essentially two techniques in use; the direct arbitrary Lagrangian-Eulerian finite element based methods (ALE-FEM) first developed by Hu[35], and methods based on the force coupling method (FCM), developed in a series of papers by Maxey et al[48]. The ALE-

FEM method requires meshing every particle in the system and remeshing at every time step. In fact, a space-time coupled solution may be required to achieve accurate steady state solutions. The FCM method can not accurately capture the EDL surrounding a particle, thus it has only been used with the electroosmotic slip boundary condition. Therefore, it could not be used for interacting particles.

Third, the results presented for the Stern layer boundary condition demonstrate that the mobility and dielectric response is highly dependent on Stern layer adsorption. However, the results presented were for adsorption of positive ions only. While this is typical it is not always the case. That is, some adsorption isotherms include non-specific adsorption of like charged ions. Also, most of the Stern layer parameters, e.g. diffusion coefficient and surface conductivity, are not experimentally obtainable making it necessary to develop the FEM model with GDSL model synergistically with experiments.

Finally, the FEM model developed in this work must be improved as describe above, but also it must be validated experimentally. The fact is that electric field guided assembly of colloidal structures may require extension of the electrokinetic theory. For example, although the theory presented in Section 2.2 does not assume the fluid and particle permittivities are not a function of applied electric field frequency, the fluid and particle permittivity are normally assumed to be constant. However, the applied electric field frequencies are considerably higher than normal operating frequencies. Thus, it may be necessary to include frequency dependent permittivities.

REFERENCES

[1] N.G. Green, H. Morgan, Journal of Physics D-Applied Physics 30 (1997) L41.

[2] P.R.C. Gascoyne, X.B. Wang, Y. Huang, F.F. Becker, IEEE Transactions on Industry Applications 33 (1997) 670.

[3] P. Bahukudumbi, W.N. Everett, A. Beskok, M.A. Bevan, G.H. Huff, D. Lagoudas, Z. Ounaies, Applied Physics Letters 90 (2007).

[4] K.H. Bhatt, S. Grego, O.D. Velev, Langmuir 21 (2005) 6603.

[5] S. Ahualli, A. Delgado, S.J. Miklavcic, L.R. White, Langmuir 22 (2006) 7041.

[6] S. Ahualli, A.V. Delgado, S.J. Miklavcic, L.R. White, J. Colloid Interface Sci. 309 (2007) 342.

[7] F.J. Arroyo, F. Carrique, S. Ahualli, A.V. Delgado, Phys. Chem. Chem. Phys. 6 (2004) 1446.

[8] F. Carrique, F.J. Arroyo, M.L. Jimenez, A.V. Delgado, J. Chem. Phys. 118 (2003) 1945.

[9] H. Ohshima, Colloid Polym. Sci. 277 (1999) 563.

[10] E.J.W. Verwey, J.T.G. Overbeek, K.v. Nes, Theory of the Stability of Lyophobic Colloids; the Interaction of Sol Particles having an Electric Double Layer. Elsevier Pub. Co., New York, 1948.

[11] W.B. Russel, D.A. Saville, W.R. Schowalter, Colloidal Dispersions. Cambridge University Press, Cambridge, New York, 1989.

[12] J. Lyklema, Fundamentals of Interface and Colloid Science. Academic Press, London, 1991.

[13] R.W. Obrien, L.R. White, J. Chem. Soc. Faraday Trans. II 74 (1978) 1607.

[14] C.S. Mangelsdorf, L.R. White, J. Chem. Soc. Faraday Trans. 86 (1990) 2859.

[15] E.H.B. Delacey, L.R. White, J. Chem. Soc. Faraday Trans. II 77 (1981) 2007.

[16] C.S. Mangelsdorf, L.R. White, J. Chem. Soc. Faraday Trans. 88 (1992) 3567.

[17] M.A. Preston, R. Kornbrekke, L.R. White, Langmuir 21 (2005) 9832.

[18] S.S. Dukhin, Adv. Colloid Interface Sci. 44 (1993) 1.

[19] S.S. Dukhin, Adv. Colloid Interface Sci. 35 (1991) 173.

[20] M.Z. Bazant, T.M. Squires, Phys. Rev. Lett. 92 (2004) 4.

[21] T.M. Squires, M.Z. Bazant, J. Fluid Mech. 509 (2004) 217.

[22] T.M. Squires, M.Z. Bazant, J. Fluid Mech. 560 (2006) 65.

[23] C.S. Mangelsdorf, L.R. White, J. Chem. Soc. Faraday Trans. 94 (1998) 2441.

[24] C.S. Mangelsdorf, L.R. White, J. Chem. Soc. Faraday Trans. 94 (1998) 2583.

[25] C.F. Zukoski, D.A. Saville, Journal of Colloid and Interface Science 114 (1986) 32.

[26] C.F. Zukoski, D.A. Saville, Journal of Colloid and Interface Science 114 (1986) 45.

[27] X.J. Wang, X.B. Wang, P.R.C. Gascoyne, Journal of Electrostatics 39 (1997) 277.

[28] T.B. Jones, M. Washizu, Journal of Electrostatics 37 (1996) 121.

[29] J.N. Reddy, An Introduction to Nonlinear Finite Element Analysis. Oxford University Press, Oxford, New York, 2004.

[30] J.N. Reddy, An Introduction to the Finite Element Method. 3rd ed., McGraw-Hill Higher Education, New York, 2006.

[31] A.V. Delgado, E. Gonzalez-Caballero, R.J. Hunter, L.K. Koopal, J. Lyklema, Pure Appl. Chem. 77 (2005) 1753.

[32] S.H. Lin, J.P. Hsu, S. Tseng, C.J. Chen, Journal of Colloid and Interface Science 281 (2005) 255.

[33] V.A. Murtsovkin, Colloid Journal 58 (1996) 341.

[34] J. Lyklema, Fundamentals of Interface and Colloid Science. Academic Press, London, 1991.

[35] H.H. Hu, N.A. Patankar, M.Y. Zhu, Journal of Computational Physics 169 (2001) 427.

[36] H. Ohshima, Journal of Colloid and Interface Science 180 (1996) 299.

[37] H. Ohshima, Journal of Colloid and Interface Science 185 (1997) 131.

[38] S.S. Dukhin, J. Lyklema, Langmuir 3 (1987) 94.

[39] J. Lyklema, H.P. Van Leeuwen, M. Minor, Adv. Colloid Interface Sci. 83 (1999) 33.

[40] H. Ohshima, Colloid Polym. Sci. 274 (1996) 1176.

[41] O.D. Velev, K.H. Bhatt, Soft Matter 2 (2006) 738.

[42] S. Gangwal, O.J. Cayre, M.Z. Bazant, O.D. Velev, Phys. Rev. Lett. 1 (2008).

[43] N.G. Green, A. Ramos, A. Gonzalez, H. Morgan, A. Castellanos, Phys. Rev. E 61 (2000) 4011.

[44] A. Gonzalez, A. Ramos, N.G. Green, A. Castellanos, H. Morgan, Phys. Rev. E 61 (2000) 4019.

[45] N.G. Green, A. Ramos, A. Gonzalez, H. Morgan, A. Castellanos, Phys. Rev. E 66 (2002).

[46] N.G. Green, A. Ramos, H. Morgan, Journal of Electrostatics 56 (2002) 235.

[47] K.H. Bhatt, O.D. Velev, Langmuir 20 (2004) 467.

[48] M.R. Maxey, B.K. Patel, International Journal of Multiphase Flow 27 (2001) 1603.

VITA

Name: James G. Steuber

Address: Arkansas Tech University

Corley 224

1811 North Boulder Avenue

Russellville, AR 72801-2222

Email Address: jsteuber@atu.edu

Education: B.S., Mechanical Engineering, Arkansas Tech University, 2001

M.EN., Mechanical Engineering, Texas A&M University, 2007

Ph.D., Mechanical Engineering, Texas A&M University, 2009